Penn Center *for*
Musculoskeletal Disorders

University of Pennsylvania

# 19th Annual Scientific Symposium/Retreat

Wednesday, November 15, 2023
Smilow Rubenstein Auditorium/Commons
8:15am-6:00pm
www.med.upenn.edu/pcmd/

# Table of Contents




We gratefully acknowledge the financial support provided by the National Institute of Arthritis, Musculoskeletal and Skin Diseases of the National Institutes of Health and the University of Pennsylvania, Perelman School of Medicine for our Center.

# Penn Center for Musculoskeletal Disorders
# Scientific Symposium Agenda

## November 15, 2023
## Smilow Rubenstein Auditorium ♦ University of Pennsylvania

08:15 – 09:15am **Registration and Poster Set-up**

09:15 – 09:35am **Welcome and Overview**
*Louis J. Soslowsky, Ph.D.*

09:35 – 10:20am **Session I: Affiliate Member Session** (Moderator: Xiaowei Sherry Liu, Ph.D.)
- *Stephanie G. Cone, Ph.D., University of Delaware, "Knee Joint Biomechanics in the Rat Model."*
- *William Querido, Ph.D., Temple University, "Imaging Bone Composition at Submicron Spatial Resolution: Applications of O-PTIR Spectroscopy."*
- *Sriram Balasubramanian, Ph.D., Drexel University, "Recent Advances in Computational Modeling for Pediatric Spine Deformity Diagnosis and Treatment."*

10:20 – 11:05am **Break and Poster Session (Even Numbered)**

11:05 – 11:50am **Session II: New Member Session** (Moderator: Ling Qin, Ph.D.)
- *Damaris N. Lorenzo, Ph.D., "A Novel Cytoskeleton-based Pathway Required for Maintenance of Mitochondria Dynamics and Energetics in Skeletal Muscle."*
- *Eric C. Liao, M.D., Ph.D., "Translation Gap in Functional Genomics of Orofacial Clefts."*
- *Holly L. Stewart, V.M.D., Ph.D., "Translational Animal Models for Understanding the Relationship Between Bone Marrow Lesions and Subchondral Bone Disease."*

11:50 – 12:30pm **Introduction: Penn Center for Achilles Tendinopathy Center of Research Translation**
- *Overview: Louis J. Soslowsky, Ph.D.*
- *Project 1: Nat Dyment, Ph.D.*
- *Project 2: Su Chin Heo, Ph.D.*
- *Core: Josh Baxter, Ph.D.*

12:30 – 01:30pm **Poster viewing and lunch (provided) in Smilow Commons**

1:30 – 02:30pm **Session III: Pilot Grantee Session** (Moderator: Maurizio Pacifici, Ph.D.)
- *Christoph Thaiss, Ph.D., "Intestinal Regulation of Exercise Performance."*
- *Michael Hast, Ph.D., "Exploring the Efficacy of Zinc as a Biomaterial for Orthopaedic Implants."*
- *Melike Lakadamyali, Ph.D., "Super-Resolution Imaging of Chromatin in Diseased Musculoskeletal Cells."*

02:30 – 03:15pm **Break and Poster Session (Odd Numbered)**

03:15 – 04:15pm **Keynote Speaker** (Moderator: Louis Soslowsky, Ph.D.)

*Keynote Speaker Title: "Navigating the NIH: The Program Director Perspective."*
*Charles Washabaugh, Ph.D., Orthopaedics Research Program Director at the National Institutes of Health*

*04:15 – 04:30pm* ***Final Comments Preceding Poster Session and Reception***

04:30 – 06:00pm **Poster Session, Presentation of Poster Awards and Reception in Smilow Commons**

Penn Center *for*
Musculoskeletal Disorders

University *of* Pennsylvania

# Center

# Components

Penn Center *for*
Musculoskeletal Disorders

University *of* Pennsylvania

# Center Overview

## OVERVIEW OF THE PENN CENTER FOR MUSCULOSKELETAL DISORDERS

**Director: Louis J. Soslowsky, PhD** (soslowsk@upenn.edu)
**Associate Director: Maurizio Pacifici, PhD** (PacificiM@email.chop.edu)

Musculoskeletal-related conditions in the United States account for 132 million visits to physicians' offices, 29 million visits to emergency rooms, 15 million hospital outpatient visits, and cost over $850 billion each year. Further, musculoskeletal injuries in the United States cause workers to miss more than 440 million days of work annually. In fact, more than one in four Americans has a musculoskeletal impairment. With the widespread increase in athletic and recreational activities, and the increase of the elderly population at large, these numbers are expected to rise substantially. Musculoskeletal injuries represent a critical health concern which must be better understood and better treated. To do so, a dedicated and focused strategic effort is required that optimizes research translation from the bench to the bedside in an efficient and effective manner.

The Penn Center for Musculoskeletal Disorders (PCMD) will continue to enhance the research productivity of, and provide critical resources and programs to, investigators to address multidisciplinary research strategies for musculoskeletal problems. The overall goal of this Center is to promote cooperative interactions among investigators, accelerate and enrich the effectiveness and efficiency of ongoing research, foster new collaborations and new research, and ultimately, translate our research efforts into better and new therapies for musculoskeletal disorders. The central theme of the Center will continue to be "Musculoskeletal Tissue Injury and Repair". This theme is broad (as it includes all musculoskeletal tissue types, such as bone, cartilage, disc, ligament, meniscus, muscle, and tendon), focused (as takes advantage of commonalities in approaches across tissue types), and clinically significant (as it fosters development of assays, procedures and knowledge in preclinical animal and human models of translational relevance). It is important to note that our PCMD is not a "bone center" nor is it a "muscle center". Rather, it is truly a "musculoskeletal center" and has emerged as the recognized home for musculoskeletal research across the Penn campus and as a technical and intellectual resource for the broader Philadelphia musculoskeletal research community.

One focus of our Center is to translate research themes, approaches, and paradigms that are consistent across different tissues. Musculoskeletal tissues have much in common and their similarities are often overlooked when focus is restricted to a single tissue type. For example, the role of inflammatory cytokines is well studied in several tissue injury and repair scenarios; yet specific findings in one tissue-type are not always known and applied in other tissues. Similarly, the availability of technologies for imaging blood vessel formation in vivo to monitor healing in a given tissue is not always known and available to researchers focusing on other tissues. Given that approaches routinely used to evaluate mechanisms in one tissue could aid researchers in other areas, our Center will work to foster this critical cross-talk.

To provide a further focus for our Center, we will continue to develop programs with an emphasis on small animal models utilizing unique and sophisticated methods that can cross length scales to pre-clinical large animal models and human testing. Although large animal models for many human diseases exist and are essential for translational studies, small animals (e.g., mouse and rat) have become more commonly used for fundamental discovery of disease mechanism and initial therapeutic development due to availability of transgenic and knockout approaches and molecular tools, low cost, ease of handling and housing, and other practical issues. However, performing certain assays and experiments in mice and rats can be challenging and these difficulties often cannot be overcome in single investigator laboratories. The PCMD will provide unique expertise and sophisticated analytical tools to investigate musculoskeletal tissues across length scales.

Thus, the primary overall aims of this Center are to enhance and advance the research productivity of investigators in musculoskeletal tissue injury and repair by:

**Aim 1:** Providing innovation within critical resource core facilities in areas that cross disciplines, length scales, and hierarchies. These core facilities are μCT Imaging, Biomechanics, and Histology.

**Aim 2:** Developing a pilot and feasibility grant program for investigators, with direct mentorship, whereby new approaches, ideas, and collaborations can be developed prior to seeking extramural funding.

**Aim 3:** Developing educational and research enrichment programs spanning tissue types, research approaches, and paradigms, through which members can learn from national leaders and from each other.

High quality musculoskeletal research is currently being conducted by many groups at Penn. While many bring sophisticated approaches to bear on musculoskeletal problems, few groups have the required expertise and facilities to perform high quality and specialized assays in their own labs. Furthermore, most investigators are not aware of approaches utilized, and results obtained, in other tissues that may have direct relevance on their research questions. Ultimately, close cooperation, communication, and collaboration among researchers across musculoskeletal tissue types and from a wide variety of disciplines will significantly enhance the research of our members. The Center will provide opportunities to integrate multi-disciplinary techniques to determine mechanisms for tissue function, injury, degeneration, repair, and regeneration, with the ultimate goal of advancing the diagnosis, treatment, and prevention of diseases and injuries of the musculoskeletal system.

In addition to the specific features described in this proposal, there is an intangible feature of our Center that should not be overlooked. Although our musculoskeletal program is strong nationally, the Penn biomedical research community is large and diverse. As such, the Center serves as an essential mechanism to highlight our successes and the importance and excitement of musculoskeletal research across campus, as well as to institutional leadership. Having a strong voice for musculoskeletal researchers is critical to support our collective and individual research goals. In these ways, the Center - with essential support from the P30 - has become and remains an indispensable resource and advocate for our community.

Penn Center *for*
Musculoskeletal Disorders

University *of* Pennsylvania

# Core I

# Biomechanics

## Biomechanics Core

**Core Director:** Michael Hast, Ph.D. (hast@pennmedicine.upenn.edu)

**Technical Director:**

The overall objective of the Biomechanics Core is to develop and provide a wide range of innovative biomechanical approaches to evaluate musculoskeletal tissue function in the context of damage, repair, and regeneration, and to provide training and funding for new projects and collaborations utilizing these assays. Over the last decade, our Biomechanics Core at the Penn Center for Musculoskeletal Disorders (PCMD) has grown into a thriving resource for the University of Pennsylvania and Philadelphia area musculoskeletal research community. In this submission, we will further expand our services to meet the increased demand for specialized techniques and develop new and innovative methods that address the multi-scale mechanics of musculoskeletal tissues. These developments will provide customized services that enhance the research productivity of our members. The Specific Aims of the Biomechanics Core are:

- To provide guidance and training on the capabilities, advantages, and disadvantages of the various methodologies to assess musculoskeletal tissue biomechanical function through formal educational enrichment programs and one-on-one interactions.

- To provide expertise and service for biomechanical assays of musculoskeletal tissues

- To develop innovative biomechanical testing techniques that will be applicable to Musculoskeletal research, and in particular those that provide information across tissue length scales.

- To provide funding for the development of new projects and collaborations and to develop preliminary and/or feasibility data for investigators.

Successful completion of these aims will significantly enhance the environment and the capabilities of researchers at the University of Pennsylvania, leading to new approaches to address musculoskeletal disorders and new collaborations between Center faculties who may have not previously included biomechanical function approaches in their musculoskeletal research programs.

Penn Center *for*
Musculoskeletal Disorders

University *of* Pennsylvania

# Core II

# Histology

## Histology Core

### Overview and Mission

The mission of the Penn Center for Musculoskeletal Disorders (PCMD) Histology Core is to provide comprehensive, high quality histology services to musculoskeletal researchers at the University of Pennsylvania and the broader research community.

The Specific Aims of the core are:

- To provide guidance and training on the capabilities, advantages, and disadvantages of the various methodologies to assess musculoskeletal tissue structure and composition through formal educational enrichment programs and one-on-one interactions.
- To provide expertise and service for histological and histomorphometric assays of musculoskeletal tissues.
- To develop new histologically-based techniques that will be applicable to musculoskeletal research.
- To provide funding for development of new projects and collaborations and to develop preliminary and/or feasibility data for investigators.

### Services Offered

The core offers a complete spectrum of services from sample preparation and processing, to sectioning, staining and analysis, with capabilities for paraffin, plastic and frozen histology. The core provides state of the art equipment in each of these areas, which can be accessed either on a self-service basis (upon completion of training) or a full-service basis through our full-time histology technician. Service fees are highly competitive, with significant subsidies offered for PCMD members.

- Consultation and protocol development (no charge for first 6 hours)
- Paraffin processing, embedding and sectioning
- Plastic processing and sectioning
- Frozen sectioning, including cryofilm method for undecalcified bone and teeth
- Routine histochemical staining
- Imaging and histoquantitation
- Training in histology techniques

If you are using the core for the first time, we highly recommend scheduling a meeting with one of the core co-directors and the core technician to discuss the scope of your project and specific needs.

We are very happy to provide letters of support for grant applications. To request a letter, please contact the core co-directors and provide the project title, a brief description of the project and core services you propose to use.

Please visit the core website for more information: www.med.upenn.edu/pcmd/histologymain.html

Co-Directors

Ling Qin, Ph.D. (Plastic and Frozen Histology)
Professor of Orthopaedic Surgery
qinling@pennmedicine.upenn.edu
215 898 6697

Lachlan Smith, Ph.D. (Paraffin Histology)
Associate Professor of Orthopaedic Surgery
lachlans@pennmedicine.upenn.edu
215 746 2169

Penn Center *for*
Musculoskeletal Disorders

University *of* Pennsylvania

# Core III

# MicroCT

## MicroCT Core

**Director: X. Sherry Liu, Ph.D.** (xiaoweil@pennmedicine.upenn.edu)

X-ray computed tomography (CT) imaging is an established and powerful tool to successfully analyze and clarify questions in musculoskeletal development, disease, injury and repair. In particular, the development of high-resolution micro-CT (μCT) over the last two decades has revolutionized the quantitative assessment of calcified and X-ray dense tissue morphology. With the capability of non-destructive, three-dimensional (3D) visualization of tissue structure, μCT has largely supplanted traditional histomorphometry and has become a gold standard for calcified tissue density and microstructure evaluation.

Due to the low intrinsic X-ray contrast of non-mineralized tissues, traditional applications of μCT in musculoskeletal research have been limited to mineralized tissue. However, the development of contrast-enhanced imaging methods has greatly broadened applications of μCT to include musculoskeletal soft tissues. This not only enables characterization of soft-tissue morphology, but also yields insight into tissue composition, such as glycosaminoglycan (GAG) density, which is essential for soft-tissue function and mechanics. Another important advance in the past decade is *in vivo* μCT imaging of living small animals, which enables longitudinal and non-invasive evaluation of changes in the same animal over time. This imaging strategy minimizes the number of animals required while enhancing statistical power. Further, high-resolution peripheral quantitative CT (HR-pQCT), a relatively recent μCT modality for clinical imaging of calcified tissue microstructure, has inaugurated a new era of non-invasive quantitative skeletal imaging and become a powerful tool for clinical research of musculoskeletal disorders. These new developments in μCT enable a detailed and quantitative understanding of the genetic influences on the skeleton, as well as modeling and remodeling events in hard and soft tissues during repair, treatment, and altered loading scenarios.

Over the past 4 years, our μCT Imaging Core (μCTIC) at the Penn Center for Musculoskeletal Disorders (PCMD) has grown into a thriving resource for the University of Pennsylvania and the region's musculoskeletal research community, serving a vibrant and growing base of 73 active PMCD faculty members and more than 170 trainees from their laboratories. The overall objective of the μCTIC is to develop and apply a wide range of standard and innovative μCT imaging approaches to evaluate musculoskeletal tissue development, disease, injury and repair, and to provide training and funding for new projects and collaborations utilizing these approaches.

The Specific Aims for the μCTIC are:

- To provide guidance and training on the capabilities, advantages, and limitations of using μCT imaging methods for musculoskeletal research through formal educational enrichment programs, online educational tutorials, and one-on-one interactions.
- To provide a range of μCT imaging resources, expertise, and services for the study of the structure, function, and physiology of the musculoskeletal system in laboratory animals and humans.
- To develop new μCT imaging-based techniques that support emerging needs and catalyze innovative musculoskeletal research.
- To provide funding for the development of novel, exploratory projects and collaborations, and to acquire preliminary and/or feasibility data for junior and senior investigators to seek external funding.

By implementing these Aims, the μCTIC will continue to serve as a unique and indispensable resource for researchers at UPenn, the Philadelphia region, and neighboring states, catalyzing innovative and high impact musculoskeletal research, and stimulating new collaborations between current and new PCMD members who may have not previously included μCT imaging approaches in their musculoskeletal research programs.

Penn Center *for*
Musculoskeletal Disorders

University *of* Pennsylvania

# Pilot Grant Program

**PENN CENTER FOR MUSCULOSKELETAL DISORDERS**
**PILOT AND FEASIBILITY GRANT PROGRAM**

The Penn Center for Musculoskeletal Disorders has an ongoing Pilot and Feasibility Grant Program. Submissions should be related to musculoskeletal tissue injury and repair which is the broad focus of the Center and Grants are only eligible for Center members (if you are not a member but would like to become one, please contact pcmd@pennmedicine.upenn.edu). For more information on our Cores and Center in general, please see our web site at www.med.upenn.edu/pcmd . The next Center grant submission deadline is February 14, 2024.

*Eligibility*

- Only Full Center members are eligible. If you are not currently a member, please go to the link: http://www.med.upenn.edu/pcmd/memberinfo.shtml
- Categories of applicants include: 1) Established investigators with a proposal to test the feasibility of a new or innovative idea in musculoskeletal tissue injury and repair representing a clear and distinct departure from their ongoing research, 2) Established investigators with no previous work in musculoskeletal tissue injury and repair interested in testing the applicability of their expertise on a problem in this area, and 3) New investigators without significant extramural grant support as a Principal Investigator to develop a new project.
- Pilot and Feasibility Grants must use at least one of the Center's Research Cores.
- Pilot project awardees are eligible for one year, with a second year to be considered (budgets will be for $20-50,000 per year and timelines should be for one or two years). The second year of funding, the dollar amount of which would only be for up to half the year one budget, will be considered based on the progress report submitted after the first year of funding and funding availability in the Center. Please note that second year funding will often not be awarded, and when awarded, will be done so primarily to new investigators; second year funding to senior investigators will be quite rare.
- It is expected that these Pilot grants will lead to funding through other independent, extramural mechanisms. Therefore, the likelihood of future extramural funding will enter into the evaluation of these proposals.

*Format*

- Applications should be formatted loosely in the style of an NIH R03 grant (http://grants.nih.gov/grants/guide/pa-files/PA-18-488.html). The main body of the application (Specific Aims through Research Design and Methods-sections 4-7 below) is limited to five pages. The application should be in a single pdf file. The format should be:

1) Cover Page (not NIH face page) with grant title, PI name (and co-PI name if applicable), affiliation, contact information
2) Budget and brief justification (note that equipment is not allowed) (Please use form PHS398, Page 4)
3) NIH Biosketch of PI (and co-PI if applicable) (in the new NIH format)
4) Specific Aims
5) Significance
6) Innovation
7) Approach
8) Brief Statement of Category of Investigator per guidelines above
9) Brief Statement of How this Funding will lead to other Extramural Funding
10) Human Subjects and/or Vertebrate Animal Subjects (if applicable)
11) Consultants (if applicable)
12) Literature Cited
13) Certification of Patient Oriented Research (if applicable)

The completed proposal are submitted via the PCMD website by going to the uploaded as a single PDF file.

Please do not hesitate to email pcmd@pennmedicine.upenn.edu with any questions or comments.

**Penn Center for Musculoskeletal Disorders Pilot & Feasibility Grants**
**(all grants awarded since inception of Center)**

***Awarded 2022-2023***
Chider Chen, Ph.D., Department of Oral and Maxillofacial Surgery/Pharmacology, School of Dental Medicine: "mTOR Mediated Ribosome Biogenesis Regulates CD4+ T Cell Activation in Osteoporotic Mice"

Carla R. Scanzello, M.D., Ph.D., Department of Medicine, Perelman School of Medicine: "Biophysical Regulation of Macrophage Fate and Function in OA"

Eiki Koyama, D.D.S., Ph.D., Translational Research Program in Pediatric Orthopaedics, Division of Orthopaedic Surgery, CHOP: "The Molecular Mechanisms Underlying Osteophyte Onset and Growth and its Pharmacologic Intervention"

***Awarded 2021-2022***
Christop Thaiss, Ph.D., Department of Microbiology, Perelman School of Medicine: "Microbiome Control of Musculoskeletal Physiology"

Melike Lakadamyali, Ph.D., Department of Physiology, Children's Hospital of Philadelphia, and Perelman School of Medicine: "Chromatin Structural Regulation of Chondrocyte Fate in Cell Therapy"

Michael Hast, Ph.D., Department of Orthopaedic Surgery, Perelman School of Medicine: "Development of Load-Bearing Trauma Implants Using Bioresorbable Zinc Alloy Scaffolds"

***Awarded 2020-2021***
Kyu Sang Joeng, Ph.D., Department of Orthopaedic Surgery, Perelman School of Medicine: "The Function of Mtorc1 Signaling in the Regulation of the Provisional Matrix During Tendon Healing" *(awarded extramural funding from NIH/NIAMS R01AR079486)*

Patrick Seale, Ph.D., Department of Cell and Developmental Biology, Institute for Diabetes, Obesity and Metabolism, Perelman School of Medicine: "Fat and Synovial Tissue Development and Disease Remodeling in Joints" *(awarded extramural funding from NIH/NIAMS R21 AR078650-01A1)*

Josh R. Baxter, Ph.D., Department of Orthopaedic Surgery, Perelman School of Medicine: "Stimulating Muscle-Tendon Healing by Prescribing Mechanical Loading" (awarded extramural funding from R21 AR081497-01)

***Awarded 2019-2020***
Jaimo Ahn, M.D., Department of Orthopaedic Surgery, Perelman School of Medicine: "The Interplay of Notch Suppression and Hypoxia on Bone Regeneration"

Riccardo Gottardi, Ph.D., Department of Pediatrics, CHOP Pulmonary Medicine: "Impact of Scaffold Microporosity in Guiding Local Stem Cell Differentiation for Osteochondral Repair"

Lachlan Smith, Ph.D., Departments of Neurosurgery/Orthopaedic Surgery: "Emergent Nucleus Pulposus Cell Heterogeneity during Intervertebral Disc Development and Growth" *(awarded extramural funding from NIH/NIAMS R21AR077261)*

***Awarded 2018-2019***
Miltiadis Zgonis, M.D., Department of Orthopaedic Surgery, Perelman School of Medicine: "Development, Maturation, and Function of Meniscal Radial Elements"

Joel Boerckel, Ph.D., Departments of Bioengineering/Orthopaedic Surgery, Perelman School of Medicine: "Role of Yap/Taz in Osteoprogenitor Cell-Induced Angiogenesis for Vascularized Bone Repair" *(awarded extramural funding from NIH/NIAMS R01AR074948 and R01AR073809)*

***Awarded 2017-2018***
Nathaniel Dyment, Ph.D., Department of Orthopaedic Surgery, Perelman School of Medicine: "Murine Anterior Cruciate Ligament Reconstruction Model to Understand the Cellular Origins and Mechanisms of Repair" *(awarded extramural funding from NIH/NIAMS R01 AR076381)*

Yangqing Gong, Ph.D., Department of Medicine, Perelman School of Medicine: "Role of Plasminogen in Mesenchymal Stem Cell Function and Post-Injury Bone Regeneration"

Carla Scanzello, M.D., Ph.D., Department of Medicine, Perelman School of Medicine: "Importance of Macrophage Responses in Osteoarthritis" *(awarded extramural funding from NIH/NIAMS R01 AR075737and T21 RX001757)*

Susan Volk, V.M.D., Ph.D., D.A.C.V.S., Department of Small Animal Surgery, School of Veterinary Medicine: "The Regulatory Roles of Type III Collagen in the Cartilage Collagen Network: Implications for Osteoarthritis Prevention and Treatment" (*awarded extramural funding from NIH/NIGMS R01 GM124091*)

***Awarded 2016-2017***
Joseph Baur, Ph.D., Department of Physiology Institute for Diabetes, Obesity and Metabolism, Perelman School of Medicine: "Targeting Nad Metabolism in Muscular Dystrophy" *(awarded extramural funding from Elysium Health)*

Yongwon Choi, Ph.D., Department of Pathology and Lab Medicine, Perelman School of Medicine: "Cell Adhesion Regulation of Multiple-Myeloma Induced Bone Destruction"

X. Sherry Liu, Ph.D., Department of Orthopaedic Surgery and Bioengineering, Perelman School of Medicine: "Mechanical Consequences of Modeling- vs. Remodeling-Based Bone Formation" *(awarded extramural funding from the NSF Award #1661858)*

Hongtao Zhang, Ph.D., Department of Pathology and Lab Medicine, Perelman School of Medicine: "Novel Cartilage-Targeting Fc Fusion Proteins as Novel and Effective Treatments For Osteoarthritis"

***Awarded 2015-2016***
Yejia Zhang, M.D., Ph.D., Department of Physical Medicine and Rehabilitation, Perelman School of Medicine: "Inhibition of Adam-8 to Reduce Intervertebral Disc Degeneration" *(Awarded extramural funding from the VA Meri t; VA Competitive Pilot Fund)*

Oren Friedman, M.D., Department of Otorhinolaryngology, Perelman School of Medicine: "Effect Of Injury To Cartilage And Recovery Treatment With Fgf-18"

Harvey Smith, M.D., Department of Orthopaedic Surgery, Perelman School of Medicine: "Impact of Pre-Culture and In Vivo Remobilization on Engineered Disc Replacement" *(Awarded extramural funding from the VA RX002274-01A1)*

Tejvir Khurana, M.D., Ph.D., Department of Physiology, Perelman School of Medicine: "Role of the Il-15 / Il-15rα Axis in Modulating Muscle-Tendon-Bone Adaptation and Repair"

***Awarded 2014-2015***
Joshua F. Baker, M.D., MSCE, Department of Rheumatology & Epidemiology, Perelman School of Medicine: "Assessment of Intramyocellular Fat Accumulation in Rheumatoid Arthritis Using MR Spectroscopy" *(Awarded extramural funding from American Federation for Aging Research Foundation)*

Russ P. Carstens, M.D., Department of Renal-Electrolyte and Hypertension Division, Perelman School of Medicine: "Roles of Epithelial Splicing Regulatory Proteins in Craniofacial Development" *(awarded extramural funding NIH 1R56DE024749 and awarded R01 NIDCR)*

Foteini Mourkioti, Ph.D., Department of Orthopaedic Surgery, Perelman School of Medicine: "A Novel Molecular Mechanism in Chronic Skeletal Muscle Injury" *(awarded extramural funding R01AR075914 NIH/NIAMS)*

Chamith Rajapakse, Ph.D., Department of Radiology, Perelman School of Medicine: "Biomechanics of Hip Fracture Assessed by MRI" *(Awarded extramural funding from the NIH R01 AR068382)*

***Awarded 2013-2014***
X. Sherry Liu, Ph.D., Department of Orthopaedic Surgery, Perelman School of Medicine: "Structure and Strength Recovery in Post-Lactation Bone" *(awarded extramural funding from the NIH R03 AR065145 and NSF Career Award #1653216)*

Ling Qin, Ph.D., Department of Orthopaedic Surgery, Perelman School of Medicine: "Novel Anabolic Treatment for Radiation-Induced Osteoporosis" *(awarded extramural funding from the NIH R01AR066098)*

Lachlan Smith, Ph.D., Departments of Neurosurgery/Orthopaedic Surgery, Perelman School of Medicine: "Molecular Mechanisms of Failed Vertebral Bone Formation in Mucopolysaccharidosis VII" *(awarded extramural funding from the NIH R03 AR065142 and the MPS Society)*

Hansell H. Stedman, M.D., Department of Surgery, Perelman School of Medicine: "Molecular Pattern Recognition in Acute and Chronic Injury to Muscle and Myotendinous Junction" *(awarded extramural funding from the NIH R01NS094705)*

***Awarded 2012-2013***
Jason Burdick, Ph.D., Department of Bioengineering, School of Engineering and Applied Science: "Acelluar Fibrous Scaffolds for Stem Cell Recruitment and Cartilage Repair" *(awarded extramural funding from the NIH R01 EB008722)*

James L. Carey, M.D., MPH, Department of Orthopaedic Surgery, Perelman School of Medicine: "Development of a Large Animal Model of Osteochondritis Dissecans" *(awarded extramural funding from the NIH R01 EB008722)*

Andrew Kuntz, M.D., Department of Orthopaedic Surgery, Perelman School of Medicine: "Effects of Intra-Articular Glenohumeral Injection of a Nonsteroidal Anti-Inflammatory Drug on Shoulder Joint Mechanics in a Rat Model"

Arjun Raj, Ph.D., Department of Bioengineering, School of Engineering and Applied Science: "Single Cell Analysis of Molecular and Micromechanical Heterogeneity in Mesenchymal Stem Cells and Engineered Tissues"

***Awarded 2011-2012***
Struan F.A. Grant, Ph.D., Department of Pediatrics, Children's Hospital of Philadelphia and Perelman School of Medicine: "Utilization of ChIP-seq to Identify Genes Regulated by Osterix"

Motomi Enomoto-Iwamoto, DDS, Ph.D., Department of Orthopaedic Surgery, Children's Hospital of Philadelphia and Perelman School of Medicine: "Tendon Repair by Retinoic Acid Receptor Agonists" *(awarded extramural funding from the NIH R21 AR062193)*

Ian N. Jacobs, M.D., Department of Otorhinolaryngology: Head and Neck Surgery, Children's Hospital of Philadelphia and Perelman School of Medicine: "A Pilot Study for the Development of a Rabbit In-Vivo Tissue- Engineered Cartilage Graft for Pediatric Laryngotracheal Reconstruction" *(awarded extramural funding from The Triological Society)*

***Awarded 2010-2011***
Susan W. Volk, VM.D., Ph.D., Dipl ACVC, Department of Small Animal Surgery, School of Veterinary Medicine: "The Role of Type III Collagen in Bone Repair and Regeneration"

Jaimo Ahn, M.D., Ph.D., Department of Orthopaedic Surgery, Perelman School of Medicine: "Toward the Identification of Molecular Pathway Alterations in Aged Fracture Healing: A Pilot Study Utilizing a Genetic Model of Senescence" *(awarded extramural funding from the NIH R03 AG040670)*

Shannon Fisher, M.D., Ph.D., Department of Cell and Developmental Biology, Perelman School of Medicine: "Requirement for Osterix in Skull Formation and Maintenance of Adult Bone in Zebrafish" *(awarded extramural funding from the NIH R21 DE021509)*

***Awarded 2010-2011 (Jointly with IOA)***
Olena Jacenko, Ph.D., Department of Animal Biology, School of Veterinary Medicine: "Aging of the Hematopoietic Niche" *(awarded extramural funding from the NIH R01 DK088334-01)*

Eileen M. Shore, Ph.D., Departments of Orthopaedic Surgery and Genetics, Perelman School of Medicine: "Modulation of Progenitor Cell Differentiation through BMP Signaling" *(awarded extramural funding from the NIH R01 AR041916-15)*

Kurt D. Hankenson, DVM, Ph.D., Department of Animal Biology, School of Veterinary Medicine: "Notch Signaling in Bone Regeneration" *(awarded extramural funding from the DOD CDMRP)*

***Awarded 2009-2010***
Ling Qin, Ph.D., Department of Orthopaedic Surgery, Perelman School of Medicine: "Mechanisms of EGFR Action on Bone" *(awarded extramural funding from the NIH R01 DK095803)*

Steven Scherer, M.D., Ph.D., Department of Neurology, Perelman School of Medicine: "Are N-cadherin and L1 Adhesion Molecules Required for Recovery of Muscle Strength after Nerve Injury?"

Nader M. Hebela, M.D., Department of Orthopaedic Surgery, Perelman School of Medicine: "A Pre-Clinical Rodent Model of Intervertebral Disc Autograft Transplant" *(awarded extramural funding from the DOD/CDMRP/PROP OR090090)*

***Awarded 2008-2009***
Sunday O. Akintoye, BDS, DDS, MS, Department of Oral Medicine, School of Dental Medicine: "Orofacial Bone Marrow Stromal Cells Promote Bisphosphonate-Associated Jaw Osteonecrosis" *(awarded extramural funding from the NIDCR R21 DE022826)*

Margaret M. Chou, Ph.D., Departments of Cell and Developmental Biology, Perelman School of Medicine: "Mechanisms of TRE17/USP6 Function in the Etiology of Aneurysmal Bone Cyst" *(awarded extramural funding from the NIH-NCI R01 CA168452 and R21-CA18601)*

Kenneth W. Leichty, M.D., Department of Surgery, Perelman School of Medicine: "The Role of Inflammation in Regenerative Fetal Tendon Wound Healing" *(awarded extramural funding from the NIH DP2 DK083085)*

Kathleen M. Loomes, M.D., Department of Pediatrics, Children's Hospital of Philadelphia: "The Role of Jag1 in Osteogenesis"

Eileen M. Shore, Ph.D., Departments of Orthopaedic Surgery and Genetics, Perelman School of Medicine: "Analysis of an ACVR1 Knock-in Mouse Model for FOP*" (awarded extramural funding from the NIH R01 AR041916-15S1)*

***Awarded 2007-2008***
Sherrill L. Adams, Ph.D., Department of Biochemistry, School of Dental Medicine: "Collagen III-deficient Mice as a Model for Musculoskeletal Wound Repair"

Kurt D. Hankenson, DVM, Ph.D., Department of Animal Biology, School of Veterinary Medicine: "Regulation of Bone Formation by Novel Activators of Canonical Wnt Signaling"

***Awarded 2006-2007***
Robert J. Pignolo, M.D., Ph.D., Department of Medicine, Perelman School of Medicine: "Stem Cell Rescue of the Osteoporotic Phenotype in a Mouse Model of Accelerated Aging" *(awarded extramural funding from the NIH R01 AG028873)*

Robert L. Mauck, Ph.D., Department of Orthopaedic Surgery, Perelman School of Medicine "Meniscus Repair with a Novel Aligned Nanofiber Scaffold" *(awarded extramural funding from the NIH R01 AR056624 and the VA RR & D)*

Christopher S. Chen, M.D. Ph.D., Department of Bioengineering, School of Engineering and Applied Science: "Mechanotransduction in Mesenchymal Stem Cells" *(awarded partial funding as Co-Investigator on NIH P41 EB001046)*

Pedro K. Beredjiklian, M.D., Department of Orthopaedic Surgery, Perelman School of Medicine: “Role of Hyaluronic Acid Receptors in Tendon Healing” (*awarded extramural funding from the NIH R21 AR052393*)

Penn Center for Musculoskeletal Disorders

University of Pennsylvania

# Visiting Professorship Series 2023-2024

**Visiting Professorship Series-Academic Year 2023-2024**

**Tuesday, May 14, 2024, 130pm-230pm/CRB Austrian Auditorium/Joint with IRM**
*Title: "Interrogating Osteoclast Biology by Live Cell Imaging Reveals Novel Insight into their Cellular and Resorption Dynamics"*
**Sarah L. Dallas, Ph.D.,** University of Missouri Curator's Distinguished Professor, Lee M. and William Lefkowitz Endowed Professor, University of Missouri-Kansas City

**Monday, April 15, 2024, 3pm-4pm/CRB Austrian Auditorium/Joint with Pennsylvania Muscle Institute**
*Title: "Mechanisms of Hippo Pathway Dysregulation in Sarcomas."*
**Munir Tanas, M.D.,** Associate Professor of Pathology, Carver College of Medicine, University of Iowa Health Care

**Tuesday, March 19, 2024, 130pm-230pm/CRB Austrian Auditorium/Joint with IRM**
*Title: "Bone Building Molecular Targets: Lessons from Mechanical Signaling in Skeletal Tissues"*
**Alexander Robling, Ph.D.,** Chair, Anatomy, Cell Biology & Physiology, Indiana University, School of Medicine

**Tuesday, February 20, 2024, 130pm-230pm/CRB Austrian Auditorium**
*Title: TBD*
**Ronen Schweitzer, Ph.D.,** Interim Director of Research, Shriners Hospital for Children – Portland, Professor in Orthopaedics and Cell, Developmental and Cancer Biology, Oregon Health & Science University

**Tuesday, January 23, 2024, 130pm-230pm/CRB Austrian Auditorium/Joint with IRM**
*Title: "Myostatin: A Molecular Rheostat for Muscle Mass"*
**Se-Jin Lee, M.D., Ph.D.,** Presidential Distinguished Professor, Genetics and Genome Sciences, Joint Appointment, The Jackson Laboratory for Genomic Medicine, MD/PhD Executive Committee Chair, University of Connecticut

**Tuesday, December 12, 2023, 130pm-230pm/CRB Austrian Auditorium**
*Title: "Understanding Joint Health through Whole Joint Biomechanics and Mechanobiology"*
**Hai Yao, Ph.D.,** Professor and Ernest R. Norville Endowed Chair, Associate Chair for CU-MUSC Bioengineering Program, Department of Bioengineering, Clemson University

**Wednesday, November 15, 2023, 8am-630pm/Smilow Rubinstein Auditorium & Commons**
**Annual Scientific Symposium**
*Title: "Navigating the NIH: The Program Director Perspective"*
**Keynote Speaker: Charles Washabaugh, Ph.D., Program Director, National Institute of Arthritis and Musculoskeletal and Skin Diseases, National Institute of Health**

**Tuesday, October 17, 2023, 130pm-2:30pm/CRB Austrian Auditorium**
*Title: "My Journey to Demystify the Marvelous Misunderstood Meniscus"*
**Suzanne Maher, Ph.D.,** Senior Scientist, Research Institute, Co-Director, Orthopedic Soft Tissue Research Program, Research Institute, Associate Director, Department of Biomechanics, Hospital for Special Surgery

**Tuesday, September 12, 2023, 130pm-2:30pm/CRB Austrian Auditorium**
*Title: "Decorin: A Central Player of Cartilage Extracellular Matrix in Health and Disease"*
**Lin Han, Ph.D.,** Associate Professor, School of Biomedical Engineering, Science and Health Systems
Drexel University

**Visiting Professorship Series-Academic Year 2022-2023**

**Tuesday, May 23, 2023, 12:00pm-1:00pm/CRB Austrian Auditorium/Joint with IRM**
*Title: "Thinking Outside the Joint: Can Targeting the Intestine support OA Disease Modification?"*
**Michael Zuscik, Ph.D.,** Mack Clayton Professor and Vice Chair of Research, Department of Orthopedics, University of Colorado

**Tuesday, April 18, 2023, 1:30pm-2:30pm/CRB Austrian Auditorium**
*Title: Biomechanical & Energetic Factors Associated with Physical Activity Limitations in Osteoarthritis*
**Kharma C. Foucher, M.D., Ph.D.**, Associate Professor, Department of Kinesiology and Nutrition
Director, Biomechanics and Clinical Outcomes Laboratory, University of Illinois at Chicago

**Tuesday, March 28, 2023, 1:30pm-2:30pm/CRB Austrian Auditorium**
*Title: From Bench to Human Trials: How did we get there?*
**Patrick Mooney, M.D., Ceo and Director**
**Christopher Natale, Ph.D., Co-Founder and VP, Research**
Linnaeus Therapeutics

**Tuesday, February 21, 2023, 130pm-2:30pm/CRB Austrian Auditorium**
*Title: Immunoengineering in the Musculoskeletal System*
**Jennifer Elisseeff, Ph.D.,** Morton Goldberg Professor; Wilmer Eye Institute and Biomedical Engineering
Translational Tissue Engineering Center; Board of Maryland's Technology Development Corporation (TEDCO)
Johns Hopkins University

**Tuesday, January 24, 2023, 1:30pm-2:30pm/CRB Austrian Auditorium**
*Title: Life, Death and Transformation in the Transition Zone, Implications for Bone Healing*
**Ralph Marcucio, Ph.D.,** Professor of Orthopaedic Research; Director, Laboratory for Skeletal Regeneration
Orthopaedic Trauma Institute; Co-Director, Oral and Craniofacial Science Graduate Program, University of California, San Francisco

**Tuesday, December 13, 2022, 1:30pm-2:30pm/CRB Austrian Auditorium**
*Title: The Physiology and Pathophysiology of FGF23 in Skeletal and Mineral Biology*
**Michael T. Collins, M.D., FASBMR**
Senior Investigator; Chief, Section on Skeletal Disorders and Mineral Homeostasis; National Institute of Dental and Craniofacial Research, National Institute of Health

**Wednesday, November 16, 2022, 8:15am-6:30pm/Smilow Rubinstein Auditorium/Commons**
ANNUAL SCIENTIFIC SYMPOSIUM (all day event)
**Keynote Speaker - Lori A. Setton**, Ph.D., Lucy and Stanley Lopata Distinguished Professor & Chair of Biomedical Engineering, Washington University in St. Louis

**Tuesday, October 25, 2022, 1:30pm — 2:30pm**
*Title: Biomanufacturing, Biomaterials and Biomechanics for Improved Treatment of Volumetric Muscle Loss Injuries*
**Chuanju Liu, Ph.D.**
Professor and Director, Translational Orthopaedic Research Laboratory; Department of Orthopaedic Surgery and Cell Biology, NYU Grossman School of Medicine

**Tuesday, September 20, 2022, 1:30pm — 2:30pm**
*Title: Building Tissues Engineering Complexity Through Biomaterial Design*
Brendan A. Harley, Sc.D., Robert W. Schaefer Professor, Department of Chemical and Biomolecular Engineering, Cancer Center at Illinois (CCIL); Carl R. Woses Institute for Genomic Biology, University of Illinois at Urbana-Champaign

Penn Center for Musculoskeletal Disorders

University of Pennsylvania

# Symposium Participants

| Last Name | First Name | Email | Affiliation |
|---|---|---|---|
| Agnello | Kimberly | kagnello@vet.upenn.edu | UPenn |
| Angelozzi | Marco | angelozzim@chop.edu | CHOP |
| Assi | Sereen | Assi@seas.upenn.edu | UPenn |
| Azar | Tala | talaazar@seas.upenn.edu | UPenn |
| Balasubramanian | Sriram | sb939@drexel.edu | Drexel University |
| Baldomero | Genevieve | genevieve.m.baldomero@gmail.com | Jefferson University |
| Baxter | Josh | josh.baxter@pennmedicine.upenn.edu | UPenn |
| Bergstrom | Annika | abergs01@villanova.edu | Villanova University |
| Berlew | Erin | erinber@seas.upenn.edu | UPenn |
| Bertels | Josh | bertelsj@chop.edu | CHOP |
| Betts | Rebecca | rebecca.betts@pennmedicine.upenn.edu | UPenn |
| Binder-Markey | Benjamin | bb983@drexel.edu | Drexel University |
| Blanch | Tyler | tblanch@seas.upenn.edu | UPenn |
| Blank | Jon | jonathon.blank@pennmedicine.upenn.edu | UPenn |
| Boakye | Lorraine | lorraine.boakye@pennmedicine.upenn.edu | UPenn |
| Bockman | Jenna | jenna.bockman@pennmedicine.upenn.edu | UPenn |
| Boerckel | Joel | boerckel@pennmedicine.upenn.edu | UPenn |
| Bonelli | Hannah | hbonelli@seas.upenn.edu | UPenn/CHOP |
| Boyes | Madeline | mboyes@vet.upenn.edu | UPenn |
| Burt | Kevin | kevin.burt@pennmedicine.upenn.edu | UPenn |
| Butler | Rachel | rmbutler@upenn.edu | UPenn |
| Canonicco | Maria | mjc7530@psu.edu | Penn State University |
| Capalbo | Maggs | mhc5270@psu.edu | Penn State University |
| Carey | James | james.carey@pennmedicine.upenn.edu | UPenn |
| Casila | Joseph Lance | jcasila@seas.upenn.edu | UPenn |
| Chandrashekar | Harshini | hchand@seas.upenn.edu | UPenn |
| Chen | Kailin | ckailin@seas.upenn.edu | UPenn |
| Chen | Mengcun | chenmc0603@gmail.com | Jefferson University |
| Chen | Chider | chenc10@upenn.edu | UPenn |
| Chen | Mei | chenmei@pennmedicine.upenn.edu | UPenn |
| Chen | Xiaowen | xwchen@pennmedicine.upenn.edu | UPenn |
| Cheng | Zhiliang | zcheng@seas.upenn.edu | UPenn |
| Ching | Stephen | chings@pennmedicine.upenn.edu | UPenn |
| Cho | Peter | dc3457@drexel.edu | Drexel University |
| Choi | Eirene | exc125@students.jefferson.edu | Jefferson University |
| Ciuciu | Alexandra | axc497@students.jefferson.edu | Jefferson University |
| Collins | John | john.collins2@jefferson.edu | Jefferson University |
| Cone | Stephanie | sgcone@udel.edu | University of Delaware |
| Cui | Mingshu | Mingshu.Cui@jefferson.edu | Jefferson University |
| Dehghani | Bijan | bijan.dehghani@pennmedicine.upenn.edu | UPenn |
| Dev | Isha | ishadev@temple.edu | Temple Univeristy |
| Dinella | Susan | sdinella@pennmedicine.upenn.edu | UPenn |
| DiStefano | Michael | micdis@seas.UPenn.edu | UPenn |
| Duffy | Michael | mpduffy@upenn.edu | UPenn |
| Duncan | Andrew | andrew.duncan@pennmedicine.upenn.edu | UPenn |
| Dyment | Nat | dyment@pennmedicine.upenn.edu | UPenn |
| Eekhoff | Jeremy | jeremy.eekhoff@pennmedicine.upenn.edu | UPenn |
| Evans | Mary Kate | mkevans@seas.upenn.edu | UPenn |
| Fainor | Matthew | matthew.fainor@pennmedicine.upenn.edu | UPenn |
| Foster | Brad | Brf5277@psu.edu | Penn State University |
| Frankfurter | Max | maxwell.frankfurter@pennmedicine.upenn.edu | UPenn |
| Freeman | Terry | theresa.freeman@jefferson.edu | Jefferson University |
| Friday | Chet | Chet.Friday@Pennmedicine.upenn.edu | UPenn |
| Fung | Ashley | afung@seas.upenn.edu | UPenn |
| Gaesser | Angela | agaesser@upenn.edu | UPenn |
| Gao | Siqi | siqi.gao@pennmedicine.upenn.edu | UPenn |
| Gibson | Eve | Eve.Gibson@Pennmedicine.upenn.edu | UPenn |
| Godshall | Stanton | stanton.godshall@pennmedicine.upenn.edu | UPenn |
| Gottardi | Riccardo | gottardir@chop.edu | UPenn/CHOP |

| Last Name | First Name | Email | Affiliation |
|---|---|---|---|
| Grant | Struan | grants@chop.edu | CHOP/UPenn |
| Guo | Hanli | hanliguo1025@gmail.com | UPenn |
| Halloran | Daniel | hallorand@chop.edu | CHOP |
| Hast | Mike | hast@pennmedicine.upenn.edu | UPenn |
| He | Qi | qi.he@pennmedicine.upenn.edu | UPenn |
| Heo | Su Chin | heosc@pennmedicine.upenn.edu | UPenn |
| Heo | Yuna | yunaheo@seas.upenn.edu | UPenn |
| Hickok | Noreen | Noreen.Hickok@jefferson.edu | Jefferson University |
| Hilliard | Brendan | hilliard@temple.edu | Temple University |
| Hilman | Melanie | mhilman@seas.upenn.edu | UPenn |
| Houston | Bryson | bryson.houston@pennmedicine.upenn.edu | UPenn |
| Hubmacher | Dirk | dirk.hubmacher@mssm.edu | Mount Sinai |
| Hullfish | Todd | todd.hullfish@pennmedicine.upenn.edu | UPenn |
| Iyer | Keerthana | keerthana.iyer@pennmedicine.upenn.edu | UPenn |
| Jacenko | Olena | jacenko@vet.upenn.edu | UPenn |
| Jalloh | Umu | jalloh79@students.rowan.edu | Rowan University |
| Jester | Cherie | cherieg@pennmedicine.upenn.edu | UPenn |
| Jiang | Xi | jiangxi@pennmedicine.upenn.edu | UPenn |
| Jin | Vincent | yvjin22@seas.upenn.edu | UPenn |
| Joeng | Kyu Sang | joeng@pennmedicine.upenn.edu | UPenn |
| Johnson | Talayah | talayahj@seas.upenn.edu | UPenn |
| Jones | Erica | emjones7@pennmedicine.upenn.edu | UPenn |
| Jones | Brandon | Bcjones@seas.upenn.edu | UPenn |
| Kamalitdinov | Tim | timkam@seas.upenn.edu | UPenn |
| Kamona | Nada | nkamona@seas.upenn.edu | UPenn |
| Karvande | Anirudha | karvandea@chop.edu | CHOP |
| Kim | Dong Hwa | kimd1@pennmedicine.upenn.edu | UPenn |
| Kim | Sung Yeon | sungyk@seas.upenn.edu | UPenn |
| Kim | Minwook | kimmin@rowan.edu | Rowan/Virtua |
| Koehnken Sawall | Jasmin | koehnkensj@chop.edu | CHOP |
| Kokubun | Takanori | kokubun-takanori@spu.ac.jp | UPenn |
| Kolasinski | Sharon | sharon.kolasinski@pennmedicine.upenn.edu | UPenn |
| Koo | Bonhyeock | Bonhyeock.Koo@penmedicine.upenn.edu | UPenn |
| Kotsaris | Georgios | Georgios.kotsaris@pennmedicine.upenn.edu | UPenn |
| Kupratis | Meghan | meghan.kupratis@pennmedicine.upenn.edu | UPenn |
| Kust | Shu-Jin | shu-jin.kust@temple.edu | Temple |
| Kwon | Michelle | michelle.kwon@pennmedicine.upenn.edu | UPenn |
| Ladik | Maria | mml025@jefferson.edu | Jefferson University |
| Lakadamyali | Melike | melikel@pennmedicine.upenn.edu | UPenn |
| Landis | Cassidy | cassidy.landis@pennmedicine.upenn.edu | UPenn |
| Lanzolla | Giulia | giulia.lanzolla@pennmedicine.upenn.edu | UPenn |
| Lashbrooks | Elisabeth | elisabeth.lashbrooks@jefferson.edu | Jefferson University |
| Laslow | Brittany | Brittany.Laslow@Pennmedicine.upenn.edu | UPenn |
| Lee | Se-Hwan | Se-Hwan.Lee@pennmedicine.upenn.edu | UPenn |
| Lee | Ji-Hyung | ji-hyung.lee@pennmedicine.upenn.edu | UPenn |
| Lee | Hannah | hannah.lee1@pennmedicine.upenn.edu | UPenn |
| Lee | Wonsae | wonsae.lee@pennmedicine.upenn.edu | UPenn |
| Lefebvre | Veronique | lefebvrev1@chop.edu | CHOP |
| Lemmon | Elisabeth | elemmon@vet.upenn.edu | UPenn |
| Levin, MD | Scott | scott.levin@pennmedicine.upenn.edu | UPenn |
| Li | Anita | anita.li@villanova.edu | Villanova |
| Li | Lun | Lun.li@pennmedicine.UPenn.edu | UPenn |
| Li | Qiaoli | Qiaoli.li@jefferson.edu | Jefferson University |
| Li | Zizhao | lizizhao@seas.upenn.edu | UPenn |
| Liao | Eric | liaoce@chop.edu | CHOP |
| Linardi | Renata | rlinardi@upenn.edu | UPenn |
| Liu | Sherry | xiaoweil@pennmedicine.upenn.edu | UPenn |
| Lorenzo | Damaris | damaris.lorenzo@pennmedicine.upenn.edu | UPenn |
| Lounev | Vitali | vlounev@pennmedicine.upenn.edu | UPenn |
| Love | Stacy | lovest@rowan.edu | Rowan University |

| Last Name | First Name | Email | Affiliation |
|---|---|---|---|
| Lozano Pérez | Mística | Mistica@seas.upenn.edu | UPenn |
| Lucas | Abigail | abigail.lucas@jefferson.edu | Jefferson University |
| Ma | Nuoying | nuoying@seas.upenn.edu | UPenn |
| Madi | Rashad | rmadi@upenn.edu | UPenn |
| Mansalay | Abu | abu.mansalay@students.jefferson.edu | Jefferson University |
| Maparu | Auhin | auhin.maparu@pennmedicine.upenn.edu | UPenn |
| Marcelin | Jonathan | jmarce@seas.upenn.edu | UPenn |
| Marcellus | Yveeka | ym429@drexel.edu | Drexel University |
| Mauck | Rob | lemauck@pennmedicine.upenn.edu | UPenn |
| McGinley | Timothy | tm3292@drexel.edu | Drexel University |
| McLaughlin | Eric | eric.mclaughlin@jefferson.edu | Jefferson University |
| Mehmood | Sofia | sofia.mehmood@temple.edu | Temple University |
| Mejias-Rivera | Loreilys | loreilys.mejias@pennmedicine.upenn.edu | UPenn |
| Melvage | Autumn | autumn.melvage@students.jefferson.edu | Jefferson University |
| Meyers | Michelle | meyersm9@seas.upenn.edu | UPenn |
| Miller | Liane | liane.miller@pennmedicine.upenn.edu | UPenn |
| Moreira Perez | Matheus | mym582@jefferson.edu | Jefferson University |
| Mourkioti | Foteini | fmour@pennmedicine.upenn.edu | UPenn |
| Mundy | Chrissy | matticolac@chop.edu | CHOP |
| Murphy | Lance | lance.murphy@pennmedicine.upenn.edu | UPenn |
| Nadruz | Veridiana | vnadruz@upenn.edu | UPenn |
| Narayan | Sweta | sweta.narayan@pennmedicine.upenn.edu | UPenn |
| Nijsure | Madhura | mnijsure@seas.upenn.edu | UPenn |
| Ning | Yue | ny@pennmedicine.upenn.edu | UPenn |
| Niu | Yunyi | yunyiniu@seas.upenn.edu | Upenn |
| Nixon | Jacob | jacobnix@seas.upenn.edu | UPenn |
| Nuethong | Sittinon | snueth@seas.upenn.edu | UPenn |
| Nuss | Courtney | cnuss@pennmedicine.upenn.edu | UPenn |
| O'Brien | Erin | emo38@drexel.edu | Drexel University |
| Orozco | Brianna | orozco.brianna10@gmail.com | UPenn |
| Ortved | Kyla | kortved@vet.upenn.edu | UPenn |
| Pace | Jesse | jesse.pace@pennmedicine.upenn.edu | UPenn |
| Pacifici | Maurizio | pacificim@chop.edu | CHOP |
| Pan | Xuanbei | xuanbeip@seas.upenn.edu | UPenn |
| Panebianco | Christopher | christopher.panebianco@pennmedicine.upenn.edu | UPenn |
| Panek | Wojtek | wkp@upenn.edu | UPenn |
| Pedaprolu | Krishna | kup225@psu.edu | Penn State University University |
| Pereda | Guillermo | Guillermo.Pereda@Pennmedicine.upenn.edu | UPenn |
| Pham | Kenneth | Kenneth.pham@pennmedicine.upenn.edu | UPenn |
| Piasecki | Liz | elizabeth.piasecki@pennmedicine.upenn.edu | UPenn |
| Pinto | Felicia | felicia.pinto@pennmedicine.upenn.edu | UPenn |
| Pleshko | Nancy | npleshko@temple.edu | Temple University |
| Qin | Ling | qinling@pennmedicine.upenn.edu | UPenn |
| Querido | William | william.querido@temple.edu | Temple University |
| Rajagopal | Karthikeyan | Karthikeyan.Rajagopal@Pennmedicine.Upenn.edu | UPenn |
| Rajapakse | Chamith | chamith@pennmedicine.upenn.edu | UPenn |
| Rajpar | Sam | ibtesam.rajpar@jefferson.edu | Jefferson University |
| Ramesh | Sadhana | rameshs1@chop.edu | CHOP |
| Rizokulova | Shahrizoda | shahrizoda.rizokulova@gmail.com | Temple University |
| Roberts | Doug | doug.roberts@pennmedicine.upenn.edu | UPenn |
| Russo | Devyn | devyn.russo@pennmedicine.upenn.edu | UPenn |
| Sang | Wen | wen.sang@pennmedicine.upenn.edu | UPenn |
| Santillan | Jaime | jaime.santillan@pennmedicine.upenn.edu | UPenn |
| Santos | Marina | marina.santos07@hotmail.com | UPenn |
| Scanzello | Carla | cscanz@pennmedicine.upenn.edu | UPenn |
| Schaer | Thomas | tpschaer@upenn.edu | UPenn |
| Schipani | Ernestina | Ernestina.Schipani@Pennmedicine.upenn.edu | UPenn |
| Sedigh | Ashkan | asedigh@villanova.edu | Villanova University |
| Seidl | Elizabeth | eseidl@seas.upenn.edu | UPenn |
| Seravello | Donna | donnaser@upenn.edu | UPenn |

| Last Name | First Name | Email | Affiliation |
|---|---|---|---|
| Sharma | Riti | ritis@seas.upenn.edu | University of Pennsylvania |
| Shore | Eileen | shore@pennmedicine.upenn.edu | UPenn |
| Silvestro | Elizabeth | esilve@seas.upenn.edu | UPenn |
| Slaweski | Amber | ays396@jefferson.edu | Jefferson University |
| Smith | Lachlan | lachlans@pennmedicine.upenn.edu | UPenn |
| Smith | Aiden | aiden.smity@gmail.com | UPenn |
| Smith | Carly | cxs947@students.jefferson.edu | Jefferson University |
| Smith | Gail | smithgk@upenn.edu | UPenn |
| Smith | Kyra | smithkw@chop.edu | UPenn/CHOP |
| Sonchen | Anna | annasonchen@gmail.com | Jefferson University |
| Song | Ke | ke.song@pennmedicine.upenn.edu | UPenn |
| Soslowsky | Lou | soslowsk@upenn.edu | UPenn |
| Spiller | Kara | kls35@drexel.edu | Drexel |
| Spitsin | Sergei | Spitsins@upenn.edu | UPenn |
| Stewart | Holly | hstew@vet.upenn.edu | UPenn |
| Stoeckl | Brendan | bstoeckl@pennmedicine.upenn.edu | UPenn |
| Strand | Katy | strandk@seas.upenn.edu | UPenn |
| Sudhesh | Reshma | reshma.sudhesh@temple.edu | Temple University |
| Sun | Wei | wei.sun@pennmedicine.upenn.edu | Upenn |
| Sung | Samuel | ss4954@drexel.edu | Drexel |
| Szczesny | Spencer | ses297@psu.edu | Penn State University University |
| Tamburro | Maggie | margaret.tamburro@pennmedicine.upenn.edu | UPenn |
| Tang | Waixing | waixing@pennmedicine.upenn.edu | PCMD Histology Core |
| Tate | Quinn | quinn.tate@pennmedicine.upenn.edu | UPenn |
| Thaiss | Christop | thaiss@pennmedicine.upenn.edu | UPenn |
| Thurlow | Nat | nthurlow@seas.upenn.edu | UPenn |
| Tomlinson | Ryan | ryan.tomlinson@jefferson.edu | Jefferson University |
| Ulsh | Joe | joeulsh@seas.upenn.edu | UPenn |
| Usami | Yuna | usami-yuna@spu.ac.jp | Saitama prefectural University |
| Vega | Sebastian | vegas@rowan.edu | Rowan University |
| Vining | Kyle | viningk@upenn.edu | UPenn |
| Wagner | Maggie | magwag@seas.upenn.edu | UPenn |
| Wang | Dian | Dian.Wang@pennmedicine.upennedu | UPenn |
| Wang | Chang | chanwang@seas.upenn.edu | UPenn |
| Wang | Bin | bin.wang@jefferson.edu | Jefferson University |
| Wang | Catherine | catwxy@seas.upenn.edu | UPenn |
| Washabaugh | Charles | washabac@mail.nih.gov | National Institutes of Health |
| Weiss | Stephanie | weisssn@gmail.com | UPenn |
| Whipple | Sam | whipples1@chop.edu | CHOP |
| Whitaker | Ricardo | rw688@drexel.edu | Drexel University |
| Winkelstein | Beth | winkelst@seas.upenn.edu | UPenn |
| Xi | Jeffrey | jeffxi@sas.upenn.edu | UPenn |
| Xu | Jimmy | xupei@pennmedicine.upenn.edu | UPenn |
| Xu | Xiaoyu | Xiaoyu.Xu@pennmedicine.upenn.edu | UPenn |
| Xu | Karen | klxu@seas.upenn.edu | UPenn |
| Yang | Shuying | shuyingy@upenn.edu | UPenn |
| Yang | Yanmei | yanmei.yang@jefferson.edu | Jefferson University |
| Zemel | Babette | Zemel@chop.edu | CHOP |
| Zhang | Deyu | deyuz@pennmedicine.upenn.edu | UPenn |
| Zhang | Yejia | yejiazhang07@gmail.com | UPenn |
| Zhu | Frederik | frez@seas.upenn.edu | UPenn |
| Zion | Samuel | S.zion@comcast.net | Jefferson University |

Penn Center *for* Musculoskeletal Disorders

University *of* Pennsylvania

# Speaker Abstracts

## Knee Joint Biomechanics in the Rat Model

**Stephanie Cone, PhD**
**Assistant Professor**
**Department of Bioengineering | University of Delaware**

Biomechanical analyses of small animal joints have previously been limited to constrained testing, often in an individual tissue or in a single degree of freedom. Novel implementation of a miniature 6 degree-of-freedom robotic testing arm in small animal testing applications reveals the multi-axial functional behavior of rat knee joints, both in intact states and in response to complete ACL transection. Using a technique similar to prior studies in human cadavers and large animal models, this work reveals a major destabilization in the rat knee joint with ACL injury, identifies the ACL as the primary restraint to anterior tibial translation, and characterizes the functional role of the soft tissues in the knee in both healthy and injured states. Ongoing work with this technique will further our understanding of small animal model joint biomechanics and will provide clinically translational functional outcomes in the preclinical research setting.

## O-PTIR Spectral Imaging of Bone Composition at Submicron Spatial Resolution

**William Querido, PhD**
**Research Assistant Professor**
**Tissue Imaging and Spectroscopy Lab**
**Department of Bioengineering | Temple University**

As a beautifully hierarchical structure, the basis of bone quality and strength relies on its submicron-scale building blocks—mineralized collagen fibrils and bundles on the order of 500 nm. Vibrational spectroscopy techniques, such as Fourier transform infrared (FTIR) spectroscopy and imaging, have often been used to assess bone composition and molecular structure via their “spectral fingerprint” bands, which can be used to identify and quantify bone mineral and collagen properties. However, a limitation of conventional techniques is their micrometer-scale spatial resolution. Here, we apply the cutting-edge vibrational spectroscopy modality optical photothermal infrared (O-PTIR) spectroscopy to image the submicron composition of thick bone samples. This innovative approach brings a great advantage to the bone research field because it enables examining samples at 500 nm regions of interest without the need for cumbersome thin-sectioning of calcified tissue. We analyzed two different types of bone samples aiming to demonstrate the feasibility and unique application of this new method—human femoral neck sections (1 mm thick) and mouse tibia and human iliac crest biopsies embedded in polymethyl methacrylate (PMMA) blocks (22 mm thick). Importantly, minimal sample preparation was necessary other than ensuring the tissue surface was exposed and smooth. In both sample types, the O-PTIR spectra of cortical and trabecular tissues had excellent quality and showed typical bands of bone apatite and collagen. In the embedded tissues, there was little to no influence of PMMA in the bone spectra. Spectral imaging enabled visualizing the distribution of bone mineral, protein, and quantified mineral content (mineral/protein ratio) throughout individual osteons (cortical bone) and trabeculae at submicron resolution, as well as identifying tissue porosity associated with Haversian canals and osteocyte lacunae. Interestingly, quantification of mineral content demonstrated the typical alternating lamellae across the osteon, as well as the trabeculae mineralization pattern aligned to its longitudinal axis. In PMMA-embedded tissues, imaging of cortical porosity based on the mineral/PMMA peak ratio showed great spatial correlation between O-PTIR and scanning electron microscopy (SEM) images, opening new avenues to analysis of structure-composition associations in bone tissue. In conclusion, O-PTIR spectroscopy and imaging offers a new approach to assess bone tissue composition at the submicron scale in thick samples. In particular, application of this method to analyze PMMA-embedded bone tissues is of clear clinical significance, and could provide a new approach to advance assessment of bone biopsies at unprecedented detail.

Recent Advances in Computational Modeling for Pediatric Spine Deformity Diagnosis and Treatment.

**Sriram Balasubramanian, Ph.D.**
Associate Professor
School of Biomedical Engineering, Science and Health Systems

Abstract:
The diagnosis and assessment of progression of spine and rib cage deformities associated with Adolescent Idiopathic Scoliosis (AIS) are routinely evaluated using radiographs, and their clinical management strategies range from observation to bracing to surgical intervention, depending on the extent of curve progression. Manual measurements of Cobb angle, kyphosis and other clinical indices from radiographs are time consuming and prone to measurement error. Automated vertebral segmentation and Cobb angle measurements may improve accuracy and expedite clinical assessment.

Curve progression in scoliosis is modulated by asymmetric vertebral growth, which is influenced by local stress distribution and skeletal maturity. Therefore, prediction of curve progression can inform decisions of intervention type and timing. Also, Finite element (FE) modeling has been utilized previously to simulate asymmetric growth; however, without incorporating skeletal maturity.

In this talk, we will discuss the use of Machine Learning (ML) methods to perform automated clinical assessment for AIS, as well as to predict curve progression in AIS. We will also discuss advances in computational modeling methods to simulate and validate curve progression in AIS subjects using patient-specific (PS) FE (PS-FE) models of stress-modulated spine growth incorporating skeletal maturity. The use of such advanced PS-FE models to simulate the performance of novel growth modulating deformity correction devices will also be presented.

## A Cytoskeleton-Based Pathway Regulates Skeletal Muscle Bioenergetic Capacity

**Damaris N. Lorenzo, PhD**
**Associate Professor**
**Department of Cell and Developmental Biology**

Skeletal muscle performs a broad range of pivotal functions, from thermoregulation to maintenance of whole-body metabolic homeostasis. Most notably, through its contractile properties, skeletal muscle drives movement and supports motor control, strength, endurance, posture, and autonomic tasks. To adapt to mechanical and energetic stressors, including exercise, skeletal muscle relies on its remarkable plasticity. Both spontaneous bouts of exercise and endurance training result in sustained molecular and structural muscle remodeling to match the high energy demand and protect its structural integrity. Mitochondria remodeling is central to skeletal muscle bioenergetic capacity and stress responses, and dysfunctional mitochondria can result in mitochondrial myopathies, fatigability, sarcopenia, and insulin resistance. However, our knowledge of the molecular pathways of muscle mitochondria dynamics and adaptation to physiological perturbations is incomplete. We will discuss a novel pathway that depends on the cytoskeleton scaffolding protein ankryin-B (AnkB), which is required to maintain mitochondria remodeling and bioenergetic homeostasis in skeletal muscle under energetic stress.

## Translation Gap in Functional Genomics of Orofacial Clefts

**Eric C. Liao, MD, PhD**
**Director, Center for Craniofacial Innovation**
**Surgery Vice Chair of Academic Affairs**
**Presidential Scholar Endowed Chair**
**Children's Hospital of Philadelphia**
**Professor of Surgery, University of Pennsylvania**

Liao lab research program

Genome sequencing technology continues to advance with ever increasing speed and efficiency and decreased cost. It is now possible to obtain genomic sequencing data in clinical time frame even during the prenatal period. However, the exponential and accelerated growth of genomic data has only exacerbated and underscores the difficulty in translating this data to clinically actionable information. For example, whether it is somatic sequencing data from tumors or germline sequencing data from congenital conditions, resolving the sequence information down to a causative gene has for the most part defied computational tools; often requiring experimental evidence to impute pathogenicity. Further, newer systems and tools need to be developed to handle the integration and analysis of genomic data. To realize the vision of personalized medicine for pediatric and congenital conditions, fundamental studies on gene function are essential.

Our research program aims to bridge genomic data to clinical actionable diagnosis and treatment. We focus on craniofacial conditions such as orofacial clefts and the biology that underpin craniofacial development. We are focused on transcriptional and signaling pathways that are clinically important, and carry out focused discovery to identify molecular drivers of development and disease. This work has lead us to focus on cranial neural crest cells and embryonic epithelial cells, investigating the genetic requirement of ALX1, IRF6, ESRP1, CTNND1 and many other genes implicated in craniofacial malformations. We employ developmental biology approaches in human iPSC, mouse and zebrafish models for these studies.

Our lab currently consists of 5 post-doctoral fellows, 2 research scientists, 3 technicians and graduate students that are rotating in the lab.

## Translational Animal Models for Understanding the Relationship Between Bone Marrow Lesions and Subchondral Bone Disease

**Holly L. Stewart, VMD, PhD**
**Charles W. Raker Assistant Professor of Equine Orthopedic Surgery**
**New Bolton Center, University of Pennsylvania School of Veterinary Medicine**

Bone marrow lesions within the subchondral bone appear to be early indicators of inflammation which may precede alterations in the articular cartilage and accelerate degenerative processes within the joint. The goal of this research was to develop translational animal models that recapitulate naturally occurring disease and can be used to better understand bone marrow lesions and their relationship to osteoarthritis. Furthermore, advanced volumetric imaging modalities were optimized to characterize these changes within bone. A more comprehensive understanding of the contributions of subchondral bone to joint health is necessary to address degenerative joint disease more effectively.

# Penn Achilles Tendinopathy Center of Research Translation
# Admin Core

Lou Soslowsky, PhD, Director
Casey Humbryd, MD, Associate Director
Rob Mauck, PhD, Associate Director

The Achilles Tendinopathy Center of Research Translation (AT-CORT) at the University of Pennsylvania will foster fundamental discovery research to guide translation, as well as employ and develop translational resources, models and technologies, to address the highly significant research and unmet clinical challenge of Achilles tendinopathy. Despite the high frequency and increasing prevalence of tendinopathy to young and old patients alike, the significant pain and disability, as well as the associated high cost to society, evaluation and development of effective treatment modalities is hindered by the lack of fundamental guiding data on the mechanobiology of tendon etiology and pathogenesis. At the University of Pennsylvania, we are uniquely positioned with a critical mass of multidisciplinary scientists and clinicians with strong interest and expertise in these and related areas. The Center's efforts will span from the nucleus, to the cell, to the tissue, to in vivo animal models and to living human subjects in a coordinated "back-and-forth" manner across scales to guide innovative approaches to Achilles tendinopathy. The Center's research will discover fundamental physiologic processes to guide translation. It will also as serve as a test bed for defining the role, as well as the scientific and translational rigor, of a repetitive use Achilles tendinopathy animal model through implementation of an exciting series of in vivo longitudinal assays to be conducted in parallel in both animal and human subjects.

The **Specific Aims** of this Administrative Core are to:

- Aim 1, Provide leadership for Center components and activities and advise the Center Director regarding current or potential future activities of the Center.
- Aim 2, Manage, evaluate and monitor the Center components and activities.
- Aim 3, Communicate the Center's activities to the scientific, clinical, and lay communities.
- Aim 4, Administer the Pilot and Feasibility Grant Program and its associated funding and reporting.
- Aim 5, Implement an Enrichment Program. The Core and Research Projects have been carefully developed in concert to bridge the fundamental and applied while being highly interactive.

With regular guidance from our Committee structure (External Advisory, Executive, Communication, Enrichment), we will adapt our efforts to address our translational theme in the most efficient, effective, and productive manner possible. Our Pilot and Feasibility Grant program will foster new and innovative project directions consistent with our theme as well as support development of novel technologies to bring to our projects and for translation of our efforts. Our approach will serve as a critical paradigm for other tendon and indeed other musculoskeletal disorders and we will build on these efforts. A well organized and well-structured Administrative Core is absolutely essential to accomplish the Aims of the Center's highly interdisciplinary and interactive Research Projects and Core, and to maximize research activity, efficiency, productivity, communication, and ultimate impactful translation of our efforts to the scientific and lay community.

**Penn Achilles Tendinopathy Center of Research Translation: Research Project 1**

Nathaniel Dyment, Ph.D.,
[1]Assistant Professor of Orthopaedic Surgery

Joel Boerckel, Ph.D.
Associate Professor of Orthopaedic Surgery Bioengineering
University of Pennsylvania

Project 1 of the Penn Achilles Tendinopathy Center of Research Translation (PAT-CORT) aims to 1) determine how tendinopathic disease impacts Achilles tensional homeostasis across the spectrum of disease, 2) define the mechanotransductive mechanisms of healthy and diseased tendon cells, and 3) determine how rehabilitative loading restores Achilles tensional homeostasis for translational impact. This talk will introduce the science and personnel of this Project to the PCMD community, including the research team led by Project Leads, Drs. Dyment and Boerckel.

## Penn Achilles Tendinopathy Center of Research Translation: Research Project 2

[1]Su Chin Heo, Ph.D., [2]Melike Lakadamyali, Ph.D.
[1]Assistant Professor of Orthopaedic Surgery and Bioengineering
[2]Associate Professor of Physiology
University of Pennsylvania

Tendon degenerative diseases, such as tendinopathy, alter the chemo-physical environment and change biophysical inputs to resident cells (called tenocytes). Both normal and aberrant phenotypes in tendon cells are defined by the dynamic spatio-temporal organization of their genome. However, it remains unclear how pathological changes in the microenvironment with degeneration affect genome organization in tenocytes, and whether these changes scale with disease progression. Hence, gaining a comprehensive understanding of how Achilles tendinopathy influences genome organization, epigenetic landscapes, 3D chromatin structures, and gene regulation in tenocytes becomes a matter of utmost importance for advancing treatments for tendinopathy. To address these crucial questions, the objective of Research Project 2 is to investigate the regulatory impact of Achilles tendinopathy on the epigenetic landscape and 3D chromatin structure in tenocytes and to assess its influence on cell behavior and phenotype. Additionally, the study aims to determine if these alterations can be reversed through employing a combination of mechanical stimuli and epigenetic modifications. This research holds substantial significance, as it will provide invaluable insights how mechanical variations across the spectrum of tendon diseases influence genome organization and the behavior of tendon cells. Furthermore, these studies will identify novel epigenetic mechanisms related to Achilles tendon pathology and the onset of the disease. It will also introduce new paradigms for mechanical loading and highlight the potential of small epigenome-modifying molecules. These finding will play a pivotal role in advancing mechano-epigenetic strategies aimed at enhancing the effectiveness of targeted physical therapy protocols.

**Penn Achilles Tendinopathy Center of Research Translation: Tissue Core**

Josh Baxter, Ph.D.
Research Core Lead
Assistant Professor of Orthopaedic Surgery

Daniel Farber, M.D.
Associate Core Lead
Associate Professor of Clinical Orthopaedic Surgery

Louis Soslowsky, Ph.D.
Associate Core Lead
Professor of Orthopaedic Surgery

The Achilles Tendinopathy Tissue Core provides our Research Projects with patient and clinically relevant rat tendon samples. These tissues range from healthy to degenerated, combined with the most complete set of longitudinal in vivo assays to maximize the translational impact of our Research Projects. Our core also develops technologies to enhance Achilles tendinopathy clinical research at Penn by improving real-world monitoring and longitudinal imaging strategies. We will update the PCMD on our progress over the P50's first year and outline our plans going forward.

## Intestinal Regulation of Exercise Performance

**Christoph A. Thaiss, Ph.D.**
**Assistant Professor of Microbiology**

Exercise is possibly the single most important and accessible lifestyle component that offers protection from a large range of diseases. The sedentary lifestyle of modern human societies enhances the risk for metabolic, neurological and neoplastic conditions, highlighting the urgent need for targeted efforts to reverse this trend. The ability to exercise is the result of a complex interplay between the musculoskeletal system, cardiovascular and respiratory factors, and the motivational state. We recently identified a metabolite-triggered gut–brain connection that regulates the motivation for exercise, linking the intestinal microbiome to midbrain dopamine signaling via afferent sensory neurons. This pathway may offer opportunities to increase the engagement in regular physical activity through intestinal interventions.

## Exploring the Efficacy of Zinc as a Biomaterial for Orthopaedic Implants

**Michael W. Hast, PhD**
**Research Assistant Professor of Orthopaedic Surgery**

Advances in biomaterials and additive manufacturing (3D printing) are rapidly changing the way orthopedic implants are designed and implemented. Zinc and zinc alloys are attractive biomaterials because they are relatively strong, and Zinc is known to stimulate new bone formation. Additive manufacturing techniques can be leveraged to create implants with customized infills and surface textures that may inspire bone growth, but we do not fully understand these complex relationships. To address this, our lab has created implants with unique infills and surface textures using two novel additive manufacturing (AM) processes. In the first study, we created implants with gyroidal internal lattice structures. With these samples, we characterized the material properties of the implants and subjected them to an in vitro cell culture experiment. In the second study, we altered the surface texture of test coupons and performed another in vitro cell culture study. Our findings suggest that changes to lattice architecture and surface texture both have “sweet spots” that significantly influence cellular behavior. This preliminary work will be used to guide the design and development of Zinc implants for use in an upcoming in vivo study.

# “Super-Resolution Imaging of Chromatin in Diseased Musculoskeletal Cells”

Melike Lakadamyali, Ph.D.
Associate Professor of Physiology

Super-resolution microscopy has been playing an instrumental role in providing new insights into how the genome is folded and packaged inside intact nuclei in single cells. I will present our work on using super-resolution microscopy to visualize and quantify the spatial organization of chromatin with nanoscale spatial resolution in single cells. Our work has revealed that at the nucleosomal level chromatin is a disordered fiber composed of groups of nucleosomes packaged at varying densities, which we named nucleosome clutches. Despite the heterogeneity of nucleosome clutch organization, the size and packing density of nucleosome clutches is cell-type specific and correlates with cell fate. Our recent results also show that nucleosome clutches and chromatin nano-structure can be remodeled via chemo-mechanical cues. In particular degenerative chemo-mechanical cues during disease lead to aberrant chromatin nano-structure and loss of mechano-epigenetic memory, potentially leading to alterations in cell phenotype.

# NIH Grant Awards: Perspectives, Challenges and Tips

**Charles H. Washabaugh, PhD**
**Orthopaedic Research Program Director**
**Division of Extramural Research**
**NIAMS, National Institutes of Health**

To investigators seeing support for their research, the NIH grants process is a like black box and understanding how the process works enables a greater chance for success. The goal of this presentation is to introduce the NIH and the processes for submission and review of grant applications, identify updates to the grants process, demystify the challenges, provide some tips and tricks for investigators to be successful. At the conclusion, attendees will have a clearer picture of this very complex, but necessary, process by which the NIH supports basic, translational and clinical research.

Penn Center *for*
Musculoskeletal Disorders

University *of* Pennsylvania

# Micro CT Abstracts

# Pharmacologic inhibition of HIF2 prevents trabecular bone loss in ovariectomized mice

Giulia Lanzolla[1], Elena Sabini[1], Mohd Parvez Khan[1], Brittany M. Laslow[1], Dian Wang[1], Xiaowei Sherry Liu[1], Ernestina Schipani[1]

[1] Department of Orthopaedic Surgery, University of Pennsylvania, Perelman School of Medicine, Philadelphia, 19104, PA, USA

Cells of the osteoblast lineage are exposed to a gradient of oxygenation in the adult bone marrow. The transcription factors Hypoxia Inducible Factor 1 (HIF-1) and HIF-2 are key mediators of the cellular response to hypoxia. Loss of HIF2 in the osteoblast lineage promotes bone formation and augments bone mass. Therefore, HIF2 could represent a novel therapeutical target for the treatment of low bone. The study was aimed at evaluating whether the pharmacologic inhibition of HIF2 prevents trabecular bone loss in ovariectomized mice. Eight-week-old female mice (FVB/N) were ovariectomized (OVX) or sham-operated. Next, mice were randomized to be treated with either PT2399 (50 mg/kg), a selective inhibitor of HIF2, or with vehicle by oral gavage, twice daily for 5 weeks. As expected, a significant increase in body weight and a decrease in uterus weight were observed 6 weeks upon ovariectomy. The trabecular bone compartment in both vertebral bodies and distal metaphysis of femurs was analyzed by micro-CT and histomorphometry. Micro-CT analysis showed a significant decrease in bone volume/tissue volume ratio (BV/TV), trabecular number (Tb.N), trabecular thickness (Tb.Th.), and bone mineral density (BMD) in OVX mice treated with vehicle compared to sham-operated, whereas trabecular spacing (Tb.Sp) was increased. More importantly, no difference was detectable in any of the parameters listed above between OVX mice treated with PT2399 and sham-operated treated with vehicle. Histomorphometry confirmed micro-CT data. Furthermore, number of osteoblasts over bone surface (Ob.N/BS) was significantly lower in vehicle-treated OVX mice compared to sham-operated. This decrease was prevented by PT2399 administration. Although osteoclast number over BS (Oc.N/BS) did not differ between the four groups, the BS/BV ratio, which is an index of resorptive activity, was significantly higher in OVX mice treated with vehicle compared to sham-operated. PT2399 treatment again normalized this parameter in OVX mice. Double calcein labelling showed a significant increase in mineralizing surface/bone surface ratio (MS/BS), mineral apposition rate (MAR) and bone formation rate/bone surface ratio (BFR/BS) in OVX mice given PT2399 compared to those who received the vehicle, with no difference between PT2399-treated OVX mice and the control group, suggesting that PT2399 prevents bone loss through a direct action on bone formation. Taken together, PT2399 fully prevented trabecular bone loss due to ovariectomy in mice, thus representing a new potential anabolic agent to be tested for treating postmenopausal osteoporosis. Modest anemia occurred in mice treated with PT2399, likely due to reduction of renal EPO, which is a direct downstream target of HIF2. Further studies are needed to target PT2399 specifically to bone to prevent anemia and clarify the mechanisms by which PT2399 prevents bone loss.

**Activation of SIRT6 regulates mitochondrial function and reduces the severity of age-associated osteoarthritis in mice**

Matheus M. Perez[1], Pranay Ramteke[1], Bahiyah Watson[1], Ashley Coleman[1], Owen Haslam[1], Susan Chubinskaya[3], Ryan E. Tomlinson[1], Mandy J. Peffers[4], Richard F. Loeser[2], Makarand V. Risbud[1], Theresa A. Freeman[1], John A. Collins[1,2]

1 Thomas Jefferson University, Philadelphia, PA, USA; 2University of North Carolina, Chapel Hill, NC, USA; 3 Rush Medical College, Chicago, IL, USA; 4 University of Liverpool, Liverpool, UK.
Correspondence: mym582@jefferson.edu

INTRODUCTION: Sirtuin 6 (SIRT6) is a nuclear localized histone deacetylase that epigenetically regulates several age-associated pathways, including senescence, longevity, inflammation, redox balance, metabolism, and genomic stability. We have previously demonstrated that SIRT6 activity significantly declines with age, promoting oxidative stress conditions and catabolic signaling events implicated in osteoarthritis (OA). *In vivo*, we recently reported that cartilage-specific loss of *Sirt6* repressed pro-anabolic Insulin Growth Factor 1 (IGF-1) signaling and increased surgery-induced and age-related OA severity in mice. The objective of this study was to determine whether systemic administration of MDL-800, a small molecule activator of SIRT6, reduced the severity of age-associated OA in mice.

METHODS: All animal studies were approved by the Thomas Jefferson University Animal Care and Use Committee and were performed using male C57BL/6 mice. 18 month old mice received weekly intraperitoneal injections of MDL-800 (75 mg/kg) or vehicle control for six months, and OA severity was analyzed at 24 months of age (vehicle control group; $n$=13, MDL-800 group, $n$=15). MicroCT was used to analyze bone volume fraction (BV/TV), trabecular thickness (Tb.Th), and trabecular separation (Tb.Sp). Sectioned limbs were stained with H&E and toluidine blue for analysis of Articular Cartilage Structure (ACS), proteoglycan content, and osteophyte formation. RNA sequencing was conducted on primary human chondrocytes treated in the presence or absence of MDL-800 (12.5 uM, 24 hours), and the effect of MDL-800 to regulate mitochondrial function was analyzed using the MitoCarta 3.0 database and gene set enrichment analysis (GSEA).

RESULTS: Mice receiving MDL-800 displayed a reduction in age-associated OA severity characterized by significantly lower summed ACS scores, toluidine blue scores, and osteophyte scores, compared to controls. MicroCT analysis on the MTP demonstrated that mice receiving MDL-800 displayed lower BV/TV and Tb.Th values, and higher Tb.Sp values when compared to controls, indicating a decrease in subchondral bone sclerosis in the MDL-800 treated group. RNA sequencing analysis revealed 2250 differentially expressed genes (1419 upregulated, 831 downregulated), as compared to controls. GSEA analysis revealed that MDL-800 treatment was associated with significant enrichment of multiple mitochondrial pathways, including ‘detoxification’ and ‘small molecule transport’.

DISCUSSION: These results show that chronic administration of the SIRT6 activator, MDL-800, reduces age-associated OA severity in mice. RNA sequencing analysis revealed that SIRT6 may regulate key mitochondrial pathways critical for protein quality control. Mitochondrial dysfunction is a hallmark of aging and is well documented to contribute to the development and progression of OA. Thus, targeted therapies that activate SIRT6 may represent a novel strategy to slow or stop OA progression by preserving homeostatic mitochondrial function during aging.

# *Ex Vivo* Optimization and *In Vivo* Measurement of Nucleus Pulposus Oxygen, Glucose, and Lactate in a Goat Model of Disc Degeneration

Karthikeyan Rajagopal[1,2], Thomas P. Schaer[1,2], Kyle D. Meadows[3], Madeline Boyes[1], Rachel Hilliard[1], John C. O'Donnell[1], George R. Dodge[1], Dmitriy Petrov[1], Dawn M. Elliott[3], Robert L. Mauck[1,2], Lachlan J. Smith[1,2], Neil R. Malhotra[1]
[1]University of Pennsylvania and [2]CMC VA Medical Center, Philadelphia, USA, and [3]University of Delaware, Newark, USA
karthikeyan.rajagopal@pennmedicine.upenn.edu

**Disclosures:** Karthikeyan Rajagopal (N); Thomas P. Schaer (5-PSI; ReGelTec, Peptilogics, Acuitive Technologies, PAX Therapeutics, OrimTech, SINTX Technologies, OsteoCentric Technologies, DePuy Synthes, Alcyone Therapeutics, Camber Spine, Heraeus); Kyle D. Meadows (N); Madeline Boyes (N), Rachel Hilliard (N); John C. O'Donnell (N); George R. Dodge (4-MechanoTherapeutics); Dmitriy Petrov (N); Dawn M. Elliott (9-ORS Board of Directors); Robert L. Mauck (5-4Web Medical, 4-MechanoTherapeutics; 8-JOR Spine); Lachlan J. Smith (8-JOR Spine, Connective Tissue Res; 9-ORS Spine Section); Neil R. Malhotra (N).

**INTRODUCTION:** Chronic low back pain is a leading contributor to disability and imposes a substantial socioeconomic burden worldwide [1]. A primary cause of this pain is intervertebral disc degeneration. Although the precise pathophysiological mechanisms driving disc degeneration remain elusive, early indicators include reduced vascular supply, consequent alterations within the microenvironment, and the disappearance of notochordal cells [2]. Emerging treatments such as mesenchymal stem cells (MSCs) to regenerate the central nucleus pulposus (NP) have shown promise; however, the degenerate disc microenvironment negatively impacts MSC survival and therapeutic efficacy [2]. Quantification of this microenvironment, including changes in nutrient availability as a function of degeneration severity, is therefore critical for development of more effective MSC-based treatments. Previous studies using contrast-enhanced imaging and computational modelling have predicted reduced glucose and oxygen levels with degeneration [4]; however, direct experimental evidence is lacking, partly due to lack of appropriate *in vivo* models and sensor limitations. Here we adapt Licox oxygen probes and microdialysis catheters, widely used for brain tissue monitoring, for *in situ* measurement of NP tissue oxygen, and glucose and lactate, respectively. To accomplish this, measurement parameters were first optimized in an *ex vivo* bovine caudal disc model and then applied *in vivo* to investigate changes in NP oxygen, glucose and lactate concentrations in a preclinical goat model of disc degeneration [5].

**METHODS:** *Ex Vivo Optimization:* Bovine tails purchased from a commercial vendor were utilized to optimize *in situ* oxygen, glucose and lactate measurements in the NP **(Fig 1A)**. A 16G needle was used to place a Licox oxygen probe (Integra) or microdialysis catheter (M Dialysis) into the center of the NP of caudal discs (C1-C5). Oxygen levels (n=4 discs) were monitored for 90 mins. For glucose and lactate measurements, perfusion fluid was pumped through microdialysis catheters (10 mm, 20 kDa) at one of 2 flow rates: 0.3µL and 1µL/min (n=3 discs each). Microdialysates were collected at 30-min intervals for 150 mins. Glucose and lactate contents in microdialysates were assessed using two independent assays: the ISCUSflex Microdialysis Analyzer (M Dialysis) and single analyte high-sensitivity (HS) detection kits (Abcam and Sigma). *In Vivo Assessment of NP Oxygen, Glucose, and Lactate:* With IACUC approval, under general anesthesia and using an open, left, retroperitoneal, transpsoatic approach, a custom 16G spinal needle under fluoroscopy was used to position Licox probes and/or microdialysis catheters in the lumbar disc NPs (L1-L5) of 3 large frame goats. Oxygen was monitored for 30-45 mins (n=6-7 discs), and microdialysates were collected at a flow rate of 0.3 µL/min for 150 mins (n=5-6 discs). Disc degeneration was then induced by injecting chondroitinase ABC (ChABC, 2U in 200ul) into the NP. After 12 weeks, oxygen and microdialysis measurements were repeated at the same levels in a second surgery. Glucose and lactate were assessed using HS kits. Differences in oxygen, and glucose and lactate levels in healthy vs degenerate discs were determined using Mann-Whitney tests ($p<0.05$ significant). To confirm degeneration, *in vivo* magnetic resonance imaging (MRI) was performed at baseline and 12 weeks. *Postmortem Histology and MicroCT:* Following euthanasia at 12 weeks, isolated spine segments were fixed in formalin and microCT used to image the vertebral endplates of degenerate and adjacent healthy discs. Samples were then decalcified and processed into paraffin, and midsagittal sections stained with Alcian blue and picrosirius red for assessment of disc condition.

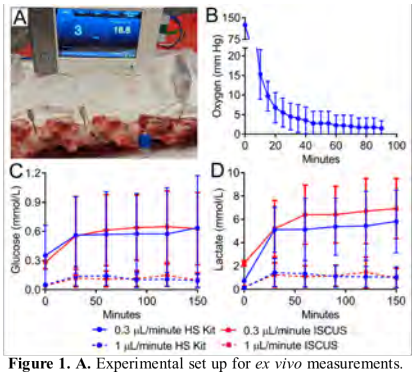


**Figure 1. A.** Experimental set up for *ex vivo* measurements. **B.** Oxygen levels in the NP over time. **C.** Glucose and **D.** Lactate levels over time measured using two different flow rates and analysis methods. N=3-4 discs; mean±SD.

**RESULTS:** *Ex Vivo Optimization:* In bovine discs, oxygen measurements equilibrated after ~45 mins, recording levels of 1.5 ± 1.6 mmHg after 90 mins (**Fig 1B**). Glucose and lactate levels measured using microdialysis reached equilibration after 30 mins **(Fig 1C** and **D)**. Both glucose and lactate levels were higher in samples collected at 0.3µL/min compared to 1µL/min after 150 mins ($p<0.05$ for lactate). Measurements were approximately equivalent for both detection methods. *In Vivo Assessment of NP Oxygen, Glucose, and Lactate:* MRI confirmed that discs injected with ChABC exhibited progressive degeneration. Following equilibration, median baseline oxygen in healthy discs was 50.0 mmHg. In degenerate discs, median oxygen was significantly higher at 108.0 mmHg (**Fig 2A**). With respect to glucose and lactate, following equilibration, median baseline levels in healthy discs were 0.063 and 0.069 mmol/L, respectively. In degenerate discs at 12 weeks, median glucose and lactate levels were 0.104 and 0.883 mmol/L, respectively, with lactate significantly higher than baseline (**Figs 2B** and **C**). MicroCT revealed increased vertebral end plate porosity in all degenerate discs compared to healthy discs (**Fig 3A**). Histology demonstrated moderate to severe degeneration in ChABC-injected discs (**Fig 3B**).

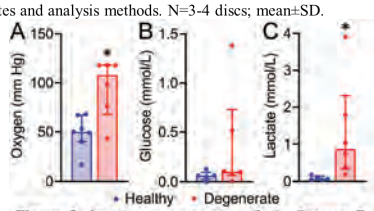


**Figure 2.** In *vivo* measurement of: **A.** Oxygen **B.** Glucose and **C.** Lactate in the NPs of healthy and degenerate goat discs. N=5-7; *p<0.05; median/IQR.

**DISCUSSION:** Here we successfully optimized techniques, including probe placement, equilibration time, flow rate and detection method, for the *in-situ* measurement of oxygen, glucose, and lactate within the disc NP, and applied these techniques to evaluate changes with disc degeneration in a preclinical large animal model. Notably, for glucose and lactate, collection flow rate impacted results, suggesting that lower flow rates are necessary for accurate measurements due to the low levels of these metabolites in the NP. Interestingly, while increased lactate with degeneration was expected, contrary to expectations [6] increased oxygen levels were also measured. Potential explanations could be reduced disc height (reducing nutrient diffusion distances), increased cell death (reducing overall metabolite consumption) or increased vertebral end plate porosity (enabling more ready diffusion of nutrients from the adjacent bone) in degenerate discs. Ongoing work is aimed at elucidating the microstructural and cellular contributions to altered metabolites using this model. Our ultimate goal is to leverage these insights in order to modify the disc microenvironment to enhance the efficacy of therapeutic stem cells.

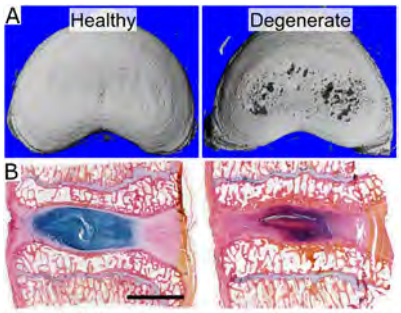


**Figure 3. A.** Representative axial microCT images showing increased porosity of a vertebral end plate adjacent to a degenerate disc. **B.** Representative histology of healthy and degenerate goat discs. Mid sagittal; Alcian blue/picrosirius red stain; scale=5mm.

**SIGNIFICANCE:** Physiologically accurate characterization of the degenerate disc metabolic microenvironment is essential for developing effective cell-based disc regeneration strategies.

**REFERENCES:** [1] Vos+ Lancet 2015; [2] Smith+ Dis Model Mech 2011; [3] Urban+ Arthritis Res Ther 2003; [4] Urban+ Spine 2004; [5] Gullbrand+ Osteoarthritis Cartilage 2017; [6] Huang+ Nat Rev Rheumatol 2014.

**ACKNOWLEDGEMENTS:** Funding from the National Institutes of Health (R01 AR077435) and the Department of Veterans Affairs (I01 RX001321).

# Exploring the Efficacy of Additively Manufactured PLGA Implants for Fracture Repair at Early Time Points

Kathryn S. Strand[1], Anna N. Smith[1], Joseph B. Ulsh[1], Trent J. Levy[1], Michael W. Hast[1]
[1]McKay Orthopaedic Research Lab, Department of Orthopaedic Surgery, University of Pennsylvania, Philadelphia, PA
strandk@seas.upenn.edu

**Disclosures:** None

**INTRODUCTION:** Bone fractures can result in significant physical disabilities, chronic pain, increased healthcare costs, and an overall lower quality of life [1]. It has been established that micromotion at the fracture site can improve healing outcomes, so there is new interest in developing less rigid implants such as non-metallic plates [2]. Poly-lactic-co-glycolic acid (PLGA) is an attractive candidate material for bone plates due to its relatively high mechanical strength, biocompatibility, and controllable degradation kinetics, all of which make it suitable for fracture repair [3]. Additionally, its degradation products have been shown to promote osteogenesis and angiogenesis [4]. PLGA has been used in a variety of bone healing applications via additive manufacturing (AM) [5]. However, we still do not know if AM PLGA can be used to create effective fracture implants. The purpose of this in vitro and in vivo study was to explore the potential for AM PLGA implants as devices for fracture repair at early healing time points. We hypothesized that AM PLGA implants would have decreased mechanical strength in comparison to non-degradable control implants, and that the bone healing response between groups would be similar.

**METHODS:** In an IACUC-approved study, 19 male Sprague-Dawley rats underwent bilateral osteotomies of the femora (**Fig. 1**). Each femur was fixed with either a PLGA (Lattice Medical) or BioMed Clear Resin (Formlabs) implant. PLGA implants were fabricated on a fused deposition 3-D printer with 85:15 PLGA filament (Prusa i3 MK3 3-D), and the resin implants were synthesized via photocuring (Formlabs Form 3). Because PLGA could not be sterilized in an autoclave, PLGA implants were soaked in 70% ethanol for 30 minutes. Resin implants were autoclaved. The polymer plates (19x5x5 mm) were held in place with 4 non-locking screws (0-42 x 3/8"). The rats were allowed to weight-bear immediately after surgery. Rats were sacrificed at 3 and 6 weeks. Histology (n=6) and micro-CT analyses (n=6) were conducted at 3 and 6 weeks post-surgery. Torsional testing of healing femora was conducted at 6 weeks by performing a 90 º internal rotation of the femur at 3º/sec (n=7). Micro-CT outcome measures of the fracture callus included bone volume (BV) mean density, total volume (TV) mean density, and the BV/TV fraction. Histological analysis included Safrinin-O/FastGreen, hemotoxylin and eosin (H&E), and Picrosirius Red staining. Implants were harvested from all sacrificed animals and kept frozen at -20°C. To assess differences between in vitro and in vivo degradation of PLGA implants, additional PLGA and resin implants were manufactured (n=10 per group) and incubated. Specimens were kept at 37°C on a rocker in a solution of 30% fetal bovine serum, 69% PBS, and 1% v/v Penicillin-Streptomycin-Fungizone. Serum changes were completed every 3-4 days. Harvested implants from the in vivo study and in vitro implants were subjected to torsional testing at 0, 3, and 6 weeks (90º rotation at 1º/sec). The primary mechanical testing outcome measure was virtual torsional rigidity (VTR). T-tests were used to make comparisons between groups at each time point. Paired t-tests were used to compare bones within each rat. A one-way ANOVA with a Holm-Sidak post-hoc test was conducted to compare outcomes from each implant type across all time points. Kruskal-Wallis tests with Dunn's post-hoc were used on nonparametric data sets. Significance was set to $p<0.05$.


***Figure 1.*** *Left: Schematic of surgical procedure. Right: Relevant study timepoints including micro-CT, histology, and mechanical testing.*

**RESULTS:** Micro-CT analysis revealed that PLGA significantly increased callus bone volume mean density from 3 to 6 weeks, but resin did not (**Fig. 2A**). Significant increases in total volume mean density **(Fig. 2B)** and BV/TV fraction (**Fig. 2C**) existed for both implants between timepoints, but there were no differences between groups. Torsional testing of the femora at 6 weeks revealed no differences in VTR (**Fig. 2D**). Histology results were still pending at the time of writing this abstract. In vitro degradation demonstrated significantly stiffer PLGA implants than resin at 0 and 3 weeks, but not 6 weeks (**Fig. 3A**). PLGA implants retrieved from the in vivo study were different at all time points, and there were no significant differences between groups at 3 and 6 weeks (**Fig. 3B**).

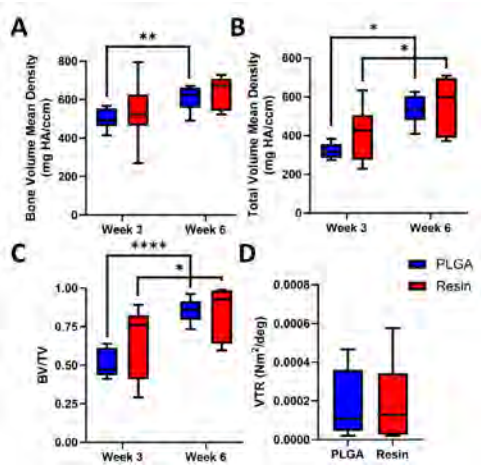


***Figure 2.*** *Quantitative assessment of bone callus healing via micro-CT (A-C) and mechanical testing (D). *p<0.05, **p<0.01, ****p<0.0001.*

**DISCUSSION:** To our knowledge, this is the first study to investigate the effects of AM PLGA implants at early time points in fracture repair. At 3 and 6 weeks, we observed fracture healing, as indicated by the increase in BV mean density, TV mean density, and BV/TV. Notably, use of PLGA and resin implants led to similar bone healing responses. In vitro and in vivo analysis of the implant degradation demonstrates that mechanical loading in vivo significantly increased the degradation rate of the PLGA implants. These results reveal that unloaded in vitro degradation assays do not accurately reflect the degradation kinetics of AM PLGA, which is important for future experiments that will focus on PLGA implant form and function. Importantly, we found that PLGA implants did not have any detrimental effects on fracture healing progression at short time points (3-6 weeks). Further analyses at longer time points, when the strength of PLGA implants begins to go to zero, are necessary to determine the long-term relationships between AM PLGA implant degradation on mechanotransduction during bone healing.

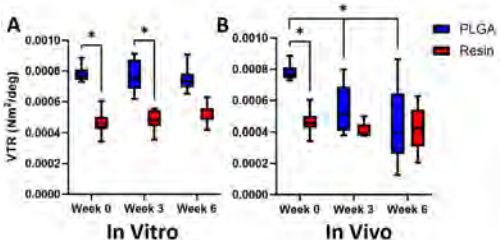


***Figure 3.*** *Mechanical testing results from in vitro (A) and in vivo (B) PLGA and resin implants. *p<0.05.*

**SIGNIFICANCE/CLINICAL RELEVANCE:** At early time points in the fracture healing process, the mechanical properties of biodegradable PLGA fracture implants were similar to matched non-degradable resin devices. Bone healing responses were similar between the two groups. We are encouraged by this finding, and we believe that the benefits of implant degradation at longer time points will lead to accelerated and improved bone repair.

**REFERENCES:** [1] Wu et al. (2019) Lancet Healthy Longev. [2] Goodship et al. (1985) J Bone Joint Surg. [3] Zhao et al. (2020) Bioact. Mater. [4] Hu et al. (2018) J Mater Chem. [5] Jin et al. (2021) Acta Biomater.

# Injury-induced and Spontaneous Heterotopic Ossification in a New Acvr1 R206H Mouse Model for FOP

Chakkalakal SA, Roberts DW, Xi J, Pacifici M, Shore EM
Perelman School of Medicine, University of Pennsylvania; Children's Hospital of Philadelphia

Fibrodysplasia ossificans progressiva (FOP) is a rare disorder of heterotopic endochondral ossification (HO). In FOP, HO occurs in the absence or in response to tissue injury. Most patients with FOP share a heterozygous single nucleotide substitution (c.617G>A; R206H) in *ACVR1* that encodes the bone morphogenetic protein type I receptor ALK2. A conditional *Acvr1*$^{R206H/+}$ knock-in mouse (*Acvr1*$^{[R206H]FlEx/+}$) was previously created to investigate disease pathogenesis. Once induced, the *Acvr1*$^{R206H}$-expressing mice formed HO in response to injury. However, the engineered allele in this model is null for Acvr1 prior to Cre-recombination, a possible complication. We developed an alternative knock-in mouse (*Acvr1*$^{ARC-R206H/+}$) in which the engineered allele expresses wild-type R206 Acvr1 prior to Cre recombination and R206H following Cre. Here, we characterize the HO phenotype of this new model. Using our established approach for injury-induced HO, *Acvr1*$^{R206H}$ expression was activated globally via rt-tetO-Cre and leg skeletal muscle was then injured by cardiotoxin (ctx). Progression to HO was examined by histology and HO volume quantified by microCT over 2 weeks post-injury. Previously defined histologic stages of HO progression and altered muscle repair were identified, but with more robust chondrogenesis (5 dpi) and an apparent slower transition from cartilage to bone. We used the same rt-tetO-Cre system to examine 'spontaneous' HO progression in the absence of ctx injury. We found that HO developed more slowly than in response to ctx tissue injury. Little HO was detected by microCT at 3 weeks, but consistently formed by 4 weeks. Upon specific expression of *Acvr1*$^{R206H}$ in skeletal mesenchymal progenitor cells (*Acvr1*$^{ARC-R206H/+}$*;Prrx1-Cre*), no extra bone was detected during embryogenesis; however at birth, development effects were indicated by reduced body length, malformed limbs with webbed digits, fused joints, and spine and skull malformations. Within 2 weeks after birth, spontaneous HO occurred that was more robust and rapidly progressive than that induced by global Cre induction, supporting the importance of cell interactions to regulate cell fate. Overall, our new FOP mouse shows more robust phenotypes than a previously described model. It is the first model for global induction of spontaneous (non-injury-induced) HO, providing a novel, patient-relevant system to investigate the initiation, progression, and cell mechanisms that regulate heterotopic ossification.

This work was first presented at the ASBMR 2023 Annual Meeting, Vancouver, BC. October 13-16, 2023.

# Conditional Deletion of PTH/PTHrP Receptor 1 in Osteocytes Abolishes Lactation-induced Alterations in Canalicular Pericellular Space and Increases Bone Microstructure Deterioration

Xiaoyu Xu[1], Yilu Zhou[1], Rosa M. Guerra[2], Yongqiang Vincent Jin[1], Yuanhang Li[1], Wonsae Lee[1], Tala Azar[1], Kira Lu[1], Liyun Wang[2], X. Sherry Liu[1]
[1] McKay Orthopaedic Research Laboratory, University of Pennsylvania, Philadelphia, PA. xiaoyu.xu@pennmedicine.upenn.edu
[2] Center for Biomechanical Engineering Research, University of Delaware, Newark, DE.

**Disclosures:** All authors have nothing to disclose.

**INTRODUCTION:** Pregnancy and lactation are unique physiological events for women that induce significant changes in maternal calcium and bone metabolism. Due to the demands of infant growth and milk production, the maternal skeleton experiences substantial mineral loss and structural deterioration during lactation, followed by partial recovery after weaning [1,2]. Osteocytes, the orchestrators of bone mass maintenance, have been considered to play a key role in lactation-induced maternal mineral metabolism by resorbing their surrounding bone matrix through perilacunar/canalicular remodeling (PLR) [3], resulting in a transient increase in dimensions of the lacunar canalicular system (LCS) in maternal bone during lactation. Moreover, our previous study suggested that increased dimensions of osteocyte LCS driven by PLR would amplify the transductions of mechanical and biochemical signals to osteocytes, leading to increased osteocyte mechanosensitivity, which in turn enhances the mechanical adaptation of the maternal skeleton to maintain its load-bearing function [4-5] (Fig.1A). However, the exact role of PLR in regulating maternal bone adaptations during lactation is still unclear. Therefore, the objective of this study was to investigate the impact of PLR on lactation-induced changes in the ultrastructure of the LCS and microstructure of the maternal bone. We hypothesized that abolishing osteocyte PLR would prevent changes in the pericellular matrix and LCS dimensions, leading to more significant bone loss and bone microstructure deterioration during lactation. In order to abolish lactation-induced PLR, PTH/PTHrP Receptor 1 (PPR) was conditionally deleted in osteocytes using a Dmp1-Cre; $PPR^{fl/fl}$ mouse model. Skeletal morphology, osteocyte LCS dimension, and pericellular ultrastructure were examined at different stages of reproduction to elucidate the role of osteocyte PLR in lactation-induced maternal alternations.

**METHODS:** All animal experiments were IACUC approved. ***Animals***: Female C57BL6 mice with osteocyte deletion of PPR (cKO: 14kb-Dmp1-Cre; $PPR^{fl/fl}$) and the matched wildtype controls (WT: $PPR^{fl/fl}$ littermates) were both randomly assigned to three groups: Virgin, Lactation, and Post-weaning (n = 4-6 per group for both cKO and WT). Lactation and Post-weaning mice were mated at 11 and 9 weeks old, respectively, and underwent 3 weeks of pregnancy followed by 12 days of lactation. To ensure consistent suckling intensity, litter sizes were normalized to 5-6 pups per mother within 48 hours after birth. Post-weaning mice were allowed to recover for 14 days after 12 days of lactation. At 16 weeks old, Lactation and Post-weaning mice were euthanized with the age-matched Virgin mice. ***Histomorphometry:*** Longitudinal sections (6-μm) were prepared from the paraffin-embedded tibia (right) and subjected to Photon silver nitrate staining to evaluate the LCS dimensions in all groups (n = 3-4 per group; n = 30-35 lacunae per sample). ***Transmission electronic microscope (TEM):*** Bone marrow was washed out from the tibia (left) immediately after dissection. After fixation, the tibial midshaft was transversely cut into 1mm thick sections using a low-speed saw and processed for TEM imaging to analyze the ultrastructure of canaliculi (290-300 canaliculi per group). A Matlab program was developed to evaluate the pericellular area and cell process area of the osteocyte dendrites and the total canalicular area. ***μCT imaging:*** The trabecular bone of the lumbar vertebra L4 was scanned and analyzed using a microCT 45 (Scanco; 7.5 μm voxel size). Microstructural parameters, including bone volume fraction (BV/TV), trabecular thickness (Tb.Th), SMI, and connectivity density (Conn. D) were acquired. ***Statistics:*** One-way ANOVA with Bonferroni correction was used to detect the difference in relevant parameters across Virgin, Lactation, and Post-weaning groups. Significant differences were considered when $p < 0.05$.

**RESULTS:** In WT mice, 12-day lactation resulted in 20% and 9% greater lacunar area and perimeter, respectively, which returned to baseline levels as in Virgin mice 14 days after weaning (Fig.1B&C). These lactation-induced alternations were not found in mice lacking osteocyte PPR (Fig.1B-D). Although the number of canaliculi per lacuna remained consistent across Virgin, Lactation, or Post-weaning for both WT and cKO mice (Fig.1D), the ultrastructure of canaliculi adapted differently between WT and cKO mice during lactation. The pericellular area around osteocyte dendrites increased by 48% in WT lactating mice (Fig.1E), resulting in a 30% increase in total canalicular area compared to Virgin mice (Fig.1G). Following the weaning period, the recovery of canaliculi ultrastructure in WT mice was evidenced by the significant reduction in the pericellular area 14 days after weaning (Fig.1E). Unlike the alternation in WT mice, deleting PPR in osteocytes mitigated lactation-induced increases in pericellular and canalicular areas (Fig.1E&G). Moreover, the post-weaning recovery observed in WT did not appear in cKO mice, as both pericellular and canaliculi areas remained elevated after 14 days post weaning (Fig.1E&G). The dendrite process area remained at similar levels at different reproductive stages in WT and cKO mice (Fig.1F). At the tissue level, cKO mice displayed greater bone loss and microstructure deterioration during lactation than WT mice, demonstrated by significant reductions in BV/TV (-48%), Tb.Th (-26%), Conn.D (-34%), and a higher SMI (2.5 in cKO *vs.* 2.23 in WT) in cKO relative to WT (Fig.1H-K). Nevertheless, both WT and cKO mice fully recovered in bone microstructure post weaning (Fig.1H-K).

**DISCUSSION:** Our results demonstrated the important role of osteocyte PLR in mediating alternations of the LCS ultrastructure and maternal bone microstructure in response to lactation. By deleting PPR in osteocytes, lactation-induced osteocyte PLR activities were abolished in the mouse maternal skeleton, demonstrated by the unchanged lacunar area and perimeter across different reproductive statuses in the cKO mice. TEM results provided further evidence of the functions of osteocyte PLR in altering the pericellular matrix of osteocyte dendrites and dimensions of canaliculi during lactation. According to the LCS fluid flow model established by Weinbaum *et al.* [6], the enlarged LCS and pericellular fluid space could contribute to increased flow-mediated mechanical stimulation and enhanced mechano-signals on osteocytes and their processes when subjected to loading, thus enhancing bone's mechano-responsiveness during lactation. This may partially explain the accelerated bone loss in lactating cKO mice with lactation-induced osteocyte PLR significantly inhibited.

**SIGNIFICANCE:** This is the first study that quantified the lactation-induced alterations in canaliculi ultrastructure and demonstrated active remodeling of the pericellular matrix surrounding osteocyte dendrites during lactation and post-weaning. Future studies will continue to elucidate the critical roles of osteocyte PLR in regulating the balance between mineral resorption and mechanical integrity of the maternal skeleton.

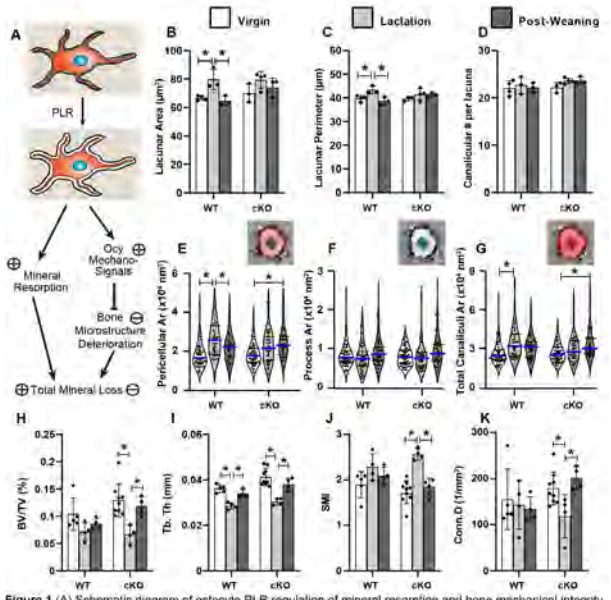


**Figure 1** (A) Schematic diagram of osteocyte PLR regulation of mineral resorption and bone mechanical integrity. (B) Lacunar area, (C) lacunar perimeter , and (D) canaliculi number per lacuna derived from Photon silver nitrate staining images of cKO and WT mice with different reproductive statuses. (E) Pericellular area of Ocy dendrite processes (area between the two red dashed lines), (F) process area (central area highlighted in blue), and (G) total canaliculi area (the area highlighted in red) derived from TEM images of tibial cortical bone of cKO and WT mice with different reproductive statuses. (H-K) L4 trabecular bone morphometry by μCT (7.5 μm) in cKO and WT Virgin, Lactation, and Post-weaning mice. Asterisk (*) indicates a significant difference among Virgin, Lactation, and Post-weaning of cKO or WT mice by one-way ANOVA ($p<0.05$).

**REFERENCES:** [1] Kovacs, *Physiol Rev,* 2015; [2] Liu X *et al*., *Biomech*, 2019; [3] Qing H *et al*., *JBMR,* 2012; [4] Lai X *et al*., *Bone*, 2021; [5] Li Y *et al*., *Bone*, 2021; [6] Weinbaum *et al*., *J Biomech*, 1994.

**ACKNOWLEDGEMENTS**: NIH/NIAMS R01-AR077598, P30-AR069619.

Penn Center *for*
Musculoskeletal Disorders

University *of* Pennsylvania

# Biomechanics Abstracts

# In Vivo Measurement of Tether Tension in a Pig Model of Spinal Deformity

Madeline Boyes[1], Axel C. Moore[2], Klaus Hopster [1], Benjamin Sinder[3], Jason Anari[3], Sriram Balasubramanian[4], Edward Vresilovic[2], Thomas P. Schaer[1], Dawn M. Elliott[2], Brian D. Snyder[5], Patrick J. Cahill[3]

[1]University of Pennsylvania School of Veterinary Medicine, Kennett Square, PA, [2]University of Delaware, Newark, DE, [3]Children's Hospital of Philadelphia, Philadelphia, PA, [4]Drexel University, Philadelphia, PA, [5]Boston Children's Hospital, Boston, MA.

mboyes@vet.upenn.edu

**Disclosures:** Thomas Schaer (1-PSI, 1,3B,4,5-ReGelTec, 3B-Peptilogics, 3B,4,5-Acuitive Technologies, 3C-PAX Therapeutics, 3C-OrimTech, 3C,5-SINTX Technologies, 3C-OsteoCentric Technologies, 5-DePuy Synthes, 5-Alcyone Therapeutics, 5-Camber Spine, 6-Heraeus), Brian Snyder (3B-Orthopediatrics)

**INTRODUCTION:** Ian Stokes[1] hypothesized that spinal deformity progresses as a "vicious cycle" due to asymmetric stresses/strains applied to the growing spine over time and space. Predicated on the Heuter-Volkmann principle[2] (i.e., tension applied to an apophysis/physis stimulates growth, compression inhibits growth), interventions such as Vertebral Body Tethering[3] (VBT) attempt to correct scoliosis, while preserving spinal motion, by predictably modulating spine growth via mechanical manipulation of affected functional spinal units. Currently, it is unknown how asymmetric loading alters the growth of the developing spine. In this proof-of-principle study in a growing pig we created a reciprocal model of scoliosis by applying a posterolateral tether to a straight spine to induce an asymmetrical bending moment to provoke spinal deformity. While a set tether tension is applied during surgery, it is not constant, there is great variation in applied stresses/strains in time and space owing to superimposed dynamic forces and moments generated during gait and changes in posture that result in stochastic loading which may be more influential in regulating the adaptive response of the growing spine. The purpose of this study was to determine the *in vivo* variation in tether tension during gait and changes in posture in a swine model of spinal deformity induced by growth modulation.

**METHODS:** Under IACUC approval, in a 6-week-old, 20 kg, female Yorkshire pig, a lateral bending moment was induced by tethering the thoracic to lumbar spine using a subcutaneous posteriorly placed, laterally offset stainless-steel cable spanning two posterior pedicle screw clusters with a lateral off-set at T9-10 and L4-5 respectively (Fig.1). The applied *in-vivo* cable force was measured in real time using an in-line spring assembly combined with a calibrated submersible load cell (rated at 50lbf full scale capacity; 32Hz sampling rate). Cable force was recorded during surgery and following recovery from general anesthesia at rest, during posture changes and ambulation in a 4x4 pen 3x/week for 7 days. Measured cable force values were synchronized with video recordings of the pig during representative activity states.

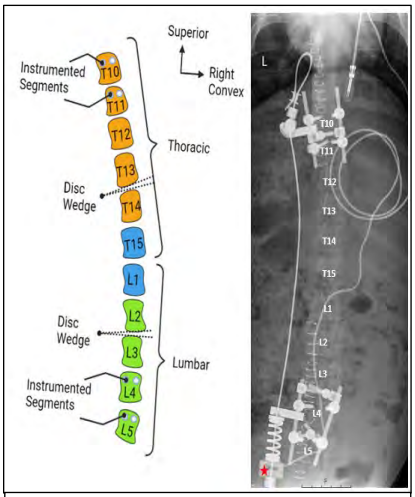


***Figure 1:*** *Radiograph and schematic illustration following placement of the spinal implants and installing the tether assembly. Vertebrae segmented by anatomical region: thoracic (orange), thoracolumbar (blue), lumbar (green). The red star in the dorso-ventral radiograph at the lumbar cluster depicts the location of the load cell in line with the spring assembly composing the tether construct.*

**RESULTS SECTION:** During surgery, maintaining the spine in neutral position, ~40N of tension (Fig. 2A) was applied to the cable connecting the thoracic and lumbar anchor points. Immediate postoperative CT revealed a Cobb angle of 2°. A progressive (~24hrs) decline in cable force to ~15-20N was observed – reflecting the viscoelastic stress relaxation of the connective soft tissues (Fig. 2B). Motion capture videos synchronized with cable force data revealed highly dynamic variation in cable forces associated with movement. *In vivo* cable forces measured 7 days following surgery revealed that ambulation produced tether forces with a range in amplitude up to 40N (Fig. 2C). CT imaging of the spine at postoperative day 7 with the pig positioned in neutral sternal recumbency demonstrated mild natural kyphosis angle of 7° and a cable force of 7 N. Right and left bends obtained under general anesthesia demonstrated that lateral bending of 8° towards the convex side produced a cable tension of 24N while a 35° lateral bend towards the concave side resulted in a cable force of 10N (Fig. 2D-F).

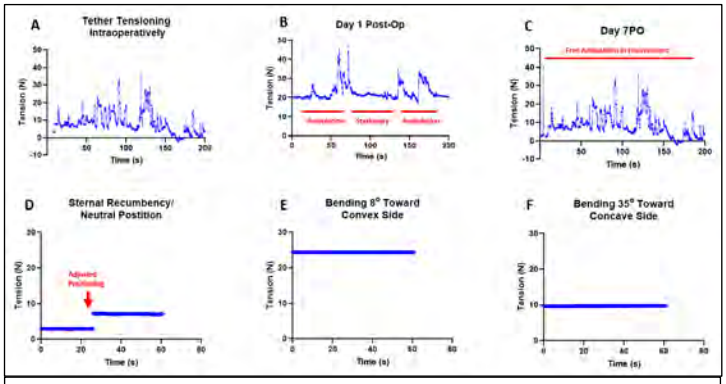


***Figure 2.*** *Measurement of tether tension in vivo. A) In vivo tensioning of the tether monitored during surgery as tension is applied around 40N. B) Day 1 postoperative after the tether tension was set in vivo to 40N, we noticed that the tether tension declined to ~20N, likely due to viscoelasticity of the spine. C) In the days after surgery, in vivo tether tension was periodically collected. Representative data shown here highlights variation in tether tension with activity and movement. D-F) Day 7 postoperative, CT imaging and tether tension recordings in the anesthetized animal under 3 different postures: sternal/neutral (D), 8 ° bending towards convex side (E) and 35 ° bending towards concave side (F).*

**DISCUSSION:** Cable tether tension rapidly declined after it was set intraoperatively because of viscoelastic stress relaxation. Depending on the type of activity and movement, superimposed forces were highly dynamic, exhibiting a wide range of amplitudes and frequencies. Analytic models of mechanically induced growth modulation based on Heuter-Volkmann principle that assume static stresses and strains will need to be modified to incorporate the stochastic nature of applied *in vivo* forces and moments. Future work will focus on longer-term studies to monitor the dynamic forces generated by the tether during controlled treadmill walking combined with real-time motion capture imaging to determine the kinematics and kinetics of spinal motion and develop stochastic models to predict the mechanical manipulation of spine growth.

**SIGNIFICANCE/CLINICAL RELEVANCE:** Tether based surgeries for correction of scoliosis in humans are increasing in prevalence and patient outcomes are predicated on growth modulation driven by tether forces. Understanding the nature of stochastic *in vivo* tether forces will afford an enhanced understanding of the tissue response with the potential to improve patient outcomes.

**REFERENCES:** [1] Stokes IA. Eur Spine J. 2007. [2] Heuter, C. Archiv fur pathologische Anatomie und Physiologie und fur klinische Medizin. 1863. [3] FDA. The Tether™ - Vertebral Body Tethering System – H190005, 2019.

**ACKNOWLEDGEMENTS:** This work was supported by funding from the Wyss Campbell Center for Thoracic Insufficiency Syndrome (Children's Hospital of Philadelphia).

Investigating dynamic loading-induced fluid effects on bone cells in 3D

Kailin Chen, PhD

It's been well-established that physical activity has a positive effect on bone remodeling process. While macro-scale mechanical loading on bone matrix has been extensively studied, the intrinsic cellular-level responses under dynamic mechanical loading remain largely unknown. As two main mechanically sensitive bone cells, osteocyte and osteoblast contribute positively to bone formation by translating external mechanical stimuli to biological signals. The mechanical environment surrounding osteocyte has been well-defined both theoretically and experimentally, where a lacuna-canaliculi structure around osteocyte conveys forces from both matrix and interstitial fluid shear to osteocyte surface. However, it is less known as for the mechanical environment around osteoblast. In addition, current experiments are mainly focused on the independent effects from either matrix deformation or fluid shear stress on mechanical responses of osteoblasts, mostly with a 2D cell monolayer. Therefore, it is vital to develop a platform which integrates effects of both matrix deformation and fluid shear for characterization of osteoblast mechanical responses.

In the current work, a micro-scale three-dimensional hollow TiO2 lattice structure is designed as the scaffold with osteoblastic-like cells seeded on. Different dynamic loading processes are applied to the in-vitro cell-matrix system submerged in culture media. By characterizing F-actin formation after the stimulation, it is found that in this case the osteoblasts react more actively to increased loading frequency compared with increased matrix stress/strain. In addition, the fluid field induced by dynamic loading under different frequencies are calculated based on a theoretical squeezing flow model, which shows a different shear stress field in the same area as shown in Fig. 1. This indicates that the fluid shear stress induced by the dynamic loading process might be the main contributor to activate osteoblasts.

Future work would land on validations of two hypothesis we obtained based on current results. First, the magnitude of fluid shear stress in this case is calculated to be of magnitude of millipascal, which implies that osteoblasts can be activated in a very low fluid shear regime. In addition, the shear stress field in the lattice is expected to have a gradient from corner to the center, which potentially results in different responses for cells at different locations.

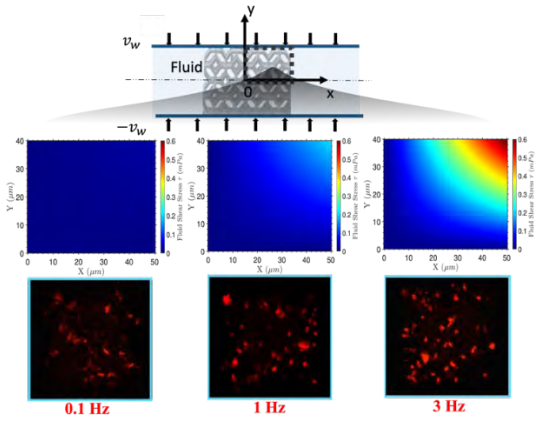


**Figure 1**. More F-actin (red fluorescence) recruitment with increased loading frequency, corresponding to a larger fluid shear stress field.

POSTER 9 WAS REMOVED

# Biomechanical Analysis of Writhing Technique for Sternal Single-Wire Closure

Peter D. Cho[1], Amba Viswanathan[1], Kathryn S. Strand[2], Chet S. Friday[2], Michael W. Hast[2], Uday Dasika[1]
1) Reading Hospital, Tower Health
2) McKay Orthopaedic Research Laboratory, University of Pennsylvania

## Objective

Despite the technological advancements in sternal closure like sternal plates and cables, single stainless steel wires are still used predominantly due to their cost-effectiveness. The traditional sternal wire closure technique in median sternotomy procedures requires cutting the loose ends of the wire to 1 centimeter (cm) after looping the wires around the sternum.[1] However, overtightening the loop at a relatively short length can result in sternal wire fracture.[1] In order to avoid the time-consuming nature of repairing a sternal wire fracture, we propose a modified sternal closure technique. The purpose of this experiment was to test a modified and novel writhing sternal closure method using traditional steel wires to prove that our technique has equal efficacy to that of the traditional method and is able to withstand an equal amount of force. We hypothesized that this experimental technique will minimize the risk of wire fracture during closure and sternal dehiscence by transferring some of the wire twisting force from the sternum to the wires, and thus decreasing fracture risk.

## Methods

Eight synthetic sternum models were used in the study. Samples were bisected with four Tekscan I-scan 6900 force sensors positioned between the two halves (**Fig. 2)**. The conventional sternal closure method (wire ends = 1 centimeter (cm) prior to twisting) and novel writhing closure method (wire ends = 10 cm prior to twisting) were defined as the control and experimental group, respectively. Eight trials were carried out in each of the two groups on the synthetic sternal models. Thin-film pressure sensors were used to measure maximum compressive forces applied on the sternum across four different areas (the manubrium, an upper middle point of the sternum, a lower middle point of the sternum, and the xiphoid process). Compressive forces were plotted against time to compare the process of overtightening between the methods.

## Results

There were no significant differences in total forces applied to the models when comparing the control (181.50±44.35 N) to the experimental group (163.09±38.75 N, P=0.39) (**Fig. 1**). The traditional method showed significantly higher force in the xiphoid process (29.02±8.22 N) than controls (19.40±4.27 N, P=0.011). Across the four areas on the sternum, the manubrium experienced the overall lowest compressive force in both the control group (3.37±2.61 N) and the experimental group (13.64±4.32 N, P=0.60). During the process of overtightening, the traditional method resulted in wire fracture 8 out of 8 times, while the experimental method underwent a twist-to-writhe transition and plateaued at an average compressive load of 97.57 N.

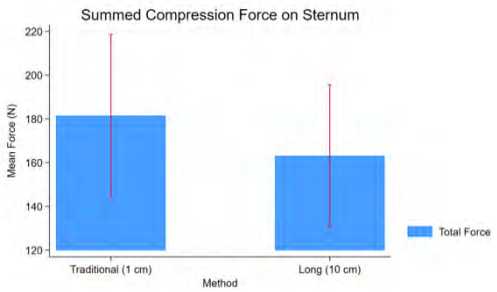


***Fig 1:*** *Summed compression forces on sternum in control and experimental groups*

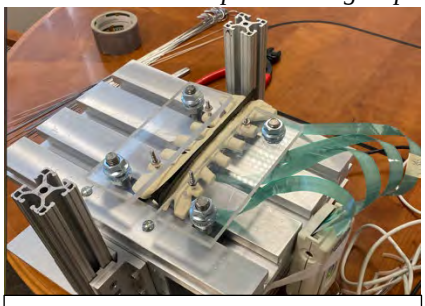

***Fig 2:*** *Sternum model setup with Tekscan force sensors in place*

## Conclusion

Results suggest that the experimental method can provide a similar compressive force on the sternum laterally to that of the traditional technique. Implementation of the writhing method for sternal closure may safely prevent sternal dehiscence and wire fracture during sternal closures.

Citations:

1. Lau, Edward. "CTSNet Step-by-Step Series: Sternal Closure Using Stainless Steel Wires." *CTSNet*, https://www.ctsnet.org/article/ctsnet-step-step-series-sternal-closure-using-stainless-steel-wires.

## COX2-independent Effects of the NSAID Naproxen on Bone

Alexandra Ciuciu, Ryan E. Tomlinson
Thomas Jefferson University, Philadelphia, PA

Non-steroidal anti-inflammatory drugs (NSAIDs) inhibit the cyclooxygenase (COX) enzymes COX1 and COX2 that produce prostaglandins driving pain and inflammation. We reported that adult female C57BL/6J mice treated with naproxen for 15 days had significantly decreased bone toughness, reduced strain adaptive bone remodeling, and diminished woven bone formation during stress fracture repair. We also found that naproxen decreased osteocyte dendrite number and the number of MMP13+ osteocytes as compared to vehicle in male mice. Since these effects on bone toughness and healing were not observed in mice treated with the COX2-specific inhibitor, celecoxib, we hypothesized that the effects of naproxen on osteocytes and bone toughness were COX2-independent. To test this hypothesis, naproxen sodium (10.9 mg/kg) or vehicle (dd$H_2O$) was administered to adult (15-18 weeks old) Ptgs2-Y385F and wild-type (WT) mice for 15 days. Mice received six bouts of axial forelimb compression using a 2 Hz rest-inserted sinusoidal waveform of 3 N for 100 cycles. Calcein and alizarin red were injected on day 5 and 12 respectively; drinking water was refreshed every 2-3 days. Right femurs were stored in PBS-soaked gauze at -20ºC before analysis. Both forelimbs were harvested, fixed, embedded in PMMA, sectioned using a low-speed saw, and imaged using confocal microscopy. First, we observed that naproxen significantly decreased trabecular bone volume fraction in Ptgs2-Y385F male mice (-21.5%, p=0.0055) as compared to vehicle treated mice; this effect was not significant in WT male mice or in female mice of either genotype. Next, we found that naproxen significantly decreased bone toughness by three-point bending across all genotypes and sexes (male: p=0.0004; female: p=0.0279; by two-way ANOVA). Surprisingly, naproxen also significantly decreased whole bone bending (section modulus vs. bending moment) intercepts in WT mice (male: p=0.0204; female: p=0.0399) but not Ptgs2-Y385F mice. Finally, we observed that naproxen treatment significantly diminished relative periosteal bone formation rate per bone surface in male Ptgs2-Y385F and WT mice (-28% in Ptgs2-Y385F; -58% in WT; p=0.047 by two-way ANOVA) by dynamic histomorphometry. These results demonstrate COX2-independent effects of naproxen on bone toughness. On-going studies will identify these COX2-independent mechanisms to improve therapeutic options for relief of musculoskeletal pain without impairing bone mechanical properties.

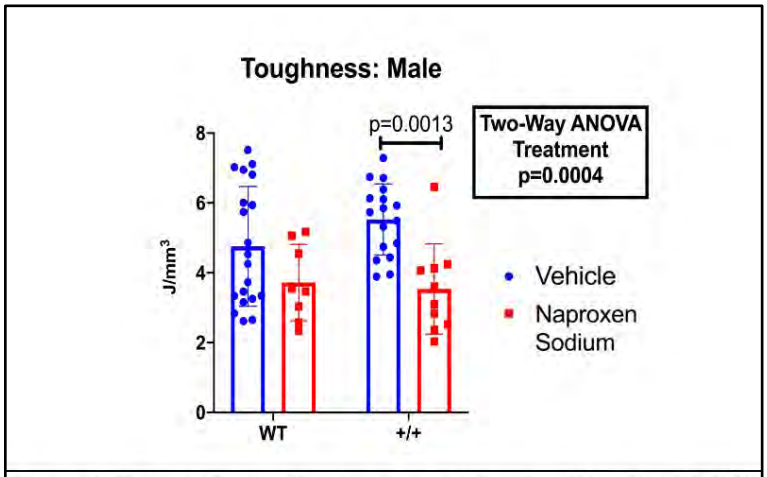


Figure 1: Average bone toughness as determined by standard 3-point bending for vehicle and naproxen sodium treated wild-type (WT) and Ptgs2-Y385F (+/+) mice. (n=8-20 per genotype)

# Collagen XII is a Critical Regulator of Supraspinatus Tendon Mechanics and Collagen Fiber Realignment Across Sex

Michael S. DiStefano[1], Stephanie N. Weiss[1], Andrew F. Kuntz[1], Louis J. Soslowsky[1]
[1]McKay Orthopaedic Research Laboratory, University of Pennsylvania, PA
micdis@seas.upenn.edu

**Disclosures:** AF Kuntz (5, Integra Lifesciences, Orthofix, Inc., FX Shoulder; 9, Orthopaedic Research Society, American Shoulder and Elbow Surgeons, American Board of Orthopaedic Surgery), no other disclosures

**INTRODUCTION:** Collagen XII is a Fibril-Associated Collagen with Interrupted Triple Helices (FACIT) that regulates collagen fibril assembly and is primarily expressed throughout tendon growth and development. Mutations in the *Col12a1* gene result in myopathic Ehlers-Danlos syndrome, a connective tissue disorder in which patients exhibit weakness at birth, absence of deep tendon reflexes and distal joint hypermobility and contracture [1]. Our novel tendon-targeted collagen XII mouse model demonstrated that patellar tendons exhibited reduced elastic, viscoelastic, and dynamic collagen fiber realignment properties across sex [2]. However, the role of collagen XII on the supraspinatus tendon, which experiences a complex, region-specific (insertion and midsubstance) loading environment within the rotator cuff of the shoulder, remains unknown. Therefore, the objectives of this study are to (1) elucidate the regulatory role of collagen XII on supraspinatus tendon whole-tissue and regional mechanics and dynamic response to load in mature mice using tendon-targeted (Scleraxis-Cre) collagen XII deficient and knockout mice and (2) understand whether the role of collagen XII on supraspinatus tendon biomechanical function and dynamic response to load is dependent on sex. We hypothesized that tendon-targeted deficiency and knockout of collagen XII would result in decreased supraspinatus tendon whole-tissue and regional elastic mechanics, whole-tissue viscoelasticity, and regional collagen fiber realignment across sex.

**METHODS:** Supraspinatus tendons from male and female, day 60 tendon-targeted collagen XII heterozygous (HET) mice (ScxCre;*Col12a1*$^{f/wt}$, n=8-9/group), knockout (KO) mice (ScxCre;*Col12a1*$^{f/f}$, n=6-9/group) and wild-type (WT) control mice (Cre- littermates, n=7-9/group) (IACUC) were subjected to our established mechanical testing protocol and collagen fiber realignment method [3]. Tendons underwent stress relaxation testing at 3, 5, and 7% strain each with subsequent dynamic frequency sweeps at 0.1, 1, 5, and 10 Hz, followed by a quasistatic ramp-to-failure. Throughout the ramp-to-failure, dynamic collagen fiber realignment was quantified using cross-polarization imaging, and regional fiber alignment data was interpolated with a polynomial fit as a function of strain from the load-displacement data. Images were also used to optically measure strain to calculate regional moduli (insertion and midsubstance). For each sex, comparisons between genotypes were conducted using one-way ANOVAs followed by Bonferroni post-hoc tests. Significance was set at $p \leq 0.05$ and trends at $p \leq 0.1$.

**RESULTS:** Cross-sectional area (CSA) was not different between male tendons, while female KO tendons exhibited a trending decrease in CSA relative to WT (data not shown). Consistent with our hypothesis, linear stiffness was significantly decreased in KO mice across sex and between female HET and KO mice (**Fig. 1A**). Moreover, insertion modulus was significantly reduced in HET and KO tendons across sex whereas midsubstance modulus was significantly reduced in male KO tendons and female HET and KO tendons (**Figs. 1B, C**). Further, genotypic differences were observed in viscoelastic properties across sex. Percent relaxation was significantly increased in KO tendons across sex at all strain levels (5% strain shown in **Fig. 1D**). Additionally, dynamic modulus was significantly decreased in male KO tendons and in female HET and KO tendons, while phase shift was significantly increased in KO tendons across sex across at all strain levels and frequencies (5% strain at 1Hz shown in **Figs. 1E** and **1F**, respectively). These results are supported by reductions in collagen fiber realignment in HET and KO tendons across region and sex, as demonstrated by significantly greater normalized circular variance values for insertion and midsubstance regions from 3-7% strain (**Figs. 2A-D**), encompassing the toe and linear elastic regions of these tendons.

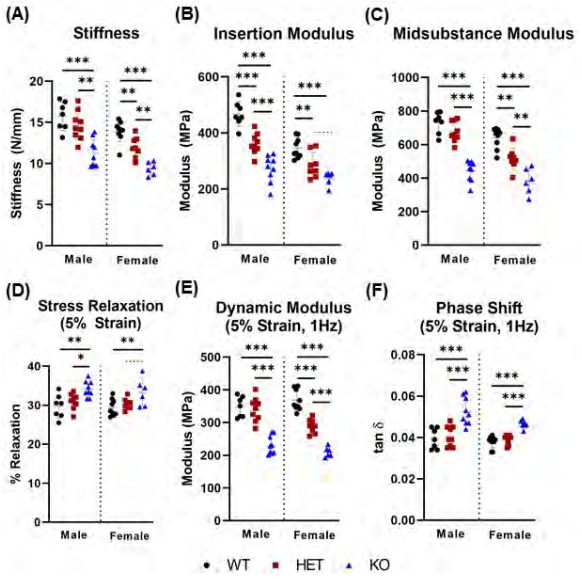


**Figure 1.** Differences between male and female elastic (A-C) and viscoelastic (D-F) mechanical properties of WT, HET, and KO supraspinatus tendons. Data as mean ± standard deviation (---$p \leq 0.1$ *$p \leq 0.05$, **$p \leq 0.01$, ***$p \leq 0.001$).

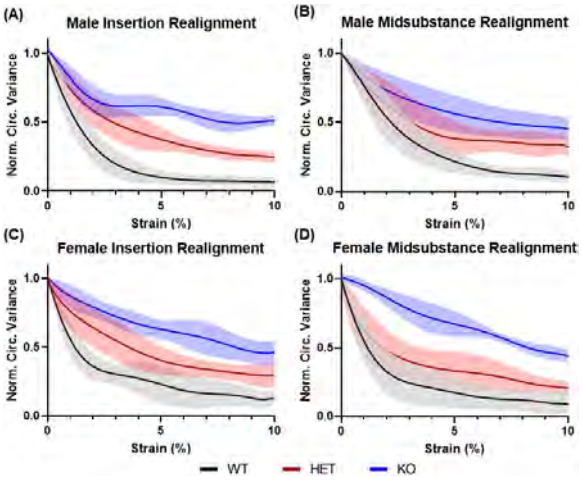


**Figure 2.** Collagen fiber realignment distribution differences for male (A-B) and female (C-D) WT, HET, and KO supraspinatus tendon insertion and midsubstance regions. Decreased normalized circular variance is indicative of increased collagen fiber realignment.

**DISCUSSION:** This study investigated the role of collagen XII on supraspinatus tendon elastic and viscoelastic mechanics and dynamic collagen fiber realignment using tendon-targeted male and female ScxCre;*Col12a1*$^{f/wt}$ and ScxCre;*Col12a1*$^{f/f}$ mice. Consistent with previous data [2], we showed that tendon-targeted collagen XII knockout resulted in striking reductions in regional and whole-tissue elastic and viscoelastic mechanical properties and regional collagen fiber realignment. Further, reductions in these properties in our collagen XII deficient HET tendons, highlight the allele-dependency of collagen XII on tendon mechanical function and dynamic collagen fiber realignment. These mechanical deficits could be due to the improper hierarchical assemblies of HET and KO tendons resulting in disorganized tendon matrices with an inferior ability to respond to load. This was evidenced by marked reductions in the HET and KO tendons' responses to realign resulting in inferior mechanical properties, especially whole-tissue stiffness, regional moduli, and dynamic modulus. Although similar differences in elastic and viscoelastic mechanical properties were present across sex in response to collagen XII deficiency and knockout, more genotypic differences were present in female mice. Genetic variations in the *Col12a1* gene have been associated with an increased risk of ACL ruptures in women [4], implicating potential sex-specific effects of collagen XII deficiency and knockout. Overall, our results demonstrate that decreased collagen XII expression detrimentally affects supraspinatus tendon mechanical properties and dynamic collagen fiber realignment across sex.

**SIGNIFICANCE/CLINICAL RELEVANCE:** This study elucidates the critical role of collagen XII in regulating male and female supraspinatus tendon regional and whole-tissue mechanics and dynamic structural response to load within the complex loading environment of the rotator cuff of the shoulder. Clinically, understanding the effects of collagen XII in tendon across sex can be used to develop and evaluate potential treatments modalities for myopathic Ehlers-Danlos syndrome.

**ACKNOWLEDGEMENTS:** We thank Ashley Fung for her assistance. This study was supported by NIH/NIAMS R01AR078790 and Penn Center for Musculoskeletal Disorders (NIH/NIAMS, P30AR069619).

**REFERENCES:** [1] Punetha et al. *Muscle Nerve*. 2017. [2] Fung et al. *ORS Annual Meeting*. 2021. [3] Connizzo et al. *Interface Focus*. 2016. [4] Posthumus et al. *Br J Sports Med*. 2010.

# In Situ Delivery of Microspheres to Promote Local Vascularization in Composite Structures

Matthew Fainor[1,2], Janai Augustin[2,3], Robert L. Mauck[1,2], Sarah E. Gullbrand[1,2]
[1]University of Pennsylvania, Philadelphia, PA; [2]Corporal Michael J. Crescenz VA Medical Center, Philadelphia, PA; [3]City College of New York, NYC, NY
**Disclosures:** MF – Matthew.Fainor@pennmedicine.upenn.edu (N), JA (N), RLM (8), SEG (6)

**INTRODUCTION**: The success of tissue engineered interventions relies heavily on implant vascularization [1]. Research efforts towards improved bone repair have therefore been focused on leveraging the hypoxia inducible factor (HIF)-1 signaling pathway in order to couple osteogenesis with angiogenesis [2]. A variety of small molecules [3, 4], including deferoxamine (DFO), an FDA approved stabilizer of the HIF-1α protein have been used. Previous work has focused on releasing HIF-1α stabilizers directly from implantable scaffolds or from microspheres for *in vivo* delivery via injectable hydrogels [5,6]. However, no studies have combined these approaches for tissue engineered constructs that require spatially-controlled drug delivery upon implantation *in vivo* following a period of *in vitro* pre-culture, where osteogenic and angiogenic induction is not desirable. In this study we developed and characterized an injectable microsphere-laden hydrogel for the purpose of delivering deferoxamine *in situ* to the endplate region of a larger composite total tissue-engineered disc immediately before implantation. To accomplish this, we created four custom mold geometries to pattern salt-leached PCL endplate scaffolds with either cylindrical pores or rectangular channels into which a sodium alginate hydrogel containing deferoxamine-loaded PLGA microspheres could be injected.

**METHODS:** DFO-loaded microspheres were prepared using an oil-in-water double emulsion method [9]. The inner phases of the emulsion consisted of 20 mg/ml DFO in diH20 and 10% 50:50 PLGA with an average molecular weight of 31 or 45 kDa in dichloromethane (DCM). DFO encapsulation was evaluated using an iron chloride assay [8]. To assess DFO release over time, 100 mg of microspheres from each group were suspended in 3 ml PBS and agitated on a rocker at 37 °C for up to 6 days. At each time point, the supernatants were withdrawn after centrifugation, replaced with 3 ml of fresh PBS, and analyzed using the iron chloride assay. Hydrogels were prepared by crosslinking medium viscosity sodium alginate with 2.3 g/L calcium sulfate at various ratios (50:50, 60:40, 70:30, 80:20, and 90:10 sodium alginate: calcium sulfate). Viscosity was assessed via timed inversion of 200 µl hydrogel and extrusion through a 30G needle. Four custom polydimethylsiloxane (PDMS) molds (1.5Pores: 1 mm deep, 1.5mm diameter cylinder; 2Pores: 1 mm deep, 2 mm diameter cylinder; 3Channels: 3 rectangular channels, 1 mm deep, 2mm wide; 4Channels: 4 rectangular channels, 1 mm deep, 1.5 mm wide) were generated from 3D-printed negatives **(Figure 2A)**. Salt-leached PCL scaffolds 16 mm in diameter and 2mm in height were then fabricated using each PDMS mold, as previously described [9] and imaged using SEM. Scaffold moduli, with or without injection of 70:30 sodium alginate hydrogel, was assessed via compressive mechanical testing (0.5 N-3 N, 3 cycles, 1 Hz). To assess the hydrogel's ability to deliver microspheres homogeneously, 250 µl of 70:30 sodium alginate hydrogel containing 42 mg of 45 kDa microspheres loaded with cell tracker red was injected into the channels of each scaffold and imaged using confocal microscopy.

**RESULTS:** Both 31 kDa and 45 kDa microspheres encapsulated a similar mass of DFO **(Figure 1A)**. However, 45 kDa microspheres released more DFO over the course of 6 days **(Figure 1B)**. Following viscosity and extrusion tests, the 70:30 sodium alginate:calcium sulfate hydrogel was selected for microsphere encapsulation, due to its intermediate viscosity and extrusion properties (**Figure 1C-D**). Four different scaffold morphologies were modeled; All scaffold morphologies were successfully fabricated, except for the 1.5Pores scaffolds **(Figure 2B)**. This scaffold geometry proved too intricate, and scaffolds did not survive demolding. Neither modification of scaffold morphology nor incorporation of the 70:30 hydrogel into scaffold structures significantly altered the scaffolds' compressive moduli **(Figure 2C)**. Repeatable injection of the hydrogel/microsphere composite into the pore design was more difficult than into the channels. Upon confocal imaging, microspheres were found to be uniformly distributed within the channels of channel scaffolds **(Figure 2D)**.

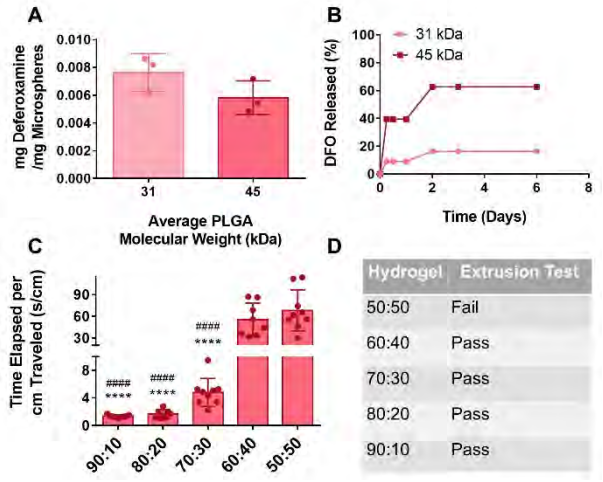


**Figure 1:** (A) DFO encapsulated by and (B) released from 31 kDa and 45 kDa PLGA microspheres. Hydrogel viscosity characterized by measuring the (C) downward travel time of the hydrogel following inversion (* = p<0.0001 in comparison to 60:40; # = p<0.0001 in comparison to 50:50) and (D) extrusion through a 30G needle where successful extrusion = pass.

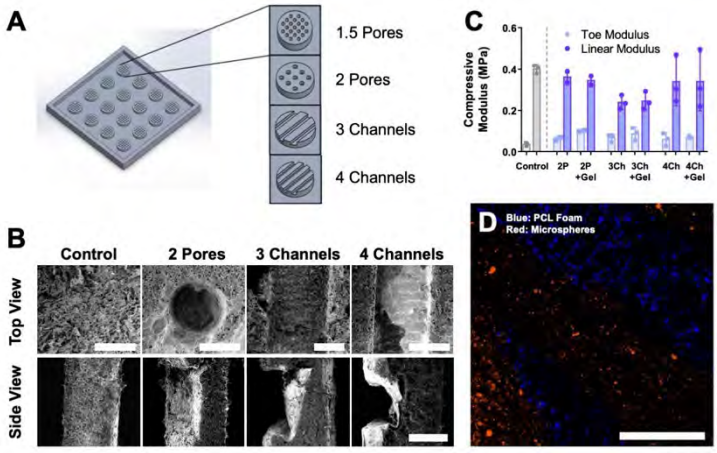


**Figure 2:** (A) SolidWorks model of 3D-printed positive mold-forms for 4 different custom designs and (B) SEM images of each successfully molded salt-leached PCL scaffold (Scale = 1.0 mm). (C) Compressive moduli of PCL scaffolds with or without 70:30 sodium alginate hydrogel. (D) Z-stack confocal image of 45 kDa microsphere-laden 70:30 hydrogel injected into the channels of a 4Channels scaffold (Scale =1.0 mm).

**DISCUSSION:** Ultimately, we were able to successfully deliver fluorescently-loaded microspheres to a discrete scaffold region *in situ* using an injectable sodium alginate hydrogel without compromising scaffold mechanics. Additionally, we were able to encapsulate the highly hydrophilic small molecule DFO into two different molecular weight PLGA microspheres and demonstrate its release profile over the course of 6 days. The burst release of DFO observed in both groups could be attenuated via the incorporation of a lipid coating, such as Labrafil®, into the microsphere fabrication process [10]. Incorporation of microspheres into hydrogels has also been shown to produce a more gradual drug release profile [11]. Scaffold geometry could also be further tuned by generating shallower (0.5mm) and narrower channels, which may promote higher levels of vessel infiltration [12]. Overall, our results show promise for application in composite tissue-engineered implants that require regions of boney vascularization after *in vivo* implantation. Future work will implement these new endplate designs in conjunction with the hydrogel-microsphere composite to assess the development of vascularized bone adjacent to our tissue engineered discs following implantation *in vivo* in a large animal model.

**SIGNIFICANCE:** Enabling the controlled delivery of cost-effective small molecules is critical to the success of many composite tissue engineered therapies, such as those that seek to promote discrete, regionalized vascularization, including a multi-compartment tissue-engineered total disc replacement.

**REFERENCES:** [1] Auger+ *Annu. Rev. of Biomed. Eng.*, 2013 [2] Shipani+ *JBMR*, 2009 [3] Sefcik+ *Organogenesis*, 2008 [4] Selvaprithviraj+ *Curr. Med. Chem.*, 2017 [5] Jahangir+ *J Mater. Sci.: Mater. Med.*, 2019 [6] Vignesh+ *Colloids Surf B*, 2018 [9] Kim+ *Acta Biomater 111*, 2020 [8] Jia+ *Society for Biomaterials*, 2016 [9] Kim+ *Acta Biomater 114*, 2020 [10] Kim+ *UPOJ*, 2016 [11] Rassu+ *Carbohy. Polym.*, 2015 [12] Chen+ *Sci. Rep.*, 2018

**ACKNOWLEDGEMENTS:** This work was supported by the Department of Veterans' Affairs and the Penn Center for Musculoskeletal Disorders.

# Functionally Graded Lattices in Additively Manufactured Rib Implants Result in Similar Biomechanics

Richa Gupta[1], Lauren Judkins[2], Chet S. Friday[1], Joseph B. Ulsh[1], Stephen Kovach[1], Samir Mehta[1], Charles Tomonto[3], Guha Manogharan[2], Michael W. Hast[1]
[1]McKay Orthopaedic Research Lab, Department of Orthopaedic Surgery, University of Pennsylvania, Philadelphia, PA; [2]SHAPE Lab, Department of Mechanical and Nuclear Engineering, Pennsylvania State University, University Park, PA, [3]Johnson and Johnson 3D Printing, Miami, FL
hast@pennmedicine.upenn.edu

**Relevant Disclosures**: RG (None), LJ(None), CSF (None), JBU (None), SK (None), SM (None), CT(3A), GM (None), MWH (None)

INTRODUCTION: Rib fractures are difficult to treat surgically due to large variability in bone size, curvature, and mechanical properties of the natural bone. Titanium alloy (Ti6Al4V) rib implants are used when open reduction internal fixation is required for reconstruction. Undesirable clinical outcomes such as chest tightness, component loosening, and secondary fracture at the ends of implants are often reported, with revision surgery required in up to 15% of patients.[1] Rib implants may be improved with 3D printing or additive manufacturing (AM), because this process allows for creation of patient-specific geometries and tuning of mechanical properties of implants. In a previous study, we printed 100 x 10 x 1.5 mm Ti6Al4V beams, and decreased bending stiffness up to 15% by uniformly changing the internal lattice structure.[2] Decreasing the mechanical stiffness towards the ends of rib implants may reduce incidence of secondary fracture, but interfragmentary fixation strength cannot be compromised. In the current study, we sought to characterize the biomechanics of functionally graded lattice designs by testing implants in a biofidelic synthetic bone model. We hypothesized that, by making gradient- based changes in internal lattice architecture, we could maintain requisite construct rigidity at the fracture line and decrease the likelihood of secondary fracture at implant ends.

METHODS: This study included 6 implant designs (n=6), with 5 custom AM implants, and a traditionally manufactured titanium control group (MatrixRib, DePuy Synthes, **Fig. 1A**). Custom implants were manufactured with variable rectilinear infill patterns between the 0.5 mm floors and roofs of the plates. Groups included a sparse infill group, 3 functionally graded infill groups (Gradients 1, 2, and 3) and a solid infill group. Custom implants had a similar width (10 mm), thickness (1.5 mm), and length (70 mm) as control implants, but did not include notches to allow for maximization of infill volume. All custom implants were additively manufactured from Ti-6Al-4V powder via laser-powder bed fusion and heat-treated using standard processing conditions. Custom 4th generation Sawbones were designed and manufactured to represent a transverse fracture at the apex of curvature on a 50th percentile male's 4th rib on the left side. Components were implanted with six 2.7 mm diameter nonlocking cortical screws by fellowship-trained orthopaedic surgeons. To simulate post-operative respiration, ribs were compressed in a two-point bend test to generate flexural moments between 0 – 0.5 Nm at the fracture line. Tests were run at 3 Hz for 360,000 cycles to simulate 17.5 days of post-operative breathing (**Fig. 1B**).[3] 3D motion capture was performed at 100 Hz to measure 6 degrees of freedom of interfragmentary motion during cyclic loading. Following cyclic testing, the plates were subjected to ramp-to-failure tests at a rate of 1 mm/s and failure mechanisms were recorded. Differences in cyclic stiffness, 3D interfragmentary motions, ramp-to-failure stiffness, maximum load, and work to failure were tested for significance using one-way ANOVA tests with post-hoc Holm-Sidak pairwise comparisons.

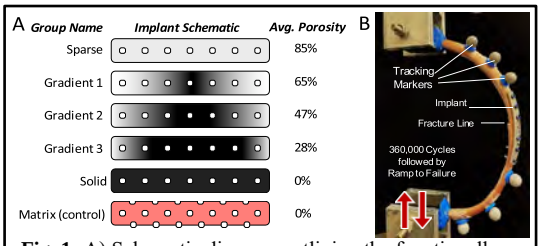


**Fig. 1:** A) Schematic diagram outlining the functionally graded implant designs tested in the experiment, along with average porosities of the infill for each design. B) Photograph of a synthetic rib undergoing 2-point bend testing. 3D motion tracking markers were used to quantify interfragmentary motions.

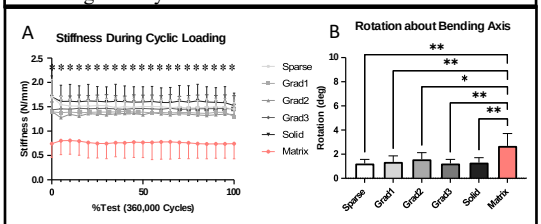


**Fig. 2:** A) Load-cell-measured stiffness throughout cyclic loading, with significant differences between the control (pink) and experimental (gray) groups. B) Mean interfragmentary rotations about the bending axis during cyclic loading. * = p < 0.05; ** = p<0.001

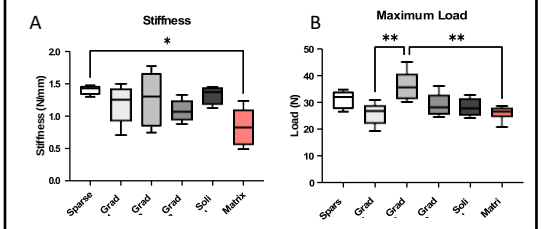


**Fig. 3:** Box and whisker plots showing changes in A) load-cell measured stiffness and B) maximum load withstood during 2-point bend ramp-to-failure testing.
* = p < 0.05; **= p<0.001

RESULTS: During cyclic testing the Control group demonstrated significantly decreased construct stiffness, as measured by the load cell (0.76 ± 0.28 N/mm), compared to all AM implant designs (means between 1.35 – 1.61 N/mm) (**Fig. 2A**). 3D motion capture indicated that the Control group bone fragments rotated significantly more about the bending axis (2.7 ± 1.3 deg) than the other groups (means between 1.2 – 1.6 deg) (**Fig. 2B**). There were no significant differences between groups for the other 5 degrees of freedom. Ramp to failure testing showed that Control group bending stiffness (0.84 ± 0.28 N/mm) was significantly lower than the stiffness of the Sparse group (1.40 ± 0.07 N/mm), but not other groups (**Fig. 3A**). Ultimate force values were highest for the Gradient 2 group (35.8 ± 5.6 N, which was significantly different from the Gradient 1 (25.8 ± 4.2 N) and Control (25.9 ± 2.7 N) groups (**Fig. 3B**). There were no significant differences between groups for work prior to failure. All constructs failed via bone fracture at the most posterior screw hole.

DISCUSSION: Results from this study only prove a portion our initial hypothesis. Using Control implant behavior as a gold-standard, our implant designs were largely successful in controlling interfragmentary motion and showed no signs of permanent deformation during the cyclic load test. The lack of notches in AM designs likely caused increased resistance to bending. Interestingly, changes in functionally graded lattice architecture did not lead to many significant differences in AM implant performance throughout the experiment. Our designs did not result in predictable stepwise changes to stiffness or maximum load, and functional grading of the lattice did not change the failure mechanism, which was the same for all test specimens. These results are likely confounded by the thin cross-sectional area of the implants and small volume of bone available for screw purchase. Additional studies are ongoing to map changes in mechanical behavior of functionally graded implants.

SIGNIFICANCE/CLINICAL RELEVANCE: Additive manufactured orthopaedic implants may benefit from the use of functionally graded lattice structures. In the case of rib implants, it is likely that the screw hole – not implant stiffness – creates the stress riser responsible for secondary fractures at implant ends.

REFERENCES: [1] Lafferty et al. JBJS A, 2011 [2] Judkins et al. ASME IMECE, 2021 [3] Bottlang et al. Eur J Trauma Emerg Surg, 2010

ACKNOWLEDGMENTS: This study was supported by the Manufacturing Pennsylvania Innovation Program and NIH/NIAMS P30AR069619. DePuy Synthes provided materials and technical support.

# Scleraxis Targeted Deletion of Collagen XI Impairs Tendon Mechanical Function During Postnatal Development

Jordan S. Cohen, Ashley K. Fung, Stephanie N. Weiss, Nathaniel A. Dyment, Louis J. Soslowsky
McKay Orthopaedic Research Lab, University of Pennsylvania, Philadelphia, PA

**Author Disclosures**: Jordan S. Cohen (N), Ashley K. Fung (N), Stephanie N. Weiss (N), Nathaniel A. Dyment (N), Louis J. Soslowsky (N)

**INTRODUCTION**: Mutations in the *Col11a1* gene are implicated in Type II Stickler Syndrome and result in joint problems including hypermobility and early arthritis [1]. Beyond its role in Stickler Syndrome, collagen XI is highly expressed during tendon postnatal development and interacts with collagen I and II during heterotypic fibril formation [2]. We previously showed that during patellar tendon postnatal development, tendon-targeted (ScxCre) collagen XI deficiency disrupts tendon structure, resulting in tenocyte nuclear disorganization, larger diameter collagen fibrils, and increased tendon length [3]. However, whether these structural findings result in alterations in tendon mechanical function is unknown. Therefore, the objective of this study was to define the role of collagen XI in the acquisition of tendon mechanical function during postnatal development using tendon-targeted collagen XI knockout mice. We hypothesized that tendon-targeted collagen XI knockout would result in inferior tendon mechanical properties.

**METHODS**: Tendon-targeted ScxCre;*Col11a1*$^{flox/flox}$ (KO), ScxCre;*Col11a1*$^{flox/wt}$ (HET), and Cre- littermate control (CTRL) mice were used (IACUC approved). Patellar tendons were harvested at postnatal days (P) 10, 20, and 30 for mechanical testing (n=12/group). The tibia-patellar tendon-patella complex was dissected, tendon cross-sectional area was measured, and the tibia was potted in polymethylmethacrylate. The patella was gripped with sandpaper (P10 and P20) or clamped directly (P30) using custom fixtures, and tendons were subjected to a protocol consisting of preconditioning, stress relaxations at 3, 4, and 5% strain each followed by a dynamic frequency sweep (0.1-10 Hz), and a ramp to failure at 0.1% strain/s. For each age, genotypes were compared using a one-way ANOVA with Tukey post-hoc tests. Significance was set at $p \leq 0.05$.

**RESULTS**: Tendon-targeted collagen XI knockout resulted in substantial alterations in patellar tendon mechanical properties. Cross-sectional area (**Figure 1A**) of KO tendons was greater only at P10, while KO tendons (**Figure 1B**) were significantly longer than CTRL tendons at all ages, consistent with previous histological findings. Stiffness (**Figure 1C**) and failure load (**Figure 1D**) of KO tendons were dramatically reduced compared to CTRL and HET tendons. Material properties of KO tendons showed similar trends, with marked reduction in modulus (**Figure 1E**), failure stress (**Figure 1F**), and failure strain (**Figure 1G)** at all ages compared to CTRL and HET tendons. Dynamic modulus was similarly reduced in KO tendons at all ages (data not shown).

**DISCUSSION**: Previous work evaluating the role of collagen XI in postnatal development found that tendon-targeted knockout disrupts tendon structure, resulting in tenocyte nuclear disorganization, larger diameter collagen fibrils, and increased tendon length [3]. Results of the present study further elucidate the importance of collagen XI in regulating tendon structure-function during early postnatal development. The mechanical differences in KO mice were particularly striking, with KO patellar tendons demonstrating substantial reductions in modulus of 45%, 78%, and 60% at P10, P20, and P30, respectively. These findings are consistent with previous mechanical findings in mature (day 60) KO tendons [4,5], but the emergence of these stark mechanical differences as early as postnatal day 10 point to a critical and previously undescribed role for collagen XI in the initial establishment of tendon hierarchical structure. In tendon, collagen XI is most highly expressed during embryonic development with minimal expression during adulthood [2], and therefore, inferior mechanical function in KO tendons may be due to alterations in fibril nucleation and assembly. Additionally, motivation for this study was primarily driven by the observation of significant patellar tendon lengthening and the presence of granulation tissue in mature tendons. Our findings suggest the absence of collagen XI leads to the deposition of substantially weakened matrix, resulting in injury and elongation following the initiation of ambulation around postnatal day 10. Preliminary gene expression findings at P10 (not shown) support a pathological response with increased expression of genes associated with non-collagenous matrix proteins and remodeling, and studies are ongoing to further elucidate the mechanisms underlying the role of collagen XI in tendon development.

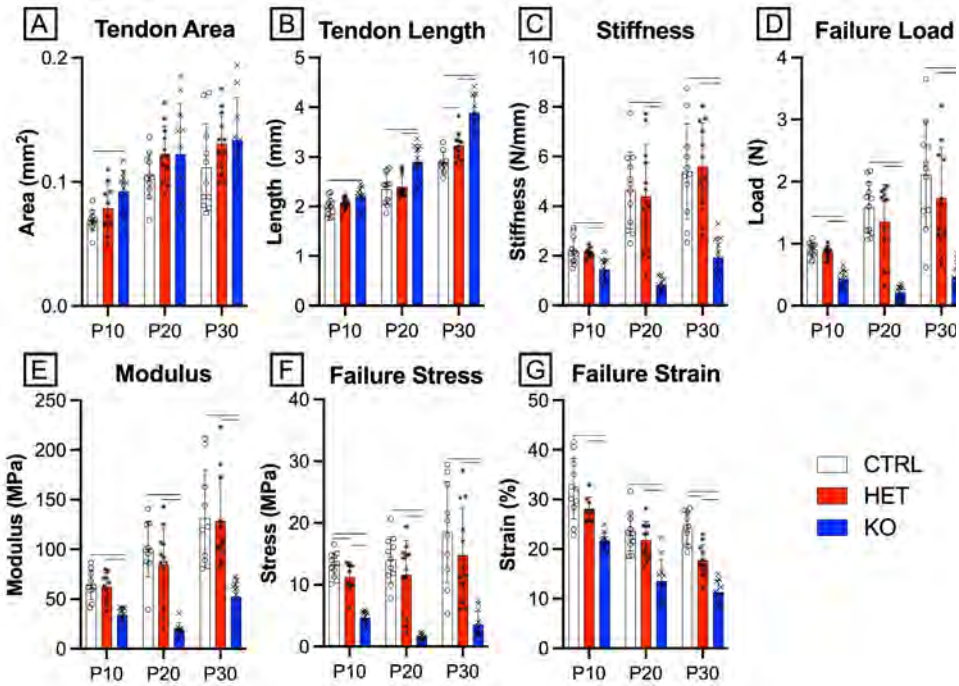


**Figure 1**: Patellar tendon (A) cross-sectional area was higher in KO tendons at p10, while (B) tendon length was greater at all ages. (C) Stiffness and (D) failure load were significantly reduced in KO tendons at all ages compared to CTRL and HET tendons. (E) Elastic modulus, (F) failure stress, and (G) failure strain were significantly reduced in KO mice compared to CTRL and HET tendons at all ages. (—p<0.05)

**SIGNIFICANCE:** Collagen XI is critical in the establishment of tendon structure and mechanical function during postnatal tendon development. These findings highlight the need to further define the regulatory role of collagen XI in tendon development and healing, which could lay the foundation for future therapeutic applications.

**REFERENCES**: [1] Cattalini M et al., Pediatr Rheumatol Online J, 2015. [2] Wenstrup RJ et al., J Biol Chem, 2011. [3] Stein MK. et al., ORS Annual Meeting, 2022. [4] Ye Y et al., ORS Annual Meeting, 2019. [5] Sun M et al., Matrix Biol, 2020.

**ACKNOWLEDGMENTS**: This study was funded by NIH/NIAMS R01AR073231 and the Penn Center for Musculoskeletal Disorders (P30 AR069619).

# ASSESSING THE EFFECT OF JOINT ANGLE POSITION ON ULTRASOUND SHEARWAVE ELASTOGRAPHY MEASUREMENT IN ACHILLES AND PATELLAR TENDON IN HEALTHY SUBJECTS

Bryson Houston[1], Andrew North[1], Rachana Vaidya[2], Stephane Cui[2], Menghan Chen[2], Josh Baxter[1], Jennifer Zellers[2]

[1]Department of Orthopaedic Surgery, University of Pennsylvania, Philadelphia, PA, USA
[2]Department of Physical Therapy, Washington University in St. Louis, St. Louis, MO, USA

**Background:** Tendon mechanical properties such as shear modulus, have been proposed as biomarkers for injury and recovery. The use of ultrasound shearwave elastography (SWE) is a non-invasive technique for assessing these properties. Joint angle position affects the tensile load of the Achilles tendon and can influence its mechanical properties, such as stiffness and elasticity. However, the effect of joint angle position on SWE measurements is not well understood.

**Methods:** We recruited 28 healthy subjects, average age 30.5 years old. The subjects were made up of 17 females and 11 males. Body mass index was reported from 27 subjects with an average BMI of 22.1 kg/m$^2$. Subjects were randomized to scan either the right or left lower extremity. SWE measurements were taken at neutral, 10° plantar flexion, and 20° dorsiflexion ankle positions for the Achilles tendon and in a 90° flexed and 180° extended knee position for the patellar tendon. We utilized the GE E10 ultrasound machine to collect all data. The mean and standard deviation of shear wave velocity were calculated for each position.

**Results:** In the patellar tendon, the shear wave velocity was significantly higher in the flexed position (6.44 ± 3.12 m/s,) compared to the extended position (3.93 ± 1.36 m/s,) ($p<0.05$). In the Achilles tendon, shear wave velocity was significantly higher in both plantarflexed (4.01±1.76 m/s,) and dorsiflexed positions (3.79 ±1.15 m/s,) compared to neutral position (2.98±0.68 m/s,) ($p<0.05$).

**Conclusion:** Our findings suggest that joint angle position significantly affects SWE measurement magnitude and variability of tendon mechanical properties in healthy subjects. As SWE is increasingly used as a non-invasive tool for assessing tendon health and monitoring response to treatment, imaging at a consistent joint position and establishing a standardized protocol for assessing tendon mechanical properties using SWE is necessary to ensure consistency of measurements.

**Acknowledgements:** This work was funded by NIH/NIAMS R01AR078898 and P50AR080581.

# Reduced Postnatal Loading after Sciatic Nerve Resection Impairs Achilles Tendon Growth and Maturation.

Talayah Johnson[1], Natalie L. Fogarty[1] Bryan Kwok[2], Alisia Lin[1], Tonia K. Tsinman[1], Xi Jiang[1], Eiki Koyama[3], Lin Han[2],
Josh R. Baxter[1], Robert L. Mauck[1], Nathaniel A. Dyment[1]
[1]McKay Orthopaedic Research Laboratory, University of Pennsylvania, Philadelphia, PA.
[2]Nanobiomechanics Laboratory, Drexel University, Philadelphia, PA. [3]Children's Hospital of Philadelphia, Philadelphia, PA.
talayahj@seas.upenn.edu

**Disclosures**: Mauck (4, Mechano-Therapeutics, LLC; 5, 4Web Medical; 8, JOR Spine Editor)

INTRODUCTION: Mechanical forces are key regulators of musculoskeletal tissue formation and maintenance. Load bearing tissues, such as tendons, respond to mechanical loading events to maintain tensional homeostasis by fine tuning the formation and degradation of extracellular matrix proteins [1]. Both excessive and insufficient loading are implicated in the disease etiology of tendons. For example, overuse tendinopathies, which commonly inflict the Achilles tendon, account for 7% of musculoskeletal disorders in the US [2]. Manipulation of mechanical loads via rehabilitative loading exercises promotes repair processes that may culminate in improved restoration of normal tendon structure and function [3]. While loading has been shown to influence tendon composition in adults and healing tendons, it is less clear how mechanical forces influence Achilles tendon growth during early postnatal stages when there is a rapid accrual of extracellular matrix. Growth of the Achilles is predominantly governed first by cell proliferation during embryonic stages and then transitions to extracellular matrix (ECM) production shortly after birth. Here, we performed sciatic nerve resection (SNR) in neonatal mice on post-natal day 1 (P1) to explore how reduced muscle loading impacts Achilles tendon growth and maturation during this critical time window. We hypothesized that reduced mechanical loading of the hindlimb after SNR would result in reduced growth and development of the Achilles tendon, resulting in changes in tissue morphology and mechanical properties.

METHODS: All animals and procedures were IACUC approved. Sciatic Nerve Resection Procedure. Unilateral left sciatic nerve resection (SNR) was performed on post- natal day 1 (P1) in male and female CD1 mice (**Fig. 1a**) with evaluation at post-natal day 42 (P42). Gait Analysis. The CatWalk XT system was used to measure gait parameters in SNR and control mice. MicroCT. Excised hindlimbs from each group of mice were scanned on a Scanco μCT45 scanner to measure tibia length. Biomechanical Testing. Achilles tendons were dissected, cross-sectional area was measured using a custom laser device, placed in custom grips, preconditioned, and loaded to failure (0.1%/sec). Structural and material properties were calculated using custom MATLAB scripts. Cryohistology. Hindlimbs were harvested, formalin-fixed, embedded in OCT, and cryosectioned (8 μm) in the transverse plane using Cryofilm 2C. Fluorescent imaging with a nuclear counterstain followed by brightfield imaging with toluidine blue staining was performed. Image Analysis. Achilles tendon cross-sectional area and cell density were quantified using Fiji. Statistics. Gait parameters between SNR and control groups were compared via one-way ANOVA with Tukey's HSD post-hoc comparisons ($p<0.05$). SNR limb vs. contralateral limb were compared via paired t-tests for all other assays ($p<0.05$).

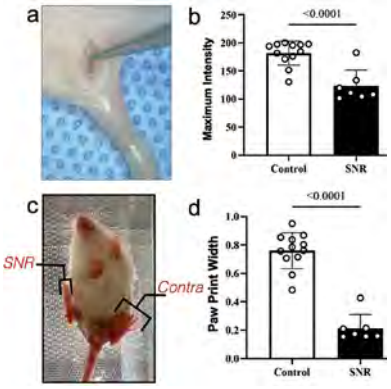


**Fig. 1**: SNR procedure (a) resulted in reduced maximum stride intensity (b) and paw width (c-d) for detectable strikes measured via the CatWalk XT gait analysis system.

RESULTS: SNR resulted in sustained gait impairments. CatWalk XT analysis at P42 was used to assess changes in gait parameters that would inform hindlimb loading patterns. SNR mice exhibited marked gait abnormalities with over 50% of strides being below the detectable threshold in the operated limb compared to 100% detection in contralateral limbs and control limbs. Additionally, SNR resulted in marked reductions in maximum stride intensity (**Fig. 1b**) and paw print width (**Fig. 1c-d**) compared to unoperated control limbs ($p < 0.0001$), a hallmark of sciatic denervation. SNR resulted in smaller posterior musculature and bone shortening. Gross microscopic images revealed smaller posterior musculature in the hindlimbs (data not shown). As previously reported [4], we also found that the tibiae in the SNR limbs were shorter than unoperated controls (16.7±0.1 vs. 17.8±0.4, $p<0.01$). SNR resulted in smaller Achilles tendons. The Achilles tendons in the SNR limbs were shorter (**Fig. 2c**) with reduced birefringence and cross-sectional (**Fig. 2d**) ($p<0.05$). The total number of cells per cross section was also reduced (**Fig. 2e**, $p<0.05$) while there was an increasing trend in cell density (**Fig. 2f**, $p=0.08$) in the SNR tendons. SNR resulted in impaired mechanical properties of the Achilles tendons. To further examine the role of early postnatal loading in Achilles tendon growth and maturation, we performed uniaxial tensile testing. The stiffness, failure force, and modulus were all significantly reduced in the Achilles tendon of the SNR limb (**Fig. 3a-c**, $p<0.05$, Figure 4), with a decreasing trend in maximum stress (**Fig. 3d**, $p=0.1$).

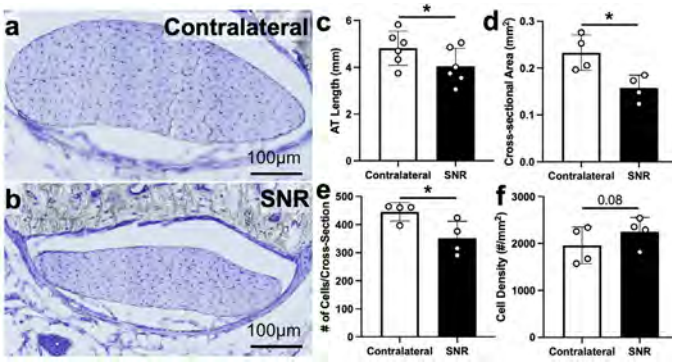


**Fig. 2**: SNR Achilles tendons (ATs) were markedly smaller than contralateral ATs (representative images in a-b). AT length (c) and cross-sectional area (d) were significantly reduced. The # of cells/cross section was also reduced (e) and there was a trending increase in cell density (f). * $p < 0.05$.

DISCUSSION: The role of mechanical loading in maintaining Achilles tendon homeostasis is well established and chronic aberrant loading can contribute to tendinopathies. The effect of applied loading during periods of active cell proliferative- and matrix-driven growth are not well understood. Using a surgical denervation model, we found persistent gait alterations with smaller posterior musculature and tibia shortening, which is consistent with previous findings [4]. We also found that the reduced loading had profound effects on the growth and maturation of the Achilles tendon, yielding smaller tendons with reduced mechanical properties (structural and material). These results suggest that the cells are producing less and possibly inferior extracellular matrix, which we plan to investigate in future studies. Cell proliferation also contributes to postnatal growth and we interestingly found a trending increase in cell density in the SNR limbs, which warrants future study.

SIGNIFICANCE/CLINICAL RELEVANCE: Understanding how mechanical loading regulates tendon growth and maturation may inform novel therapies to treat disease and injuries.

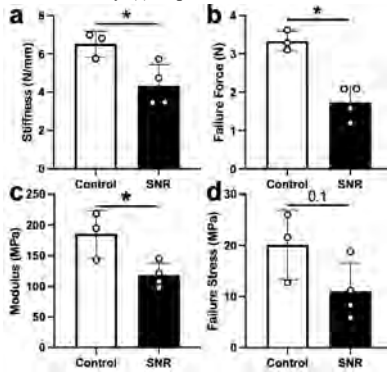


**Fig. 3**: SNR Achilles tendons displayed inferior mechanical properties: stiffness (a), failure force (b), modulus (c), and failure stress (d). * $p < 0.05$.

REFERENCES: [1] Wang JH, et al, *J Biomech*. 2006; [2] Rutland M, et al, *N Am J Sports Phys Ther*. 2015; [3] Langberg H, et al, *J Phys*. 1999 [4] Killion CH, et al, *Mol. Biol. Cell*. 2017.

# A Small Molecule TGF-β Agonist Drives Fibrous Tissue Formation in Meniscus Tissue after Injury

Lemmon EA[1-3], Dehghani B[1,3], Kwok B[4], Han L[4], Mauck RL[1,2,3]

Departments of [1]Orthopaedic Surgery and [2]Bioengineering, University of Pennsylvania, Philadelphia, PA, [3]Translational Musculoskeletal Research Center, Philadelphia VA Medical Center, Philadelphia, PA, [4]Nanobiomechanics Laboratory, Drexel University, Philadelphia, PA

elemmon@vet.upenn.edu

**Disclosures**: EAL (None), BD (None), BK (None), LH (None), RLM (4, 5, 8)

**Introduction:** The meniscus, a crucial load-bearing fibrocartilaginous structure in the knee, is commonly injured and has a poor innate healing capacity despite surgical apposition of tear edges.[1] A contributing factor to this poor healing is the loss of matrix at the tear interface, resulting in a substantial tissue gapping.[2] To address this, numerous factors have been explored to promote cell migration and tissue deposition at this interface.[3-5] Namely, TGF-β, a pleiotropic cytokine, can stimulate meniscal fibrochondrocytes (MFCs) matrix production and promotion of tissue integration both in vitro and in vivo. However, the cost and propsensity for loss of biologic activity when incorporated into drug delivery systems make application of this molecule a challenge. A small molecule agonist of this pathway may be better suited for these applications. To that end, we evaluated whether the small molecule TGF-β signaling agonist, SRI-011381 hydrochloride (referred to as SRI) could promote anabolic matrix production in MFCs. We first queried the structural and micromechanical changes local to vertical meniscus tears over 3 weeks following injury to identify ideal treatment windows. Next, we evaluated the ability of SRI to promote myofibroblastic conversion of MFCs in vitro on a stiff substrate. Using this information, we then tested whether the SRI could successfully promote anabolic gene expression of MFCs in fibrin, a softer 3D delivery vehicle commonly used in meniscus tear augmentation strategies.

**Methods:** Minipig Surgery Model: Juvenile (6-month-old) Yucatan minipigs underwent bilateral parapatellar surgery and each medial meniscus received a vertical longitudinal tear (1/2 arc length, red-white zone) (n=1 animal/time point) (**Fig 1A**). Animals were euthanized at 1, 2, or 3 weeks and menisci were harvested for a series of micro- and macro-scale analyses. Atomic Force Microscopy (AFM) Nanoindentation: Histology guided AFM (**Fig 1B-C,D**) was applied to 40 μm–thick cryo-sections (n=2/group) in PBS using a microspherical tip ($R \approx 6$ μm, nominal $k \approx 0.6$ N/m) and Dimension Icon AFM. For each region (defect edge and body), the effective indentation modulus was calculated[6] for 50-75 locations. 2D MFC Activation Assay: Bovine MFCs were cultured in chemically defined medium (CM) on glass slides and maintained in either 1) CM, 2) CM + TGFβ (10 ng/mL), or 3) CM + SRI (10 μM) for 4 days. Vehicle control = DMSO. Cells were then fixed and stained for actin and αSMA with a DAPI nuclear counterstain. Confocal z-stacks were obtained at 20x (n=10/group), and the αSMA:actin correlation coefficient and cell area were measured using CellProfiler (**Fig 2A-C**). 3D MFC Activation Assay: MFCs (~50,000) were suspended in 75 μL of fibrin adhesive (Tisseel™) and cross-linked into cylindrical constructs (n=3/group) for 5 minutes (**Fig 3A**). Constructs were cultured for 14 days, maintained in either 1) CM, 2) CM + TGFβ-3 (10 ng/mL), or 3) CM + SRI (10 μM). Constructs were rinsed with sterile PBS (3x) and processed for RNA extraction and cDNA synthesis followed by qRT-PCR for anabolic genes downstream of TGF-β. Statistical Analyses: For AFM of meniscus defect edge and body, paired t-tests were used. 1-way ANOVA with repeated measures and Sidak's correction for multiple comparisons was used to evaluate αSMA:actin correlation, cell area, and qPCR.

**Results:** The region adjacent to a meniscus tears had a decreased indentation modulus within 1-week post injury, compared to regions further removed from the injury site, with a similar trend seen at both 2- and 3-weeks (**Fig 1A-D**). MFCs cultured on a stiff substrate (glass) responded to SRI by increasing their αSMA:actin correlation coefficients and cell area, reaching levels similar to that of TGFβ-3 treated MFCs (**Fig 2A-C**). In 3D culture, fibrin + MFCs supplemented with SRI showed increased expression of genes downstream of TGF-β, including DCN, SOX9, YAP, COL1A1, and ACTB, reaching levels higher than constructs treated with TGFβ-3 (**Fig 3A-B**).

**Discussion:** Our findings show that the edges of meniscus defects decrease in stiffness within 1-week of injury. This rapid loss in matrix integrity soon after defect creation indicates that delivery of factors to promote matrix deposition and prevent local degradation would be best delivered soon after the injury has occurred. Notably, when treated with the TGF-β agonist SRI in vitro, MFCs showed evidence of myofibroblastic conversion (higher αSMA:actin correlation and cell area)[7]. This transition correlates with an increase in cell contractility and ECM deposition, necessary functions at the defect edge to promote tissue formation[8]. MFCs cultured in fibrin treated with SRI also showed increased expression of TGF-β induced genes, even in this softer microenvironment. Taken together, these data indicate that SRI may be a promising small molecule to deliver to the site of meniscus injury to promote repair. Future work will evaluate the efficacy of SRI when delivered to meniscus tears in a large animal injury model.

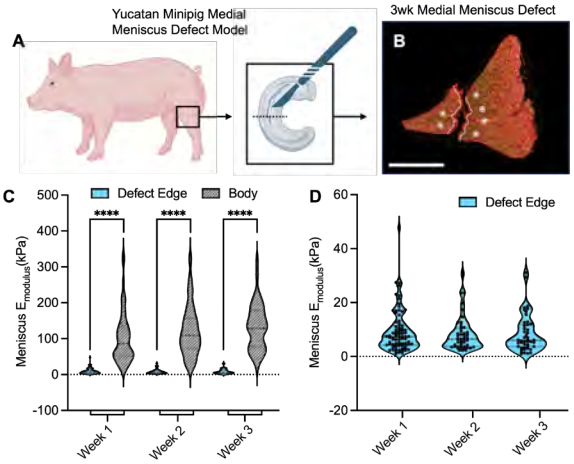


**Fig 1.** (A) Schema of meniscus injury model (black line = orientation of sectioning) and (B) representative Picrosirius Red staining (10x, white line = defect edge and ◉ = body indentation regions, scale bar = 1mm). AFM modulus of (C) defect edge vs. body and (D) defect edge for all timepoints. Mean +/- SD, ****indicates p<0.001.

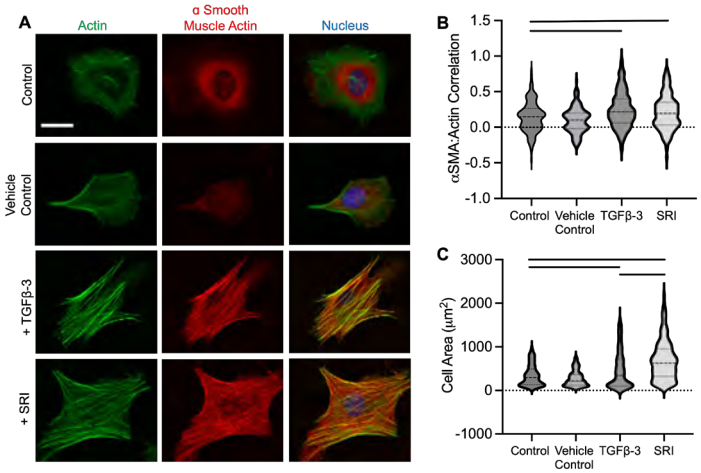


**Fig 2.** (A) Representative MFCs stained for actin and αSMA after exposure to TGFβ-3 or SRI. (B) αSMA:actin correlation coefficient and (C) cell area. Mean +/- SD, bars indicate p<0.05. Scale: 15μm.

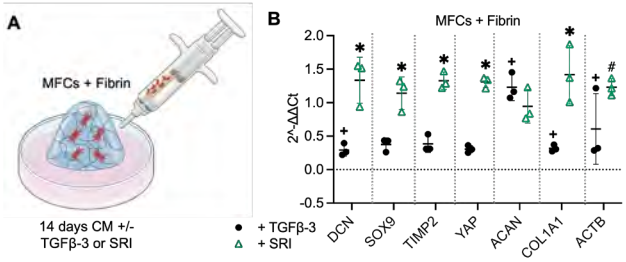


**Fig 3.** (A) Schema of MFCs + fibrin construct fabrication. (B) qPCR results (dotted line indicates no treatment (CM) group). *indicates (p<0.05) or # (p<0.1) vs. TGFβ-3, + indicates difference (p<0.05) vs. CM alone.

**Significance/Clinical Relevance:** We show that a novel small molecule agonist of TGF-β signaling can promote anabolic MFC function in a clinically translatable fibrin adhesive. This may be used to improve outcomes by delivering a stable, efficacious small molecule directly to the meniscus repair site.

**Acknowledgements:** This work was supported by the NIH (R01 AR056624 and T32 GM007170) and the VA (I01 RX003375, IK1RX003932-01A1).

**References:** 1. Fernandes+ *Biorheol*, 2002; Bansal+ *JOR*, 2021; 3. Lee + Sci *Transl Med*, 2014; 4. Qu+ *Nat Commun*, 2017; 5. Heo+ *Sci Adv*, 2020; 6. Diamitridis+, *Biophys J* 2002+; 7. Li+ *Nat Materials*, 2017; 8. Hinz+ *Am J Pathol*, 2007.

**Physiological Storage Solution Decreases Whole Muscle Passive Mechanical Properties**

Timothy McGinley[1] and Benjamin I Binder-Markey[1,2]
[1]School of Biomedical Engineering, Science and Health Systems & [2]Department of Physical Therapy & Rehabilitation Sciences, Drexel University, Philadelphia Pa
Corresponding email: tm3292@drexel.edu

**Introduction:**

Understanding muscle structure and function relationships are essential in determining muscle performance and recovery following injury or disease. Muscle active force generating mechanics and properties have been widely characterized to scale linearly across muscle tissue's scales from the single muscle fiber up to the whole muscle [1]. However, passive muscle mechanics (the muscle's elastic properties) are less well understood for their properties do not scale linearly [4]. One problem contributing to this dearth of knowledge is multiscale mechanical testing is difficult to complete in a single day due to the time required to test multiple scales before rigor sets in the muscle. Thus, samples are often stored in a physiological storage solution to preserve the sample prior to testing. This storage solution preserves the active mechanics [1,4]; however, it is unknown how the storage solution affects the passive mechanics of the muscle. Therefore, the purpose of this study is to begin to understand how a commonly used glycerinated physiological storage solution affects whole muscle passive mechanical properties.

**Methods:**

Passive mechanical characteristics of fresh and stored samples were collected from four muscle types, lateral gastrocnemius (LG), rectus femoris (RF), semimembranosus (SM) and tibialis anterior (TA), differing in structure and function, from 12 to 16-week C57BL6 mice. To test the mechanics of fresh whole muscles, the muscles were dissected from origin to insertion and immediately tested. To test the effect of storage solution on muscle mechanics, an additional set of muscles were dissected from origin to insertion. These muscles were placed in a glycerinated physiological storage solution [2] and stored for 2-weeks at -20°C prior to testing. For mechanical testing, the fresh and stored muscle samples were placed in a physiological bath and then fastened to a 5N force transducer. Muscle slack length was determined. Each muscle was then lengthened in ~5% fiber strain increments from 0%-50% strain being held for 3-minutes at each strain. Force at the end of each hold was recorded. Following testing, the samples were weighed. Muscle passive forces were normalized to physiological cross-sectional area (PCSA), and muscle strain was converted from fiber strain using fiber length-ratio [2]. The normalized passive stress-strain data were fit to an exponential curve. The stiffness was compared across muscles: fresh vs. storage solution using a two-way ANOVA. The mass of both fresh and stored tissue (post-testing) was compared using a 2-tailed unpaired t-test with a Welch's correction.

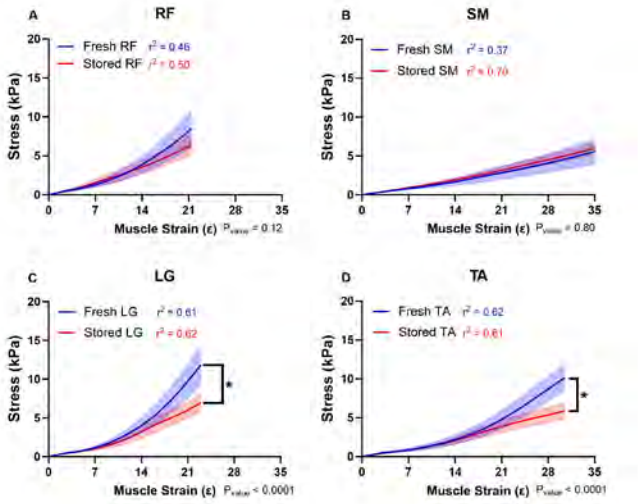


**Figure 1:** Normalized Stress-Strain Curve for fresh (blue) and stored (red) of the A) RF, B) SM, C) LG, & D) TA. Data shown as averages±SD. $n_{fresh}$=7-8; $n_{stored}$=7

*Table 1: Physiological Properties of Fresh and Stored Muscle *p<0.05 compared to fresh*

| | Mass (mg) | | Av. % Difference |
|---|---|---|---|
| | **Fresh** | **Stored** | |
| **RF** | 98.4±5.23 | 114.9±1.37* | 16.7% |
| **SM** | 135.2±7.13 | 140.3±4.08 | 3.8% |
| **LG** | 86.9±4.00 | 96.5±6.39 | 11.1% |
| **TA** | 60.1±3.01 | 71.5±3.01* | 19% |

**Results & Discussion:**

The muscles stored in glycerinated storage solution demonstrated higher masses with an average 12.7% higher mass across all muscles (Table 1). Normalized stress-strain curves shown, demonstrates moderate to good fits with significant decreases in stiffness following storage in the LG and TA muscles ($p<0.05$) (Fig. 1). The stored LG and TA were approximately 40% and 62% less stiff than their fresh counterparts, respectively. Stored RF stiffness trended to decreasing stiffness but did not demonstrate significant differences ($p=0.12$) from its fresh tissue counterpart. The stored SM stiffness was not significantly different to the fresh tissue ($p=0.80$). The 40-62% decrease in LG and TA muscle stiffness following storage cannot be accounted for by the change in PCSA due to 12.7% increase in mass. This points to a decrease in structural integrity of the muscle following storage in a glycerinated storage solution. Since passive fiber mechanics remain intact following storage in a glycerinated solution [3], it is likely that this storage solution damages the connective tissue in the extracellular matrix, reducing muscle tissue stiffness.

**Significance:**

Glycerinated physiological storage solution did not preserve the passive mechanics at the whole muscle scale for two of the four muscles presented. Following storage, muscles demonstrated muscle mass increase and reduced muscle stiffness. Future studies will explore the sources of decreased passive mechanics by further studying the mechanics at the fascicle, single fiber scale, and intramuscular connective tissue. Additional studies will explore other types of physiological storage solutions that do not contain glycerol.

**References:**

[1] Winters, T.M et al. J. Biomech. 2011. **(44) 109–115**. [2] Eastwood A.B. et. al., Tissue & Cell 1979. **11 (3) 553-566** [3] Einarsson, F. et al. J. Ortho Surg., 2008. **3:22** [4] Ward et al. Front. Physiol. 2020. **11:211**

**Tendon Degeneration is Not Due to Altered Local Tissue Strains in Fatigue-Loaded Mouse Achilles Tendons**

Krishna Pedaprolu, Spencer Szczesny
Department of Biomedical Engineering, The Pennsylvania State University

Tendinopathy is a painful and debilitating condition that can cause major disability. However, the etiology of the disease is unclear. One primary risk factor for tendinopathy is overuse or, more specifically, fatigue loading. Overuse or fatigue loading of tendons results in structural changes in the load-bearing matrix and reduces the mechanical properties of the tendon. It also leads to an increase in catabolism, inflammatory factors, and deposition of abnormal non-tenogenic components like lipids, calcium, and cartilage-like deposits, which can further weaken the tendon. This degenerative behavior is hypothesized to be the response of tendon cells to altered physical stimuli. In vitro studies suggest that high longitudinal strains lead to tendon cell degeneration. However, in vitro models are unable to capture the multiple complexities (cellular density, cell-cell contacts, cell-matrix contacts, hierarchal structure, etc.,) of the native tendon environment. Therefore, the physical cues that drive tendon degeneration and mechanotransduction pathways that transduce these cues to cell remain unknown. Explant models enable the investigation of mechanobiology in the native cell environment while also ensuring precise control over loading, environmental conditions, and pharmaceutical agents to determine the mechanisms driving cell behavior. Using our previously established explant model of mouse Achilles tendon degeneration, this study aimed to a) investigate if a mechanotransduction pathway (actin mediated contractility) is responsible for transducing physical cues to the cells in the degenerated tendon, and b) determine whether local tissue strains change with fatigue loading and if they can predict mitochondrial dysfunction, a marker for cellular degeneration. We hypothesized that a) actin mediated cell contractility is essential for tendon cell degeneration, and b) there will be changes in local tissue strain fields and high longitudinal strains will be predictive of cellular degeneration. To achieve our first objective, we perturbed the actin cytoskeleton of statically and cyclically loaded mouse Achilles tendon explants with 10 uM of cytochalasin D and processed the samples for gene expression via RT-qPCR. For our second objective, we used a DIC algorithm to measure the local tissue strains in our fatigue loaded mouse Achilles tendon explants that were stained with DRAQ-5 (nuclear stain) to track nuclei and tetramethyrhodamine (TMRM, dye for polarized mitochondria) to visual mitochondrial health. We found that fatigue induced degeneration in our explant model was eliminated with cytochalasin D treatment. Contrary to our hypothesis, there were no changes in the averages or standard deviations of the longitudinal, transverse, or shear strains between fatigue-loaded and freshly harvested tendons. Using a multiple linear regression model, we also found that local tissue strains are a weak predictor of mitochondrial health. Our data suggest that mechanotransduction via an intact actin cytoskeleton is necessary to induce tendon degeneration. This is in agreement with a previous in vitro study that showed that non-tenogenic differentiation of tendon progenitor cells induced by cyclic loading can be prevented by inhibiting actin contractility. We surprisingly found that there were no changes in local strain fields with fatigue loading. While counterintuitive, these findings are consistent with prior work and help explain why we also found that the local tissue strains were not predictive of mitochondrial dysfunction. While previous in vitro studies of isolated cells show that high tensile strains (8%) can produce degenerative cell behavior, our findings indicate that the longitudinal strains in mouse Achilles tendons never exceed 2%, which suggests that the loading conditions in prior experiments are supraphysiologic. Rather than altered tissue strains, it is possible that local structural damage (e.g., collagen disorganization or denaturation) is responsible for initiating cellular degeneration in fatigue-loaded tendons.

**Collagen Integrity Assessment in Bone: ATR-FTIR Spectroscopy Validated Approach**

Shahrizoda Rizokulova, Nancy Pleshko, and William Querido*
Department of Bioengineering, College of Engineering, Temple University, Philadelphia PA
*William.Querido@temple.edu

Collagen integrity in bone is a pivotal determinant in our comprehension of bone degeneration and diseases. Collagen type I, the predominant protein in bone, forms the structural scaffold for the mineralization of bone tissue. Fourier-Transform Infrared spectroscopy (FT-IR) stands as a powerful and versatile tool for assessing the molecular composition and structural characteristics of materials, exploiting absorbance bands related to chemical bonds within the sample. Among the sampling techniques available, attenuated total reflection (ATR) stands out as one of the most straightforward, requiring minimal sample preparation. However, despite the potential of ATR spectroscopy, there has been a lack of consensus in the literature regarding which parameters can effectively assess collagen quality in bone. This study aimed to validate an approach for quantifying collagen integrity in bone using ATR spectroscopy. To achieve this, we conducted experiments involving porcine cortical bone and collagen type I pellets. These were precisely cut into 3x3 mm pieces and subjected to varying temperature conditions (50, 65, 80 and 95° C) to induce progressive denaturation of the collagen fibers. ATR spectra were acquired using a ThermoFisher Nicolet iS5 FT-IR spectrometer with an iD7 ATR accessory, averaging 32 scans with a 4 $cm^{-1}$ spectra resolution. Data analysis involved smoothing, baseline offset correction, normalization, and 2nd derivative processing to quantify peak intensities associated with collagen composition and structure. Specific peaks of interest, such as amide I (1690, 1660, 1630 $cm^{-1}$), amide II (1550 $cm^{-1}$), amide III (1235 $cm^{-1}$), and CH (1450 and 1338 $cm^{-1}$), were analyzed, and peak ratios were evaluated across the samples. Among the various peak ratios investigated, the 1235/1450 ratio exhibited the most significant trends during collagen denaturation in both bone and collagen samples. This ratio consistently decreased with increasing collagen denaturation, showing a strong negative correlation of -0.96 with temperature. Our findings demonstrate that the 1235/1450 ratio is a valid spectroscopic parameter for quantifying collagen integrity in bone using ATR spectroscopy. This validation holds significant implications for research in bone health, disease, and related fields. It provides a reliable and straightforward approach that requires minimal sample preparation, making it a valuable tool for studying changes in collagen integrity. Ultimately, our research addresses a critical gap in understanding collagen quality and offers a method with broad applications in various research endeavors related to bone health and therapeutic interventions.

# Collagen Fibril Deformation is Not Observed in Developing Mouse Patellar Tendon Regardless of Collagen XI Expression

Jaime A. Santillan, Jeremy D. Eekhoff, Stephanie N. Weiss, Louis J. Soslowsky
McKay Orthopaedic Research Laboratory, University of Pennsylvania, Philadelphia, PA
Jaime.santillan@pennmedicine.upenn.edu

**Disclosures**: Jaime A. Santillan (N), Jeremy D. Eekhoff (N), Stephanie N. Weiss (N), Louis J. Soslowsky (N)

**INTRODUCTION:** The development of functional tendons requires proper collagen assembly in hierarchical structures [1]. As part of this process, collagen XI co-assembles with collagens I and II during heterotypic fibril formation and its disruption leads to abnormal extracellular matrix development [2]. Deficiency of collagen XI disturbs tendon structure, causing nuclear disorganization, increased lateral growth of fibrils, and degradation of mechanical properties [1,4]. However, how nanoscale mechanisms contribute to the weakened mechanical integrity of collagen XI deficient tendon is unknown. Therefore, the goal of this study was to elucidate the role of collagen XI in the fibril deformation mechanisms in developing mouse patellar tendon. We hypothesized that tendon-targeted knockout of collagen XI would result in increased deformation of collagen fibrils.

**METHODS:** Male and female wild-type control (WT), *Scx-Cre;Col11a1*$^{flox/wt}$ heterozygous (HET), and *Scx-Cre;Col11a1*$^{flox/flox}$ knockout (KO) mice at 30 days of age were used (n=7-8/group, IACUC approved). Tibia-patellar tendon-patella complexes were isolated, and the cross-sectional area of all samples was measured using a custom laser-scanning device. The tibia was embedded with polymethyl methacrylate (PMMA) and the patella was gripped with sandpaper and secured in a metal fixture. Tendons were preloaded to 0.025N and subjected to a testing protocol consisting of 10 cycles of preconditioning followed by a 1-minute hold. Based on loading curves obtained from preliminary quasi-static ramp-to-failure data using the abovementioned mouse models [4], tendons were strained at a rate of 0.1% strain/second to the toe region (1% strain for all genotypes) or linear region (8.9%, 6.2%, or 4.4% strain for WT, HET, or KO, respectively) of the stress-strain curves. Then, the samples were flash-frozen at the target strain, precisely cut free from the tibia and patella, and placed in a cryo-embedding medium. Subsequently, tendons were cryo-sectioned at 20µm thickness and fixed in formalin. To observe changes at the nanoscale, a Bioscope Catalyst Atomic Force Microscope was used in tapping mode on tendon sections to obtain topographical images of the sample surfaces. A minimum of five 2.0µm x 2.0µm images at a resolution of 512x512 pixels were acquired within 1mm of the tibial insertion, where tissue strains were expected to be the greatest [5], across 3 sections per sample. The length of the d-band periodicity of collagen fibrils was measured using Fourier analysis in MATLAB. Changes in the average d-period with applied tendon strain were taken as indicative of fibril deformation, and changes in the average variance in the d-period within individual images and across the entire sample were taken as indicative of local and global variation in fibril deformation, respectively [6]. Data was analyzed using two-way ANOVAs with the main effects of genotype and applied strain (i.e., toe vs. linear regions). Significance was set at $p < 0.05$.

**RESULTS:** Qualitative analysis of the AFM images revealed the presence of a heterogeneous population of collagen fibrils with larger diameters in the HET and KO groups compared to WT controls (Fig. 1), showing evidence of the poorly regulated lateral growth of fibrils. Despite this difference, the average d-period length was not different across genotypes and did not change across strain levels (Fig. 2A). Similarly, local and global variance in the collagen fibril d-period were not affected by genotype or applied strain (Fig 2B, C).

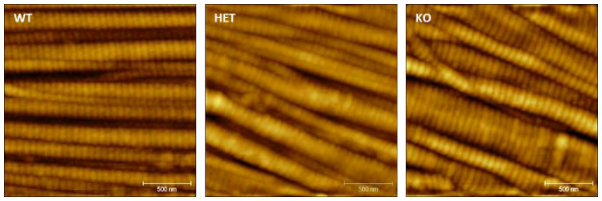


**Figure 1**. Representative AFM images of collagen fibrils of the three different genotype groups (Wild-type, heterozygous, and knockout group, respectively)

**DISCUSSION:** Tensile mechanical testing of tendons was performed to apply macroscale strains and subsequently measure the fibril deformation of collagen fibrils at the nanoscale. We found that tendon-targeted collagen XI knockout disrupted the nanoscale organization and increased the heterogeneity of fibril morphology. This abnormal fibril structure is consistent with prior work that used transmission electron microscopy to observe the collagen fibrillar matrix [1]. Based on previous studies, fibril deformation was expected when different levels of strain were applied to the tendon [6,7]. Contrary to our hypothesis, the fibril d-period did not increase over the applied strain range in the patellar tendon. This result may indicate differences in the nanoscale loading mechanism that occurs within the patellar tendon in comparison to other tendons, which could be due to the patellar tendon's unique structure with two bony attachments. Further work is needed to explain these surprising findings and investigate the role of collagen XI in the deformation mechanism of other tendons.

**SIGNIFICANCE:** Collagen XI regulates collagen fibrillogenesis and is essential during the development of tendons. This study shows that the deficiency or absence of collagen XI causes structural changes in collagen fibrils at the nanoscale and emphasizes its importance in the assembly of tendon hierarchical structure.

**ACKNOWLEDGEMENTS:** This study was supported by NIH/NIAMS (R01AR073231) and the Penn Center for Musculoskeletal Disorders (P30 AR069619)

**REFERENCES:** [1] Sun et al. *Matrix Biol* 2020. [2] Linsenmayer et al. *J Cell Biol* 1993. [3] Holmes et al. *Current Topics in Developmental Biology* 2018. [4] Cohen et al. *ORS* 2022. [5] Gilday et al. *J Biomech* 2013. [6] Connizzo BK et al. *J Biomech* 2014. [7] Rigozzi et al. *Journal of Structural Biology* 2011.

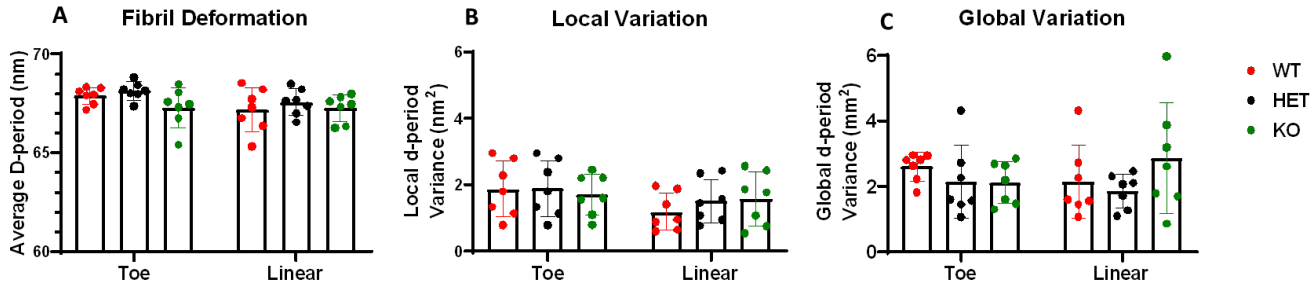


**Figure 2**. Fibril deformation (A), local variation (B), and global variation (C) were unaffected by genotype and applied strain. Data is shown as mean ± SD.

# MRI-Based Finite Element Modeling Approach to Quantify the Relationship between Femoral Geometry and Atypical Femoral Fracture

Ashkan Sedigh[1], Brandon Jones[2], Nada Kamona[2], Christiana Cottrell[2], Rasleen Grewal[2], David Baretto[2], Achala Kankanamge[2], Jianna Kim[2], Elaine Li[2], Kevin Li[2], Makayla Clark[2], Ganen Chinniah[2], Caroline Paik[2], Reva Bhatt[2], Ryan Shams[2], Maegan Sojan[2], Chamith S. Rajapakse[2], Ani Ural[1]

[1] Department of Mechanical Engineering, Villanova University, Villanova, PA, USA
[2] Departments of Radiology and Orthopaedic Surgery, University of Pennsylvania, Philadelphia, PA

## Abstract:

Atypical femoral fracture (AFF) that occurs at the subtrochanteric or midshaft region of the femur has been associated with long-term bisphosphonate use. The current clinical population-based studies have not been able to explain the underlying mechanisms of AFF. Moreover, femoral geometrical properties that increase AFF risk have not been conclusively identified. Thus, this study aims to develop a novel MRI-based finite element (FE) modeling approach to identify the relationship between femoral geometry and AFF.

Five female human cadaveric femurs were scanned via magnetic resonance imaging (MRI) at an isotropic resolution of 341 µm. The images were segmented and processed using Simpleware ScanIP to generate FE meshes (~700k elements). The meshes were imported into the FE analysis software, Abaqus, and were subjected to stance loading (Fig. 1A). The fracture process was modeled by the cohesive extended finite element method (XFEM). Homogeneous material properties were assigned with an elastic modulus of 15,000 MPa, ultimate strength of 109.5 MPa, and critical energy release rate of 1.196 N/mm based on the literature. The load-displacement data were extracted to assess the influence of femur geometrical properties (neck shaft angle, neck variation angle, neck length, femur neck thickness, and midshaft diameter) on femoral mechanical properties.

The simulation results showed that the stiffness, peak load, and displacement at the peak load corresponding to crack initiation at the AFF site correlate with the shaft diameter (R=0.79, 0.69, -0.95, respectively) (Fig. 1B). No statistically significant difference relationships were observed between stiffness, peak load, displacement at the peak load, and other geometrical parameters.

This study established a modeling approach incorporating MRI and fracture mechanics-based FE modeling for evaluating the influence of femoral geometrical properties on the mechanical response at the AFF site. The variation in mechanical properties with femoral geometry under the same material properties indicates the significant contribution of femur geometry to the fracture resistance at AFF sites. The modeling process developed here can be adapted to incorporate additional MRI-based geometrical measurements, such as bowing angle, and parameters, such as bone volume fraction, cortical porosity, and collagen fraction. As a result, MRI-based FE models provide a promising new approach for the noninvasive assessment of the femur's geometrical and material properties and identify the multifactorial determinants of AFF.

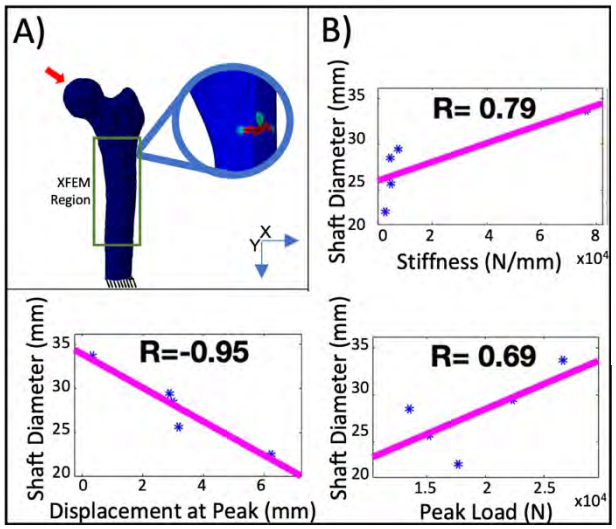


**Figure 1.** A) Femur FE model with the applied load (red arrow) and crack initiation at the AFF site. B) Variation of mechanical properties of femur and shaft diameter showing Pearson correlation coefficients.

**Resolving Nanoscale Deformations of Mineralized Collagen Fibrils in 3D**

*Riti Sharma*, Ottman Tertuliano
University of Pennsylvania, Mechanical Engineering and Applied Mechanics

Osteoarthritis (OA) is a degenerative whole-joint disease that causes degradation of the articular cartilage and is known to affect the subchondral bone. Clinically, the disease has been associated with fragility fractures, an effect noticed at the macroscale. However, the fundamental mechanisms occurring at the microscale that result in the progression of this disease and these anomalous fractures are still unclear. This is primarily due to the hierarchical structure of the bone. Traditionally, most studies have focused on the larger length scales of the bone – the organ, osteonal, or trabecular levels. Our aim is to isolate and quantify the nanoscale mechanisms facilitating pathogenesis and understand how much of the change in mechanical properties of the bone is due to the fundamental building blocks – mineralized collagen fibrils.

We introduce a novel *3D imaging* technique using synchrotron X-ray tomography to visualize *individual* nanoscale mineralized collagen fibrils in bone with 30 nm voxel resolution (Fig 1). First, we mill 50 x 10 x 10 $\mu m^3$ bone beams using a FIB-SEM. Then, we lift them out and place them on silicon supports etched on 2 x 2 mm wafers to perform X-ray tomography experiments at the Brookhaven National Laboratory. Next, we segment the mineralized collagen fibrils and nanoscale pores from the reconstructed images to visualize the 3D orientation of the fibrils in these beams, including orientation near cracks. Further, we tested the feasibility of a synchrotron X-ray *in-situ* nanoindentation experiment. We found *in-situ* radiography to be a robust technique for observing real-time nanoscale deformations and adaptation of fibrils under applied loads and near cracks.

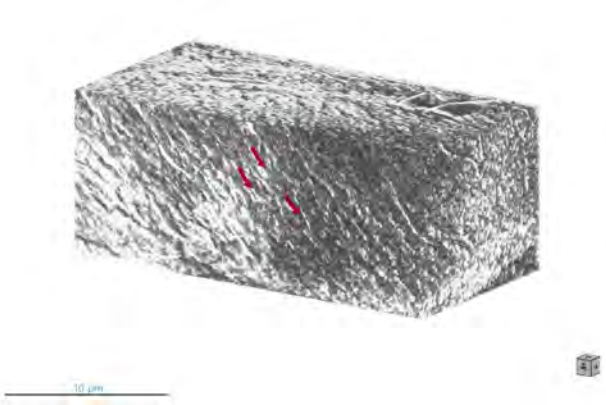

Fig 1. 3D reconstructed bone beam imaged using synchrotron x-ray tomography.

Next steps include measuring the strain and displacement fields of the deformed mineralized collagen fibrils. We intend to use Digital Image Correlation (DIC) to quantify the deformation observed using *in-situ* radiography. After testing and validating this technique, we aim to spatially resolve deformations in OA tissue. We will take site-specific samples throughout the cross-section of the joint – from the subchondral bone undergoing sclerosis to the interior trabecular substructure.

**Markerless motion capture estimates of lower extremity biomechanics are comparable to marker-based across 8 movements**

Ke Song[1*], Todd J. Hullfish[1], Rodrigo Scattone Silva[2], Karin Grävare Silbernagel[2], Josh R. Baxter[1]
[1]University of Pennsylvania, Philadelphia, PA; [2]University of Delaware, Newark, DE
*Corresponding author's email: ke.song@pennmedicine.upenn.edu

**Introduction:** Accurate motion capture and analysis are essential for assessing human biomechanics [1-3]. Marker-based motion capture is the standard, but marker misplacement [2], skin artifact [3], cost, experimental setup, and processing time all limit its utility in large-scale and real-world applications. Markerless motion capture potentially overcomes these barriers, but its fidelity in quantifying human biomechanics has not been verified across common human movements. The few validation studies to date have focused on walking [4], running [5], or kinematic-only measures [4, 6]. In this study, we directly compared lower extremity kinematics and kinetics estimated from marker-based and markerless motion capture across 8 movements. We hypothesized that markerless estimates would match marker-based at the ankle and knee during most movements, while differences would be larger at the hip and during faster movements.

**Methods:** We quantified lower extremity kinematic and kinetics in 10 healthy subjects (5M/5F, 22 ± 2 y/o, BMI = 23.8 ± 2.4 kg/m$^2$) in this IRB-approved study. We concurrently recorded data using 12 marker-based cameras, 8 markerless video cameras (both 100Hz), and 3 force platforms (1000Hz) while subjects performed 8 movements: heel raises, walking, step-down, running, double-leg squat, sumo squat, countermovement jump, and run-and-cut. We used a marker-based link-segment model [7] and a markerless deep learning algorithm (*Theia3D*) [4] to simultaneously estimate 5 pairs of right leg kinematic (angle) and kinetic (moment) measures: ankle dorsi-plantarflexion, knee flexion, hip flexion-extension, ad-abduction, and internal-external rotation. We calculated Pearson correlation ($R_{xy}$) and root-mean-square difference (RMSD) between markerless and marker-based estimates of each angle and moment in each movement. We averaged each $R_{xy}$ and RMSD across 10 subjects to determine an overall between-system agreement ($R_{xy}$) and magnitude difference (RMSD). We defined $R_{xy} \geq 0.7$ strong and $\geq 0.9$ very strong [8], RMSD $\leq 5°$ small for joint angles, $\leq 2.5\%$ Height × Weight for moments.

**Results:** Markerless kinematic and kinetic estimates both matched marker-based for most movements (**Figure** shows running). We found strong correlations in ankle, knee, and hip sagittal angles ($R_{xy} \geq 0.877$) and moments ($R_{xy} \geq 0.785$). Hip ad-abduction angle ($R_{xy} \geq 0.739$) and moment ($R_{xy} \geq 0.819$) also strongly correlated, while transverse rotation angle had weaker correlation ($R_{xy} \leq 0.601$). RMSD was small for most angles ($\leq 5.9°$) except hip sagittal or transverse angles (6.7° – 15.9°), and moments ($\leq 2.66\%$ H×W) except running / run and cut (up to 7.15%).

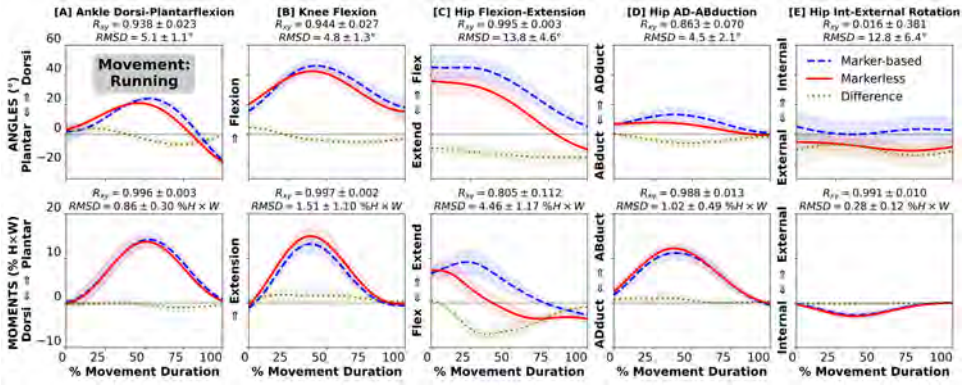


**Figure:** Joint angles (top) and moments (bottom) during *running*: [A] ankle dorsi-plantarflexion, [B] knee flexion, [C] hip flexion-extension, [D] ad-abduction, and [E] internal-external rotation. Waveforms = group mean (line) ± 1SD (shade) for marker-based (dash), markerless (solid), and their difference (dot). *Full results of all 8 movements can be found in our preprint article (link in **Acknowledgements**).*

**Discussion:** The results confirmed our hypothesis that markerless estimates of lower extremity kinematic and kinetics match marker-based during most movements, with strongest agreements in sagittal joint angles. Our finding supports prior evidence on the kinematic fidelity of markerless motion capture [4] and is the first to show that joint moments from markerless also match marker-based during most movements. Thus, we conclude that marker-based and markerless motion capture are comparable when estimating lower extremity biomechanics. Larger between-system disagreements during faster movements can be explained by marker-based skin artifacts. Such errors are expected at the hip given the known artifacts and difficulties to identify bony landmarks [2, 3]. We speculate that the markerless system better characterized hip kinetics such as late-stance flexion (**Figure**, bottom C), but verifying its accuracy requires comparison to gold-standard fluoroscopy. Our results are limited by model differences between systems, which may have caused hip angle offsets (**Figure**, top C/E). Future studies should match model definitions to confirm whether markerless systems reliably estimate hip measures.

**Significance:** Markerless motion capture can facilitate large-scale and real-world analyses not previously feasible with marker-based techniques. The biomechanics community should continue to verify, validate, and establish best practices for markerless motion capture, thereby advancing collaborative research and expanding real-world assessments needed for clinical translation.

**Acknowledgements:** NIH R01AR078898, R01AR072034, R37HD037985. We thank Madison Woods, Audrey Lehneis, and Liliann Zou for data processing. A preprint associated with this study is on *bioRxiv* at biorxiv.org/content/10.1101/2023.02.21.526496v1.

**References:** [1] Camomilla 2017 *Biomed Eng Online*; [2] Della Croce 2005 *Gait Post*; [3] Leardini 2005 *Gait Post*; [4] Kanko 2021 *J Biomech*; [5] Tang 2022 *Bioengineering*; [6] Ito 2022 *JSAMS+*; [7] Slater 2018 *BMC Musculoskelet*; [8] Schober 2018 *Anesth Analg*.

# Mechanical Properties of 3D Printed Clavicles are Closer to Cadaveric Bones than 4th Generation Sawbones

Kathryn S. Strand[1], Elizabeth Silvestro[1], Iman Naqvi[1], Michael W. Hast[1]
[1]McKay Orthopaedic Research Lab, Department of Orthopaedic Surgery, University of Pennsylvania, Philadelphia, PA
strandk@seas.upenn.edu

**Disclosures:** None

INTRODUCTION: Synthetic bone models have increasing utility in experimental research and education [1]. Their benefits include lower costs, less variability than cadaveric bone, no institutional oversight, and no ethical considerations. Commercially available synthetic bones (4th Generation Sawbones) are created with injection molding techniques and have been validated to be equivalent to human bones in a variety of ways [2], [3]. The rise in additive manufacturing (AM) presents an opportunity for synthetic bone models to be custom-made for mechanical testing purposes. Little is known about the efficacy of these custom 3D printed models. Prior studies have examined the mechanical properties of AM bones, but they only tested small segments of bone and did not evaluate 3D prints under varied loading conditions [4], [5]. The clavicle is an attractive testbed for such testing for several reasons. First, clavicular fractures are difficult to repair surgically, and implant design testing could benefit from an improved model. Second, the clavicle is the only horizontal long bone and undergoes a wide variety of loading paradigms during activities of daily living [6]. Applying different and physiologically relevant loading paradigms allows for a thorough analysis. Thus, the purpose of this study was to directly compare the mechanical properties of 3D printed, commercially available, and human cadaveric clavicles under variable loading scenarios. We hypothesized that 3D printed clavicles would better mimic the human condition in axial compression and bending, but not in torsion due to the layered structure of the AM specimens.

METHODS: Four different experimental groups (n=6) were analyzed for this study; fresh-frozen human cadaveric clavicles (3 left, 3 right, from 3 donors, 2 M, 1F, aged between 65-68 years), two groups of 3D printed clavicles printed in Verowhite (VW) and a composite of TissueMatrix and BoneMatrix (TB), and commercially available 4th generation Sawbones (SB) composite clavicles (Model 3408-1; Pacific Research Laboratories, Vashon, WA). Custom models were fabricated with a Stratasys (Eden Prairie, MN) J850 Digital Anatomy Printer. All samples were oriented to print layers along the long axis of the bone. Mechanical tests included nondestructive 4-point bending, torsion, and axial compression in a randomized order, followed by a final compressive test to failure. Testing protocols were based on previous studies and utilized triangular waveforms [7]. All specimens were potted in poly(methyl methacrylate) (PMMA) and loaded on a universal test frame (Electroforce 3550, TA Instruments, Eden Prairie, MN) with a 15 kN load cell. For 4-point bending, the upper anvils were displaced a total of 1 mm at 0.25 Hz for 10 cycles [7]. Bending was applied in both the anterior-posterior (AP) and superior-inferior (SI) directions and bending rigidity was calculated. For compressive and torsional testing, specimens were oriented vertically with the lateral end positioned upwards. Compressive testing loaded specimens between 10 and 315 N for 10 cycles [7]. Torsional testing rotated specimens to ±3º at 0.25 Hz for 500 cycles, and torsional rigidity was averaged across cycles 10, 100, 200, 300, 400, and 500 for anterior and posterior rotation of the sternal end [8]. For compressive testing to failure, specimens were compressed at a rate of 0.63 mm/sec [9]. Significant differences between groups were tested with a one-way ANOVA with Holm-Sidak post-hoc tests ($p<0.05$). When tests for normality and equal variances failed ($p<0.05$), Kruskal-Wallis tests with a Dunn's post-hoc was used.

RESULTS: The axial stiffness of the SB group was significantly higher than the Cadaveric, VW, and TB groups, but there were no differences between the cadaveric specimens and either 3D printed group (**Fig. 1**). Results from torsional testing indicated similar results, where the SB group was significantly stiffer than Cadaveric and TB groups, respectively (**Fig. 2**). Bending tests also showed that the SB group had higher bending rigidity than all groups in the SI direction (**Fig. 3A**), but these findings were not as clear in AP bending. Notably, cadaveric samples had higher bending rigidity than the TB group during both bend tests, and higher bending rigidity than the VW group in the SI bend tests (**Fig. 3A&B**). The failure loads for Cadaveric, SB, VW, and TB groups were 3350±1999 N, 4670±969 N, 2611±321 N, and 1883±282 N, respectively, with significant differences between SB and TB groups (**Fig 4**).

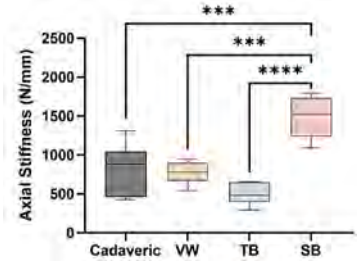


***Figure 1.*** *Average axial stiffness across 10 cycles. ***p<0.001, ****p<0.0001.*

DISCUSSION: We observed no differences between the Cadaveric and VW groups in any testing condition except for SI 4-point bending. Additionally, the SB group was significantly different from the cadaveric specimens in every outcome measure except for AP 4-point bending. These results demonstrate that commercially available synthetic models may be too rigid to accurately emulate the mechanical behavior of cadaveric clavicles. These findings partially disprove our original hypothesis that the layered materials in AM specimens would fail easily in torsional testing. As expected, the cadaveric group had the most variability across all outcome measures. However, the variances within the 3D oriented groups (TB and VW) were much lower, demonstrating consistency within this printing method which may lead to less noisy mechanical testing outcomes. Taken together, these results demonstrate that AM bone models can effectively mimic the mechanical behavior of human bones under a variety of physiological conditions. In particular, our findings suggest that the VW materials and printing protocol may be an attractive option for 3D printed complete synthetic bone models in both torsion and axial/transverse loading conditions.

SIGNIFICANCE/CLINICAL RELEVANCE: The results of this study suggest that AM specimens created with VW material are the most comparable to human cadaveric tissues under varied mechanical loading conditions. These findings present AM bone models as an accessible and physiologically relevant option, opening doors to utilize AM in developing patient-specific bone models for more wholistic and clinically relevant mechanical testing applications.

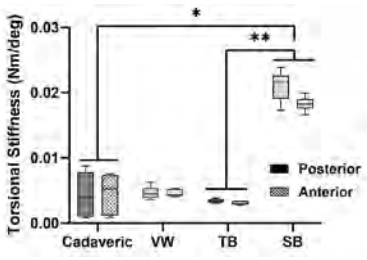


***Figure 2.*** *Average torsional stiffness across representative cycles. *p<0.05, **p<0.01.*

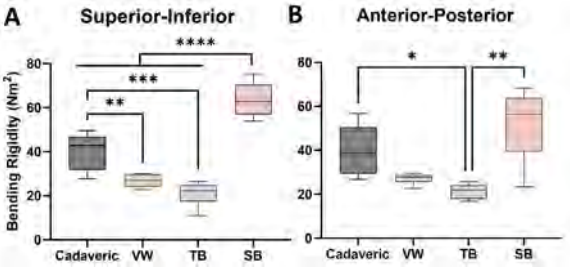


***Figure 3.*** *Average bending rigidity across 10 cycles in the A) SI and B) AP directions. *p<0.05, **p<0.01, ***p<0.001, ****p<0.0001.*

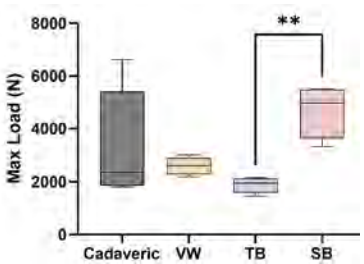


***Figure 4.*** *Maximum loads during compressive failure tests. **p<0.01.*

REFERENCES: [1] Elfar et al. (2014) J Am Acad Orthop Surg. [2] Chong et al. (2007) J Biomech Eng. [3] Chong et al. (2007) Ann Biomed Eng. [4] Husemoglu et al. (2020) J Med Innov Tech. [5] Nägl et al. (2022) 3D Print Med. [6] Iannolo et al. (2010) J Shoulder Elbow Surg. [7] Schmidt et al. (2021) Clin Biomech. [8] Uzer et al. (2017) J Shoulder Elbow Surg. [9] Sánchez-Molina et al. (2020) Biomed. Eng. Appl. Basis Commun.

# The Role of Bone Water in Proximal Femur Stiffness

Reshma Sudhesh[1], Michael W. Hast[2], Chamith S. Rajapakse[2,3], Nancy Pleshko[1], William Querido[1*]

[1] Department of Bioengineering, Temple University, Philadelphia, PA
[2] Department of Orthopaedic Surgery, University of Pennsylvania, Philadelphia, PA
[3] Department of Radiology, University of Pennsylvania, Philadelphia, PA
* William.Querido@temple.edu

The hallmark of osteoporosis is impaired bone mechanical strength, with hip fractures being one of its most debilitating threats. While bone mineral density (BMD) is the primary bone property used for the diagnosis of osteoporosis and the prediction of hip fracture risk, it is well recognized that assessment of BMD alone is a poor predictor of bone mechanics. Bone mechanical function is determined by a combination of factors, including the extent of tissue-level hydration, which we have explored in this study. Water molecules in bone are present in different locations—generally defined as loosely or tightly bound to collagen or mineral. The term “loosely bound” refers to water present at the surface and interface of collagen fibrils and mineral crystals (physical adsorption), which can be removed through lyophilization. “Tightly bound” water is trapped within the collagen triple helix or the mineral crystal lattice (chemical adsorption), requiring high-temperature conditions for removal. Here, we present a multivariate analysis of the role of total and tightly bound bone water in proximal femur stiffness of human cadaver bones (Figure 1). Whole femurs from twelve donors were obtained from the National Disease Research Interchange. Stiffness at the proximal femur was assessed by testing under loading conditions simulating a sideways fall onto the hip at the Penn Center for Musculoskeletal Disorders Biomechanics Core. The water content of cortical and trabecular tissues was quantified in hydrated and lyophilized femoral neck cross-sections by near-infrared (NIR) spectroscopy, using a LabSpec 4 spectrometer with a fiber optic probe. Spectral analysis was carried out to quantify peak intensity ratios that reflect total water content (hydrated samples; 5300/5800 $cm^{-1}$) and tightly bound water content (lyophilized samples; 5300/5800 $cm^{-1}$). Correlation analysis revealed a statistically significant negative relationship between bone stiffness and both total ($r = -0.63$) and tightly bound ($r = -0.55$) cortical and trabecular water content. Employing partial least squares (PLS) regression, we obtained strong models ($R^2 > 0.85$) to predict stiffness based on different combinations of bone water parameters (Figure 2). Our findings highlight the role of bone water in proximal femur stiffness, indicating that lower tissue water content correlates with greater bone stiffness. This study sheds light on the potential of bone water as a critical biomarker for proximal femur mechanical function and, by extension, overall bone health.

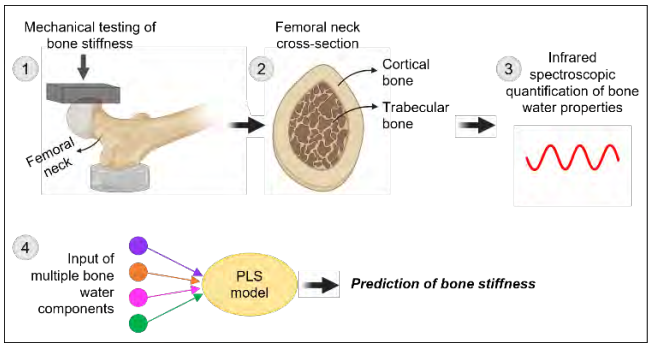


Figure 1: Study design and methods

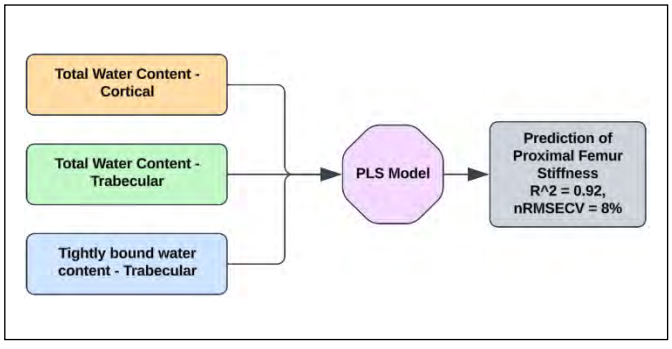


Figure 2: Strongest PLS model. nRMSECV: normalized root mean squared error of cross-validation

# Collagen III Haploinsufficiency Alters Fibril Size but Not Mechanical Properties in Uninjured, Young Adult Male Murine Tendons

Margaret K. Tamburro[1], Jaclyn A. Carlson,[1,2] Stephanie N. Weiss,[1] Susan W. Volk,[2] Louis J. Soslowsky[1]
[1]McKay Orthopaedic Research Laboratory, University of Pennsylvania, Philadelphia, PA, [2]School of Veterinary Medicine, University of Pennsylvania, Philadelphia, PA
Margaret.Tamburro@pennmedicine.upenn.edu
**Disclosures**: Margaret K. Tamburro (N), Jaclyn A. Carlson (N), Stephanie N. Weiss (N), Susan W. Volk (N), Louis J. Soslowsky (N)

INTRODUCTION: Clinically, *Col3a1* mutations present as vascular Ehlers-Danlos syndrome (vEDS), a rare but life-threatening condition due to abnormalities in the matrix of the vasculature and hollow viscera. Additional patient morbidity from tendon pathology[1,2] indicates a consequential role for type III collagen (Col3) in tendon. While a role for Col3 in matrix homeostasis has been established in the vasculature,[3] cutaneous skin,[4] articular cartilage,[5] meniscus,[6] and bone,[7] the involvement of Col3 in tendon structure and function is poorly understood. Early investigations focused on understanding the role of Col3 in female murine tendon,[8] but biological sex is known to influence tendon health, Col3 levels,[9] and vEDS presentation,[10] motivating investigation of the role of Col3 in male tendon. Therefore, the objective of this study was to elucidate the role of Col3 in tendon homeostasis using a murine model of male vEDS. We hypothesized that Col3 haploinsufficiency would alter fibrillogenesis and fibril maintenance yielding decreased large diameter fibrils and mechanically inferior tendons.

METHODS: Tendons from male wild-type (WT) Balb/cJ and heterozygous *Col3a1*$^{+/-}$ mice at 90 days of age were assessed (IACUC approved). Patella-patellar tendon-tibia complexes were dissected and prepared as described[11] for mechanical testing ($n \geq 9$/group). Tendons were assessed with a viscoelastic testing protocol consisting of: 1) preconditioning, 2) stress relaxation at 3% and 6% strain with a subsequent sinusoidal frequency sweep (10 cycles at 0.1, 1, 5, and 10 Hz) at each strain level, 3) return to gauge length, and 4) ramp to failure at a strain rate of 0.1% strain/s. Images were captured during the ramp to failure for elastic modulus measurement. Patellar tendons were fixed, processed, and imaged using transmission electron microscopy as described[12] to measure collagen fibril diameters (n=3/group). T-tests were used to determine the impact of genotype on mechanical properties. A Kolmogorov-Smirnov test was used to assess the effect on collagen fibril diameter distributions. Significance was set at $p \leq 0.05$.

RESULTS: Compared to WT tendons, *Col3a1*$^{+/-}$ tendons were not significantly different in any quasistatic or viscoelastic mechanical property including stiffness (Fig 1A), elastic modulus (Fig 1B), dynamic modulus (Fig 1C), phase shift (Fig 1D), and percent relaxation (data not shown). In contrast, collagen fibril size distributions were significantly different between genotypes (Fig 2, $p < 0.0001$). WT tendons had a characteristic bimodal fibril diameter distribution (Q1: 70.0 nm, Q2: 116.5 nm, Q3: 154.2 nm). *Col3a1*$^{+/-}$ tendons had a tighter fibril diameter distribution (Q1: 80.6 nm, Q2: 125.0 nm, Q3: 154.0 nm) with a smaller proportion of small diameter fibrils (< 70 nm) and a greater proportion of intermediate and large diameter fibrils (> 110 nm).

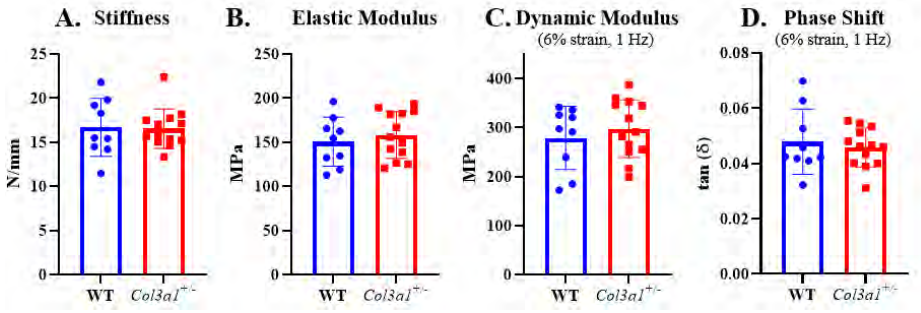


**Figure 1. Collagen III haploinsufficiency does not impact male tendon mechanical properties.** No differences in stiffness (A), elastic modulus (B), dynamic modulus (C), phase shift (D), or percent relaxation (data not shown) were observed between genotypes. No differences were seen in other strain or frequency levels (data not shown).

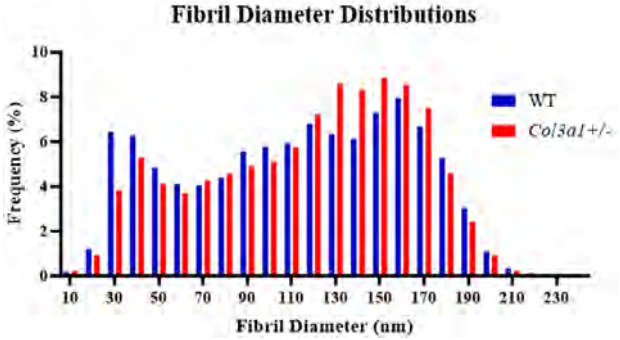


**Figure 2. Collagen III haploinsufficiency alters collagen fibril size.** Collagen fibril diameter distribution was characteristically bimodal in WT tendons. *Col3a1*$^{+/-}$ tendons had significantly different fibril distribution ($p < 0.0001$) with a lower proportion of smaller fibrils (< 70 nm) and a higher proportion of intermediate and large fibrils (> 110 nm).

DISCUSSION: We studied the role of Col3 in tendon homeostasis using a murine model of male vEDS. In contradiction to our hypothesis, Col3 haploinsufficiency in young adult male mice did not alter uninjured patellar tendon quasistatic or viscoelastic mechanical properties. However, in support of our hypothesis, Col3 haploinsufficiency did significantly alter the fibril diameter distribution. This alteration in matrix structure may have mechanical consequences in settings where fibrillogenesis and maintenance are altered, such as in injury and/or aging. Importantly, genotype-dependent changes to fibril diameter in male mice differ from those observed in female mice. In developing female mice, Col3 haploinsufficiency resulted in a decrease in large diameter fibrils, [8] in contrast to the increase in large diameter fibrils observed in the present study. Interestingly, this indicates a differential influence of biological sex on tendon matrix structure in the context of Col3 haploinsufficiency. Conclusions from this study should be interpreted in the context of a conventional haploinsufficiency mouse model which conflates developmental and regulatory effects. Moreover, dose-dependent effects of Col3 insufficiency cannot be investigated due to perinatal lethality of *Col3a1*$^{-/-}$ mice. Further, in recognition of the critical importance of Col3 in the provisional healing matrix, subsequent investigations will define the effects of Col3 knockdown in injury and advanced aging contexts. Future studies will leverage the power of inducible Col3 knockdown to further delineate the sex-, dose-, and age-dependence of the tendon response to Col3 knockdown in homeostatic and injury environments.

SIGNIFICANCE: In addition to direct implications for patients with *Col3a1* mutations, insights from this study reveal contributions of Col3 to tendon structure which serve as an important foundation for future investigations of sex-based differences in the regulatory role of Col3.

REFERENCES: [1] Byers et al. Am J Med Genet. 2017. Review. [2] Shirley et al. Sports Health. 2012. [3] Mizuno et al. J Biochem. 2013. [4] Volk et al. Cells Tissues Organs. 2011. [5] Wu et al. J Biol Chem. 2010. [6] Wang et al. Matrix Biol. 2020. [7] Miedel et al. J Orthop Res. 2015. [8] Carlson et al. ORS Poster. 2022. [9] Stevenson et al. Clin Interv Aging. 2007. [10] Cooper at al. Vet Pathol. 2010. [11] Miller et al. J Biomech Eng. 2012. [12] Dunkman et al. Matrix Biol. 2013.
ACKNOWLEDGEMENTS: This study was supported by the Penn Center for Musculoskeletal Disorders (P30AR069619), R01AR080029 and R01GM124091.

# Frequency and Timing of Mechanical Loading Influences Degradation Kinetics of 3D Printed PLGA

Joseph B. Ulsh, Chet S. Friday, Stephen Ching, Michael W. Hast

McKay Orthopaedic Research Laboratory, University of Pennsylvania, Philadelphia Pennsylvania

**INTRODUCTION:** Bone fractures are painful injuries that often require surgical intervention to repair. In cases of large, critical-sized bone defects, biocompatible scaffolds are used to provide mechanical support and to encourage bone growth during healing. Poly lactic co-glycolic acid (PLGA) is an attractive biomaterial for this purpose, as it is already used in drug delivery [1], it has excellent mechanical properties [2], and its degradation profile is applicable to fracture healing [3]. PLGA can now be 3D printed, giving bioengineers the ability to fabricate scaffolds with complex geometry. While degradation kinetics of PLGA are well understood in the context of drug delivery, the timelines of degradation for 3D printed PLGA trauma implants are not well established. The aim of this study was to understand how changes in compression loading frequency and timing influence the degradation of PLGA devices. We hypothesized that applying compressive loads in higher numbers (1000, 10000, and 100000 cycles), at higher frequencies (1 Hz vs 2 Hz), and in bouts (continuous loading vs. 3 bouts/day for 5 days) would lead to accelerated loss of mechanical properties.

**METHODS:** 112 10 mm cubes were tested in this study. To fabricate the cubes, 85:15 PLGA filament (Lattice Medical, France) was used in a Prusa i3 Mk3 printer (Prusa Research, Czech Republic) with a nozzle temperature of 215 °C, layer height of 0.2 mm, and an extruder velocity of 80 mm/s. Test coupons were designed with no solid perimeters or shells (**Fig 1**). Three different infill densities were produced, 15%, 80%, and 100%. The 15% and 80% infill groups used the gyroid pattern while the 100% infill group was completely solid and created with a rectilinear pattern. All samples were soaked in 70% ethanol solution for 30 minutes to mimic sterilization before implantation. Day 0 testing consisted of compression tests performed at 1.3 mm/min [4] (Instron 8874, Instron, USA). To determine the effects of bathing in solution without loading, samples were submerged in phosphate buffer solution (PBS), in an incubator at 37 °C and 5% atmospheric $CO_2$ for 5 days. To test the effects of loading frequency, groups of samples were subjected to cyclic loading in a heated bath under 6% strain at 1 Hz and 2 Hz for 1000, 10,000, and 100,000 cycles. The effects of bout loading were tested by subjecting samples to 10,000 cycles over the course of 5 days (2,000 cycles per day, 667 cycles per bout, 3 hours of rest between bouts). When samples were not being loaded, they remained at rest in a tank of 37 °C PBS. At the conclusion of all cyclic loading, samples were subjected to the ramp to failure tests. One-way ANOVA tests were used to analyze results from the Day 0 and Day 5 incubation groups. The restricted maximum likelihood mixed-effect model was used along with two-way ANOVA in the analysis of all other treatment groups. Tukey correction tests were also used on all comparison statistics, with significant differences set at $P<0.05$.

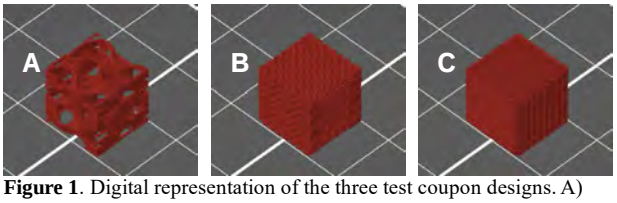


**Figure 1**. Digital representation of the three test coupon designs. A) 15% gyroid infill. B) 80% gyroid infill. C) 100% rectilinear infill.

**RESULTS:** Increases in infill density led to significant changes in stiffness, yield force, and maximum force (**Fig. 2A-C**) and resting in a bath for 5 days led to no significant changes (not shown). Applying 1000, 10000, and 100000 cycles led to increases in stiffness, yield force, and maximum force for the 80% group, but not others (**Fig. 2A-C**). We observed sensitivity to strain rate, as the 80% and 100% infill groups had decreased mechanical properties when subjected to loads at 2 Hz (**Fig. 2 D-F**). Lastly, delivering 10,000 cycles in bouts rather than continuously led to significant losses of yield force and maximum force in the 80% group, but not 100% (**Fig. 2G-I**).

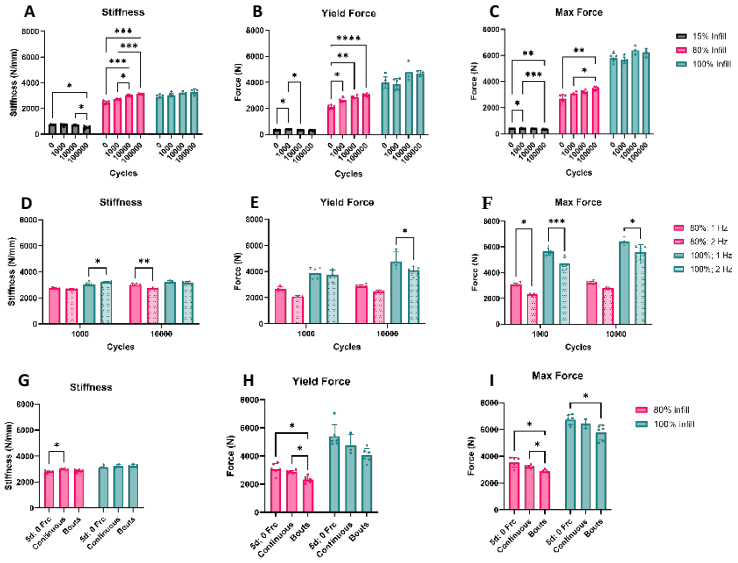


**Figure 2**. Summary of Compressive Mechanical Testing. A-C) Impact of number of cycles. E-F) Impact of frequency. G-I) Impact of bout loading over time. * = $P \leq 0.05$, **** = $P \leq 0.0001$

**DISCUSSION:** This study explored the losses in mechanical properties of 3D printed PLGA caused by compressive cyclic loading. Tested PLGA coupons displayed evidence of cyclic hardening, which rejected the first portion of our hypothesis. This resulted in increased stiffness, yield force, and maximum force as more cycles were applied (**Fig. 2A-C**). This did not occur in the 100% infill group, so we suspect that the collapse of the internal architecture of samples may be responsible for these effects [5]. Results from the frequency testing were in line with our hypothesis, as higher frequency testing resulted in significant losses in yield force and maximum force (**Fig. 2 E-F**). Finally, the last portion of our hypothesis was also confirmed, as bout loading led to significant decreases in yield force and maximum force in comparison to continuous loading. This study had several limitations, including only testing samples in compression and a limited sample size.

**SIGNIFICANCE:** Results from the study suggest that interval-based loading of implants, as experienced in vivo, represents the most severe scenario for degradation of 3D printed PLGA devices. This information will be used to develop future experiments that characterize PLGA degradation and to guide the design and development of trauma implants fabricated with 3D printed PLGA.

**REFERENCES**: [1] S. Jin et al. Acta Biomater. 2021 [2] L. Leung et al. Biomed. Mater 2008 [3] M.L. Houchin et al. J. Pharm. Sci. 2008 [4] ASTM D695-23 [5] Y. Rotbaum et al. Mater. Sci. Eng. 2019

# Molded Ankle Foot Orthoses of variable stiffness offload Achilles Tendon during ambulation.

Stanton Godshall, Todd Hullfish, Lorraine A.T. Boakye, Josh Baxter
University of Pennsylvania, Philadelphia, PA
stanton.godshall@pennmedicine.upenn.edu

INTRODUCTION: Mid-substance Achilles tendinopathy is a painful and debilitating condition that affects 2.35 per 1,000 adult individuals [1]. Mechanical overload is thought to be a primary driver of pathology. The clinical standard of care for severe tendinopathy is to wear an immobilization boot to offload the Achilles tendon to relieve symptoms and promote tissue healing. However, patients do not tolerate these immobilizing boots for longer periods and are often reevaluated after one month to undergo surgical debridement. Our clinic uses a molded ankle foot orthosis (MAFO), which is a custom-fit and non-articulating brace. Anecdotally, we find that patients with MAFOs are willing to wear the MAFO for greater periods of time and experience better outcomes with lower rates of surgical intervention. However, the basic mechanical mechanisms that facilitate these improved outcomes are unknown. For this reason, we developed techniques to quantify the biomechanical loading environment during ambulation as we prepare to longitudinally study a cohort of patients at Penn Medicine. We hypothesized that 1) MAFOs reduce Achilles tendon loading compared to shod ambulation and 2) stiffer MAFOs offload the Achilles tendon more than compliant MAFOs during ambulation.

METHODS: We tested three custom fit MAFOs of a '*stiff*', '*intermediate*', and '*compliant*' on a single healthy control subject (Male, Age: 21 y/o, BMI: 26) in this IRB approved study. These MAFOs are representative of the prescribed range of MAFO designs. We instrumented the three MAFOs with a strain gauge on the back of the MAFO near the Achilles **(Figure 1)** to quantify loads carried by the brace. We determined the relative stiffness of each of these MAFOs by fixing them to a table and pulling on the shin strap with a tensile loadcell until the MAFO buckled. The test subject walked at slow, medium, and fast speeds in a motion capture laboratory in the three MAFOs and regular shoes. We synchronously captured 1) total ankle loading using inverse dynamics using the external motions of the lower extremity captured using a 12-camera motion capture system and force plates, 2) Achilles tendon loading using our validated instrumented insole (Loadsol, Novel) paradigm that was placed under the foot to measure the loads produced by the calf muscle and experienced by the Achilles Tendon [2], and 3) MAFO loading using the calibrated strain gauge secured to the back of each MAFO. The data from these insoles were streamed to a wireless device (Ipod Touch, Apple) running a manufacturer provided app (Loadsol App, Novel). We analyzed 5 gait cycles for each of the 12 conditions (4 MAFO/shoe x 3 speed). We compared the peak Achilles tendon loads – normalized by the participant's bodyweight – across each test condition. We performed this initial proof of concept study to determine best laboratory practices to quantify Achilles tendon loading in patients wearing their custom fit MAFO in our follow-up clinical study.

RESULTS SECTION: Achilles Tendon load was 27% greater in the shod condition than all the MAFO conditions. We found that the '*stiff*' MAFO was 2.3 times stiffer than the '*intermediate'* MAFO and the '*compliant*' MAFO was 2.1 times more compliant than the *'intermediate'* MAFO. Despite these large differences in compliances, we did not detect large differences in Achilles tendon loading across these three MAFOs. The greatest difference in Achilles Tendon load was 6% between MAFOs.

DISCUSSION: Our study confirmed our primary hypothesis that a custom-fit MAFO brace offloads the Achilles Tendon during ambulation compared to shod walking. However, we also expected that stiffer MAFOs would further decrease the loading. This was not the case, as all three MAFOs resulted in nearly identical walking forces. This proof-of-concept study focused on technology development and an experimental protocol to rigorously characterize biomechanical loading in a single, healthy experimenter. Our ongoing work is applying this wearable sensor paradigm in a cohort of patients with mid-substance tendinopathy to identify the link between MAFO-mediated Achilles tendon loading with patient outcomes. We expect that our novel instrumented MAFO paradigm will provide new opportunities to determine the mechanical mechanism that explain symptom relief in patients receiving conservative treatment for mid-substance Achilles tendinopathy.

SIGNIFICANCE/CLINICAL RELEVANCE: This experiment is a necessary step towards developing precision rehabilitative care for patients with tendinopathy. We expect that by linking patient biomechanics with tendon healing and symptoms, we will establish evidence-based tendon loading profiles that improve patient outcomes and decrease the need for surgical treatment. Minimizing surgical treatment is critical to improve outcomes for many patients who are bad candidates for surgery because of comorbidities like smoking and diabetes.

REFERENCES: [1] de Jonge, S., et al., Br J Sports Med, 2011, [2] Hullfish, TJ et al. J. Biomech., 2020.

ACKNOWLEDGEMENTS: This research was supported by NIH/NIAMS P50AR080581 and the University of Pennsylvania Thomas B. McCabe and Jeannette E. Laws Fund.

IMAGES AND TABLES:

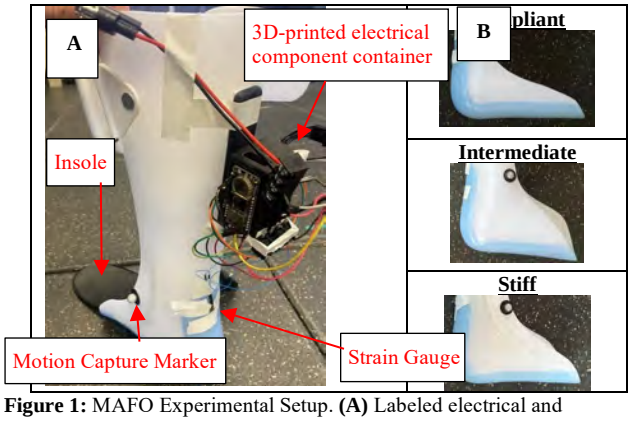


**Figure 1:** MAFO Experimental Setup. **(A)** Labeled electrical and mechanical instrumentation of MAFO. **(B)** Representative images of ankle region of MAFO, demonstrating varying levels of supporting material

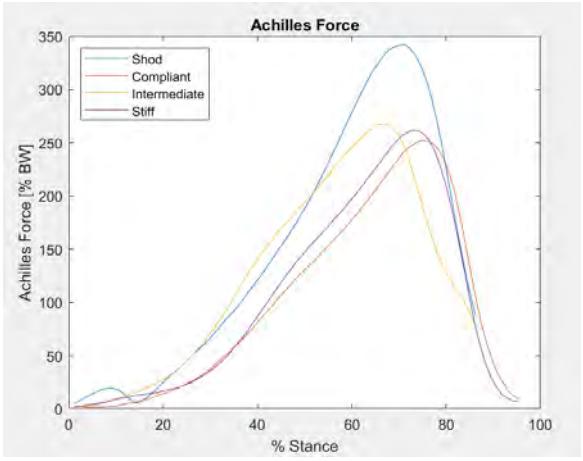


**Figure 2:** Achilles Tendon force during stance for shod, compliant MAFO, intermediate MAFO, and stiff MAFO

Penn Center *for*
Musculoskeletal Disorders

University *of* Pennsylvania

# Histology Abstracts

# *In Situ* and *In Vivo* Mechanoactivation of Anti-Inflammatory Tension-Activated Repair Patches

Mohammed S. Abdullah*[1,2], Bijan Dehghani*[1,2], Julie B. Engiles[1], Caitlin Barrett[1,2], Kevin G. Burt[1,2], Robert L. Mauck[1,2], Thomas P. Schaer[1], Harvey E. Smith[1,2], Sarah E. Gullbrand[1,2]

[1]University of Pennsylvania, Philadelphia, PA; [2]Corporal Michael J. Crescenz VA Medical Center, Philadelphia, PA *These authors contributed equally

**Disclosures:** MA mohammed.abdullah@pennmedicine.upenn.edu – (N), BD (N), CB (N), KGB (N), RLM (4,5,8), HES (N), SEG (6)

**INTRODUCTION**: 2-3% of the world is affected by disc herniations, which are associated with tears the annulus fibrosus (AF) due to injury or advanced intervertebral disc degeneration. The management of disc herniations through microdiscectomy surgery can alleviate symptoms but leaves the annulus unrepaired. Due to the poor capacity of the AF to heal following injury, 10-30% of patients experience recurrent disc herniation [1]. The lack of repair and the acute inflammation that arise after injury further compromises the disc and can result in disc-wide degeneration in the long term. To address this clinical need, we developed tension-activated repair patches (TARPs) for annular repair. TARPs transmit physiologic strains to mechanically-activated microcapsules (MAMCs) embedded within, which activate and release encapsulated biomolecules in response to physiologic loading [2,3]. In this study, we assessed *in vitro* and *in situ* activation thresholds for the MAMCs within the TARPs. Furthermore, we evaluated *in vivo* expression of physiologically relevant proinflammatory cytokines and neurofilament proteins in the anterior and posterior AF after TARP repair to determine if TARP- mediated delivery of an anti-inflammatory drug (IL-1Ra, Anakinra) improved repair.

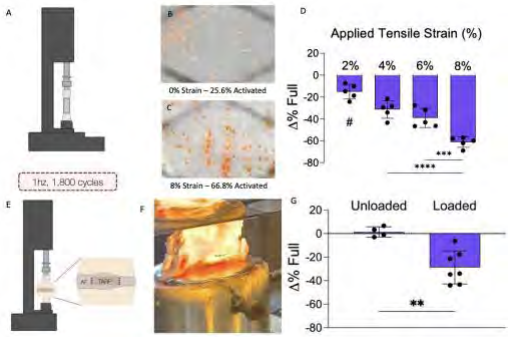


**Figure 1.** A) Schematic of uniaxial tension loading of the TARPs. B-D). Image and quantification of MAMC activation across a range of applied tensile strains. E-F). Schematic and photograph of in situ testing of the TARP and G). Quantification of MAMC activation. * p<0.05, # p<0.05 compared to all other groups.

**METHODS**: *In Vitro* and *In Situ* TARP mechanoactivation: TARPs were fabricated by melt-stamping MAMCs between two hydrated PCL-PEO scaffold strips 10 mm in length and 3.5 mm in width. Mechano-activation strain thresholds for MAMCs were established *in vitro* via 1,800 cycles of tensile loading at varying strain levels (0%, 2%, 4%, 6%, 8%, n=5 samples/strain level, **Fig. 1A**). For *in situ* testing, a 5mm x 2.5 mm cruciate laceration was created in the anterior annulus of goat cervical vertebra-disc-vertebra motion segments, with full thickness needle puncture (2.1mm diameter) to the nucleus. TARPs were sutured to the AF overlying the defect using 6-0 Gortex suture. Seven motion segments were then subjected to 1,800 cycles of cyclic compression from 0 to 300N at 1Hz (**Fig. 1E-F**). 4 additional motion segments were utilized as unloaded controls. Following *in situ and in vitro* mechanical loading, each TARP was gently peeled apart and fluorescent microscopy was utilized to image the outer shell (580nm) and the inner contents (AlexaFluor 488nm) to quantify the number of full versus empty MAMCs. *In Vivo* TARP Annular Repair: To study the physiologic consequences of TARP mechanoactivation and local release of Anakinra (IL-1Ra), BSA-loaded TARPs (E-TARPs) and Anakinra loaded TARPs (A-TARPs) were implanted in a large animal cervical disc annular injury model [2]. Following IACUC approval, eight female goats underwent annular injury of the cervical intervertebral discs, as described above, followed by repair with either the E-TARP (n=4) or A-TARP (n=4) over the injury site at either C2-3. C3-C4 severed as an injury only control. 4 weeks post-repair, animals were euthanized and isolated motion segments were processed for histology, sectioned in the sagittal plane at 10μm, and stained with picrosirius red and imaged with polarized light microscopy. Immunofluorescence was performed on additional sections to assess protein expression levels of inflammatory cytokines (TNF-α and IL-6) along with expression of Neurofilament Heavy Chain (NFH) and Protein Gene Product (PGP 9.5). Mean fluorescent intensity (MFI) and % fluorescent area were quantified in the anterior and posterior AF for each level using Image J. Statistical analysis was performed via one-Way ANOVA with a Tukey's post-hoc test.

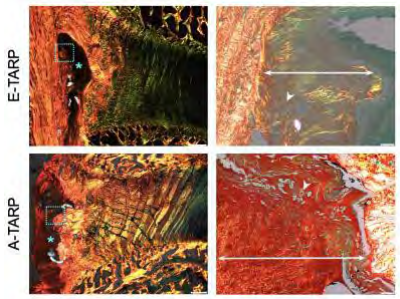


**Figure 2.** Polarized light microscopy of the anterior annulus of TARP repaired discs. The * denotes location of TARP, the right panel is a higher magnification (scale=100μm) of the area denoted in the dashed box on the left panel (scale=1mm).

**RESULTS**: *In vitro and in situ TARP mechanoactivation*: Tensile loading of the TARP *in vitro* resulted in increasing MAMC activation with increasing levels of applied strain (**Fig. 1B-C**). Compressive loading of spinal motion segments resulted in circumferential strain transfer through the disc to the TARP, significantly increasing MAMC rupture compared to TARPS sutured to the AF but not loaded (**Fig. 1G**). *In-Vivo* TARP Repair: Polarized light microscopy revealed increased collagenous matrix accumulation in the anterior annulus of the A-TARP group, in comparison to the E-TARP group, at 4-weeks post-repair (**Figure 2**). Post hoc analysis demonstrated a substantial reduction in the

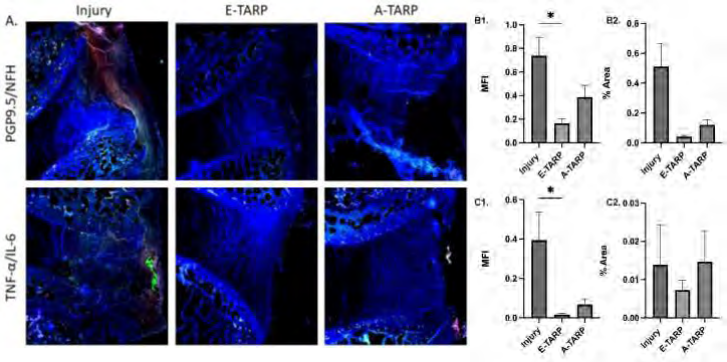


**Figure 3. (A)** Immunofluorescence microscopy of the annulus across Injury, E-TARP and A-TARP groups (red = NFH & TNF-□, green = PGP 9.5 & IL-6). Quantification of MFI and % area in the anterior and posterior annulus for B). PGP9.5& NFH and C). TNF-□and IL-6. * p<0.05.

% Area and MFI of inflammatory and nerve markers between the injury and E-TARP repaired levels, averaging 96% and 76%, respectively (p<0.05). When comparing the A-TARP repair to the injury model, there was an 82% reduction in inflammation (p=0.053) and a 76% decrease in nerve markers (p=0.24), as assessed via MFI (**Figure 3**).

**DISCUSSION:** Our studies demonstrated that MAMC rupture within the TARPS occurs in response to directly applied tensile strain and under tensile strains translated to the TARP *in situ* during compressive loading of the disc. *In vivo*, we observed an increase in collagenous matrix deposition in the anterior annulus of the A-TARP group, suggesting that the Anakinra released from the TARPS may have contributed towards enhanced AF repair. Furthermore, TARP repair demonstrated a significant attenuation of innervation and inflammation in the annulus compared to the unrepaired injury in both TARP groups. Interestingly, we observed a trend towards increased innervation and inflammation in the A-TARP group compared to the E-TARP group. Our prior studies in other joints suggest the most MAMC cargo is released over 2 weeks [4] , so it may be that the time course of inflammation and repair is shifted in the A-TARP group.

**SIGNIFICANCE:** Amid limited clinical alternatives, this work advances a novel annular repair strategy, bringing it closer to clinical implementation for patients grappling with back pain resulting from disc herniation.

**REFERENCES:** [1] Peredo+JOR Spine, 2021 [2] Peredo+BioRxiv, 2022 [3] Mohanraj+Adv. Func. Mat. 2019 [4] Zlotnick+Biofabrication, 2022

**ACKNOWLEDGEMENTS:** This study was supported by the Department of Veterans' Affairs.

# Age-Dependent Inflammatory Responsiveness and Chromatin Dynamics in Mouse Tenocytes

Tyler Blanch[1], Yujia Zhang[1], Xi Jiang[1], Zizhao Li[1], Nathaniel A. Dyment[1], and Su-Jin Heo[1]
[1]University of Pennsylvania, Philadelphia, PA
tblanch@seas.upenn.edu

**Disclosures:** Blanch (N), Zhang (N), Jiang (N), Li (N), Dyment (N), Heo (5-4WEB Medical)

**INTRODUCTION**: Tendon injuries frequently occur due to their critical load-bearing role, often leading to debilitation and limited treatment success, causing discomfort and recurring injuries **[1]**. The inflammatory stage of tendon healing promptly initiates after acute injury, marked by clot formation within the damaged tissue **[2]**. While the conventional injury response involves transient phases of inflammatory signaling in tendons, degenerated tissues associated with aging struggle to resolve these cues, resulting in prolonged matrix degradation and shifts in cell phenotypes **[2,3]**. However, the precise mechanisms underlying how inflammatory conditions impact tendon resident cells (tenocytes) and how aging influences these responses remain enigmatic. Thus, this study aims to uncover disparities in cellular reactions to inflammatory cues (e.g., tumor necrosis factor-α, TNFα) between young and mature tendon cells. Specifically, employing super-resolution microscopy (e.g., STORM), we investigate how inflammatory conditions regulate age-related histone reorganization within tendon cells. This investigation probes the underlying epigenetic mechanisms of aging, shedding light on potential epigenetic-targeted therapies to address tendon injuries.

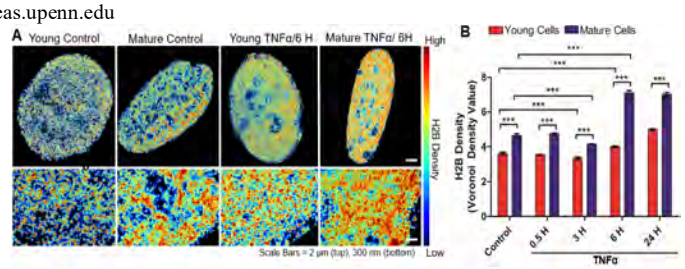


**Figure 1:** (A) Heat map of nuclear H2B localization density in young and mature mouse tenocytes under normal (Control) or inflammatory (TNFα, 6-hour) culture conditions. (B) Quantification of condensed chromatin values via STORM imaging analysis at multiple timepoints with inflammatory media-treated and untreated cells. n = 7 cells/group, ***: $p < 0.001$.

**METHODS:** Mouse tenocytes were isolated from young (<5 weeks, male) and mature (>45 weeks, male) tail tendons following established protocols **[4]**. To identify age-dependent responsiveness to inflammatory signaling, young and mature tenocytes were cultured in basal media (control) or TNFα-containing basal media (20ng/mL TNFα) for durations of 0.5, 3, 6, or 24-hours (H) prior to fixation for STORM and immunofluorescence (IF) imaging. To determine chromatin condensation status through histone H2B localization, fixed cells were immunostained for histone-H2B (Invitrogen) and a custom secondary antibody featuring activator-reporter dye pairs (Alexa Fluor 405-Alexa Fluor 647) for established STORM imaging **[5]**. Super-resolution determination of TNFα receptor density in young and mature cells was performed with tenocytes immunostained for TNFα-Receptor 1 (TNFαR1, Enzo) or -Receptor 2 (TNFαR2, Abcam) before secondary antibody incubation. STORM image reconstruction and analysis were done using the Nanoimager software (ONI), and quantification of Voronoi tessellation results for each super-resolution image was implemented in MATLAB to derive the density values **[5]**. Further, fixed cells from all treatment groups (as outlined above) underwent immunostaining for markers of transcriptional repression (or chromatin condensation, H3K27me3: the tri-methylation of lysine 27 on histone H3) or activation (or chromatin decondensation, H3K9ac: the acetylation of lysine K9 on histone H3 and H3K4me3: the tri-methylation of lysine 4 on histone H3). Mean florescence intensities of these markers within nuclei were quantified using Image-J. Statistical analyses employed a student's t-test or one-way ANOVA with Tukey's post hoc testing.

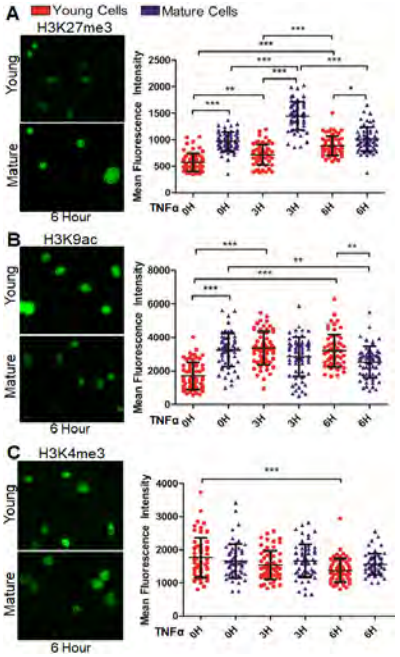


**Figure 2**: (A-C) Representative IF images (left, 6-hour TNFα treatment) and quantification of mean fluorescence intensity (right, control (0H), 3-hours (3H), or 6-hours (6H)) with TNFα-containing media. Groups were stained for H3K27me3 (A), H3K9ac (B), or H3K4me3 (C). n = 60 cells/group, *: $p < 0.05$, **: $p < 0.01$, ***: $p < 0.001$.

**RESULTS:** Super-resolution images depicting H2B localization revealed an elevated presence of nanoscale H2B density (indicating increased chromatin condensation) within mature cells compared to their young counterparts in control and all inflammatory treatment conditions **(Fig. 1A, B)**. The duration of inflammatory treatment progressively increased the global chromatin condensation in both age groups. Notably, mature cells exhibited a substantial increase in heterochromatin after 6-hours (6H) and 24-hours (24H), significantly distinguishing them from young cells **(Fig. 1B)**. Given that chromatin architecture is influenced by alterations in histone modification status, the STORM imaging results led us to question how inflammatory signals affect post-translational modifications on histone complexes in young and mature cells. The gene repression-associated histone modification marker (H3K27me3) revealed an overall increase in chromatin condensation over treatment times, with notably more pronounced changes in mature cells than in young cells **(Fig. 2A)**. Conversely, histone modification markers for gene activation (H3K9ac) exhibited contrasting trends in chromatin condensation in response to the TNFα treatment **(Fig. 2B)**, whereas H3K4me3 exhibited only moderate adjustments in both cell types **(Fig. 2C)**. To unravel contributors to age-related responsiveness to inflammatory treatment, TNFα receptor densities were quantified between the age groups. While no discernible differences in TNFαR1 distributions were noted between young and mature cells (not shown), mature tenocytes exhibited a significant increase in TNFαR2 surface density compared to young cells **(Fig. 3A, B)**.

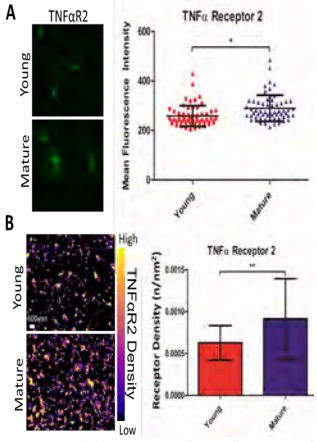


**Figure 3:** (A) Representative IF images and mean fluorescence intensity quantification for young and mature cells stained for TNFαR2, n = 60 cells/group. (B) Heat map images of TNFαR2 density (left, scale: 600 nm)) and quantification (right) for young and mature cells stained for TNFαR2, n=30 cell regions/group. *: $p < 0.05$, **: $p < 0.01$.

**DISCUSSION:** This study uncovers a distinct tenocyte response to inflammatory cues (TNFα) that correlates with age. Aging introduces alterations in the nanoscale chromatin organization and the rates of specific histone modifications within these cells. However, the application of inflammatory treatment across various time points leads to changes in these factors characterized by either opposing rates of change or entirely contrasting trends. TNFα prompts chromatin compaction, which are gene regions typically considered transcriptionally inactive. Both young and mature tenocytes exhibit an elevation of H3K27me3 with progressive TNFα treatment, although this increase is more pronounced in mature cells. Interestingly, while young cells increase in H3K9Ac under inflammation, mature cells experience a modest decrease. The interplay between changes in H3K27me3 and H3K9ac observed in young and mature cells might underlie the variations seen in chromatin condensation with H2B-STORM. These findings also suggest that the inflammatory microenvironment in aged tendons could potentially drive abnormal tenocyte behavior. Notably, TNFαR2 is elevated in mature tenocytes, possibly indicating receptor density disparities as a contributing factor to the heightened inflammatory response observed in aged populations. Ongoing studies are delving into how these nanoscale chromatin organizational changes influence transcription and protein expression in the context of tendon aging and disease.

**SIGNIFICANCE:** The study assesses the response of tenocytes to inflammation across different age groups, shedding light on the mechanisms underlying inflammation-related changes in cell phenotype to guide future treatment approaches for tendon-related disorders, including tendinopathy.

**REFERENCES:** [1] Mafulli+, Am J Sport Med, 2000; [2] Ellis+, J Immunol Regen Med, 2022; [3] Ireland+, Mat Bio, 2001; [4] Lee+, BMC Musculoskelet Dis, 2018; [5] Heo+, Nat BioE, 2023. **ACKNOWLEDGEMENTS:** This work was supported by the NIH (P50 AR080581, K01 AR077087) and NSF (CMMI-1548571).

# Decellularized meniscus (MEND) as a biomaterial that supports stem cell invasion and chondrogenesis

Hannah M. Bonelli[1,2], Kyra W. Y. Smith[1,2], Sophia Klessel[1,2], Dana D. Ragbirsingh[2], Paul M. Gehret[1,2], Riccardo Gottardi[1,2]
[1]University of Pennsylvania, Philadelphia, PA, [2]Children's Hospital of Philadelphia, Philadelphia, PA
bonellih@chop.edu

**DISCLOSURES:** PMG and RG are inventors on a non-provisional patent application for MEND technology.

**INTRODUCTION:** Cartilage damage affects 25 million people each year, arising from trauma, sports injuries, and wear and tear **[1]**. Mesenchymal stem cells (MSCs) are a frequently used cell source for tissue engineered cartilage repair because they have improved proliferation rates and are more readily accessible for clinical translation compared to chondrocytes **[2]**. However, MSCs have limitations in their chondrogenic capacity, and even when cultured in 3D hydrogels, matrix secretion outcomes can be non-uniform throughout the construct with non-robust chondrogenesis **[3]**. Given the pro-regenerative capacity of ECM scaffolds, we have previously shown how incorporating cartilage-derived ECM in hydrogel constructs can promote better chondrogenesis **[4]**. Taking this work several steps further, in the Gottardi lab we have developed a new scaffold based solely on decellularized porcine meniscus (MEND), which has sufficient mechanical properties for cartilage repair in the airway and adequate porosity to allow for native cell infiltration both *in vitro* and *in vivo* **[5]**. Notably, MEND is based on the selective removal of elastin from meniscal cartilage which preserves the bulk of its mechanical properties, creating a wealth of channels for re-cellularization. In this study we aim to (i) show that MEND can undergo recellularization with MSCs, and (ii) investigate whether MEND possesses an intrinsic pro-chondrogenic potential for MSCs. To achieve this goal, we seeded MEND with varying densities of MSCs to compare the chondrogenic response of MSCs in MEND against that of MSCs in 3D hydrogels with controlled composition such as methacrylated type I collagen (ColMA) and methacrylated gelatin-hyaluronic acid (GelMA/HAMA).

**METHODS:** *MEND Fabrication:* Porcine derived menisci were cut into 0.5-1mm radial sections, subjected to 4 freeze/thaw cycles (1h) followed by pepsin/acetic acid incubation (24h, 37C) and elastase digestion (24h, 37C) for selective enzymatic removal of elastin. Then, a 6 mm biopsy punch was used to extract cylinders from the red zone region of each section. MEND cylinders were soaked in cell culture medium containing 20% FBS for 24h at 37C before seeding. *MEND Cell Seeding:* Human bone marrow derived MSCs at P5 were used (n=3 donors). MEND cylinders were placed in a 24 trans-well, and MSCs suspended in 1% FBS medium were added directly on top of MEND at densities of either 300K, 400K, 600K, or 800K. Medium containing 20% FBS was added to the bottom well to establish a serum gradient across MEND. Media were renewed every 2 days. At day 5, a cell viability assay with Calcein AM was conducted to assess MSC distribution on the top and bottom surface. *Hydrogel constructs and pellet controls:* MSCs were suspended at 10 million cells/mL in either ColMA (8 mg/mL, 1M NaOH, lithium phenyl-2,4,6-trimethylbenzoylphosphinate, 10X PBS) or GelMA/HAMA (5% methacrylated gelatin, 2.5% methacrylated hyaluronic acid, 0.15% lithium phenyl-2,4,6-trimethylbenzoylphosphinate). For positive control of chondrogenesis, MSCs were centrifuged to form pellets (200K cells/pellet). *Analysis of Chondrogenesis:* To compare the level of chondrogenesis in each condition, all constructs were cultured for 21 days in chondrogenic differentiation medium (Fluorobrite DMEM, 10µg/mL Insulin-Transferrin-Selenium, 40µg/mL L-proline, 2% PSF, 50µg/mL Ascorbic Acid (AA), 10ng/mL TGF-β3) with medium renewed three times per week. Then constructs were analyzed by histology (Safranin-O and Alcian Blue for GAGs, Picrosirius Red with polarized light microscopy (PLM) for collagen, Van Gieson's for elastin), immunofluorescence (IF, for collagen I and collagen II), RT-qPCR (*ACAN, SOX9, COL1A1, COL2A1*), and biochemistry (total DNA/collagen/GAG content, and ratio of collagen/DNA and GAG/DNA).

**RESULTS SECTION:** *Chondrogenic Potential of MSC seeded hydrogels:* ColMA and GelMA/HAMA constructs exhibited non-uniform and variable matrix secretion over 21-day chondrogenesis, and pellet controls followed similar trends (**Figure 1**). Safranin-O and Alcian Blue stains resulted in dis-homogenous matrix in pellets and ColMA constructs relative to day 0 timepoints (data not shown), with co-localization of GAGs, collagen I, and collagen II in the remainder of the constructs. Sporadic expression in ColMA gels could be influenced by cell-mediated contraction that occurred throughout the chondrogenic culture period. GelMA/HAMA scaffolds appear more uniform across histological analyses, but the presence of hyaluronic acid might be a confounding factor for Safranin O stains. Furthermore, no difference in collagen II staining was detected between days 0 and 21 and methodological improvements are in progress to better assess matrix production within these constructs. *MEND fabrication:* Structure of MEND and formation of channels was assessed by H&E and Van Gieson's staining, and the comparison to native meniscus showed full removal of elastin and decellularization (**Figure 2, left**). MEND constructs resulted in an average porosity and channel diameter of 8% and 8 µm, respectively. This allowed for successful MSC seeding of MEND over 5 days and was confirmed by a cell viability assay and by DAPI staining for cell distribution (**Figure 2, right**).

**DISCUSSION:** Our initial data suggest that MEND is uniformly pervaded by channels, ideal for MSC seeding, which was successfully achieved. When seeded in pellets (positive controls) and in the two hydrogels, MSCs underwent chondrogenesis but with dis-homogeneous matrix secretion, as expected based on previous literature. Analysis of differentiation across all constructs by RT-qPCR and biochemistry is currently in progress. Notably, MEND contains both collagen I and collagen II as well as some hyaluronic acid. A limitation to this study is that ColMA, chosen as a collagen I only scaffold to assess the influence of MEND's main ECM component, undergoes rapid cell-mediated contracture upon seeding (within 3-4 days), creating an additional challenge to distinguish secreted vs. scaffold collagen I, which we plan to overcome using non-canonical amino acids (ncAA) to directly tag newly synthetized collagen.

**SIGNIFICANCE/CLINICAL RELEVANCE:** MEND demonstrates promise in providing a scaffold with composition close to that of cartilage and with an abundance of channels that allows it to be easily repopulated by cells, matching key requirements for clinically relevant articular cartilage engineering. Furthermore, assessing the extent to which MEND supports a robust chondrogenic phenotype of MSCs may open the way to complementing microfracture.

**REFERENCES: [1]** CODE Tech., 2017. **[2]** Le *et al.*, *J. of Tissue Eng.*, 2020. **[3]** Cote, A.J., *et al.*, *Nature Comm.*, 2016. **[4]** Rothrauff, B.B. *et al.*, *J. of Tissue Eng. & Regen. Med.*, 2018. **[5]** Gehret *et al.*, *BioRxiv*, 2022.

**ACKNOWLEDGEMENTS:** Support from the Children's Hospital of Philadelphia Research Institute, Fontaine Fellowship, NIH P30 AR069619, and T32-AR007132. Thanks to Ryan M. Friedman for ColMA protocols and Stephanie Fung for useful advice.

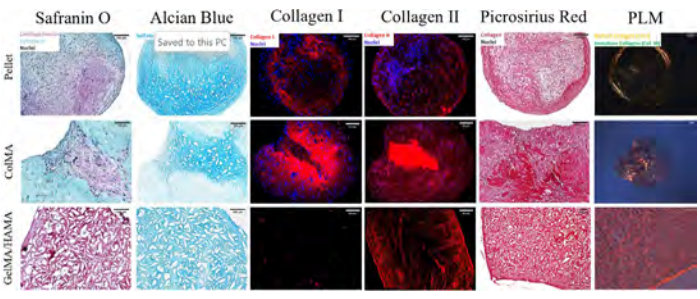


***Figure 1*** *Histological and IF images of constructs and pellets at 21 days of chondrogenesis.*

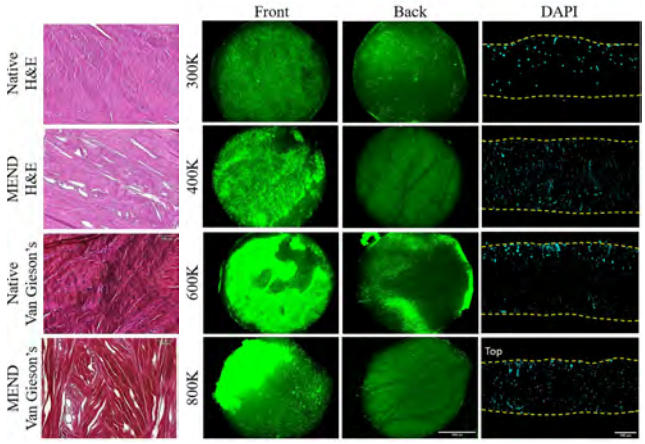


***Figure 2*** *H&E and Van Gieson's images of native meniscus and MEND **(left)** and Calcein AM/DAPI images of various MSC seeding densities into MEND **(right)**.*

# Hierarchical Evaluation of Mechanically Induced Growth Modulation of the Spine in a Growing Pig Model

Madeline Boyes[1], Axel C. Moore[2], Julie Engiles[1], Benjamin Sinder [3], Klaus Hopster[1], Jason Anari[3], Sriram Balasubramanian[4], Edward Vresilovic[2], Dawn M. Elliott[2], Thomas P. Schaer[1], Brian D. Snyder[5], Patrick J. Cahill[3]
[1]University of Pennsylvania School of Veterinary Medicine, Kennett Square, PA, [2]University of Delaware, Newark, DE, [3]Children's Hospital of Philadelphia, Philadelphia, PA, [4]Drexel University, Philadelphia, PA, [5]Boston Children's Hospital, Boston, MA.
mboyes@vet.upenn.edu

**Disclosures:** Thomas Schaer (1-PSI, 1,3B,4,5-ReGelTec, 3B-Peptilogics, 3B,4,5-Acuitive Technologies, 3C-PAX Therapeutics, 3C-OrimTech, 3C,5-SINTX Technologies, 3C-OsteoCentric Technologies, 5-DePuy Synthes, 5-Alcyone Therapeutics, 5-Camber Spine, 6-Heraeus), Brian Snyder (3B-Orthopediatrics)

**INTRODUCTION:** Intervertebral disc (IVD) distortion contributes initially to scoliotic spine deformity in juvenile and adolescent scoliosis, with subsequent vertebral wedging as deformity progresses. [1]. Ian Stokes [2] hypothesized that spinal deformity progresses as a "vicious cycle" due to asymmetric stresses/strains applied to the growing spine over time and space. Predicated on the Heuter-Volkmann principle (i.e., tension applied to an apophysis/physis stimulates growth, while compression inhibits growth), interventions such as Vertebral Body Tethering (VBT) attempt to correct scoliosis, while preserving spinal motion, by predictably modulating spine growth via mechanical manipulation of affected functional spinal units (FSU) via the application of compression across the convexity of the scoliotic curvature. However, there is evidence that cartilaginous endplate thickening secondary to compression may reduce tissue diffusivity and lead to disc degeneration. We created a reciprocal model of scoliosis by applying a posterolateral tether to a straight spine to induce an asymmetrical lateral bending moment to provoke scoliosis in a growing pig. The objective of this work is to investigate the effect of asymmetric spine loading on tissue remodeling and FSU mechanics at a hierarchical level.
**METHODS:** Under IACUC approval, to incite a progressive scoliosis, three rapidly growing 12-wk old Yorkshire pigs were instrumented with a subcutaneous CoCr cable tether spanning thoracolumbar (TL) and lumbar (L) vertebrae to create a lateral bending moment. Changes to the vertebral body (VB) and IVD anatomy over time and space were measured by serial CT, plane radiographs and MRI (T1-FLASH, T2-CPMG). CT and radiographic images were used to monitor deformity progression (Cobb angle) and vertebral body growth, while MRI was used to evaluate IVD tissue composition and geometry. MRI post-acquisition analysis included calculating T2* and ΔT1 relaxation times of the nucleus pulposus (NP) outlined manually on a mid-sagittal slice through each IVD. ΔT1 relaxation times were derived from pre and post gadolinium contrast injection images, where: ΔT1=(T1pre-T1post)/T1pre*100. Pigs were sacrificed at 20-wks after deformity generation; functional spine units (FSU) were isolated at the apex of the induced deformity for μCT and histology. Additional FSUs within the instrumented region were mechanically tested under a combined axial load of 0.54 MPa and lateral bending ± 3° for 5 cycles.
**RESULTS:** Acutely, scoliosis (17°) was mediated by IVD wedging. From 6-12 wks, scoliotic deformity (35-45°) was shared between TL (45-38%) and L (41-47%) regions, with wedging of both the IVD (40-46%) and VB (60-54%) contributing to the overall scoliosis. By 19 wks, deformity (58°) was mainly imparted by VB wedging (**Fig 1A**). MRI and histology (**Fig 1A,B,D**) demonstrate translation of the NP from the concavity to the convexity of the curved spinal segments. MRI ΔT1 relaxation times 10-wks after tethering demonstrated a 5% reduction in T1 relaxation time at all instrumented levels, relative to un-instrumented control segments, which progressively decreased to 45% in ΔT1 @ T13-T14-L1-L2-L3 IVD 19-wks after tethering (**Fig 2**). μCT (**Fig 1C**) and histology (**Fig 1I,J**) suggest that compression inhibits physeal growth manifest by diminished epiphyseal height at the concavity of the scoliosis and sclerotic bone remodeling as evidenced by: ↑6.4% bone volume fraction; ↓17.8% bony endplate (BEP) cortical porosity. Cartilaginous endplate (CEP) thickening may reduce tissue diffusivity, leading to IVD degradation as evidenced by degeneration of the annulus fibrosus (AF), indicated by chondroid metaplasia and fibrillation of the inner AF rings (**Fig 1D-G**); degeneration of the NP, indicated by multifocal loss of notochordal cells (NC) and extracellular matrix with NC necrosis (**Fig 1H**). FSU mechanics (stiffness) remained relatively symmetric, unaffected by the induced anatomic and histologic tissue asymmetry (**Fig 3**).
**DISCUSSION** These multi-level, hierarchical data (MRI, μCT, Histo) indicate that mechanically induced asymmetric spine growth affects multiple tissues: endplate, bone, AF, NP, and vasculature. Compression provoked IVD distortion and degenerative processes, initiated by CEP thickening that may reduce endplate diffusivity, followed by compression mediated physeal growth inhibition, that resulted in vertebral wedging. Vertebral wedging was accompanied by increased cortical thickness, decreased cortical porosity and increased bone volume fraction at the vertebral endplate (VEP). These structural changes serve to decrease small molecule transport across the VEP, corroborated by altered Gd contrast diffusion (**Fig 2**), thereby impairing nutrient flow to the NP. Both macroscopic imaging (CT/MRI) and microscopic histological analysis of the asymmetrically loaded IVDs revealed degenerative changes consistent with IVD degeneration observed in human and goat models of IVD degeneration [3].
**SIGNIFICANCE/CLINICAL RELEVANCE**: Understanding the multi-scale osseous and non-osseous tissue adaptations to asymmetric loading of the spine in growing children and adolescents is essential for the development of guided growth interventions that effectively mediate scoliosis without deleteriously affecting the health of the IVD. These data reveal that asymmetric compressive loading of the spine provoked by a posterolateral tether resulted in vascular remodeling and structural changes to the cartilaginous and bony endplate that reduced small molecule transport into the IVD, which incited IVD degeneration.

**REFERENCES:** [1] Will RE, et al. 2009, Spine. [2] Stokes IA. 2007, Eur Spine J. [3] Gullbrand, SE. et al. 2017. Osteoarthritis Cartilage.
**ACKNOWLEDGEMENTS:** This research was supported by The Wyss/Campbell Center for Thoracic Insufficiency (Children's Hospital of Philadelphia)

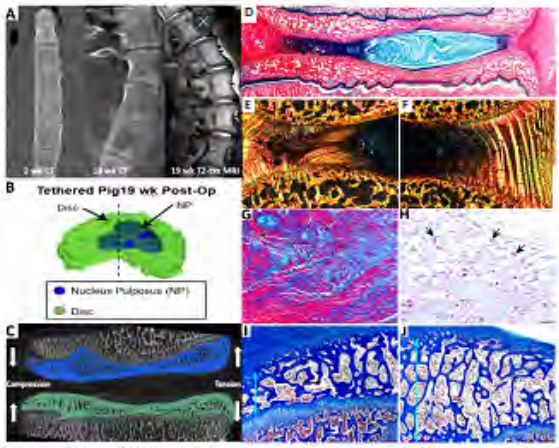


**Figure 1.** (**A**) CT and MRI coronal views demonstrate progressive vertebral body wedging and NP displacement towards convex side (**B**) highlighted by 3D reconstruction. (**C**) μCT and histology (**D-J**) at the apex of deformity T13-T14 reveal narrowing of the IVD and of the endplate epiphysis at ***concave side (compression)*** relative to ***the convex side (tension)***. (**C, I, J**) Endplate epiphysis shows narrowing and bone sclerosis at (**I**) concave side relative to (**J**) convex side. (D, G) Non-polarized and (**E, F**) polarized sections demonstrate asymmetric distortion of AF fiber alignment at concave side including fibrillation of inner AF and (**G arrows**) chondroid metaplasia. (**D**) Histology confirms NP displacement toward convex side observed in MRI (**A,B**). NP shows cell necrosis (**H, arrows**).

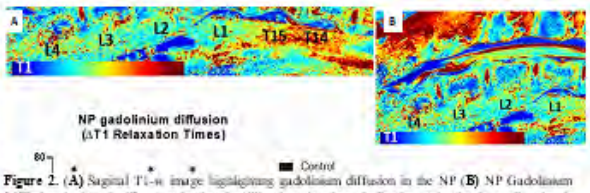


**Figure 2.** (**A**) Sagittal T1-w image highlighting gadolinium diffusion in the NP (**B**) NP Gadolinium Diffusion depicts significant reductions in ΔT1 relaxation times, indicating reduction in small molecule transport into the NP of the tethered levels compared to control discs. (**Black**=Control; **Blue**= 10 weeks Postop, **Yellow**=19 Weeks Postop).

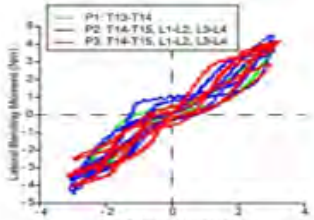


**Figure 3.** Lateral bending moment vs angular for 7 FSU within the tethered levels from 3 animals demonstrates disc-level mechanical symmetry.

# Imaging mass cytometry reveals distinct cellular phenotypes in CD14 deficient mouse synovium.

Kevin G. Burt[1,2], Sanique M. South[3], Vu Nguyen[1,2], Lance A. Murphy[1,2], Robert L Mauck[1,2], Tim Griffin[4,5], Carla Scanzello[1,2,6]
[1]Department of Orthopaedic Surgery, Perelman School of Medicine, University of Pennsylvania, Philadelphia, PA; [2]Translational Musculoskeletal Research Center, Corp. Crescenz VA Medical Center, Philadelphia, PA; [3]University of Oregon, Eugene OR; [4]Veterans Affairs Medical Center, Oklahoma City, OK, [5]Oklahoma Medical Research Foundation, Oklahoma City, OK; [6]Division of Rheumatology, Perelman School of Medicine, University of Pennsylvania, Philadelphia, PA.

**Disclosures:** KGB (N) - kevin.burt@pennmedicine.upenn.edu, VN (N), LAM (N), SMS (N), RLM (4,5,8), TG (8), CRS (8)

**INTRODUCTION:** Growing evidence has revealed that inflammation is a major driver of osteoarthritis (OA). However, previous consideration of OA as a noninflammatory disease placed early focus on mechanical and structural characterization. As a consequence, there is a knowledge gap with respect to the full description of the inflammatory state across tissues within the knee joint (synovium, meniscus, cruciate ligaments, etc.) during OA progression. Of these tissues, the synovium has been identified as a reservoir of not only inflammatory mediators but also innate (monocyte/macrophages) and adaptive (T- and B-cells) immune cells.[1] Both the diverse cell populations and unique structure of the synovium, including the lining and sublining layers, undergo unique inflammatory-mediated degenerative changes. CD14, a co-receptor to inflammatory toll-like receptor (TLR) signaling and subsequent macrophage activation, has also been identified as being upregulated in OA synovium and, in our prior work, we showed that global genetic CD14 deficiency in mice is protective against PTOA related bone-remodeling and mobility dysfunction.[2,3] *Imaging mass cytometry (IMC)* is an emerging technology that allows for the *spatial localization* of molecular species across tissue samples, facilitating investigation of cellular subtypes throughout diverse tissue structures, such as the synovium, as they change with disease. Utilizing this technology, ***we hypothesized that CD14 deficiency would modulate the innate immune cell profiles within the synovium during OA progression.***

**METHODS:** *CD14 knockout (CD14-KO) mice:* Global CD14 deficient mice of C57BL/6 background were obtained from Jackson Laboratories (#003726).[4] *OA model (n=5):* Destabilization of the medial meniscus (DMM) surgery was performed to induce OA in skeletally mature (10-12 wk old) CD14-KO or C57BL/6 (WT) mice.[5] *Flow cytometry analysis (n=5):* Synovial and fat-pad tissue from 4 knees were pooled for each biological replicate, collected at 0-(preop), 4-, 8- or 16-wks post-surgery, and cells were isolated enzymatically. Cell suspensions were split in half and stained with antibodies for monocyte (CD45, Ly6C), and macrophage (CD45, CD64) cell markers or T cell (CD45, CD3) and T-helper cell (CD45, CD3, CD4) markers. Multicolor flow cytometry was performed (BD LSR II), and data was analyzed with FlowJo software (Version 10). Monocyte/macrophage populations were expressed as percent of the CD45+ population, T cell populations were expressed as percent of the CD45+ or CD3+ populations. *IMC (n=3, 4wks-post DMM)*: Whole knee joints were fixed, decalcified, paraffin embedded, and sectioned. Sagittal sections underwent heat-mediated antigen retrieval, and overnight incubation with a 22-marker multiplex panel of metal-conjugated antibodies, followed by incubation with Intercalator-Ir nuclear stain, and imaging using a Hyperion Imaging System (Standard Biotools). *Spatial protein expression and cellular phenotype analysis (n=3):* Single cell masks were created using the nuclear stain (deepcell.org). IMACytE software was used to create t-distributed stochastic neighbor embedding (t-SNE) dimensionality reduction analysis with arcsin transformation to produce data normalization and cluster analysis.[6] Cell counts per cluster were exported for comparison between experimental groups. *Statistical analysis:* Student's t-test or two-way ANOVA (indicated in figure legends), with $p<0.05$ considered significant.

**RESULTS:** Initial analysis of immune cell populations via flow cytometry revealed general leukocyte (Ly6C-CD64-), monocyte (Ly6C+CD64-), and macrophage (Ly6C+CD64+) populations to be significantly increased compared to baseline following DMM in both WT and CD14-KO synovium (**Fig. 1A**). Comparing strains, the macrophage (Ly6C-CD64+) cell population was significantly decreased in CD14-KO mice compared to WT at 8-wks post DMM (**Fig. 1A)**. Further evaluations revealed T-helper cells (CD3+CD4+CD8-) to be increased in both WT and CD14-KO mice at 4wks post DMM (**Fig. 1B**), however at 8wks post DMM the T-helper cell population in CD14-KO mice was significantly lower than in WT synovium (**Fig. 1B**). IMC spatial protein analysis of synovial sections at 4-wks post DMM revealed notable differences in monocyte/macrophage marker expression (Ly6C, F480) within the synovial lining and sublining layers between WT and CD14-KO groups (**Fig. 2C,D**). Dimensionality reduction analysis (t-SNE) revealed 12 unique cell populations across combined experimental synovial regions, with clustering by differential expression of vasculature (CD31), nerve (PGP9.5), monocyte/macrophage (Ly6C, F4/80, CD64, MHC-II, CX3CR1), T-cell (CD3), fibroblast, and other immune cell markers (**Fig. 3A,B**). The identified clusters could be localized throughout synovial lining and sublining layers (**Fig. 3C**), and evaluation of cells within unique phenotype clusters revealed significant decreases in Cluster 2 ($p=0.021$) and Cluster 8 ($p=0.033$), and an increase in cluster 5 ($p=0.026$) in CD14-KO synovium compared to WT at 4wks post DMM (**Fig. 3D**).

**DISCUSSION:** Flow cytometry analysis revealed significant changes within the synovium following DMM to innate (monocyte/macrophage) and adaptive (T-cells) immune cell populations that persist until at least 8-wks. In contrast, CD14 deficiency reduced the persistence of post-DMM elevations in CD64+ macrophages and CD3+CD4+ T helper populations by 8-wks (to near baseline), compared to WT controls at 8-wks. IMC further supported these results via spatial visualization of monocyte/macrophage and T cell markers across the two strains post DMM. Further, t-SNE analysis of the 22-marker IMC multiplex identified differences in cell cluster populations within CD14 deficient synovium compared to WT, with decreases in two distinct cell populations containing several immune cell markers (CD45, Ly6C, Ly6G, CD56), and fibrosis markers (vimentin: VIM, tenascin C: TNC), and accompanied by an increased cell cluster expressing lining resident (CX3CR1) and general macrophage (F4/80) markers. As CD14 is commonly studied for TLR4-mediated inflammatory signaling, which can influence monocyte/macrophage phenotypic differentiation, it is possible that a global knockout of CD14 is mitigating this.[2] Future work will further identify cell types within differential clusters, their spatial localization within the membrane, and temporal changes with disease.

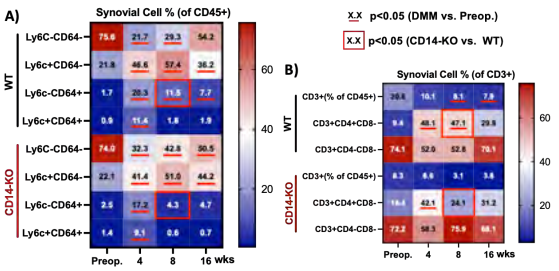


**Figure 1: Flow cytometry analysis of synovial immune cell infiltration following DMM.** (**A**) Heatmap of synovial CD45+ leukocyte (Ly6C-CD64-), monocyte (Ly6C+CD64-), and macrophage (Ly6C-CD64+, Ly6C+CD64+) cell populations (% of CD45+ synovial cells) and (**B**) T Cell (CD3+, CD3+CD4-CD8-), and helper T Cell (CD3+CD4+CD8-) populations (% of CD3+ synovial cells). p<0.05 significance by Student's T-test comparing CD14-KO to WT (2-way ANOVA).

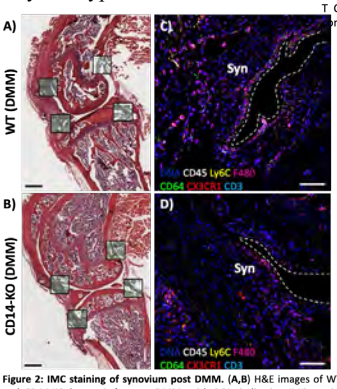


**Figure 2: IMC staining of synovium post DMM.** (**A,B**) H&E images of WT and CD14-KO knees **4wks post DMM**, with ROIs indicating IMC spatial protein analysis (grey inset). (**C,D**) Subset of select monocyte/macrophage (Ly6C, F480, CD64, CX3CR1) and T-cell (CD3) marker expression within synovial ROIs. Synovial lining = dashed white line. Scale bars = 50μm.

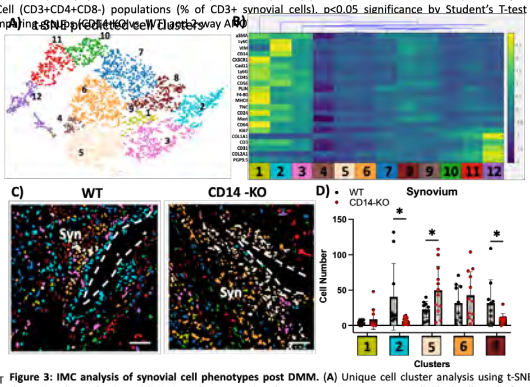


**Figure 3: IMC analysis of synovial cell phenotypes post DMM.** (**A**) Unique cell cluster analysis using t-SNE dimensionality reduction with IMC marker expression data. Data points represent individual cell masks from synovial ROIs across experimental groups. (**B**) Marker expression heatmap with cluster labels. (**C**) Single-cell unique phenotype cluster assignment within synovial ROIs. Synovial lining= white-dashed line. Scale bar=50μm. (**D**) Cell number analysis within clusters between WT and CD14-KO DMM synovial ROIs. *p<0.05.

**SIGNIFICANCE:** These results reveal that CD14 deficiency produces *distinct* immune cell clusters with distinguishable *spatial organization* within the synovium following injury, providing mechanistic support for how CD14 deficiency may be protective against PTOA-associated pathology and mobility dysfunction.

**REFERENCES:** [1]Loeser, Art & Rheum (2012), [2]Sanchez-Lopez, Nat Rev Rheum (2022), [3]Sambamurthy, PLoS One (2018), [4]Moore, J. Immuno (2000), [5]Glasson, OAC (2007), [6]Somarakis, IEEE Trans Vis (2020).

**ACKNOWLEDGEMENTS:** Caleb Marlin (OMRF) for IMC technical support. Funding, VA BLR&D (I01BX004912) and NIAMS (R01AR075737).

# Cellular and Molecular Mechanisms of Omphalocele

Xiaowen Chen, Jenna Bockman, Jisheng Yang, Mei Chen, Patricia Mericko and Mark L. Kahn

Cardiovascular Institute and Department of Medicine, University of Pennsylvania

Human omphalocele is characterized by failure to develop the abdominal wall in the peri-umbilical region, with persistent herniation of intestine and/or liver. Although abdominal wall disorders affect 1/4000 infants and are an important cause of perinatal morbidity and mortality, their etiology and pathogenesis remain poorly defined. We recently generated Hoxa13-Cre knockin mice that only targets cells that emerge from allantois, an extraembryonic mesodermal tissue that generate the umbilical cord (UC) and placenta vasculature. Detailed lineage tracing showed that ventral wall mesenchyme is completely derived from Hoxa13+ allantois and UC mesenchymal progenitor cells. We found that Hoxa13-Cre; Tgfbr1 KO animals display a fully penetrate omphalocele phenotype with a normal placenta function. Omphalocele arises in Hoxa13-Cre;Tgfbr1 mutants due to failure to form a mesenchymal population at the base of the UC insertion site. We also found that Tgfb2 is the main ligand that expressed in these mesenchymal cells. We propose that the autocrine TGFB signaling in mesenchymal cells from the allantois is key to maintain a complete ventral wall structure when the fetal liver expands massively. Our findings reveal a novel mechanism for human omphalocele and generate a new developmental paradigm for the allantois and UC.

# Differential Roles of Non-Muscle Myosin Isoforms in Skeletal and Connective Tissue Formation

Mary Kate Evans[1], Tonia K. Tsinman[1], Ellie Ferguson[1], Xi Jiang[1], Joel Boerckel[1], Lin Han[2], Eiki Koyama[3], Robert L. Mauck[1], Nathaniel A. Dyment[1]
[1]University of Pennsylvania, [2]Drexel University, and [3]Children's Hospital of Philadelphia, Philadelphia, PA
mkevans@seas.upenn.edu

**Disclosures**: RL Mauck (*8, JOR Spine*), No other disclosures.

**INTRODUCTION**: Tendon entheses often insert into bony eminences to increase mechanical advantage during ambulation. Bony eminences and the entheses attached to them are referred to as attachment units. While skeletal muscle contractile forces are key regulators of bony eminence formation [1-2], the role of non-muscle myosin (NM-II)-driven actomyosin contractility in the formation of these tissues is unknown. In drosophila, NM-II isoforms drive cell shape changes required for embryo morphogenesis [3] and are also key regulators of mechanotransduction. To determine the extent to which actomyosin contractility governs attachment unit development, we ablated the predominant NM-II isoforms, NM-IIA (Myh9 gene) and NM-IIB (Myh10 gene). We hypothesized that NM-II ablation would disrupt attachment unit growth and maturation.

**METHODS:** All animal work was approved by Institutional IACUC. Mouse Models: Allele dosages studies were conducted by crossing Myh9$^{f/f}$;Myh10$^{f/f}$ mice with Prx1Cre or ScxCre to target all limb mesenchyme or to restrict ablation to fibrous tissues, respectively. Genotypes included: Cre;Myh9$^{f/f}$, Cre;Myh10$^{f/f}$, Cre;Myh9$^{f/f}$;Myh10$^{f/wt}$, Cre;Myh9$^{f/wt}$;Myh10$^{f/f}$ and Cre;Myh9$^{f/f}$;Myh10$^{f/f}$ to interrogate the differential roles of Myh9 and Myh10. Homozygous double knockouts did not appear with the Prx1Cre driver at birth, suggesting embryonic lethality. Micro-CT: Post-weaning mutant mice along with Cre-negative littermate controls were sacrificed and analyzed in Dragonfly at 10 μm resolution [5]. Mineral labeling: To label the mineralizing front during enthesis maturation, we performed intraperitoneal injections of alizarin complexone at P20 and demeclocycline (Dem) at P27 before sacrifice at P28. Histology Sample Preparation: Knees and ankles from P28 and P112 ScxCre;Myh9$^{f/f}$;Myh10$^{f/f}$ and Cre-negative littermate control mice were fixed in formalin, cryo-embedded, and serially sectioned in the longitudinal plane. Staining: Sections were stained for calcein blue (CB), counterstained with TO-PRO-3 (nuclei), imaged, and quantified (%CB+ area). Statistics: Groups were compared via one-way ANOVA followed by Tukey-Kramer post-hoc tests (α=0.05). Data are presented as mean ± SD.

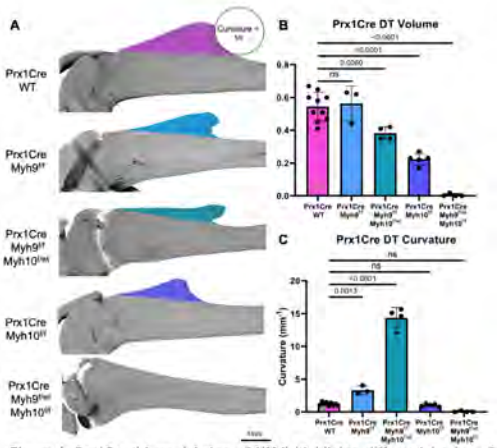


**Figure 1. Prx1Cre-driven deletion of NM-II highlights differential roles of Myh9 and Myh10 in regulating deltoid tuberosity (DT) formation, shape, and volume.** (A) 3D Micro-CT reconstructions of Prx1Cre mutant shoulders illustrating the defects in DT (B) volume and (C) curvature across all mutant genotypes.

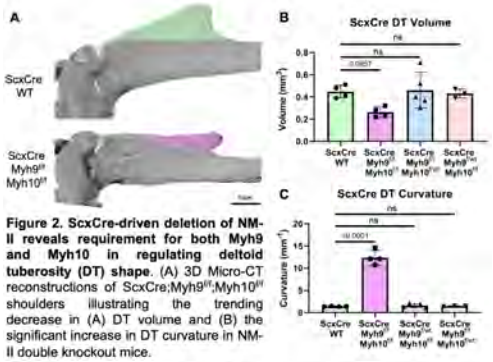


**Figure 2. ScxCre-driven deletion of NM-II reveals requirement for both Myh9 and Myh10 in regulating deltoid tuberosity (DT) shape.** (A) 3D Micro-CT reconstructions of ScxCre;Myh9$^{f/f}$;Myh10$^{f/f}$ shoulders illustrating the trending decrease in (A) DT volume and (B) the significant increase in DT curvature in NM-II double knockout mice.

**RESULTS:** NM-II regulates deltoid tuberosity (DT) size and shape. We previously showed that Prx1Cre-driven ablation of Myh9 and Myh10 resulted in severe skeletal defects, including abnormalities of the DT [4]. Upon further analysis, we found that DT volume was significantly reduced in Prx1Cre;Myh9$^{f/f}$;Myh10$^{f/wt}$ and Prx1Cre;Myh10$^{f/f}$ mice, while the DT is absent altogether in Prx1Cre;Myh9$^{f/wt}$;Myh10$^{f/f}$ mice (**Fig. 1B**). Interestingly, although DT volume was not affected in Prx1Cre;Myh9$^{f/f}$ mice, DT shape was markedly altered in both Prx1Cre;Myh9$^{f/f}$ and Prx1Cre;Myh9$^{f/f}$;Myh10$^{f/wt}$ mice (**Fig. 1C**), suggesting that Myh10 and Myh9 primarily regulate DT volume and shape, respectively. Scx cell lineage NM-II regulation of tuberosity formation and enthesis maturation: To preferentially target NM-II ablation to the tendon vs. the adjacent cartilage anlagen, we used the ScxCre driver. These mice displayed a shoulder phenotype that was strikingly similar to the Prx1Cre;Myh9$^{f/f}$;Myh10$^{f/wt}$ mice, with a trending decrease in DT volume (**Fig. 2B**) and a marked increase in DT curvature (**Fig. 2C).** Interestingly, the phenotype was rescued when mice retained a single copy of either Myh9 or Myh10, indicating the importance of both NMII-A and NM-IIB in regulating tuberosity size and shape under ScxCre-driven ablation. Further investigation into the mineralization of tendon entheses demonstrated a delay in mineral apposition at the tibial tuberosity enthesis, as evidenced by the lack of alizarin labeling in ScxCre;Myh9$^{f/f}$;Myh10$^{f/f}$ mice, resulting in a marked decrease in cumulative mineral deposition at both P28 and P112 (**Fig. 3**). Although mineral deposition was not significantly reduced at the calcaneal insertion of the Achilles tendon (data not shown), mineral apposition was disorganized and cell density was significantly reduced (264±59 vs. 198±35.2 cells/100μm$^2$, p=0.04). Importance of NM-II in maintaining tissue homeostasis: The tendon midsubstance of ScxCre;Myh9$^{f/f}$;Myh10$^{f/f}$ P112 mice was also severely disrupted, with an increase in proteoglycan content, disorganized matrix, and an elongated patellar tendon (3.39±0.12 vs. 3.91±0.18 mm, p<0.01) with reduced nuclear aspect ratio (3.70±0.28 vs. 2.47±0.11, p<0.01) and ectopic mineralization in 4/6 patellar and 5/5 Achilles tendons.

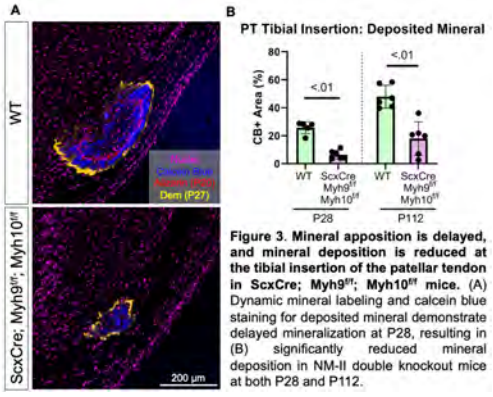


**Figure 3. Mineral apposition is delayed, and mineral deposition is reduced at the tibial insertion of the patellar tendon in ScxCre; Myh9$^{f/f}$; Myh10$^{f/f}$ mice.** (A) Dynamic mineral labeling and calcein blue staining for deposited mineral demonstrate delayed mineralization at P28, resulting in (B) significantly reduced mineral deposition in NM-II double knockout mice at both P28 and P112.

**DISCUSSION:** In addition to the established role of skeletal muscle contraction [1,2], this study indicates critical and differential roles for NM-IIA (Myh9) and NM-IIB (Myh10) in tendon and bony eminence formation, maturation, and maintenance. Interestingly, Prx1Cre;Myh9$^{f/wt}$;Myh10$^{f/f}$ mice phenocopied the complete loss (**Fig. 1A-B**) of the DT by birth previously noted in mice lacking skeletal muscle contraction [1], suggesting that NM-II is needed for proper mechanotransduction of these external forces. Further, our results indicate that NM-IIA dictated DT shape (**Fig. 1C**), which was also phenocopied by ScxCre-driven mice lacking both Myh9 and Myh10 genes (**Fig. 2C**). Maturation of the enthesis (**Fig. 3**) and maintenance of the tendon midsubstance into adulthood were also impaired by loss of NMIIA and NMIIB within Scx-lineage cells. Taken together, these data indicate that cell lineage-specific Myh9 and Myh10 expression is critical for proper formation, maturation, and maintenance of the tendon attachment unit and midsubstance.

**SIGNIFICANCE:** Establishing how actomyosin contractility regulates tissue patterning, matrix production, and organization of dense connective tissues will provide benchmarks for success and novel druggable targets for future therapies to treat disease.

**REFERENCES:** 1. Blitz, *Dev Cell*, 2009; 2. Thomopoulos, *JOR,* 2007; 3. Franke, *Current Biology*, 2005; 4. Evans, *ORS*, 2022; 5. Leek, *Dev Dyn,* 2021.

**ACKNOWLEDGEMENTS:** Work was supported by NIH P30 AR069619, R01 AR075418, T32 AR007132, and VA IK6 RX003416.

# Collagen XII Regulates Cell and Matrix Organization and Structure During Postnatal Tendon Development

Ashley K. Fung, Nathaniel A. Dyment, Louis J. Soslowsky
McKay Orthopaedic Research Laboratory, University of Pennsylvania, Philadelphia, PA
afung@seas.upenn.edu

**Disclosures**: Ashley K. Fung (N), Nathaniel A. Dyment (N), Louis J. Soslowsky (N)

**INTRODUCTION:** Collagen XII is a fibril-associated collagen with interrupted triple helices (FACIT), and mutations in the *Col12a1* gene are associated with myopathic Ehlers-Danlos syndrome (mEDS), a connective tissue disorder resulting in symptoms such as joint hypermobility and contractures [1]. Collagen XII interacts with type I collagen to mediate fibrillogenesis and has also been shown to regulate tendon cell organization and the formation of interacting cellular processes [2]. In mature tendon-targeted collagen XII knockout (ScxCre;*Col12a1*$^{flox/flox}$) mice, we previously showed that patellar tendons demonstrated reduced viscoelastic properties and collagen fiber realignment [3], further suggesting a critical role for collagen XII in establishing matrix organization for proper mechanical function. However, whether these mechanical differences in the absence of collagen XII are due to the initial deposition of disorganized matrix or disordered cell organization early in development leading to disorganized matrix is still unknown. Therefore, the objective of this study was to evaluate the role of collagen XII in regulating cell and matrix organization and structure during postnatal tendon development, prior to the establishment of significant matrix deposition. We hypothesized that collagen XII disrupts cell organization, resulting in alterations in tendon structure and organization.

**METHODS:** Postnatal day 10 tendon-targeted collagen XII knockout (KO, ScxCre;*Col12a1*$^{flox/flox}$) and control (CTRL, Cre- littermates) mice were used (IACUC approved). Tendon morphology: Knees (n=4-6/group) were fixed, paraffin processed, and sectioned in the sagittal plane. Sections were stained with toluidine blue to measure tendon length and quantify cell density. Matrix & cell organization: Knees (n=5-6/group) were fixed, and patellar tendons (PTs) were dissected from the joint. PTs were blocked and permeabilized, stained with AF 647 phalloidin and Hoechst, and optically cleared using increasing fructose concentrations (20-115% wt/vol) [4]. Z-stacks were acquired (40μm thickness) using a multiphoton microscope to visualize collagen with second harmonic generation (SHG) imaging, actin, and nuclei. Collagen density (SHG intensity), matrix alignment, and nuclear shape (sphericity) were calculated. Matrix alignment was quantified using a fast Fourier algorithm to calculate circular standard deviation of the fiber direction distribution. Fibril structure: PTs (n=4/group) were fixed, processed, sectioned, stained, and imaged via transmission electron microscopy (TEM) as described [5]. Gene expression: RNA was extracted from PTs (n=4-6/group), converted to cDNA, pre-amplified, and loaded into a Fluidigm Dynamic Array. Target genes included those of collagens, non-collagenous matrix, remodeling, cell-ECM, and cell markers. Statistics: Nuclear shape and fibril diameter distributions were compared using Kolmogorov-Smirnov tests, and all other parameters were compared using two-tailed, Student's t-tests with significance set at $p \leq 0.05$.

**RESULTS:** Tendon Morphology: PTs in KO mice were significantly longer than CTRL (**Fig 1A-B**). Matrix & cell organization: KO tendons demonstrated higher average forward SHG signal (**Fig 1C**), indicative of greater collagen density, and increased circular standard deviation of fiber directions, signifying greater collagen matrix disorganization in KO tendons (**Fig 1D-F**). Additionally, cell density was higher in KO tendons (**Fig 1G**), and nuclei were rounder (**Fig 1H**). In contrast to CTRL tendons, where actin filaments were arranged parallel with the long-axis of the tendon, actin appeared disordered and less aligned in KO tendons, consistent with matrix disorganization (**Fig 1I-J**). Irregular cell shape was also observed in TEM tendon cross-sections (**Fig 2A**). In CTRL tendons, cell protrusions interacted with those of neighboring cells towards establishing defined fibril bundles. In KO tendons, however, cell protrusions were fragmented with abundant fibripositors (white arrows). Fibril structure: The collagen fibril diameter distribution in KO tendons was more heterogeneous with a greater percentage of larger diameter fibrils compared to CTRL (**Fig 2B**). Gene expression: As expected, *Col12a1* expression was significantly reduced (**Fig 3A**), while expression of *Fn1, Mmp2, and Serpine1* (**Fig 3B-D**) was increased in KO tendons. Expression of tendon-related genes (*Col5a2, Dcn, Bgn, Tnc, Tnmd*) and those associated with cell-cell and cell-matrix interactions (*Cdh11, Cdh2, Cd44, Itgb1*) were also increased in KO tendons (data not shown).

**DISCUSSION:** During tendon development, proper cell and matrix organization is essential for establishing tendon hierarchical structure and function, and our findings indicate that collagen XII is critical in this process. In the absence of collagen XII, postnatal day 10 patellar tendons have disrupted matrix and cell organization, altered cell and nuclear shape, increased fibril diameter, and increased expression of tendon and cell-matrix related genes. Though findings support previous work in mature mice [2], interestingly, our results during early postnatal growth suggest that alterations in cell organization may precede or result in disorganized matrix deposition. Preliminary findings at postnatal day 30 show similar but less striking alterations in matrix organization and fibril diameter, further supporting a more prominent cell-mediated mechanism during early development. Additionally, increased tendon length, collagen and cell density, and fibril diameter point to a hypertrophic phenotype due to collagen XII knockout. Cornea and skin studies showed that collagen XII may be necessary for storing latent TGF-β, and its absence increased TGF-β activity [6,7]. Gene expression findings in this study support a similar mechanism in tendon, where TGF-β responsive genes such as *Serpine1* are upregulated despite no changes in *Tgfb1, 2,* or *3* expression. Studies are ongoing to explore this mechanism and further elucidate the role of collagen XII in regulating initial cell organization during embryonic tendon development.

**SIGNIFICANCE:** Collagen XII regulates cell and matrix organization and structure during postnatal tendon development, highlighting its importance in the establishment of tendon hierarchical structure and function.

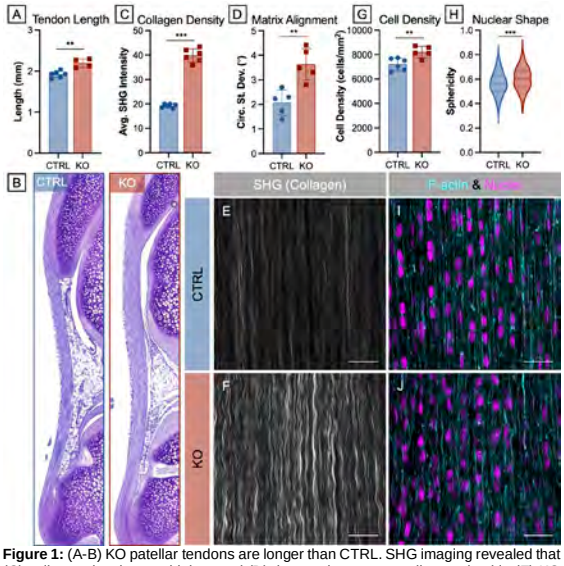


**Figure 1:** (A-B) KO patellar tendons are longer than CTRL. SHG imaging revealed that (C) collagen density was higher, and (D) the matrix was more disorganized in (E) KO tendons compared to (F) CTRL. (G) Cell density was higher and (H) nuclei were rounder in KO tendons. (I-J) Actin staining also revealed that cells were less aligned. (**p<0.01,***p<0.001, scale bar = 25μm)

**REFERENCES:** [1] Zou et al, Hum Mol Genet, 2014. [2] Izu et al, Matrix Biol, 2021. [3] Fung et al, ORS Annual Meeting 2021. [4] Ke et al, Nat Neurosci 2013. [5] Dunkman et al, Matrix Biol 2014. [6] Sun et al, Am J Pathol 2022. [7] Schönborn et al, Matrix Biol 2020.

**ACKNOWLEDGEMENTS:** We thank Courtney Nuss, Stephanie Weiss, and Alexander Bein and acknowledge support from the Penn CDB Microscopy and EMRL cores. This study was funded by NIH/NIAMS R01AR078790 and the Penn Center for Musculoskeletal Disorders (P30AR069619).

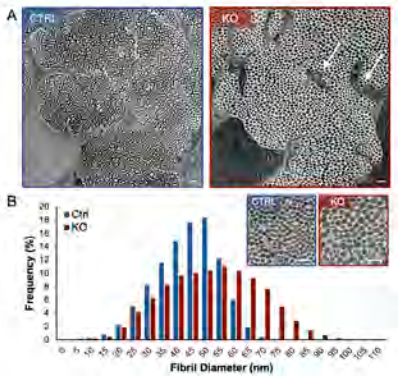


**Figure 2:** (A) Cell protrusions in CTRL tendons interact with neighboring cells and form fibril bundles, while those in KO tendons are fragmented and contain several fibripositors (white arrows). (B) KO tendons have a heterogeneous collagen fibril diameter population with a greater percentage of larger fibrils. (scale bar = 200nm)

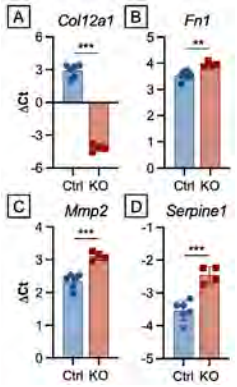


**Figure 3:** (A) *Col12a1* expression is significantly reduced in KO mice, while expression of (B) *Fn1*, (C) *Mmp2*, and (D) *Serpine1* is increased. (**p<0.01, ***p<0.001)

# Evaluation of Tendon and Ligament Microstructure in a Canine Model of Mucopolysaccharidosis I

Keerthana Iyer[1], Yian Khai Lau[1], Chet S. Friday[1], Michael W. Hast[1], George R. Dodge[1], Rahul Gawri[1,2], Margret L. Casal[1], Lachlan J. Smith[1]
[1]University of Pennsylvania, Philadelphia, USA; [2]McGill University, Montreal, Canada
keerthana.iyer@pennmedicine.upenn.edu

**Disclosures:** Keerthana Iyer (N), Yian Khai Lau (N), Chet S. Friday (N), George R. Dodge (4-MechanoTherapeutics LLC), Michael W. Hast (N), Margret L. Casal (N), Rahul Gawri (8- JOR Spine, 9-ORS Spine Section), Lachlan J. Smith (8-JOR Spine, Connective Tissue Research, 9-ORS Spine Section, National MPS Society)

**INTRODUCTION:** Mucopolysaccharidoses (MPS) I is an autosomal recessive disorder caused by deficiency of the lysosomal enzyme α-L-iduronidase (IDUA). This enzyme is required for the degradation of the glycosaminoglycans (GAGs) dermatan and heparan sulfate [1]. Abnormal accumulation of GAGs in cells leads to disease manifestation in multiple organ systems, which includes the musculoskeletal, central nervous and cardiopulmonary systems. Amongst the musculoskeletal manifestations, abnormalities of the shoulders, elbows, hips, knees, ankles and small joints of the hands and feet are prevalent, negatively impacting patient mobility and independence [2]. Current systemic treatments for MPS I show limited efficacy for improving joint disease [3]. The anterior cruciate ligament (ACL) and Achilles tendon play critical roles in the stability and biomechanical function of the knee and ankle joints, respectively; however, few studies have examined the underlying pathological changes to these tissues in MPS I, and their contributions to progressive joint disease are poorly understood. Previously, using the naturally-occurring canine model, we demonstrated that cranial cruciate ligaments (CCLs, equivalent to ACLs in humans) from MPS I animals exhibit significantly lower stiffness and failure properties compared to those from healthy animals, implicating them in progressive joint dysfunction [4]. The goal of the current study was to elucidate the microstructural basis of these functional abnormalities by undertaking comprehensive histological characterizations of both the ACL and the Achilles tendon.

**METHODS:** With institutional IACUC approval, CCLs (n=6 MPS I and n=5 control) and Achilles tendons (n=2 MPS I and n=4 control) were isolated postmortem from the stifle (knee) and ankle joints, respectively, of 12 month-old MPS I and healthy control dogs. Tissues were fixed in 10% buffered formalin for 1 week and processed into paraffin. Sections 8 µm thick were cut from the mid-substance of each sample parallel to the fiber direction. Sections were stained with hematoxylin and eosin for cellularity, Alcian blue for GAGs or picrosirius red for collagen. Semi-quantitative grading was performed for both CCL and Achilles tendon sections using parameters adapted from previously established schemes [5,6], including fiber fragmentation, fiber arrangement, rounding of cell nuclei, overall cell density, vascularity and GAG content. Each parameter was graded on a scale of 0 to 3, with 0 being normal and 3 being severely abnormal. Overall grade was calculated as the sum of individual parameters. Picrosirius red-stained sections were imaged using a polarizing microscope to determine the degree of collagen fiber disorganization quantified as circular standard deviation, using a custom Matlab program [7]. Statistically significant differences in parameters between MPS I and controls were calculated using Mann-Whitney U tests. Results are reported as median and interquartile range (IQR), with $p<0.05$ considered significant.

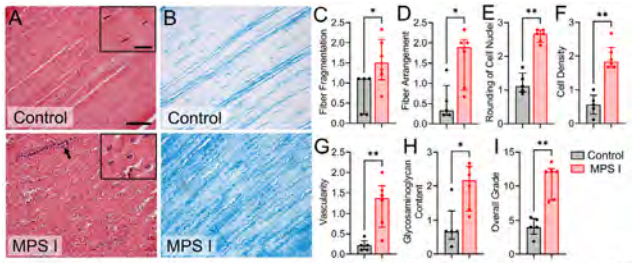


**Figure 1.** Representative histology of control and MPS I CCLs. **A.** Hematoxylin and eosin staining showing altered cellularity (inset), vascularity (arrow) and collagen fiber disorganization and **B.** Alcian blue staining showing elevated GAG content in MPS I CCLs. **C-I.** Semi-quantitative grading. *p<0.05; median/IQR; n=5-6; scale=100um (inset 20µm).

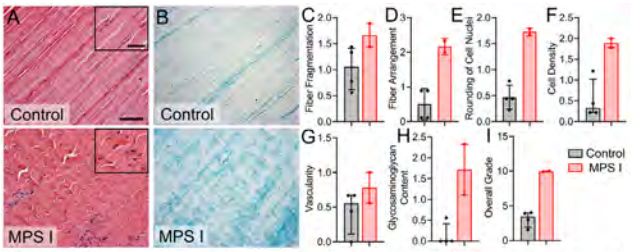


**Figure 2.** Representative histology of control and MPS I Achilles tendons. **A.** Hematoxylin and eosin staining showing altered cellularity (inset), vascularity and collagen fiber disorganization and **B.** Alcian blue staining showing elevated GAG content in MPS I tendons. **C-I.** Semi-quantitative grading. Median/IQR; n=5-6; scale=100µm (inset 20µm).

**RESULTS:** MPS I CCLs subjectively exhibited higher fiber fragmentation and disorganization, rounding of the cell nuclei, hypercellularity, vascularity, and GAG content compared to controls (**Figs 1A and B**). These findings were confirmed through semi-quantitative grading, with all parameters along with overall grade significantly worse for MPS I CCLs compared to controls (**Figs 1C-I**). With respect to the Achilles tendon, while the small sample size did not enable statistical evaluations, findings were similar to those for ACL, with clear abnormalities with respect to cellularity, GAG content and microstructure (**Fig 2**). Additionally, circular standard deviation, a quantitative measure of collagen fiber disorganization, was higher for both MPS I CCLs ($p<0.05$) and Achilles tendons compared to controls (**Fig 3**).

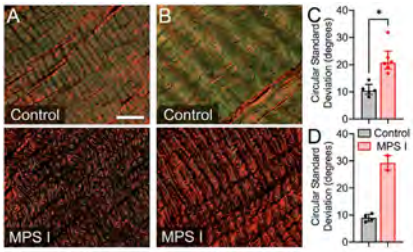


**Figure 3.** Representative polarized light histology of **A.** Control and MPS I CCLs and **B.** Control and MPS I Achilles tendons. **C.** Circular standard deviation. Picrosirius red stain; *p<0.05; median/IQR; n=2-6; scale=100µm.

**DISCUSSION:** There is lack of understanding of the roles of tendons and ligaments in progressive joint disease in MPS I, despite the critical role of these tissues in joint mechanical function. The increased GAG content observed is similar to that observed in other tissues in MPS I, as a result of IDUA deficiency. Notably, abnormal intrafibrillar GAG accumulation is frequently observed in pathologic tendons and ligaments in the general population [8]. Other microscopic abnormalities, including collagen fiber disorganization and hypercellularity, are similar to those seen in tendon overuse injuries in the general population [5,6], and are a likely basis of the diminished mechanical properties we previously reported [4]. Pathological changes may be driven in part by elevated local inflammation and collagen breakdown, secondary to GAG accumulation [9,10]. These findings demonstrate that pathological changes to both ligaments and tendons contribute to abnormal joint function in MPS I, and suggest that effective clinical management of joint disease in patients should incorporate treatments targeting these tissues.

**SIGNIFICANCE:** MPS I patients exhibit progressive synovial joint dysfunction resulting in pain and impaired mobility. Our findings implicate pathological changes to both tendons and ligaments in the etiology of joint disease in MPS I and highlight the need for improved treatments targeting these tissues.

**REFERENCES:** [1] Hampe+ Cells 2020; [2] Costi+ Diagnostic 2023; [3] Miller+ J Inherit Metab Dis 2023; [4] Lau+ ORS 2023; [5] Movin+ Acta Orthop 1997; [6] Astrom+ Clin Orthop. Relat. Res. 1995; [7] Freedman+ J Biomech 2013; [8] Han+ Nat Mater 2016; [9] Simonaro+ Am J Path 2008; [10] Natel+ J Inherit Metab Dis 2020.

**ACKNOWLEDGEMENTS:** Funding from the University of Pennsylvania and the NIH (R01AR071975, P40OD010939 and P30AR069619).

**The Effect of Bone Morphogenetic Protein-2 Peptides on 3D Stem Cell Matrix Mechanosensing.**

Umu S. Jalloh[1], Abigail McSweeny[1], Arielle Gsell[1], Sebastián L. Vega[1,2]
[1]Department of Biomedical Engineering, Rowan University, Glassboro NJ
[2]Department of Orthopaedic Surgery, Cooper Medical School of Rowan University, Camden NJ

**Introduction:** Over 100,000 patients in the United States each year suffer from severe disability because of arm and leg bone fractures that fail to heal. The standard of care for these nonunion fractures is bone autografting or allografting, which results in donor site morbidity or non-osteoinductive bone that does not remodel, respectively. Towards improving patient outcomes for nonunion bone fractures, researchers are exploring the use of biomaterials, specifically hydrogels, due to their versatility in customizable biophysical and biochemical properties. One compelling avenue of investigation centers on harnessing the regenerative potential of mesenchymal stem cells (MSCs). MSCs as a therapeutic can be allogeneic or autologous and are able to differentiate into bone-producing osteoblasts in response to biophysical and biochemical signals. Hydrogels formed with enzymatically degradable crosslinkers (Deg) play a pivotal role in promoting three-dimensional (3D) cell spreading, a crucial biophysical cue that contributes to matrix mechanosensing. Degradation-mediated 3D cell spreading influences Yes-Associated Protein (YAP) signaling which leads to nuclear YAP translocation. 3D MSC spreading is concomitant with YAP signaling and it precedes osteogenic differentiation. BMP-2 (bone morphogenetic protein 2) is a potent osteoinductive protein. Despite its osteogenic potential, BMP-2 is hindered by significant drawbacks, including high cost, the need for relatively high dosing, and the potential for off-target effects, prompting the exploration of alternative strategies for bone fracture healing. **In this study, MSCs were encapsulated in stable (Non-Deg) or enzymatically degradable (Deg) hydrogels to study how 3D cell spreading influences BMP-2 peptide osteogenesis.**

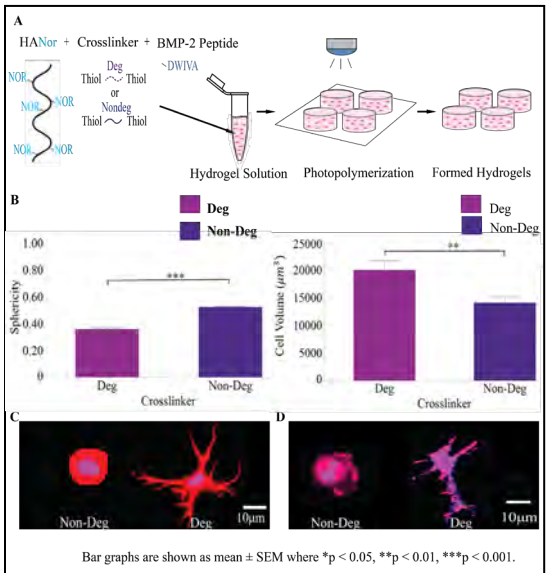


**Figure 1.** Refer to abstract for figure description.

**Methods:** Hydrogel formation involved a thiol-ene click chemistry reaction between hyaluronic acid macromers modified with norbornene (HANor) and di-thiolated degradable (Deg, sequence: G**C**NSVPMS↓MRGGSN**C**G) or non-degradable (Non-Deg, sequence: G**C**EENGGSGGSNEE**C**G) crosslinkers in the presence of a photoinitiator (I2959, 0.05 wt%) and UV light (10 mW/cm$^2$, 10 min) **(Figure 1A)**. Hydrogel solutions were prepared by combining HANor (3 wt%), Deg or Non-Deg crosslinker (2 mM), photoinitiator, and cell adhesion (RGD, 1 mM) and BMP-2 mimetic (DWIVA, sequence: GCGGGDWIVAG, 2 mM) peptides in MSC culture medium (αMEM supplemented with 10% fetal bovine serum and 1% penicillin/streptomycin). To encapsulate MSCs, MSC pellets were resuspended in hydrogel solution (1E6 cells/ml), added to clear cylindrical molds (8 mm diameter, 2 mm height), and irradiated under UV light. The hydrogels were removed from the mold, placed in a well plate containing culture media, and incubated at 37 °C. Cell viability on days 1, 3, and 7 was assessed using Live/Dead staining. Cell morphology was evaluated by staining MSC cytoskeleton (phalloidin, 1:100, 1 hour) and nuclei (Hoescht, 1:1000, 15 minutes). Samples were then imaged with a Nikon A1 confocal microscope, and ImageJ was used to quantify % live cells, ALP expression, cell volume, and sphericity.

**Results:** MSCs in HANor hydrogels with BMP-2 peptides maintained over 97% cell viability for days 1, 3, and 7, confirming biocompatibility. Crosslinker degradation influenced cell morphology, with degradable crosslinkers leading to cell spreading (volume 20043μm$^3$ ± 1653 μm$^3$; sphericity 0.36 ± 0.010) in contrast to nondegradable crosslinkers (volume 14092 μm$^3$ ± 1068 μm$^3$; sphericity 0.52 ± 0.006) representing more spherical cells (sphericity of 1 is a perfect sphere) **(Figure 1B & C).** This increased cell spreading has been strongly associated with significantly elevated alkaline phosphatase (ALP, magenta) expression, a marker of osteogenic differentiation (**Figure 1D)**.

**Conclusions:** In this study, biocompatible HA hydrogels were formed that are amenable to 3D cell culture and BMP-2 peptide functionalization. MSCs encapsulated in hydrogels formed with Deg crosslinkers spread, and this spreading results in enhanced ALP expression. Ongoing work includes investigating the effects of DWIVA peptide dosing on accelerating 3D MSC spreading and nuclear YAP localization. GCGGGKIPKASSVPTELSAISTLYLG (KIPKA) is another osteogenic BMP-2 peptide, and studies to evaluate synergy between DWIVA and KIPKA on 3D matrix mechanosensing and osteogenic differentiation are also underway. Hydrogel formulations displaying the most promising osteogenic outcomes will undergo evaluation in a preclinical femur non-union fracture rat model, with the goal of using these hydrogels to treat long bone fractures that are unable to heal.

# Graft Press-Fit Promotes Tunnel Integration After ACL Reconstruction

Timur B. Kamalitdinov[1], Keitaro Fujino[1,2], Sinaia Keith Lang[1,3], Rashad Madi[1], Xi Jiang[1], Andrew F. Kuntz[1], Nathaniel A. Dyment[1]
[1]University of Pennsylvania, Philadelphia, PA, [2]Osaka Medical and Pharmaceutical University, Takatsuki, Osaka Prefecture, Japan, [3]Columbia University, New York, NY
timkam@seas.upenn.edu

**Disclosures:** AF Kuntz (5 - Integra Lifesciences, Orthofix, Inc., FX Shoulder; 9 - American Shoulder and Elbow Surgeons, American Board of Orthopaedic Surgery). No other disclosures.

INTRODUCTION: The anterior cruciate ligament (ACL) is frequently injured, resulting in over 200,000 reconstruction procedures performed annually in the U.S. alone. The ACL reconstruction (ACLR) procedure involves drilling bone tunnels that are filled with tendon grafts to replace the native ACL. Lineage tracing studies demonstrate that the cells within the tendon graft do not actively contribute to the tunnel integration process. Instead, progenitor cells from the bone marrow outside the tendon graft activate in response to the tunnel injury, proliferate, and then migrate into the tendon graft to form mineralized fibrocartilage (MFC)-containing zonal tendon-to-bone attachment sites during the tunnel integration process [1-3]. Successful integration of the tendon graft with bone is critical to reach pre-surgical functional levels. Unfortunately, a common complication of ACLR is tunnel widening, which can be caused by improper tunnel positioning, excessive motion, or fluid effusion into the tunnels, often leading to synovial cysts in the tunnels [4]. Proper sizing of the tendon graft to the tunnel (i.e., press-fit) to minimize motion and fluid effusion is thought to be important for promoting tendon-to-bone integration while minimizing tunnel enlargement and, ultimately, graft failure [5]. Therefore, the objective of this study is to determine the extent to which graft fit affects tendon-to-bone integration following ACLR. Our hypothesis is that a properly fit tunnel will promote integration.

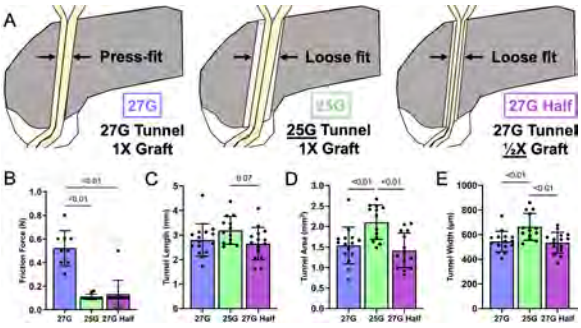


**Fig. 1:** Tunnel diameter and graft size were used to modulate the press-fit of the graft (A). Press-fit tunnels required more force to pull the graft through the tunnel (B). Tunnel dimensions at day 28 (C-E).

METHODS: All animals and procedures were approved by our institution's IACUC. Experimental Design: ACLR was performed on 43 mice, which were split into three groups. In the control group, the bone tunnels were drilled with a 27G needle and received our standard 1 mm diameter graft shown to produce zonal attachments [1-3]. We then modified the press-fit by either increasing the size of the tunnel with the same size graft (25G) or by decreasing the size of the graft with the same size tunnel (27G Half) (**Fig 1A**). Mice from all groups were assessed at 28 days post-surgery. ACL Reconstruction: The ACL was surgically transected. Tibial and femoral tunnels were drilled with 25G or 27G needles. Tail tendon autografts (~1 mm and ~0.5mm diameters for 1X and 1/2X grafts, respectively) were passed through the tunnels and anchored with external fixators. A 100-gram-force dynamometer dial gauge was used to measure the force required to pull the graft through the tunnel (n=9-12/group). Mineralized Cryohistology: Knees (n=13-15/group) were fixed in formalin, embedded, sectioned undecalcified with cryofilm, and imaged using a Zeiss Axio Scan.Z1. Image Quantification: MFC area, cyst area, tunnel length, and tunnel area were measured with ImageJ. Cyst area was defined as void spaces with curved edges in-between graft fibers, including cystic and mucoid degeneration. Average tunnel width was calculated by dividing the tunnel area by its length. Statistics: Tunnel dimensions and MFC area were compared between groups via one-way ANOVAs with Tukey's posthoc. Dynamometer readings and cyst area were compared with Kruskal-Wallis tests with Dunn's posthoc.

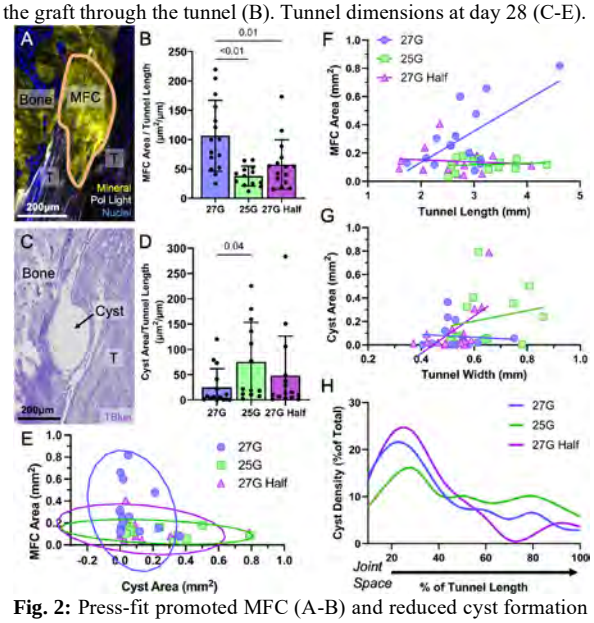


**Fig. 2:** Press-fit promoted MFC (A-B) and reduced cyst formation (C-D). MFC and cyst formation did not correlate (E). MFC (F) and Cyst (G) relationships to tunnel dimensions. Location of cysts as a function of distance from the joint space (H). T = tendon graft.

RESULTS: The force required to pull the graft through the tunnel during surgery was higher in the 27G group compared to the 25G and 27G Half groups ($p<0.01$, **Fig. 1B**). At 28 days post-surgery, the 25G group had higher tunnel area and tunnel width compared to the 27G and 27G Half groups ($p<0.01$, **Fig. 1C-E**), with tunnel widths aligning with the diameters of a 25G or 27G needle. The 27G group promoted MFC formation compared to the 25G ($p<0.01$) and 27G Half ($p = 0.01$) groups (**Fig. 2B**). Conversely, the 25G group had greater cyst area than the 27G group ($p=0.04$) but not the 27G Half group (**Fig. 2D**). MFC area did not correlate strongly with cyst area, with the 27G group having higher MFC and the other groups having higher Cyst values (**Fig. 2E**). Interestingly, MFC area positively correlated with tunnel length in the 27G group (Pearson coefficient 0.64, $p<0.01$, **Fig. 2F**), and cyst area correlated with tunnel width in the 25G group (Pearson coefficient 0.62, $p=0.01$, **Fig. 2G**). Finally, we investigated the position of cysts in the tunnel and found that cysts were generally closer to the joint space and that the 25G group had a higher percentage of cysts extending deeper into the tunnel, possibly from the loose fit and larger tunnel size (**Fig. 2H**).

DISCUSSION: During the early stages of healing post-ACLR, graft fixation plays a stabilizing role. Our histological analysis revealed greater tendon-to-bone integration (as indicated by more MFC), and less cyst formation in the tighter-fitting 27G group. In fact, hardware-free press-fit ACLR procedures, in which the graft fits tightly in the tunnels, are being investigated as techniques to reduce fluid effusion and tunnel enlargement compared to traditional ACLR procedures with fixation hardware [4,5]. As expected, the tunnels were wider in the 25G group in our study and may have contributed to higher incidence of cysts that were deeper in the tunnels. In addition, we found that tunnel length positively correlated with MFC area in tighter fitting 27G tunnels and tunnel width correlated with cyst area in the looser 25G tunnels. The looser-fitting tunnels generally had more remodeling of the tendon graft than the press-fit, potentially resulting in more opportunities for cysts formation. However, due to the nature of the tail tendon graft having multiple fascicles, the tension in each fascicle is likely different regardless of the fit of the graft in the tunnel, possibly explaining why cysts occurred in press-fit tunnels as well.

SIGNIFICANCE/CLINICAL RELEVANCE: This study emphasizes the importance of properly fitting the graft to the bone tunnel in ACLR, informing surgical practice. Additionally, this murine surgical model can elucidate specific cellular mechanisms related to press fit in the future using transgenic mice.

REFERENCES: 1. Kamalitdinov et al., *JOR*, 2020; 2. Hagiwara et al., *Ann NY Acad Sci*, 2020; 3. Kamalitdinov et al., *Osteoarthr Cartil*, 2023; 4. Rizer et al., *Skeletal Radiol*, 2017; 5. Paessler and Mastrokalos, *Orthop Clin North Am*, 2003.

ACKNOWLEDGEMENTS: Work supported by NIH R01AR076381, NIH R21AR078429, NIH R00AR067283, NIH P30AR069619, and NIH F31AR079840.

# Skeletal growth is enhanced by a shared role for SOX8 and SOX9 in promoting reserve chondrocyte commitment to columnar proliferation

Anirudha Karvande, Arnaud N. Molin, Romain Contentin, Marco Angelozzi, Ranjan Kc, Abdul Haseeb, Chantal Voskamp, Charles de Charleroy, and Véronique Lefebvre*

Department of Surgery / Division of Orthopaedic Surgery, The Children's Hospital of Philadelphia, Philadelphia, PA 19104, USA

SOX8 was linked in a genome-wide association study to human height heritability, but roles in chondrocytes for this close relative of the master chondrogenic transcription factor SOX9 remain unknown. We undertook here to fill this knowledge gap. High-throughput assays demonstrate the expression of human *SOX8* and mouse *Sox8* in growth plate cartilage. *In situ* assays show that *Sox8* is expressed at a similar level as *Sox9* in reserve and early columnar chondrocytes, and turned off when *Sox9* expression peaks in late columnar and prehypertrophic chondrocytes. *Sox8*$^{-/-}$ mice and *Sox8*$^{fl/fl}$*Prx1Cre* and *Sox9*$^{fl/+}$*Prx1Cre* mice (inactivation in limb skeletal cells) have a normal or near normal skeletal size. In contrast, juvenile and adult *Sox8*$^{fl/fl}$*Sox9*$^{fl/+}$*Prx1Cre* compound mutants exhibit a 15-20% shortening of long bones. Their growth plate reserve chondrocytes progress slowly toward the columnar stage, as witnessed by a delay in downregulating *Pthlh* expression, in packing in columns and in elevating their proliferation rate. *SOX8* or *SOX9* overexpression in chondrocytes reveals not only that SOX8 can promote growth plate cell proliferation and differentiation, even upon inactivation of endogenous *Sox9*, but also that it is more efficient than SOX9, due to greater protein stability. Altogether, these findings widen our understanding of the complex network of factors regulating skeletal growth and validate a genome-wide association study proposition that SOX8 is a determinant of human height. Specifically, they uncover a major role for SOX8 and SOX9 in promoting skeletal growth by stimulating the commitment of growth plate reserve chondrocytes to actively proliferating columnar cells. Further, by showing that SOX8 is more chondrogenic than SOX9, they suggest that SOX8 could be preferred over SOX9 in therapies to promote cartilage formation or regeneration in developmental and degenerative cartilage diseases.

# The TGFβ-Signaling enhances Cellular and Matrix Maturation in Scaffold-free Three-Dimensional (3D) Tendon Construct

Bon-Hyeock Koo[1], Kyu Sang Joeng[1]
[1]University of Pennsylvania, Philadelphia, PA

**EMAIL:** Bonhyeock.Koo@pennmedicine.upenn.edu
**Disclosures**: Bon-Hyeock Koo (N), Kyu Sang Joeng (N)

**INTRODUCTION**: Tendons are connective tissues transmitting mechanical forces between muscles and bones. Given its characteristics of strength and elasticity, tendon can prevent muscle injury by absorbing the mechanical impacts [1]. In spite of its notable tensile strength, overuse of tendons in sports or daily activity causes tendon injury, and injured tendon barely restores original structural and mechanical integrity [2]. Therefore, tendons are targets for tissue engineering and regenerative medicine. However, the biological mechanisms regulating molecular and cellular maturation are poorly understood partly due to the lack of a reliable *in vitro* system, which hinders advancing tendon tissue engineering and regenerative medicine [3]. To overcome this limitation, we previously developed a scaffold-free 3-dimensional (3D) tendon culture system and tested tenogenic maturation and mechanical properties [4]. Our previous study showed that TGFβ (Transforming growth factor β) treatment is necessary to maintain the 3D tendon constructs, but the precise function of TGFβ in 3D tendon culture was not established. In the current study, we investigated the function of TGFβ in molecular and cellular maturation in Scaffold-free 3D tendon culture.

**METHODS**: All procedures were approved by UPenn's IACUC. Both male and female mice were used in this study. We isolated mouse tail tendons at 28 days of age. These tail tendons were digested with type I collagenase for 1 hour. The tendon cells from mouse tail tendons were initially cultured in a 6-well plate with growth media (20% FBS, 2 mM L-glutamine in a-MEM medium). After 90-100 % confluency, tendon cells were passaged to 100 mm plate for further amplification. For 3D tendon culture, the amplified cells ($2.0 \times 10^6$ cells) in monolayer culture were seeded in the fibronectin-coated growth channel and cultured with differentiation media (20% FBS, 2 mM L-glutamine in a-MEM medium). After generating 3D tendon structures, we treated vehicle or TGFβ every two days until harvested. H&E staining was conducted at T14 (T0 is the initiation day of TFGβ treatment). BrdU and TUNEL assay were conducted at T3, 7, and 14. The measurement of the nucleus aspect ratio was performed by the Image J software program. We measured both height and width of the nucleus in the peripheral layer of 3D tendons and calculated the ratio at the T0, 3, 7, and 14. qRT-PCR analysis was performed to assess the expression of tendon-related gene markers in 3D tendon structures at T0, T3, T7, and 14. All quantitative data were analyzed using the student's t-test.

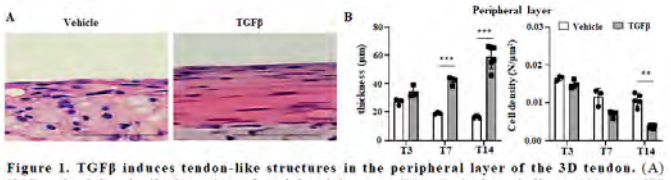

**Figure 1. TGFβ induces tendon-like structures in the peripheral layer of the 3D tendon.** (A) H&E-stained longitudinal section of peripheral layer at T14. Scale bars indicate 100 μm. (B) Quantification results of thickness and cell density of peripheral layer. ** indicates P<0.01 and *** indicates P<0.001, n=3

**RESULTS**: We previously found that the peripheral layer of 3D tendon constructs undergoes tendon-like tissue maturation. Therefore, we acquired H&E-stained images of the peripheral layer after TGFβ treatment to test the effects of TGFβ on tissue maturation, such as tissue thickness and cell density (Fig 1A). As expected, TGFβ treatment enhanced thickness and decreased cell density of the peripheral layer compared to vehicle treatment at T14 (Fig 1B). The decreased cell density in the peripheral layer of 3D tendon constructs prompted us to investigate cellular proliferation and apoptosis. We analyzed the cell proliferation and apoptosis ratio by BrdU staining and TUNEL assay in the 3D tendons at various stages (T3, 7, 14) (Fig 2A, B). The level of cell proliferation in each group decreased as the stage progressed in both layers. However, TGFβ treated groups exhibited increased cell proliferation compared to control groups in both layers as the stage progressed (Fig 2C, D). TGFβ-treated groups showed a lower apoptosis rate than those of control groups at an early stage (T3) only in the peripheral layer (Fig 2E). However, no difference was observed in apoptosis level between vehicle- and TGFβ-treated groups in the inner layer at all stages (Fig 2F). To investigate cellular phenotypes in 3D tendon constructs, we first examined the morphological changes of cells in the 3D tendon construct (Fig 3A-D). We measured the ratio of the nuclear transverse length to its length in the direction of the channel length. In this measurement, values closer to 1.0 indicates a rounder cell shape, and values closer to 0 indicate a more elongated cell shape. Gradual cell elongation was observed in the peripheral layer of both vehicle- and TGFβ-treated constructs, but TGFβ-treated constructs had more elongated cells than vehicle-treated constructs throughout the stages. To test the effect of TGFβ on tenogenic differentiation, we examined the expression of tenogenic gene markers such as Scleraxis (Scx), Tenomodulin *(*Tnmd*)*, and Collagen type 1 (Col1a1) (Fig 3E-G). TGFβ treatment significantly enhanced the expression of Scleraxis, but there was no significant effect on the expression of Tnmd and Col1a1.

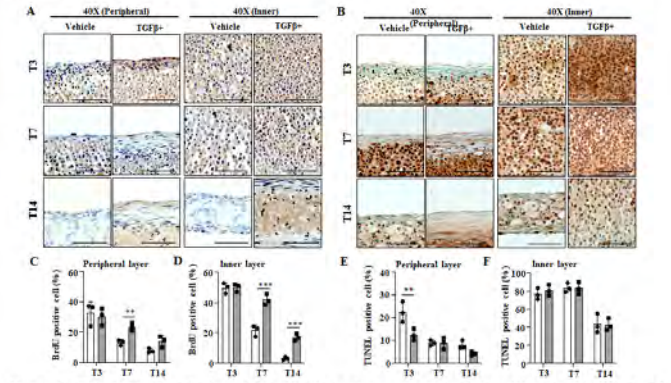

**Figure 2. Histological analysis of layer of 3D tendon constructs.** (A) BrdU-stained longitudinal sections of 3D tendon structure in both control and TGFβ+ at T3, 7, and 14 stages. (B) TUNEL assay longitudinal images of 3D tendon structure. (C, D) The quantification results of BrdU positive cells of the control and TGFβ+ groups at T3, 7, 14 stages in inner- and peripheral-layer. (E, F) The quantification results of TUNEL positive cells of the control and TGFβ+ groups at T3, 7, 14 stages in inner- and peripheral-layer. Scale bars indicate 100 μm. ** indicates P<0.01 and *** indicates P<0.001, n=3

**DISCUSSION**: Our data suggest that TGFβ treatment increased cellular proliferation in both peripheral as well as inner layers and prevented cellular apoptosis in the peripheral layer at early stages, which could explain the increased thickness of TGFβ-treated tendon constructs. TGFβ dramatically induced the expression of Scleraxis but not the expression of Col1a1 and Tenomodulin. These data suggest that cells undergo early tenogenic differentiation without further molecular maturation with TGFβ treatment.

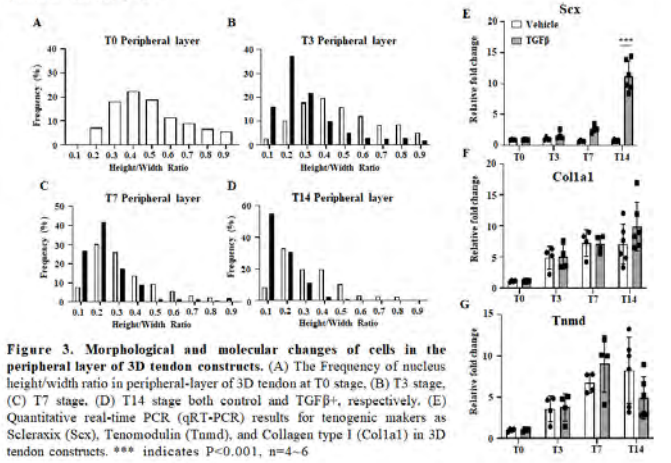

**Figure 3. Morphological and molecular changes of cells in the peripheral layer of 3D tendon constructs.** (A) The Frequency of nucleus height/width ratio in peripheral-layer of 3D tendon at T0 stage, (B) T3 stage, (C) T7 stage, (D) T14 stage both control and TGFβ+, respectively. (E) Quantitative real-time PCR (qRT-PCR) results for tenogenic makers as Scleraxix (Sex), Tenomodulin (Tnmd), and Collagen type I (Col1a1) in 3D tendon constructs. *** indicates P<0.001, n=4~6

**SIGNIFICANCE/CLINICAL RELEVANCE**: This study provides a reliable *in vitro* tendon cell culture model which can be used to screen various biological molecules that is essential for tendon regeneration.

**REFERENCES**: [1] T Roberts 2014, [2] L Galatz 2015, [3] Nichols 2019 [4] L Yeon-Ju 2022.

# Interleukin Receptor Therapeutics Attenuate Synovial Inflammation in Canines following Cruciate Ligament Injury

Lemmon EA[1,2,3,5], Kim SY[1,2,5], Kwok B[6], Laforest L[1], Hallström G[1,2,5], Burt KG[1,2,5], Han L[6], Scanzello CR[4-5], Mauck RL[1,2,5], Agnello, KA[3]
Dept. of [1]Orthopaedic Surgery, [2]Bioengineering, [3]Veterinary Medicine, and [4]Medicine, University of Pennsylvania, Philadelphia, PA, [5]Translational Musculoskeletal Research Center, VA Medical Center, Philadelphia, PA, [6]Nanobiomechanics Laboratory, Drexel University, Philadelphia, PA
elemmon@vet.upenn.edu

**Disclosures**: EAL (None), SYK (None), BK (None), LL (None), GH (None), KGB (None), LH (None), CRS (None), RLM (4, 5, 8), KAA (None)

**Introduction:** Knee injuries create instability that perpetuates inflammation, resulting in irreversible damage to all joint structures across species.[1] In companion dogs, tears to the cranial cruciate ligament (CCL), the anatomic equivalent to the human anterior cruciate ligament (ACL), are a leading cause of joint disease.[2] While treatment in both species focuses on restoring knee mechanical stability via surgical correction, few therapeutics treat the synovial pathology that perpetuates joint-wide inflammation. Despite this, recent research shows that synovial inflammatory markers in human patients after ACL injuries may be predictive of cartilage damage severity and clinical outcomes after repair.[3] We posited that canines with spontaneous CCL tears may be an ideal model to evaluate novel interventions following injury, given their similarities to human disease progression. To establish this model, we first evaluated the structural and micromechanical changes in canine knee synovium following spontaneous CCL injury in comparison to healthy donors. Next, we used RNA sequencing to identify transcriptional changes in the synovium of dogs presenting with spontaneous CCL tears relative to healthy controls. Using this information, we tested whether the IL1 receptor antagonist (Anakinra) or the IL6 receptor inhibitor (Tocilizumab) could attenuate inflammation in synovial organ cultures of dogs with CCL tears.

**Methods:** Synovium Histology and Scoring: Synovium samples were collected from healthy or CCL canine joints (n=10/group), stained with hematoxylin-eosin (H&E), and scored for synovitis per OARSI guidelines[4] by 4 blinded reviewers (**Fig 1A-B**). Atomic Force Microscopy (AFM): Histology guided AFM (**Fig 1A-B,D**) was applied to 40 µm–thick cryo-sections (healthy or CCL synovium, n=5/group) in PBS using a microspherical tip ($R \approx 6$ µm, nominal $k \approx 0.6$ N/m) and a Dimension Icon AFM. For each region (subintima and intima), the effective indentation modulus was calculated[5] for 15-20 locations. RNA Sequencing: Ilumina truSeq stranded poly-A libraries were generated and single-end reads were sequenced using an Illumina NovaSeq. Deseq2 was used for differential expression analysis (n=5/group). Gene ontology was carried out using DAVID (**Fig 2B**). qPCR of Canine Synovium: Healthy (n=10) or CCL tear (n=14) synovium was collected and processed for RNA extraction and cDNA synthesis prior to qRT-PCR. Synovial Organ Culture: CCL tear synovium (n=5/group) was collected and cultured for 3 days with either an IL1 receptor antagonist (100ng/mL) or IL6 receptor inhibitor (100ng/mL). qPCR was conducted as above (**Fig 3A-B**). Statistical Analyses: For synovium scoring, a Mann-Whitney test was used. For qPCR of healthy/diseased synovium, unpaired t-tests were used. For AFM and synovium organ culture and treatment, 1-way ANOVA was used.

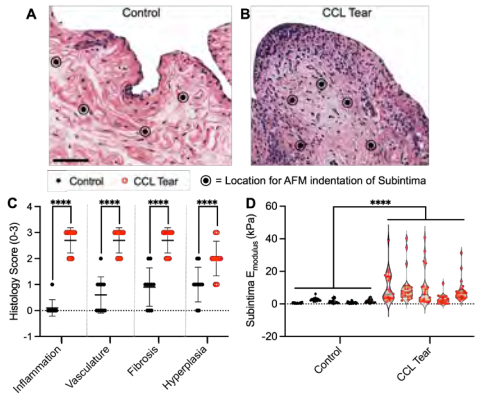


**Fig 1.** H&E images (20X) of (A) healthy control and (B) CCL tear synovium. Scale bar: 100µm. (C) Mean synovial histology score. (D) AFM modulus. Mean+/-SD, ****indicates ($p<0.001$).

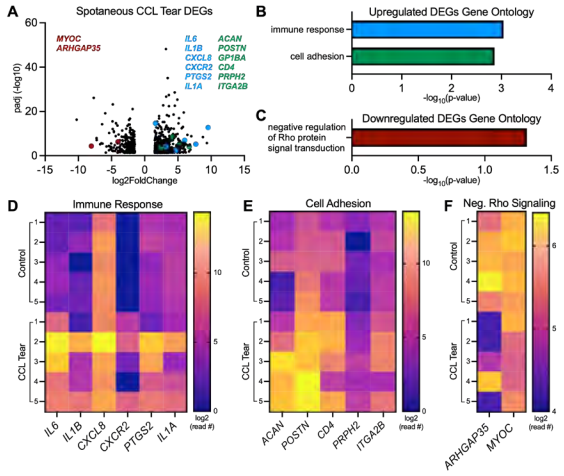


**Fig 2.** RNAseq results with (A) volcano plot of DEGs, (B) gene ontologies identified from DEGs, and (D-F) heat maps of individual genes in each pathway across the five donors.

**Results:** Synovium from dogs with CCL tears showed increased inflammation, vasculature, fibrosis, and hyperplasia compared to healthy synovium (**Fig 1A-C**). CCL synovium also had a higher indentation modulus in both the intimal (not shown) and subintimal (**Fig 1D**) regions compared to healthy controls. RNAseq revealed that CCL synovium had 766 genes upregulated and 365 genes downregulated ($p<0.0001$) compared to healthy controls. Gene ontology of these DEGs identified immune response and cell adhesion as two of the most enriched pathways, with increased expression of interleukins (IL6 and IL1) as well as ACAN (aggrecan) and POSTN (periostin) (1.5-fold cutoff, $p<0.05$) (**Fig 2A-E**). In addition, genes associated with negative regulation of Rho protein signaling were reduced (**Fig 2A-C,F**). In CCL synovium explants, expression of PRG4 (lubricin) decreased while the inflammatory markers IL1β, IL6, and PTGS2 (the gene encoding cyclooxygenase-2) increased (**Fig 3B**). When CCL synovium was treated with an IL1 receptor antagonist or an IL6 receptor inhibitor, both restored PRG4 expression to control levels while decreasing expression of IL1β, IL6, and PTGS2 (**Fig 3B**).

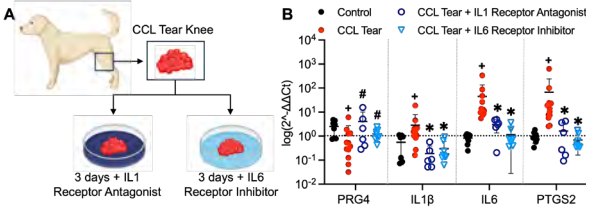


**Fig 3.** (A) Schema of diseased synovial cultures treated with IL1 receptor therapeutics. (B) qPCR of inflammatory and anabolic genes in each condition. + indicates difference ($p<0.05$) vs. control, *indicates difference ($p<0.05$) or # ($p<0.1$) vs. CCL tear synovium.

**Discussion:** This study shows that structural and mechanical synovial disease progression in canine patients with spontaneous CCL tears mimics that of human patients with ACL tears.[6] Notably, both RNAseq and AFM showed some heterogeneity across donors in terms of degree of fibrosis and activation of specific genes, with patients with a shorter history of disease showing less changes. This suggests that a tailored approach, based on the stage of disease progression, may be necessary to increase clinical efficacy of treatments. Importantly, both the human formulation of an IL1 receptor antagonist (Anakinra) and an IL6 receptor inhibitor (Tocilizumab) successfully downregulated critical inflammatory mediators, IL1β, IL6, and PTGS2, and restored expression of PRG4, a glycoprotein necessary for cartilage health.[7] While interleukin receptor targets were effective at downregulating inflammatory pathways in diseased synovium, it has not yet been established if these molecules can reverse or halt the progression of synovial fibrosis. To address this, current studies are evaluating the efficacy of interleukin receptor therapeutics in a clinical trial in which these agents are applied intraarticularly to client-owned canines with CCL tears after tear diagnosis and prior to surgical intervention.

**Significance/Clinical Relevance:** Canines with spontaneous CCL tears have a knee joint environment that mimics the structural, mechanical, and molecular phenotypes of humans with ACL tears – providing a valuable model to evaluate novel therapeutics targeted at knee joint pain and inflammation after injury.

**Acknowledgements:** This work was supported by the NIH (R01 AR056624 and T32 GM007170) and the VA (IK6 RX003416 and I21 RX004628). CCL tear synovium samples were collected by the PennVet Orthopedic Surgery Service.

**References:** 1. Scanzello+ *Arthritis Rheum,* 2011; 2. Innes+ *Vet Rec* 2000; 3. Brophy+ *Am J Sports Med*, 2022; 4. Bansal+ *Orthop. J. Sports Med*, 2021; 5. Diamitridis+, *Biophys J* 2002+ 6. Bonnevie+, *In Revision*, 2023;7. Gleghorn+ *JOR*, 2009.

# Localized Delivery of a Hedgehog Agonist from Electrospun Scaffolds Enhances Tendon-to-Bone Integration

Rashad Madi[1], Jonathan Marcelin[1], Timur B. Kamalitdinov[1], Xi Jiang[1], Sereen Assi[1], Dong-Hwa Kim[1], Robert L Mauck[1], Andrew F. Kuntz[1], Nathaniel A. Dyment[1]
[1]University of Pennsylvania, Philadelphia, PA
rmadi@upenn.edu

**Disclosures**: AF Kuntz (5 - Integra Lifesciences, Orthofix, Inc., FX Shoulder; 9 - American Shoulder and Elbow Surgeons, American Board of Orthopaedic Surgery), RL Mauck (4 - Mechano-Therapeutics, LLC; 6 - 4Web Medical; 9 - JOR Spine).

INTRODUCTION: Injuries to tendons are commonly observed at the insertion site between tendon and bone, known as the enthesis. Endogenous healing and repair of the tendon-to-bone enthesis often results in the formation of disorganized scar tissue [1]. The Hedgehog (Hh) signaling pathway plays a crucial role in orchestrating the formation and maturation of the original enthesis during growth and development [2-4]. Consequently, targeting this pathway offers a compelling strategy to improve tendon-to-bone integration by facilitating the development of a functionally graded zonal enthesis. Our prior work has shown that activating the Hh pathway, either through genetic manipulation or systemic injections of a Hh agonist, results in improved tendon-to-bone attachments following anterior cruciate ligament reconstruction (ACLR) [5]. Given the importance of the Hh pathway in several tissues and organs [6], it is imperative to develop localized therapeutic Hh interventions to mitigate off-target effects while still leveraging the therapeutic potential of the pathway. To achieve this, we fabricated scaffolds with varying concentrations of SAG, a small-molecule agonist of the Hh signaling pathway, and then implanted them with the ACLR graft to enhance tendon-to-bone integration via localized SAG delivery. The objectives of this study were to incorporate SAG into electrospun scaffolds, evaluate scaffold characteristics post-incorporation, and assess the effect of in vivo SAG release on downstream Gli1 expression and tendon-to-bone integration in a bilateral transverse tibial tunnel (TTT) integration model.

METHODS: All animals and procedures were IACUC approved. Scaffold Fabrication: Polycaprolactone (PCL) solution (35 wt%) was prepared in DMF/THF with the Hh agonist (SAG) at different concentrations (0, 0.001, 0.01, 0.1 mg/ml). The solution was spun from an 18G needle at 15kV onto a rotating mandrel (8 m/s, 2.5 ml/hr). SEM: Fiber alignment and diameter (100 fibers per sample) were measured from images acquired on an FEI Quanta 600 ESEM (**Fig. 1**). Tunnel Integration Study: TTT surgeries were performed on 24 mice. This procedure was utilized as a simpler, higher throughput model than the ACLR that we have used previously [1,5]. Graft tail tendons were harvested from the mouse, and a sterile scaffold was added to the graft bundle. A transverse tibial tunnel was drilled in the metaphysis using a 27G needle (**Fig. 2A**). The graft with the scaffold was passed through the tunnel (**Fig. 2B**). The limbs were harvested on day 14. Mineralized Cryohistology and Regional qPCR: Limbs were fixed, embedded, and sectioned undecalcified with cryofilm. The medullary canal was microdissected from tissue sections for qPCR. Adjacent sections were stained with Alizarin Complexone (AC) to visualize deposited mineral fluorescently on a Zeiss Axio Scan.Z1. AC area was normalized to the area of the tendon graft and scaffold and quantified. Statistical Analysis: Fiber diameter and orientation and *in vivo* qPCR and AC area were compared via one-way ANOVA ($p<0.05$). Outliers were identified and removed using the ROUT method.

RESULTS: SAG incorporation into electrospun scaffolds did not affect fiber orientation or diameter. Utilizing the OrientationJ plugin to analyze fiber alignment from SEM images, we found that incorporation of SAG resulted in only minor changes in fiber dispersion (**Fig. 1B**). Additionally, the average fiber diameters in scaffolds containing SAG were comparable to the blank scaffold (**Fig. 1C**). SAG release in vivo stimulated Hh signaling. The region containing the medullary canal was microdissected from transverse sections to measure Gli1 expression 14 days post-surgery. SAG release yielded a dose dependent effect on Gli1 expression, with the 0.1 mg/ml SAG group having ~3-fold higher expression ($p=0.009$, **Fig. 2D**). Localized SAG release increased mineralized fibrocartilage (MFC) formation in the tendon graft and mineral deposition in the scaffold. To monitor the tunnel integration process, we measured the deposited mineral area in the tendon graft and scaffold (red in **Fig. 3B**). We found that SAG concentration impacted AC staining in a dose-dependent manner, with the 0.1mg/ml group having higher MFC formation in the tendon graft ($p=0.044$, **Fig. 3C**) and higher mineral deposition in the scaffold region of the 0.01 mg/ml ($p=0.048$) and 0.1 mg/ml ($p=0.047$) groups (**Fig. 3D**).

DISCUSSION: This study provides key insights into the effects of SAG incorporation into PCL scaffolds, specifically concerning the scaffold architecture and SAG release on downstream Gli1 expression and MFC formation in the bone tunnels within the TTT model. Our findings show that SAG incorporation slightly altered the fiber alignment but had no detectable effect on fiber diameter. Furthermore, SAG release from the scaffold had a marked effect on Hh signaling, as evidenced by a statistically significant upregulation of Gli1 expression in the medullary canal in scaffolds with a concentration of 0.1 mg/ml SAG. Our data demonstrate that localized delivery of SAG significantly increased MFC formation in the tendon graft and mineral deposition in the scaffold, which is an indicator of improved tendon-to-bone attachment formation and tunnel integration. These findings indicate that localized SAG delivery is an effective method for increasing MFC formation and mineralization, hence potentially offering a novel therapeutic. Future studies will apply the SAG-loaded scaffolds in our more clinically relevant, yet lower throughput, ACLR model to determine if it can improve the tendon-to-bone integration process.

SIGNIFICANCE/CLINICAL RELEVANCE: This study demonstrates that localized delivery of Hh agonists is a viable and promising therapeutic strategy for enhancing tendon-to-bone integration while minimizing side effects from systemic delivery.

REFERENCES:1. Kamalitdinov et al., JOR, 2020; 2. Lu and Thomopoulos, Annu. Rev. Biomed. Eng. 2013; 3. Liu et al, PLoS One, 2013; 4. Dyment et al., *Dev Biol*, 2015; 5. Kamalitdinov et al., Osteoarthritis Cartilage. 2023; 6. Ingham PW et al., Nat Rev Genet., 2011.

ACKNOWLEDGEMENTS: Work supported by NIH R21AR078429, P30AR069619, and F31AR079840 (TBK).

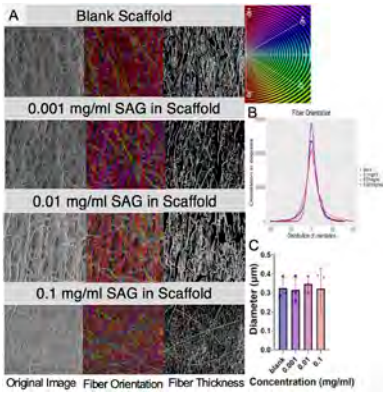


**Fig 1**. SAG did not affect scaffold fiber orientation (C) or diameter (D).

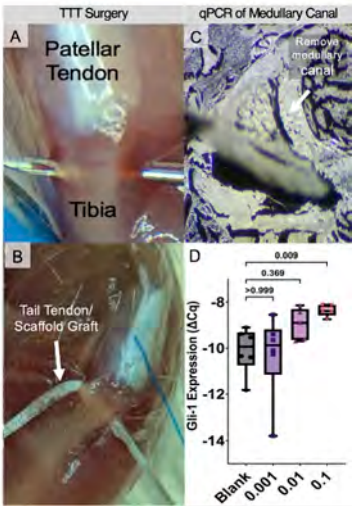


**Fig 2.** SAG release in a TTT model (A,B) stimulated Gli1 expression from micro-dissected tissues (C-D).

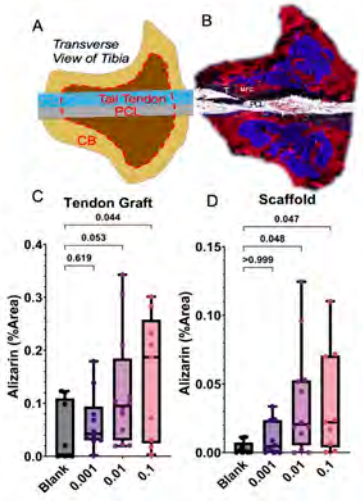


**Fig 3**. SAG release from scaffolds into the bone tunnel (A-B) promoted mineral deposition (red in B) in both the tendon graft (C) and scaffold (D).

**YAP and TAZ regulate adult bone formation and osteocytic perilacunar-canalicular remodeling**

Yasaman Moharrer [1], Ghazal Vahidi[2], Daniel Horan[3], Tala Azar[1], Annemarie Lang[1], Alexander Robling[3], X. Sherry Liu[1], Chelsea Heveran[2], Joel D. Boerckel[1].
[1]University of Pennsylvania, [2]Montana State University, [3]Indiana University

Physical activity induces skeletal adaptation by mechanotransduction. However, the mechanisms governing this adaptive response are unclear. Using genetic methods, we found that the transcriptional regulators, YAP and TAZ, regulate bone growth and osteocyte network. Here, we implement global inhibition approaches to test the roles of YAP/TAZ in adult bone growth and osteocyte peri-lacunar remodeling.

We injected 8-week-old male BL/6 mice with DMSO or verteporfin (VP) for 2 weeks. VP inhibits YAP/TAZ-TEAD interaction. We evaluated bone formation by Calcein and Alizarin labeling, injected 7 days apart, and quantified the extent of mineralized bone surface (MS/BS), mineral apposition rate (MAR), and bone formation rate (BFR) in coronal and transverse tibial sections. Using a confocal microscope, we identified fluorochrome-labeled osteocytes lacuna, quantified the fluorescence intensity, and measured the lacunae mineral extent. By immunofluorescent staining on coronal sections, we checked if YAP/TAZ inhibition impacts other cell types. We quantified fracture toughness from the maximum and the yield load (KIc-max, KIc-initiation) by a 3-point bending test.

YAP/TAZ inhibition modestly elevated endosteal MS/BS, though this difference was not statistically significant. In contrast, YAP/TAZ inhibition significantly reduced periosteal and trabecular bone MS/BS (Fig. 1 A and Fig. 1B). Reduced MS/BS values, without altered MAR indicate that YAP/TAZ inhibition reduces osteoblast activation without altering osteoblastic mineral deposition rate. Endomucin immunostaining showed a significant effect of VP treatment on vessel morphology, area, and the number of endomucin+ blood vessels, indicative of systemic YAP/TAZ that impacts cells beyond bone cells. (Fig. 1C). This finding may explain the contrasts between endosteal and periosteal bone formation responses to YAP/TAZ inhibition. By quantifying the fluorescence intensity of the labeled lacunae in posterior, anterior, lateral, and medial regions of the tibial cortex, we found that YAP/TAZ inhibition significantly reduced the intensity of the calcein-labeled lacuna, particularly in the anterior that has the highest tensile strains (Fig. 1D). Although, KIc-max and KIc-initiation values were similar among groups, the results exhibited more significant heterogeneity in VP-treated femurs.

These findings implicate YAP/TAZ signaling in bone formation and peri-lacunar mineral dynamics, dependent on local activity-associated mechanical cues.

# CD14 deficiency alters osteoclastogenesis and subchondral bone remodeling after joint injury in mice

Lance A. Murphy[1,2], Kevin G. Burt[1,2], Baofeng Hu[1,2], Vu Nguyen[1,2], Robert L. Mauck[1,2], Carla R. Scanzello[1,2]
[1]University of Pennsylvania, Perelman School of Medicine, Philadelphia, PA;
[2]CMC VA Medical Center, Translational Musculoskeletal Research Center, Philadelphia, PA
**Disclosures:** LAM (N) - Lance.murphy@pennmedicine.upenn.edu, BH (N), KGB (N), MW (N), VN (N), RLM (4, 5, 8), CRS (8)

**INTRODUCTION:** Osteoarthritis (OA) not only impacts cartilage within the joint, but it is also associated with bone changes such as subchondral sclerosis and osteophyte formation (1). Toll-like receptor (TLR) ligands have been implicated in the severity and progression of OA after tissue injury and with degeneration (2). CD14 is a GPI-anchored surface protein that is a co-receptor for several TLRs and is highly expressed in myeloid cell lineages, including the precursors of osteoclasts (OCs) (3,4). Notably, our group previously showed that CD14-deficient mice have less subchondral bone remodeling after joint injury (in a DMM (destabilization of the medical meniscus)-model of OA) (5). To understand the cellular activities underlying the differential bone remodeling observed after joint injury with CD14 deletion, we investigated how CD14-deficient OCs form *in vivo* and *in vitro*. ***We hypothesized that depletion of CD14 would protect against TLR4-dependent inhibition of osteoclastogenesis.***

**METHODS:** Destabilization of the medial meniscus (DMM): DMM or sham surgery (n=5 per group) was performed on male C57BL/6 (WT) and CD14$^{-/-}$ mice at 10-12 weeks of age. Histology (n=4-5 per group): Knees were harvested at 4 weeks post-DMM, then fixed, decalcified, and paraffin embedded. Tissue sections were stained with the Leukocyte Acid Phosphatase kit (Sigma-Aldrich). Focusing on the medial tibial plateau, cell number and trabecular surface area covered by OCs was measured across five 40X fields per mouse, and normalized by total trabecular surface area (ImageJ). Cell isolation and culture: For *in vitro* studies, bone marrow (BM) was pooled from the femora and tibiae of 3 mice for each strain (WT and CD14 knockout) mice. Cells were cultured in complete αMEM + 30 ng/mL M-CSF for 5 days to expand OC precursors. Cells were then replated and cultured with RANKL (100 ng/mL) to induce osteoclastogenesis over 4 days. LPS (1 ng/mL, to activate CD14/TLR4 signaling) and a small molecule TLR4 inhibitor (CLI-095), were added alone or in combination to some cultures. TRAP (tartrate-resistant acid phosphatase) staining and image analysis: Cells were stained for TRAP 3 or 4 days after addition of RANKL. Cells were imaged under 10X brightfield (5 images/well with 4 wells/timepoint), and OCs were identified by their TRAP staining and multinucleation. Images were quantified for percent area of the field covered with OCs (CellProfiler). Flow Cytometry (n=5-6): Freshly isolated BM cells, as well as BM cells that had been expanded for 5 days in M-CSF were analyzed by flow cytometry after staining for cell viability, and mAbs directed against CD45, CSF1R (CD115), and RANK. To quantify differences in bone marrow myeloid progenitor populations (common myeloid, megakaryocyte-erythroid, and granulocyte-macrophage progenitors), freshly isolated bone marrow was stained with a lineage cocktail for terminally differentiated cells, as well as mAbs directed against c-Kit, Sca1, CD34, CD150, and CSF1R and analyzed by flow cytometry. Statistics: Unpaired t-tests were used to test differences between groups. Holm-Sidak correction was employed when multiple t-tests were used.

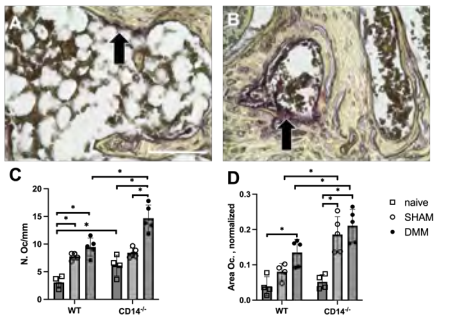


**Figure 1**: Representative pictures of TRAP staining in WT (**A**) and CD14-deficient (**B**) murine medial tibial plateaus 4 weeks post-DMM. Quantification of cell number (**C**) and trabecular surface covered by TRAP+ cells (**D**) normalized by trabecular surface area. *p<.05, scale bar = 100 µm.

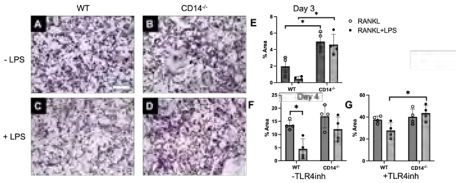


**Figure 2:** Representative images after 4 days of RANKL exposure of WT OC cultures without LPS (**A**) and with LPS (**C**) and CD14$^{-/-}$ OC cultures without LPS (**B**) and with LPS (**D**). Cell area on day 3 after RANKL with and without LPS **(E)**. Quantification of OC percent area on day 4 without TLR inhibition (**F**) and with TLR inhibition (**G**). *p<.05, scale bar = 100 µm.

**RESULTS:** Representative TRAP staining in WT (**Fig 1A**) and CD14$^{-/-}$ medial tibial plateaus (**Fig 1B**) are shown. OC number and trabecular area covered by OC increased in both strains after both sham and DMM surgeries (**Fig 1 C,D**), but were higher in both naïve and injured knees from CD14-deficient mice, indicating that OC presence increases both with injury as well as with CD14-deficiency *in vivo*. For our *in vitro* experiments, after 3 days of RANKL treatment, cells from CD14-deficient mice showed more osteoclastic differentiation than WT cells, both in the absence and in the presence of LPS (**Fig 2 E**). By day 4, WT and CD14-deficient OCs showed similar area coverage in the absence of LPS (**Fig 2F**). However when LPS was added, WT osteoclastogenesis decreased significantly by 67%, whereas CD14-deficient osteoclastogenesis decreased only by 29% and was not significant. In the presence of CLI-095, WT osteoclastogenesis decreased with the addition of LPS, whereas CD14-deficient osteoclastogenesis did not (**Fig 2 F,G**). Evaluating differences after expansion, flow cytometric analysis of culture expanded (but nondifferentiated) precursors revealed a slight increase in CSF1R positivity in CD14-deficient cells and freshly isolated bone marrow (**Fig 3A**). Interestingly, CD14-deficient precursors had less RANK positivity (**Fig 3A**). However, no difference in abundance of progenitor populations from freshly isolated BM was observed (data not shown). Within the myeloid progenitors, we found no difference in CSF1R (**Fig 3B**).

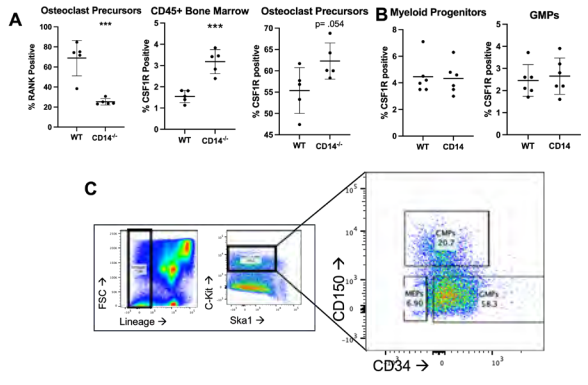


**Figure 3:** Percent positivity of CSF1R in osteoclast precursor expanded population, percent positivity of RANK in osteoclast precursor expanded population, percent positivity of CSF1R in bone marrow (A). Percent positivity of CSF1R in myeloid progenitor populations (B). Flow schematic for isolating myeloid progenitor populations (C). CMPs: Common myeloid progenitors, MEPs: megakaryocyte-erythroid progenitor, GMPs: granulocyte macrophage progenitor. *** p<.001

**DISCUSSION:** Our results show that CD14-deficient mice possess an increased presence of OCs in the medial tibial plateau both at baseline and 4 weeks after DMM or sham injury. Additionally, *in vitro,* CD14-deficient OC precursors differentiate into OCs faster than WT controls in response to RANKL, and were less sensitive to the effects of LPS. It has been shown that TLRs 1-9 are present in OC precursors and the activation of TLRs can decrease osteoclastogenesis (6). Analysis of bone marrow populations did not reveal differences in proportions of myeloid progenitor cells between strains, but did reveal a higher expression of CSF1R on OC precursors both at baseline (freshly isolated) and after exposure to M-CSF which may contribute to faster differentiation into OC. However, the decrease in RANK positivity on precursors was unexpected, and suggests that CD14 deficiency is modulating OC inhibitory pathways or activating RANK-independent mechanisms which can be explored in future work. Future work will explore the precise mechanism by which this occurs.

**SIGNIFICANCE/CLINICAL RELEVANCE:** It is possible that the protection from subchondral bone thickening observed in the DMM model (5) is due to the increased presence of OCs seen in the CD14 deficient mice. Understanding the role of CD14/TLR signaling in osteoclastogenesis may lead to new therapeutic strategies for diseases characterized by pathologic bone remodeling.

**REFERENCES:** [1] Donell, S *EFORT* 2019; [2] Miller, R+ 2019 [3] Zanoni, I+ *Front Cell Infect. Microbiol.* 2013; [4] Xue, J+ *Art Res Ther* 2020; [5] Sambamurthy, N+ *PLoS ONE 2018*; [6] Ding P+ *Bone Res* 2022

# Hypertrophic chondrocyte-autonomous roles of YAP/TAZ signaling in embryonic bone development

Christopher J. Panebianco[1,2], Joel D. Boerckel[1,2]
[1]Department of Orthopaedic Surgery, University of Pennsylvania, Philadelphia, PA
[2]Center for Engineering Mechanobiology (CEMB), University of Pennsylvania, Philadelphia, PA

**INTRODUCTION:** The appendicular skeleton forms through endochondral ossification, in which chondrocytes proliferate, undergo hypertrophy, and then are remodeled at the chondro-osseous junction to form bone.[1] Previously, we found that deleting the transcriptional regulators Yes-associated protein (YAP) and transcriptional co-activator with PDZ-binding motifs (TAZ) from Osterix (Osx)-expressing cells (YAP/TAZ cKO$^{Osx}$) caused bone fragility, perinatal lethality, growth plate hypertrophic zone (HZ) elongation, and a unique conical chondro-osseous junction.[2] Since Osx is expressed in both hypertrophic chondrocytes (HCs) and osteoblast-lineage cells, it remains unclear whether the growth plate phenotype was caused by HC-autonomous defects or by disrupted chondro-osseous junction remodeling. To address this, we established and characterized a collagen 10a1 (Col10)-specific YAP/TAZ conditional knockout (YAP/TAZ cKO$^{Col10}$).

**METHODS:** Mice featuring allele dosage-dependent deletion of YAP and TAZ in Col10-expressing cells (*i.e.*, HCs) were generated by crossing mice harboring loxP-flanked exon 3 alleles in both YAP and TAZ with Col10a1-Cre mice, which have tissue-specific activity in hypertrophic cartilage.[3] At postnatal day (P) 0, YAP/TAZ cKO$^{Col10}$ mice and Cre-negative wildtype (WT$^{fl/fl}$) littermates were harvested and imaged using microcomputed tomography (μCT) with X-ray intensity of 145 μA, energy of 55 kVp, integration time of 400 ms, and resolution of 10.4 μm. Harvested P0 mice were also stained with Alizarin red and Alcian blue for whole mount imaging. To explore the embryonic basis of potential phenotypes in YAP/TAZ cKO$^{Col10}$ mice, embryonic day (E) 17.5 mouse hindlimbs were harvested for paraffin-embedding and staining with Safranin-O/fast green. E17.5 hindlimbs were also harvested for cryo-embedding and immunostaining with YAP and TAZ to determine the efficiency and specificity of YAP/TAZ deletion in HCs. Student's t-tests were used to find significant differences between groups ($\alpha = 0.05$).

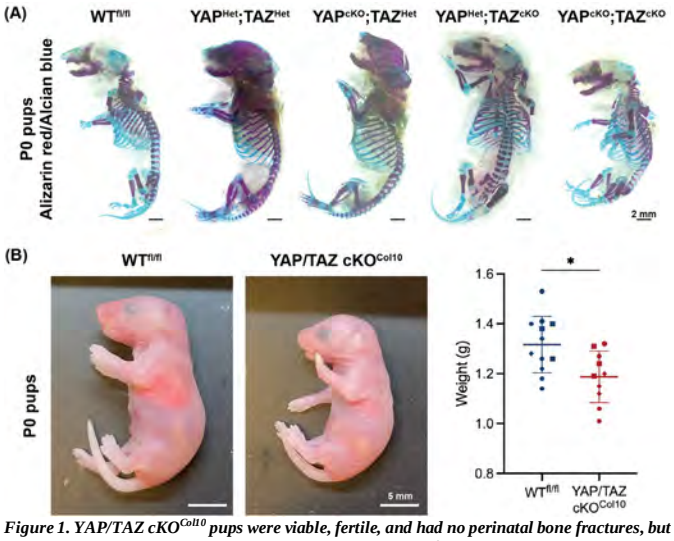


***Figure 1. YAP/TAZ cKO$^{Col10}$ pups were viable, fertile, and had no perinatal bone fractures, but were smaller than WT littermates. (A)*** *Whole mount images of P0 pups stained with Alizarin red and Alcian blue. WT = wildtype, Het = heterozygous, cKO = conditional knockout. Bar = 2mm.* ***(B)*** *P0 pups with mass. Bar = 5 mm. * = p<0.05.*

**RESULTS:** In contrast to YAP/TAZ cKO$^{Osx}$ mice, YAP/TAZ cKO$^{Col10}$ mice were viable, fertile, and had no perinatal bone fractures (**Fig 1A**). Whole mount imaging of P0 mice featuring allele dosage-dependent deletion of YAP/TAZ in Col10a1-expressing cells showed that heterozygous deletion of YAP and/or TAZ had little effect on skeletal formation. Thus, future analyses focused on homozygous YAP/TAZ cKO$^{Col10}$ mice and WT$^{fl/fl}$ littermates. Homozygous Col10a1-condition YAP/TAZ deletion reduced pup size and body mass at birth (**Fig 1B**), likely driven by reduced skeletal structure and bone volume (**Fig 2**). Next, we analyzed E17.5 embryos to better understand the embryonic basis of this phenotype. To determine the efficiency and specificity of YAP/TAZ deletion in HCs, we used immunostaining to quantify the numbers of YAP- and TAZ-expressing cells in the HZ and proliferative zone (PZ) of the E17.5 distal femur. YAP/TAZ cKO$^{Col10}$ mice exhibited significant reductions in the percentage of YAP$^{+}$ and TAZ$^{+}$ cells (60.0% and 57.7% reduction, respectively), but no significant change in the PZ. Through morphometric analysis of the developing proximal tibia, we found that YAP/TAZ cKO$^{Col10}$ mice had a normal flat chondro-osseous junction, but an elongated HZ and a shortened proliferation zone (PZ). YAP/TAZ deletion also decreased the distance between the tip of the proximal tibia and the start of the HZ (**Fig 3**).

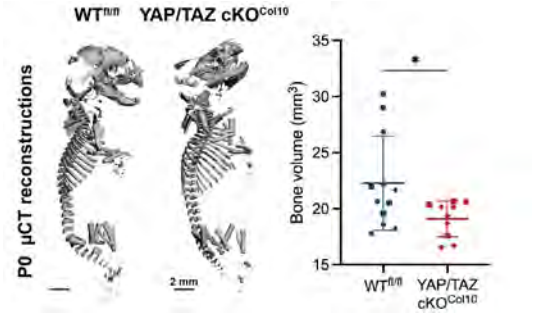


***Figure 2. YAP/TAZ cKO$^{Col10}$ pups had reduced bone volume compared to WT littermates.*** *P0 µCT reconstructions with bone volume quantification. Bar = 2 mm. * = p<0.05.*

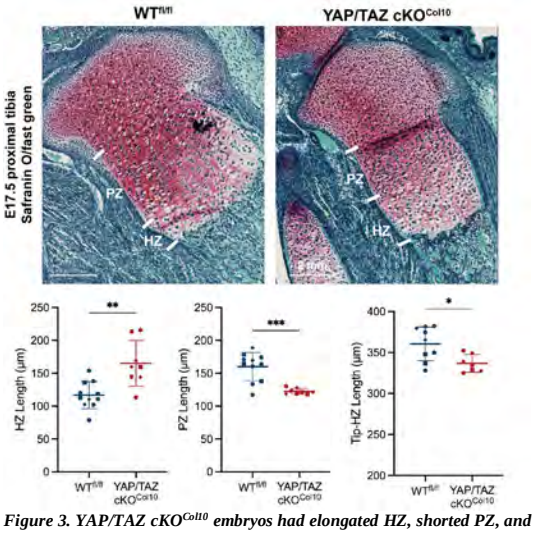


***Figure 3. YAP/TAZ cKO$^{Col10}$ embryos had elongated HZ, shorted PZ, and decreased Tip-HZ distance.*** *Safranin O/fast green stained E17.5 proximal tibia. HZ = hypertrophic zone, PZ = proliferative zone. Bar = 2 mm. * = p<0.05, ** = p<0.01, *** = p<0.001.*

**DISCUSSION:** Our results indicate an HC-autonomous contribution of YAP/TAZ signaling to endochondral ossification. Our previous work with YAP/TAZ cKO$^{Osx}$ mice suggested that deleting YAP and TAZ from both HCs and osteoblast-lineage cells impaired growth plate remodeling through both HC-autonomous and non-autonomous mechanisms.[2] Here, we demonstrate that the loss of YAP/TAZ signaling from HC's elongated the HZ and shortened the PZ of the developing growth plate, while also decreasing the distance between the tip of the tibia to the start of the HZ. Since YAP and TAZ expression was effectively suppressed in HCs, but not proliferating chondrocytes, these data indicate that loss of YAP/TAZ signaling in maturing chondrocytes induced precocious hypertrophy. Furthermore, the elongated HZ, with flat chondro-osseous junction, suggests there are defects in HC-autonomous remodeling, rather than vascular/septoclastic resorption. These phenotypes differ from YAP/TAZ cKO$^{Osx}$ mice, which had HZ elongation and a conical chondro-osseous junction. However, these phenotypes closely resemble those recently reported in collagen 2a1-specific YAP/TAZ conditional knockout (YAP/TAZ cKO$^{Col2}$), which showed that mice were smaller, displayed HZ elongation, and had a flat chondro-osseous junction without defects in PZ proliferation. Ongoing work will define the molecular mechanisms by which HC-autonomous YAP/TAZ signaling regulated hypertrophic initiation, maturation, and remodeling. Importantly, these data demonstrate that HC-autonomous YAP/TAZ signaling is necessary for proper endochondral ossification.

**SIGNIFICANCE:** This work is the first to demonstrate the HC-autonomous roles of YAP/TAZ signaling in embryonic bone development. Better understanding of how YAP and TAZ mediate endochondral ossification will help enhance treatment options for patients with developmental dysplasias and bone fractures.

**REFERENCES: [1]** Kozhemyakina+ *Development* 2015, **[2]** Collins+ *BioRxiv* 2023, **[3]** Gebhard+ *Matrix Biol* 2008, **[4]** Vanyai+ *Development* 2020

**ACKNOWLEDGEMENTS:** This work was supported by the CEMB, an NSF Science and Technology Center, under grant agreement CMMI: 15-48571.

# Developing an *in vitro* Osteochondral Micro-Physiological System for Modelling and Testing Therapeutics for Osteoarthritis

Kyra W. Y. Smith[1,2], Stephanie L. Fung[2], Hsin-Fang Wu[1,2], Irene Chiesa[2,3], Giovanni Vozzi[3], Carmelo De Maria[3], Riccardo Gottardi[1,2]
[1]University of Pennsylvania, Philadelphia, PA, [2]Children's Hospital of Philadelphia, Philadelphia, PA, [3]University of Pisa, Pisa, Italy
smithkw@chop.edu

**Disclosures:** Nothing to disclose for all authors.

**INTRODUCTION**: Musculoskeletal diseases are the leading cause of disability, and often affect a combination of tissues including bone, muscle, and cartilage **[1]**. Currently, animal models remain popular for musculoskeletal research, even though they may not accurately represent human biology **[2]**. However, poorly planned and inconsistent animal research wastes up to $24 billion per year **[3]**. *In vitro* models could be used to replace certain animal studies, but to be biologically relevant they must capture the three-dimensional nature of musculoskeletal tissues as well as their crosstalk. In this study, we develop a micro-physiological *in vitro* system that uses a biphasic bioreactor and multiple cell types and scaffolds to mimic native biology and crosstalk of the osteochondral unit of articular joints. We validate the efficacy of the model to emulate osteoarthritis (OA) by treating with inflammatory factors, and we then test relevant OA therapeutics. We show how our *in vitro* model can recapitulate cross talk across tissue types, enabling the testing of candidate therapeutics.

**METHODS:** *Seeding the Osteochondral Construct:* For the cartilage region, human bone-marrow derived mesenchymal stem cells (BM-hMSCs) are seeded in 5 %methacrylated gelatin (GelMA), 2.5 %methacrylated hyaluronic acid (HAMA), and 0.15% lithium phenyl-2,4,6-trimethylbenzoylphosphinate (LAP) for UV photo-crosslinking. Cartilage constructs are pre-differentiated for 28 days in chondrogenic medium containing 10ng/mL TGF-β3. For the bone region, BM-hMSCs are seeded onto a 3D printed 10 % GelMA, 50 % NanoHydroxyapatite, 0.2% genipin-crosslinked scaffold **[4]**. After osteogenic differentiation for 14 days with 10mM β-glycerophosphate and 10nM 1,25-dihydroxy vitamin D3, human umbilical vein endothelial cells (HUVECS) and BM-hMCSs (4:1 ratio) are seeded into the pores of the 3D printed scaffold in a 5% GelMA, 0.0025% fibrinogen, 0.00004% thrombin suspension crosslinked *in situ*, and cultured in 50:50 osteogenic and vasculogenic medium for another 14 days. The chondral and osseous components can be combined in the biphasic bioreactor prior to experiments. *Generating an Osteoarthritic Environment:* To cause inflammation in the differentiated construct, the cartilage constructs are treated with inflammatory cytokines for 7 days either alone, or while cultured in the bioreactor with the osseous constructs, using chondrogenic maintenance medium containing only 2ng/mL TGF-β3 and either: control (no additives), interleukin 1β (IL-1β) (20ng/mL), interleukin 6 (IL-6) (100ng/mL), tumor necrosis factor α (TNF-α) (1000ng/mL), combination of all three cytokines, or M1 macrophage conditioned medium (M1CM). *Analysis of Chondrogenesis and Cartilage Inflammation:* Chondrogenesis is assessed by RT-qPCR (*SOX9, ACAN, COL2*), histology, immunofluorescence (collagen II and aggrecan), and glycosaminoglycan (GAG) assay. The effect of pro-inflammatory treatments is assessed similarly with the addition of RT-qPCR for *MMP1, MMP3, MMP13, COL1, COL10*, and immunofluorescence for collagen I, and matrix metalloproteinase (MMP) assay. Osteogenic differentiation is assessed by Alizarin Red staining, RT-qPCR (*COL1, COL10, BSP2, RUNX2, ALP*), and immunofluorescence (collagen I, Runx2, ALP). Using GFP-HUVECs, vessel formation can be confirmed by microscopy.

**RESULTS SECTION:** *Cartilage Gels:* Chondrogenesis of the gels is shown in Figure 1. There is strong collagen II deposition in the matrix of the gel, and only cellular expression of collagen I. *Vascularized bone component:* There is strong calcium deposition in the osteogenic region of the scaffold, seen by Alizarin Red staining. Collagen I staining allows visualization of the vasculature formed by the HUVECS (Figure 1, white arrow) as well as matrix deposited by the osteogenic BM-hMSCs (Figure 1, yellow arrow). *Structure of Complete Osteochondral Construct:* The combined osteochondral construct shows region specific expression of bone and cartilage markers respectively (Figure 2). Masson's trichrome staining shows strong collagen deposition in both cartilaginous and osseous regions, with calcification visible in the osseous region. This is confirmed by collagen I and collagen II staining, the latter only in the cartilaginous region. Alcian blue staining shows GAG deposition in the cartilaginous region. This confirms the biphasic bioreactor supports osteochondral constructs and a separate cartilaginous and vascularized osseous region reminiscent of the osteochondral junction in articular joints.

**DISCUSSION:** Our preliminary data show that we have successfully developed a multi-tissue micro-physiological system simulating OA. Moving forward, we will probe the role of the osseous region in regulating cartilage response to pro-inflammatory stresses by comparing responses with and without the osseous region. Additionally, we aim to use this system to test OA therapeutics like Rapamycin and TNF inhibitors. A limitation of the current study is that the inflammatory conditions are not fully validated to represent the articular environment. To further validate our model in this sense, we plan to either perfuse the system with synovial fluid from OA patients.

**SIGNIFICANCE/CLINICAL RELEVANCE:** Using a micro-physiological system to test therapeutics for OA prior to animal studies can both minimize the number of animals required for preclinical testing and save on animal costs. These advance *in vitro* systems will help advance knowledge of musculoskeletal diseases development as well as allow rapid testing of potential therapeutics for treatment.

**REFERENCES:** **[1]** Selected Health Conditions and Likelihood of Improvement with Treatment. (2020). *National Academies Press.* **[2]** Allen, M. J. *et al.* (2017). *Journal of Orthopaedic Research*, 35(4), 740–751. **[3]** Little, C. B., & Hunter, D. J. (2013). *Nature Reviews Rheumatology* 9(8) 485–497. **[4]** Irene Chiesa *et al.* (2020**)** *Biofabrication* 12 025013.

**ACKNOWLEDGEMENTS:** Support from the Children's Hospital of Philadelphia Research Institute (RG), Ri.MED Foundation (RG), NIH T32-AR007132 (KWYS) and P30 AR069619, and the Fontaine Fellowship (KWYS). Thanks to the Penn Center for Musculoskeletal Disorders and CFD-Research.

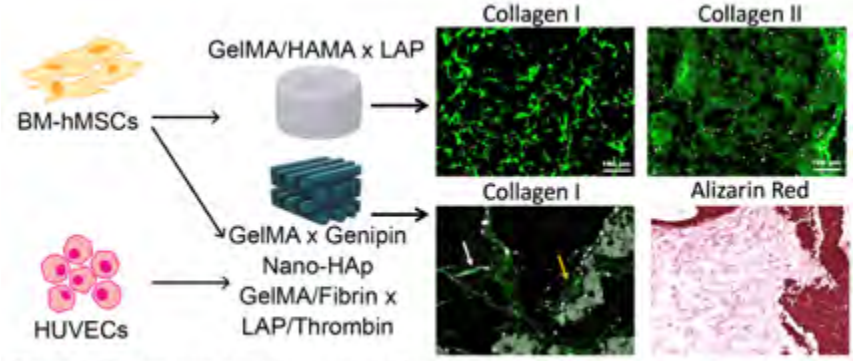


*Figure 1: The separate components accurately represent cartilage and bone respectively.*

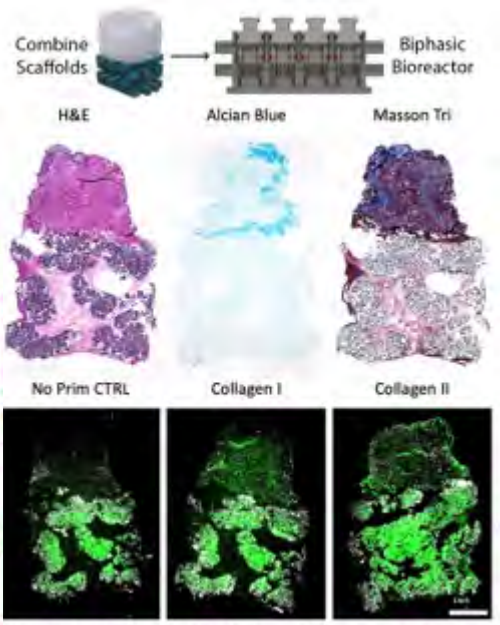


*Figure 2: Tissue specific differentiation in the bioreactor.*

Penn Center *for* Musculoskeletal Disorders

University *of* Pennsylvania

# Other Research
# (No P30 Core Use)

# Pre-Clinical Large Animal Model of Thoracic Insufficiency using Yucatan Mini Pig

Rachel Butler[1], Klaus Hopster[1], Madeline Boyes[1], Benjamin Sinder[2], Patrick Cahill[2], Brian Snyder[3], Thomas Schaer[1]
[1]University of Pennsylvania School of Veterinary Medicine, Kennett Square PA, [2]Children's Hospital of Philadelphia, Philadelphia PA, [3]Boston Children's Hospital, Boston MA
rmbutler@upenn.edu

**Disclosures:** Thomas Schaer (1-PSI, 1,3B,4,5-ReGelTec, 3B-Peptilogics, 3B,4,5-Acuitive Technologies, 3C-PAX Therapeutics, 3C-OrimTech, 3C,5-SINTX Technologies, 3C-OsteoCentric Technologies, 5-DePuy Synthes, 5-Alcyone Therapeutics, 5-Camber Spine, 6-Heraeus), Brian Snyder (3B-Orthopediatrics)

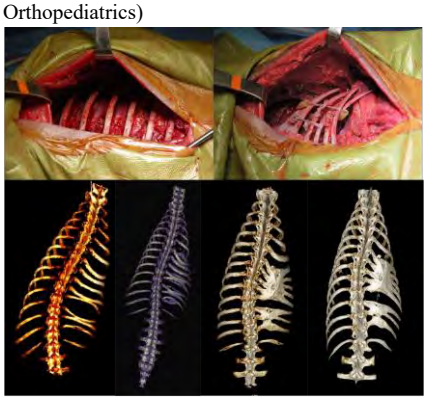


**Figure 1**. Tethering right hemithorax, ribs 5-12 (top). 3D rendering of tether-induced pathoanatomy (bottom).

**INTRODUCTION:** Thoracic Insufficiency Syndrome (TIS) represents a novel form of postnatal pulmonary hypoplasia and restrictive respiratory disease that occurs in children (<10 yrs.) with congenital or acquired anomalies of the spine and thorax [1]. These constrictive malformation of the thorax limit the space available for the lungs to grow and hinder pulmonary function, manifest clinically as: 1) hypoventilation ($\uparrow CO_2$) - the result of mechanically restricted chest wall and diaphragmatic motion; 2) impaired respiration ($\downarrow O_2$) – the result of impaired lung development with retardation of alveolarization, neovascularization and increased septal wall thickness, which increase the alveolar-arterial gradient (A-a $\nabla$) and impede $O_2$ exchange. We previously developed a rabbit model of TIS by tethering the rib cage in very young rabbits to create a thoracogenic scoliosis to parametrically evaluate the effect of thoracic deformity on the growth and development of the lung and impact on pulmonary function [2]. Similar to children, with increasing deformity there was a decrease in lung mass, and pulmonary function (↓functional residual capacity and ↓forced vital capacity). However, the diminutive size of the rabbit model prevented evaluation of clinically relevant implants and surgical interventions to mediate the life-threatening effects of TIS, diminishing its translational value. The purpose of this study was to develop a pre-clinical mini pig model of TIS induced by tethering the rib cage, similar to the rabbit model. **METHODS:** Under IACUC approval two ♀ 8-week-old Yucatan mini-pigs weighing 8 kg were used (n=1 tethered animal, TA; n=1 age-matched control, AMC). After endotracheal intubation and general anesthesia induction, the pig was positioned in left lateral recumbency. A longitudinal incision was made along the dorsal angle of ribs 5-12 to expose the ribs without disrupting the parietal pleura. Ribs were divided into three groups (cranial, mid, caudal) and tied together with fiberwire (**Fig. 1**). The incision was closed in layers. Pigs recovered in a high-oxygen environment, monitored closely by veterinary staff, maintained on an extensive analgesic regime for the first 72 hours. *Imaging*: Pigs were anesthetized for serial CT scans (OmniTom® 8-slice small-bore mobile CT): pre-operative, every other week to 32 weeks postoperatively, then @ 37, 44, 52, 64, and 68 weeks postoperatively to document progressive thoracic deformity and corresponding lung hypoplasia. The extent of scoliosis was measured as the Cobb angle on the coronal plane CT reconstruction ($\theta_S$) and the extent of kyphosis as the Cobb angle on the sagittal plane CT reconstruction ($\theta_K$). The mean lung volume (MLV) was calculated from segmented CT images using standardized thresholds to differentiate aerated lung tissue sequentially from 2 to 68 weeks (**Fig. 2**) [3]. *Pulmonary Function:* Following endotracheal intubation, animals were ventilated under volume-controlled ventilation mode, with inspiratory-to-expiratory ratio of 1:2, tidal volume of 10 mL/kg, respiratory rate adjusted to maintain an end-tidal $CO_2$ tension of 35-40 mmHg. Airway pressures were measured using a Pitot-based flow meter connected between the orotracheal tube and the Y-piece of the breathing system. Dynamic lung compliance, Cdyn, was calculated from the slope ($\Delta V/\Delta P$) of the inspiratory pressure-volume respiratory flow loops. **RESULTS**: Tethering ribs comprising the right hemi-thorax induced a convex left kyphoscoliosis ($\theta_S$=27.5°; $\theta_K$=17.8), with progression of the kyphotic deformity ($\theta_S$=25.0°; $\theta_K$=38.4° @ 68 weeks). 3D lung renderings revealed differences in morphology at 2 weeks for TA compared to AMC **(Fig 2A, B, E)**; however, by 20 weeks, the lung morphology of the TA had corrected **(Fig 2C, F)**, and by 68 weeks, the lung morphologies of TA vs. AMC were similar **(Fig 2D, G)**. MLV steadily progressed over time with thoracic growth. There was a notable difference in MLV of the TA when compared to the AMC over weeks 2 to 20; however, starting at week 22, the MLV of the TA was equivalent to the AMC. At 68-weeks, MLV for AMC=1523.3 $cm^3$ vs. for TA=1454.0 $cm^3$ **(Fig. 2H).** Rib tethering most affected respiratory mechanics: @ 2 weeks, Cdyn for TA was similar to AMC (29 vs. 28 $mL/cmH_2O$, respectively), but @ 6 weeks respiratory compliance diminished for TA relative to AMC (Cdyn=32 vs. 39 $mL/cmH_2O$, respectively), and remained unchanged at ~32 $mL/cmH_2O$ through 68-weeks, whereas AMC Cdyn continued to progress to ~48 $mL/cmH_2O$ @ 20 weeks, then plateaued through 68-weeks **(Fig 2J)**. Thus, despite normalization of MLV, there was a loss of compliance as a result of a constricted (stiff) chest wall induced by rib tethering. Intermittent positive pressure ventilation (IPPV), used clinically to expand the lungs, increased Cdyn by more than 65% for AMC @ 68 weeks, while IPPV increased Cdyn for TA by only 15% @ 68 weeks. In contrast flow-controlled expiration (FLEX) increased Cdyn for AMC from 28 to 62 $mL/cmH_2O$ @ 68 weeks, but also increased Cdyn for TA from 28 to 58 $mL/cmH_2O$. **(Fig. 2I).**

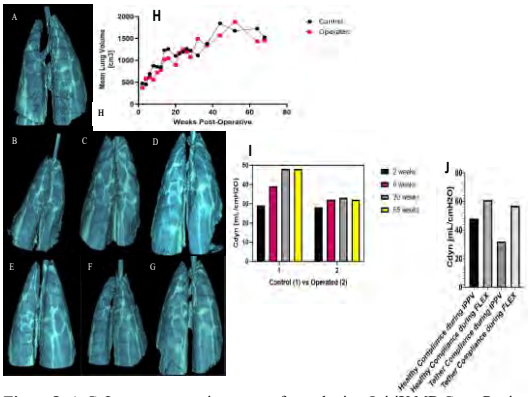


**Figure 2:** A-G: Lung segmentation was performed using OsiriX MD Grow Region software program: Threshold Interval algorithm with 3D region growing enabled. A HU interval of 1000 (range: seed point HU – 500 to seed point HU +500) was used. The resulting VOI was examined for gross errors prior to rendering the VOI as a 3D object to measure total volume. One segmentation was used to generate the entire lung VOI data set. A: Preoperative MLV TA; B: 2-week TA; C: 22-week TA; D: 68-week TA; E: 2-week AMC; F: 22-week AMC; G: 68-week AMC; H: MLV 2-68 weeks postoperative for TA compared to AMC. I: 68-week Cdyn of TA and AMC during IPPV and FLEX; J: TA and AMC Cdyn at 2, 6. 20, and 68 weeks.

**DISCUSSION:** Like children with TIS, despite normalization of overall lung volume and morphology, the result of compensatory hypertrophy of the unrestricted lung, constricting the chest wall by tethering the ribs decreased respiratory compliance in the Yucatan mini-pig model. Non-surgical treatment of TIS often requires nocturnal positive pressure ventilation, and the reduced respiratory compliance affected IPPV more than FLEX. Conventional volume-controlled ventilation is achieved by active inflation of the lungs followed by passive (elastic recoil) emptying during expiration. In contrast, FLEX ventilation is a procedure that modulates the passive expiratory phase. Reducing the initial high-expiratory peak flow to a more linear flow potentiates and prolongs the expiratory flow phase. Thus FLEX results in "energy preservation" during expiration. As such FLEX appears to better compensate for decreased respiratory compliance than IPPV by stabilizing dependent areas of the lung and preventing premature bronchial tree collapse during expiration. The exact mechanism of how this is achieved requires further investigation, including differentiating chest wall compliance from lung parenchyma tissue compliance and histological evaluation of the bronchial and alveolar morphology. **CLINICAL RELEVANCE/SIGNIFICANCE:** Developing a large pre-clinical animal model for TIS as a testing platform to evaluate normal respiratory development, the pathoanatomy associated with thoracic insufficiency and to parametrically evaluate the efficacy of different treatment strategies to ameliorate TIS is fundamental to reducing the morbidity and mortality of TIS.

**REFERENCES:**[1] Campbell et al, JBJS, 85A:399, 2003. [2] Olson et al**.** Spine, 43(15):E877-E884, 2018. [3] Busse et al. Med. Phys, 40:122503, 2013

**ACKNOWLEDGEMENTS:** This research was supported by The Wyss/Campbell Center for Thoracic Insufficiency (Children's Hospital of Philadelphia)

# Raman Arthroscopy for *In vivo* Quantitative Monitoring of Cartilage Composition in Equine Stifle Joint

Madeline Boyes[2], Erik E Ersland[1], , Keming Yan[1], Hsin Han[3], J. Todd Lawrence[4], Thomas P Schaer[2],
Mark W Grinstaff[1], Brian D Snyder[5], Mads S Bergholt[6], Michael B Albro[1]
[1]Boston University, MA; [2]University of Pennsylvania Department of Clinical Studies New Bolton Center, PA; [3]Drexel University, PA; [4]The Children's Hospital of Philadelphia, PA; [5]Beth Israel Deaconess Medical Center, MA; [6]King's College London, UK

**Introduction:** Hyaline cartilage is a viscoelastic, biphasic, composite material optimized for its mechanical performance, comprised of a type-II collagen (COL) fibril network (5-20% wet weight) that affords structure and tensile strength to constrain a negatively charged sulfated glycosaminoglycan (GAG) hydrogel matrix (5-15% wet weight) that retains interstitial water (interstitial fluid load support, *IFLS*). These components act synergistically, bestowing the compressive, rheological and tribological material properties essential to cartilage function. Osteoarthritis (OA) is an incapacitating condition in which hyaline cartilage progressively breaks down as a consequence of mechanical overloading that promulgates structural failure (fissuring/fibrillation/superficial zone delamination), tissue swelling, GAG depletion and COL network derangement. GAG depletion reduces *IFLS*, transferring load to the COLII fibril network, which subsequently breaks down, culminating in increased hydraulic permeability, decreased cartilage stiffness and lubricity. Development of disease-modifying OA therapies is impeded by a lack of non-destructive clinical assessments of cartilage composition and mechanical properties germane to tissue function. Quantitative MRI (T1r, T2*) and arthroscopic-based cartilage grading (Outerbridge) are only moderately correlated with metrics characterizing cartilage composition and material properties[1]. Raman spectroscopy is an inelastic optical light scattering technique that provides an optical fingerprint of a tissue's molecular building blocks, allowing quantification of the predominant molecular constituents of cartilage (GAG, COL, $H_2O$) that account for the material properties intrinsic to its function. We developed a novel Raman spectroscopy needle probe and real-time spectral analysis platform capable of performing both benchtop *ex vivo* and arthroscopic *in vivo* measurement of ECM-specific compositional biomarkers for cartilage with a high degree of accuracy[2] ($R^2$=0.8-0.94). Using phantoms comprised of prescribed proportions of GAG, COL and H2O that serve as biochemical standards, absolute measures of cartilage content can be derived from the Raman spectra[3]. Here we demonstrate that *in-vivo*, real-time Raman spectroscopy performed in the operating room using a needle probe to measure cartilage composition at discrete anatomical sites along the equine trochlear groove provided compositional data equivalent to *ex vivo* analysis performed on an excised equine trochlear groove and validated by biochemical assay. **Methods**: A custom *Raman probe* (In Photonics) coupled to a threaded needle tip (∅2.75mm) with a distal 2mm sapphire ball lens (AWI), fiber-coupled to a 785nm laser (100mW output; IPS), and high-performance spectrometer (Eagle; Ibsen). The spectrometer, laser, and a computer were battery-powered allowing for portability. High SNR *Raman spectra* in the fingerprint (800-1800 cm-1) and high wavenumber (2700-3800 cm-1) ranges were acquired @ 5 sec integration time. Spectra were preprocessed via background subtraction and area-under-curve normalization. The cartilage spectra (800-1800$cm^{-1}$) was fit to a multivariate linear regression model: $\mathbf{Cart_{Spectra}}=GAG_{Score}*(\mathbf{GAG_{REF}})+COL_{Score}*(\mathbf{COL_{REF}})+H_2O_{Score}*(\mathbf{H_2O_{REF}})$, where $\mathbf{GAG_{REF}}$, $\mathbf{COL_{REF}}$, and $\mathbf{H_2O_{REF}}$ are the reference spectra of purified chemicals for each ECM constituent; the "scores" are the regression coefficients reflecting the relative contribution of each constituent (Fig.2A,B). The high-wavenumber range spectra (2700-3800$cm^{-1}$) was used to compute the area under the OH peak, reflecting tissue hydration[4]. The Raman spectral analysis was performed in real time, with ECM biomarker scores and quality metrics displayed to the operator via a custom GUI. Tissue phantoms comprised of prescribed ratios of GAG (chondroitin sulfate [0-10%w/v]), COL (gelatin [0-20%w/v]), and H2O (PBS [70-100%w/v]) were used to convert Raman scores to equivalent %w/v by applying a 2nd order polynomial function of Raman scores fit to the known %w/v of the tissue phantoms to map "scores" and derive %w/v estimates of ECM composition[3]. *In Vivo Spectra Analysis*: After IACUC approval Raman needle probe spectral analysis was performed on the vertical wall of the lateral trochlear groove of two 5-year-old TB horses through a 5–6 cm mini-arthrotomy between and parallel to the middle and lateral patellar ligaments before and after creating two 15mm focal defects removing uncalcified and calcified cartilage down to the subchondral bone (Fig 1). The needle tip was autoclave and the optics draped in sterile plastic film. Measures were performed at defined anatomical sites using a thin PDMS template with 4mm diam. holes at discrete sites along a defined polar coordinate system overlaying the trochlear facet. At each site, the probe lens gently contacted the cartilage surface, with spectra acquired over a 5 sec integration time. *Ex-vivo validation*: 3mm full thickness cartilage plugs were harvested at 169 discrete anatomical sites over the surface of an excised 5-y/o equine femoral trochlear groove. The composition of each plug was determined by Raman spectral analysis and DMMB GAG assay. **Results:** Raman derived biomarkers accounted for 78% of the variance in GAG content (Fig 2E) and depicted a biochemical spatial gradient along the length of the trochlear groove, with GAG content increasing and $H_2O$ content decreasing from distal to proximal (Fig 2A-D). In the surgical setting, the needle probe achieved high quality spectral acquisition of cartilage, as evidenced by a high SNR and the strong fit of the multivariate regression model to the $\mathbf{Cart_{Spectra}}$ ($R^2$=0.93+/-0.03). *In-vivo* Raman GAG measures exhibited a similar range and spatial distribution as the *ex vivo* analysis (Fig 3). **Discussion**: This study establishes the capability of our Raman arthroscopic platform to achieve accurate quantitative *in vivo* measures of the biochemical content of cartilage in the surgical setting. The analysis is fully automated within a Matlab GUI, which provides the clinician real time measurement of tissue composition, allowing diagnostic assessments at defined anatomical sites. The accuracy of ECM composition calculated from the *in-vivo* Raman spectral analysis is supported by *ex vivo* measures of tissue composition at discrete anatomical sites over the equine trochlea, where Raman derived GAG measures accounted for 78% of the variation in GAG content. While Raman derived GAG %w/v underestimated the GAG content by ~20% (Fig.2E), this is attributable to some disparately between the regions of Raman probe interrogation (~300μm depth of penetration) vs. the full thickness cartilage plug used for DMMB assay. The successful implementation of this platform *in-vivo* supports the use of Raman arthroscopy to objectively monitor standardized biomarkers that reflect cartilage function in health and disease and to (non-destructively) longitudinally monitor the efficacy of OA treatments that preserve or regenerate the cartilage ECM in pre-clinical animal models and human clinical trials. We will perform Raman arthroscopy assessments of the regenerate tissue generated by micro-fracture at the chondral defects at 3 & 6-month follow-up on these horses, providing the first-ever longitudinal *in vivo* Raman assessment of tissue response to a chondroregenerative therapy. **Significance**: This work supports the use of Raman spectroscopy acquired through needle probes as a clinical tool to perform comprehensive diagnostics of the composition of articular cartilage in health and disease and as a non-destructive tool to monitor the tissue response to chondroprotective and chondroregenerative therapies *ex-vivo*, *in-vivo* and clinically using Raman arthroscopy. **References**:[1] Li X+ 2011, Magn Res Imag. 29(3). [2] Kroupa KR+ 2021 JOR. [3] Ersland E+ 2023 SB3C (No.461) [4] Unal M+ 2018 Osteoarthritis Cartilage; 27(2):304-313.[5]Kazemi et. al. 2023 ORS Ann. Mtg.(#339). **Acknowledgements**: Supported by NIAMS AR081393, the Arthritis Foundation, MTF Biologics, Coulter—Drexel Translational Research Partnership Program, Institute for Medical Translation New Bolton Center, and the Boston University MSE Innovation Award.

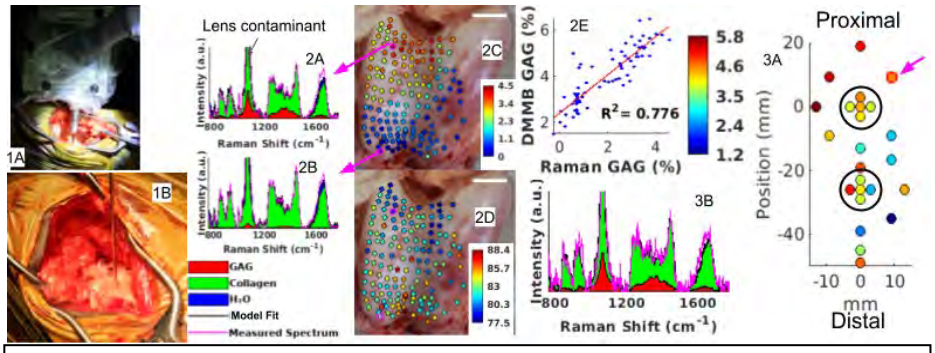


**Fig 1**: (**A**) Probe in contact with trochlea surface. (**C**) PDMS location guide aligned to tissue coordinate system.
**Fig 2:** (**A,B**) Representative 2D stacked area plot of cumulative contribution of ECM constituents to measured Raman spectra for GAG replete and depleted ex vivo tissue regions. *Ex vivo* Raman biochemical mapping of (**C**) GAG and (**D**) $H_2O$ contents (% wet weight) over surface of equine trochlea. 20mm scale bar. (**E**) Regression Raman biochemical analysis vs. DMMB GAG content. **Fig 3**: (**A**) *In vivo* Raman biochemical mapping of GAG content over surface of equine trochlea. Chondral defects (made after measurement) marked. (**B**) 2D stacked area plot of cumulative contribution of ECM constituents to *in vivo* Raman

# Exploring the Role of YAP/TAZ, MAPK, and WNT Signaling Pathways in Late Tendon Development: A Transcriptomic Analysis

Maria L. Canonicco Castro, Benjamin E. Peterson, Spencer E. Szczesny
The Pennsylvania State University, University Park, PA
mjc7530@psu.edu

**DISCLOSURE:** We have no disclosures.

**INTRODUCTION**: Tendons are essential connective tissues that transmit the force created in the muscle to the bone making joint movement possible. Given that tendon and ligament injuries constitute approximately 25% of all musculoskeletal injuries, there is significant clinical interest in developing a tissue engineered construct that can replicate the mechanical and biological functions of tendons. No tissue engineered construct has successfully mimicked mature tendon structure and function[1]. Scaffold-free constructs built through cell self-assembly have been able to replicate the mechanical and structural properties of early embryonic tendon, but they fail to match the rapid increase of structural and mechanical properties that occur during late tendon development[2,3]. A critical barrier hindering the development of tendon constructs is the lack of knowledge regarding the mechanobiological signaling pathways driving late tendon development. The objective of this study was to obtain unbiased information of the signaling pathways involved in late tendon development via RNA sequencing, differential gene expression analysis, gene ontology and pathway enrichment analysis. Our hypothesis was that during late development the mechanotransduction events driving the maturation of tendons transition from cell-cell to cell-matrix interactions, thus resulting in an increase of integrin signaling pathways and the activation of different mechanotransduction pathways.

**METHODS:** Following IACUC approval, flexor digitorum longus (FDL) and flexor digitorum brevis (FDB) digit II tendons were harvested from the hindlimbs of 18 white leghorn chicken embryos at embryonic day 16 and 20 (E16 and E20). Samples were prepared in triplicate for E16 and E20 timepoints. Each individual sample contained 8 tendons: two FDL and two FDB from the hindlimbs of two animals. Animals were sacrificed via decapitation, and the samples were immediately snap frozen in liquid nitrogen. Samples were stored in -80°C until they were shipped in dry ice for analysis. *RNA Sequencing*: Sequence reads were trimmed and mapped to the Gallus Gallus 5.0.90 reference genome. Unique hit counts were calculated and normalized by the total sample reads. *Gene Expression Analysis*: Using DESeq2, gene expression was compared between the E16 and E20 groups. The Wald test was used to generate p-values and log2 fold changes. Genes with an adjusted p-value < 0.05 and absolute log2 fold change > 1 were selected as differentially expressed genes (DEGs) for each comparison. *Gene Ontology and Pathway Analysis:* Enrichment analysis was conducted using the Database for Annotation, Visualization, and Integrated Discovery (DAVID). For gene ontology (GO), overrepresentation of DEGs within specific biological processes was assessed. Pathway enrichment analysis focused on identifying pathways enriched with DEGs. For pathway enrichment analysis, we used a non-adjusted p-value threshold of < 0.1, while for gene ontology (GO) terms, an adjusted p-value < 0.1 was applied. The statistical significance of enriched terms and pathways was determined using the hypergeometric test.

**RESULTS:** DESeq2 data showed a significant upregulation of the YAP/TAZ target genes CTGF and CYR61 in the E20 samples compared to E16. Additionally, GO and pathway analysis revealed a significant enrichment of DEGs in processes related to cell division, cell adhesion, regulation of ion transmembrane transport, intracellular signal transduction, and cellular response to transforming growth factor beta stimulus between E16 and E20. In addition, the pathway analysis showed an enrichment of the focal adhesion, MAPK and WNT pathways, suggesting their involvement in late tendon development.

**DISCUSSION:** This study investigated the mechanobiological signaling pathways involved in late tendon development, which enabled us to identify target genes that might be involved in the maturation of the structural and mechanical properties of embryonic tendons. The significantly enriched GO terms intracellular transduction and cellular response to transforming growth factor beta stimulus between E16 and E20 timepoints, along with the enrichment of the focal adhesion pathway, supports our hypothesis that there is a shift in mechanotransduction events during late tendon development. Additionally, the upregulation of CTGF and CYR61 differential expression from E16 vs E20 suggests that YAP/TAZ signaling might play a role in late tendon development. These results are comparable to previous data showing an increase in CTGF expression during early stages (E11 to E17) of tendon development[4]. In addition, the pathway enrichment analysis identified WNT and MAPK signaling as additional potential regulatory pathways involved in late tendon development. These results are supported by the fact that FGF signaling through the extracellular signal-regulated kinase (ERK) cascade has previously been demonstrated as an essential regulator of animal development[5–7], and as a downstream signaling of mechanical forces to regulate tendon differentiation during chick limb development[8,9]. Moreover, Wnt signaling pathway has also been previously identified as a key player in the process of tendon development[9–11]. However, the role of YAP/TAZ, MAPK and WNT signaling in late tendon development is still not completely understood. Future studies will include protein assays that will confirm the presence of these pathways in late tendon development, and functional assays that will determine the effect of YAP/TAZ, MAPK and WNT signaling pathways on the structural and mechanical maturation of late embryonic tendons.

**REFERENCES: 1.** Lomas, A. J. *et al.* The past, present and future in scaffold-based tendon treatments. *Adv Drug Deliv Rev* **84**, 257–277 (2015). **2.** Kalson, N. S. *et al.* An experimental model for studying the biomechanics of embryonic tendon: Evidence that the development of mechanical properties depends on the actinomyosin machinery. *Matrix Biology* **29**, 678–689 (2010). **3.** McBride, D. J., Trelstad, R. L. & Silver, F. H. Structural and mechanical assessment of developing chick tendon. *International Journal of Biological Macromolecules* **10**, 194–200 (1988). **4.** Yeung, C.-Y. C. *et al*. Chick tendon fibroblast transcriptome and shape depend on whether the cell has made its own collagen matrix. *Sci Rep* **5**, 13555 (2015). **5.** Corson, L. B., Yamanaka, Y., Lai, K.-M. V. & Rossant, J. Spatial and temporal patterns of ERK signaling during mouse embryogenesis. *Development* **130**, 4527–4537 (2003). **6.** Dorey, K. & Amaya, E. FGF signalling: diverse roles during early vertebrate embryogenesis. *Development* **137**, 3731–3742 (2010). **7.** Patel, A. L. & Shvartsman, S. Y. Outstanding questions in developmental ERK signaling. *Development* **145**, dev143818 (2018). **8.** Havis, E. *et al.* TGFβ and FGF promote tendon progenitor fate and act downstream of muscle contraction to regulate tendon differentiation during chick limb development. *Development* **143**, 3839–3851 (2016). **9.** He, P. *et al*. Comparison of Tendon Development Versus Tendon Healing and Regeneration. *Frontiers in Cell and Developmental Biology* **10**, (2022). **10.** Walia, B., Li, T. M., Crosio, G., Montero, A. M. & Huang, A. H. Axin2-lineage cells contribute to neonatal tendon regeneration. *Connective Tissue Research* **0**, 1–14 (2022). **11.** Garcia-Lee, V., Díaz-Hernandez, M. E. & Chimal-Monroy, J. Inhibition of WNT/β-catenin is necessary and sufficient to induce Scx expression in developing tendons of chicken limb. *The International Journal of Developmental Biology* **65**, 395–401 (2020).

# Bubbler Design for Altering Media Oxygen Saturation

Margaret Capalbo, Spencer Szczesny
The Pennsylvania State University, University Park, PA

**Introduction:** Previous work in our lab found that tendon degeneration due to fatigue-loading occurs only in hypoxic conditions (3% oxygen). Physiologic oxygen saturation of rodent Achilles tendons is 8%, however atmospheric oxygen is 21%[1]. When imaging Achilles tendons on a confocal microscope, the tendons are exposed to atmospheric oxygen, which changes their response to fatigue-loading. For experiments occurring within our incubator, we can change the oxygen saturation within the incubator by pumping in nitrogen, but it takes 24 hours to prime. A system that provides a quick change in oxygen saturation of media holding an Achilles tendon sample is needed. The objective of this project is to design a nitrogen bubbler that adjusts oxygen saturation of media to provide a physiologically accurate environment for Achilles tendon samples.

**Methods:** *Design:* A nitrogen tank with a gas regulator, a nitrogen flow rate indicator, and a 12V AC power supply were available in the lab. A 1000ml glass bottle with a four-port lid was chosen to be the reservoir (the location of media deoxygenation). Two tubes for media and a tube with a 16G needle for nitrogen were threaded through the ports into the bottle. The fourth port was left open to allow oxygen to escape and not build dangerous pressure within the reservoir. Two peristaltic pumps with an inner diameter (ID) of 3mm, an outer diameter (OD) of 5mm, and a flow rate range of 0-150ml/min were acquired to move the media throughout the system. Each pump was put in a series circuit with a 100-ohm potentiometer that can change the pumps' flow rates between 0-100% of the maximum flow rate. Tubing (ID 3/16" and OD 5/16") connected the reservoir to the pumps to the basin (point of sample). The basin was placed within the container of a microtensile device, which is placed on the confocal microscope for imaging. The volume of the microtensile device's container is 120 ml. To keep the sample hydrated, only enough media to cover the viewport is needed (about 3ml). Therefore, the basin restricts the volume that media can access, which helps with deoxygenation. Optimization of volume and size of the basin was needed, and each iteration was 3D printed. Each design was developed with SolidWorks. *Optimization:* There were four variables that required optimization to achieve the desired oxygen level: flow rate of nitrogen into the media, the flow rate of the pumps moving the media, the total volume of media in the system, and the size of the basin, which is exposed to the atmosphere. The flow rate of nitrogen was limited to 30-70 cfh being changed at 2.5cfh due to the measurement ability of the flow rate indicator. The peristaltic pumps used had a maximum flow rate of 150 ml/min and were connected to potentiometers which reduced the flow rate to the percentage of the maximum at which they were set. 100ml, 200ml, and 300ml of media were run through the system at the same settings. The oxygen level achieved in the basin was measured and compared between the amounts. The basin size was adjusted by changing the shape of the basin (a shelf was added in to allow space for the grips of the microtensile device, height of shelf was altered, etc.) and the width and length of the opening within the basin. Measurements were adjusted based on whether volume and/or surface area should be increased or decreased. *Oxygen Measurement:* To determine the oxygen saturation of the media, a PyroScience OXF1100 oxygen sensor, which is connected to the PyroScience FireSting-O2 oxygen meter and working in conjunction with a PyroScience Pt100 temperature probe, was used. Data is collected through the software Pyro Workbench and analyzed on Pyro Data Inspector. Data is collected continuously during the period between logging start and logging stop. Calibration of the upper limit of the oxygen sensor is completed by filling a beaker with air-saturated water, equaling 100% oxygen saturation. The sensor arrives calibrated for the lower bound at the factory, however OXCAL capsules are available, which deoxygenate deionized water for a 0% oxygen saturation measurement. The sensor and probe are fully submerged in media in the container they are measuring (basin or reservoir).

**Results:** Overall, the basin went through 5 iterations. In order, their volumes were 12.15ml, 18.6ml, 32.8ml, 19.2ml, and 10.83ml and their surface areas were 8.10cm$^2$, 15cm$^2$, 24cm$^2$, 15cm$^2$, and 8.15cm$^2$, respectively. The final shape of the basin was a slim rectangle with a step going across half of one side. The overall height was 15mm and the step height was 8mm. The step length was 25mm. A hole was also added to either end to hold the tubing in place. The system requires 200ml of media for the following settings. To achieve 8% oxygen saturation of the media, the nitrogen flow rate should be set to 55cfh, and each potentiometer should be set at 70%. The lowest oxygen level achieved was 5% with settings of 65cfh (nitrogen) and 72.5% (pumps).

**Conclusion:** Building an efficient bubbler for altering oxygen saturation of media requires a power supply of 12V, a reservoir of volume 1000ml, a basin of volume 10.83ml and surface area of 8.15cm$^2$, two peristaltic pumps, two potentiometers, and tubing with an inner diameter of 3mm. To use the bubbler to establish 8% oxygen saturation in the media, the nitrogen flow rate must be set to 55cfh and the pumps should be running at 70% maximum. To achieve 5% oxygen saturation of media, the nitrogen flow rate must be 65cfh with the pumps running at 72.5% of maximum.

**References:** 1. Gray LH, Steadman JM. Determination of the oxyhaemoglobin dissociation curves for mouse and rat blood. *J Physiol*. 1964;175(2):161-171. doi:10.1113/jphysiol.1964.sp007509
**Acknowledgements:** This work was funded by the National Science Foundation.

# Identification of immune modulating strategies to promote cartilage regeneration.

Eirene Choi[1,3], Carly Smith[1], Zoey Katz[1], Lauren O'Donnell[1], John Collins[1], and Theresa A Freeman[1,2]

[1]Department of Orthopedic Surgery, Thomas Jefferson University, Philadelphia, PA, United States.
[2]Correspondence: theresa.freeman@jefferson.edu. [3]Correspondence: eirene.choi@students.jefferson.edu.

Apoptosis Signal-Regulating Kinase 1 (ASK1) is a mitogen-activated protein kinase kinase kinase activated by stress stimuli including elevated reactive oxygen species (ROS), calcium influx, and inflammatory cytokines. Previous studies on inhibition or loss of ASK1 have shown a deregulation of apoptotic and pro-inflammatory signaling pathways. Our published studies have highlighted the role of ASK1 in chondro- and osteogenesis, development, osteoarthritis, and regeneration.[1] As genetic or pharmacological loss of ASK1 has the ability to promote cartilage regeneration after ear punch and other reports have implicated the immune response as a key modulator, we asked how the immune response was affected with the loss of ASK1 in the ear punch regeneration model. Tissue samples were taken using a 2 mm biopsy punch front the center of the cartilaginous ear of WT and KO mice (n=3).[2] Full ear punches were taken on day 0 from ear 1, day 4 from ear 2, day 11 from ear 1 and from the skin on the back. Healing ear tissue was taken as a re-punch of the area that had healed either 4 days post-punch from day 0 (ear 1), or 7 days post-punch from the day 4 (ear 2). RNA was extracted from the ear punches and gene expression was analyzed using the NanoString nCounter Immunology Gene Panel. Functional enrichments were analyzed using Gene Set Enrichment Analysis (GSEA) and Gene Set Variation Analysis (GSVA) (Fig. 1). Results indicated there were significant differences between the ASK1 KO and WT mice. GSVA showed general apoptosis was significantly decreased in the KO as expected. Interestingly, the p53 pathway that induces apoptosis in response to cellular stresses was also down regulated. Unexpectedly, the most significant decrease observed was epithelial-mesenchymal transition (EMT). In support of this was decreased IL-6-JAK-STAT3 signaling, a key EMT pathway. Upregulated in response to ASK1 loss are coagulation, allograft rejection, and apical junction pathways. GSEA-generated heatmaps of genes that significantly contributed to these pathways were generated to give additional insight into the signaling pathways involved. Taken together, this type of analysis identified unexpected alterations of functional activities and signaling pathways that support regeneration. This has provided insight to several novel ways the immune response could be manipulated to produce a more regeneration supportive environment. Future work will include analysis of other data sets from regenerative ear punch models to determine the rigor of these results.

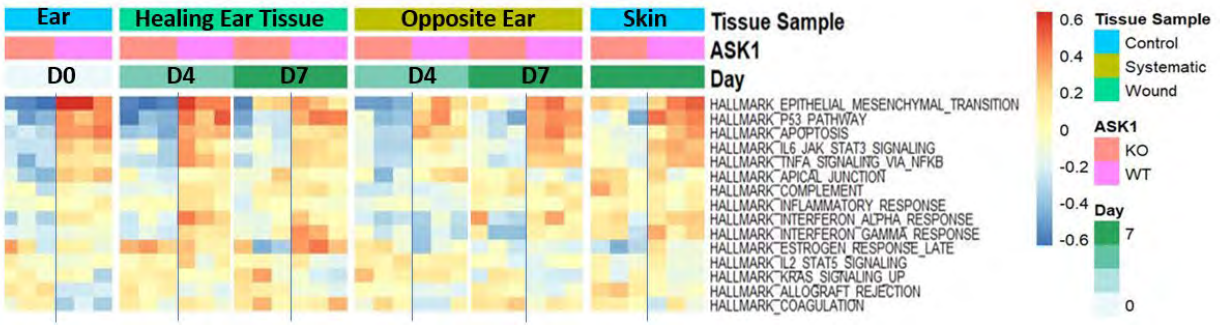


Figure 1. GSVA heatmap from NanoString nCounter Immunology Gene Pannel.

[1] Eaton, G. J., et al. (2014). "Inhibition of apoptosis signal-regulating kinase 1 enhances endochondral bone formation by increasing chondrocyte survival." Cell Death &Disease 5(11): e1522-e1522.

[2] Zhang, Q.-S., et al. (2017). "Inhibition of apoptosis signal-regulating kinase 1 alters the wound epidermis and enhances auricular cartilage regeneration." PLOS ONE 12(10): e0185803.

# Assessment of Bone Nanoscale Mineralization using Optical Photothermal Infrared (O-PTIR) Spectroscopy

Isha Dev, Sofia Mehmood, Nancy Pleshko, William Querido*
Department of Bioengineering, Temple University, Philadelphia PA
William.Querido@temple.edu

**Introduction**: Understanding the fundamental aspects of bone quality and strength relies heavily on a detailed examination of nanoscale structural elements, typically at dimensions around ~500 nm [1]. To elucidate the origins of bone health impairments, high-resolution compositional analysis at the nanoscale is indispensable. Optical photothermal infrared (O-PTIR) spectroscopy, a recent advancement, offers a unique capability for nanoscale data collection. The essential step in incorporating this technique into the study of bone tissue is its validation. In this study, our goal was to the apply O-PTIR spectroscopy to assess cortical bone tissue nanoscale composition in samples from control tissues and tissues with a known bone mineral defect (from mice with osteogenesis imperfecta, OI) to validate the method.

**Methods**: Tibias from female wildtype (WT) and oim/oim mice were procured from an IACUC-approved study at the Hospital of Special Surgery in New York, NY. These specimens, embedded in poly(methyl methacrylate) (PMMA) blocks, underwent minimal sample preparation, primarily consisting of cross sectioning the blocks into 2-4 mm thick segments at the mid-diaphysis. No further sample treatment was required. O-PTIR spectral data were collected using the Photothermal Spectroscopy Corp. mIRage infrared microscope, with line scans from endosteum to periosteum at a 500 nm resolution. The quantification of tissue mineral content and crystallinity were performed for three distinct regions of the cortical bone and based on well-established spectral peak ratios [2]. Statistical analysis was performed using t-test, with statistical significance defined at $p < 0.05$.

**Results**: O-PTIR spectra of WT and oim/oim cortical bone samples showed typical peaks of mineral and collagen (Figure 1). Quantification of peak ratios showed the mineral-to-matrix ratio, indicative of the relative amount of mineral normalized to the amount of protein, was significantly greater in oim/oim samples in all bone regions. Additionally, mineral crystallinity, indicative of the maturity and structural order of the mineral, presented generally lower values in oim/oim samples compared to the wildtype, which were only significant in the periosteal region.

**Conclusions**: Our study validates the application of O-PTIR spectroscopy in assessing bone tissue composition, mirroring established infrared spectroscopic techniques [3]. With its impressive 500 nm spatial resolution, this novel approach unveiled matrix mineralization discrepancies in various cortical bone regions (endosteum, middle, and periosteum) between wildtype and oim/oim samples. These variations are challenging to detect using conventional infrared microscopy due to their diffraction-limited resolution. Further applications of O-PTIR spectroscopy and imaging will contribute to fill gaps in understanding bone nanoscale compositional properties associated with skeletal diseases.

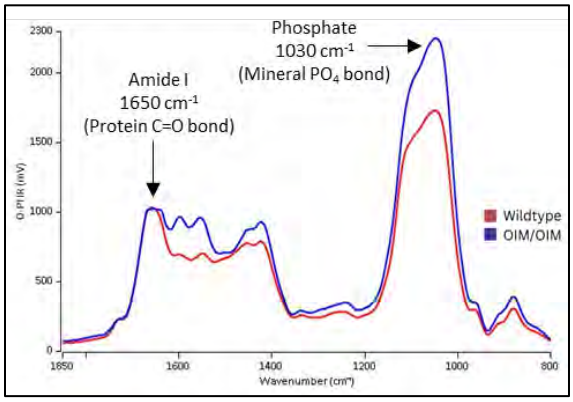


**Figure 2:** Average wildtype and *oim/oim* O-PTIR spectra normalized to the amide I (C=O) protein band.

**References:**

1. Reznikov et al. Acta Biomaterialia. 2014; 10(9):3815.
2. Querido et al. Molecules. 2021;26(4):922.
3. Taylor EA, Donnelly E. Bone. 2020;139, 115490.

**Acknowledgements:** NIH/NIAMS R21AR082129

# Identification of mesenchymal progenitor cells in human bone marrow using scRNA-seq and in vitro assays

Michael Duffy[1], Shovik Bandyopadhyay[1,2], Charles Nelson[2], Kyung Jin Ahn[2], Kai Tan[2], Ling Qin[1]
*1 Perelman School of Medicine, University of Pennsylvania, 2 Children's Hospital of Philadelphia*

Human bone marrow scRNA-seq datasets lack mesenchymal and stromal cell subsets, which murine data indicate are rich in diversity and highly express key regulatory cytokines. To address this we digested cells with dispase II and collagenase I from femoral heads collected after total hip arthroplasty (Fig 1A). Using magnetic bead separation (StemCell EasySep), we depleted RBCs (Fraction 1), used a portion for mesenchymal cell enrichment with CD45 depletion (Fraction 2) and another for hematopoietic stem and progenitor cell enrichment with CD34 selection (Fraction 3). The three fractions were merged and prepared for scRNA sequencing with the Chromium NextGEM Single Cell 3' GEM, Library, and Gell Bead Kit. Alignment and count matrices were constructed using Cellranger and GRCh38 with intronic regions. Doublets were removed and cells with between 100 and 10000 unique genes expressed and less than 10% mitochondrial RNA were kept for analysis. With 12 samples, we produced a dataset of 53,417 hemtaopoietic cells and 29,325 non-hematopoietic cells and identified 32 cell clusters, including 7 mesenchymal cell clusters (Fig 1B and 1C), a diversity not captured previously. Using CytoTrace (Fig 1D), we predicted several mesenchymal stem cell (MSC) clusters and identified Fibro-MSC as the most niave. Using flow sorting we isloated Fibro-, Thy1+-, Osteo-, and Adipo-MSCs and determined that Fibro-MSCs (expressing fibroblastic markers HAS1, DPT, and PDPN) form the greatest porportion of colony forming units (Fig 1E & F) and maintain a robust proliferative phenotype measured as cummulative population doubling time from passage 1 to 8 (Fig 1G). Additionally, Fibro-MSCs underwent adipogenic and osteogenic differentiation (Fig 1H-1K) . Our human dataset uncovers a more diverse pool of bone marrow mesenchymal cells than previously shown, and identifies a potential primitive MSC in the bone marrow (Fibro-MSC).

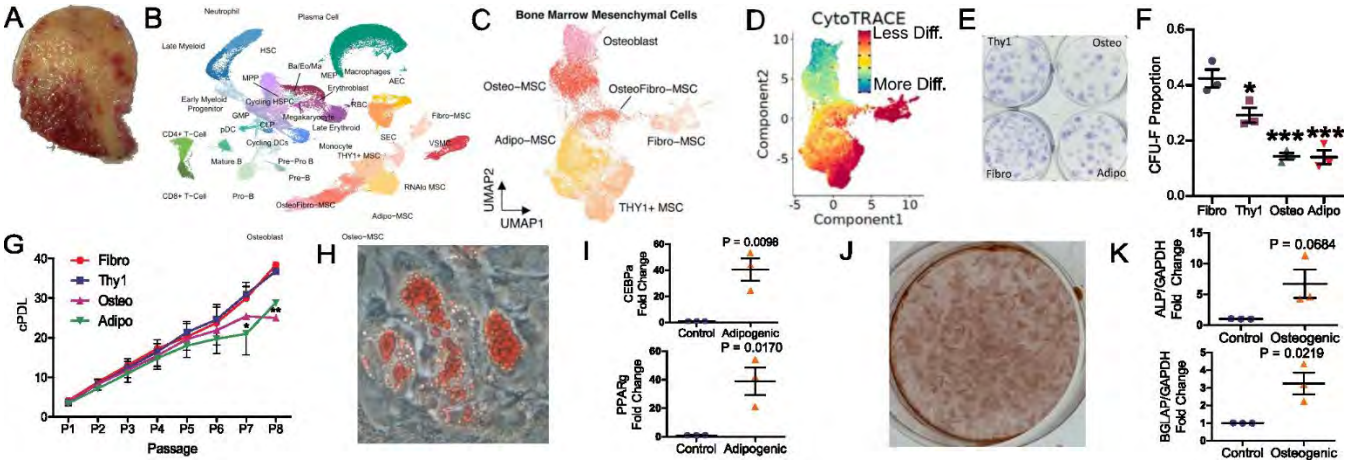


Fig. 1: A. Example sample from femoral head collected after total hip arthroplasty from Penn Presbyterian Hospital. Study design was deemed non-human subject research after review by Penn IRB. B. Clustering of 12 scRNA-seq samples captured the hematopoietic hierarchy and a diverse mesenchymal population. C. Cluster of mesenchymal cell populations. D. CytoTrace predicts Fibro-MSCs are the most primitive mesenchymal progenitor. E. Crystal violet staining of CFU-F assays of sorted Fibro-, Thy1-, Osteo-, and Adipo-MSCs (n=3). F. CFU-F proportion is greatest for Fibro-MSCs. G. Cumulative population doubling time of sorted MSCs show Fibro- and Thy1-MSCs maintain robust proliferation over eight passages compared to Adipo and Thy1-MSC (n=6-7). H. Fibro-MSC adipogenic differentiation demonstrated with Oil Red O staining. I. CEBPa and PPARg gene expression is increased adipogenic induced Fibro-MSCs (n=4). J. Fibro-MSC osteogenic differentiation demonstrate with alizarin red staining. K. ALP and BGLAP gene expression is increased after osteogenic induction of Fibro-MSC cells.

# Inducible Rosa, but not αSMA or Scx, Cre driven excision achieves substantial *Col12a1* knockdown in tendon healing

Alexander J. Bein, Ashley K. Fung, Stephanie N. Weiss, Nathaniel A. Dyment, Louis J. Soslowsky
McKay Orthopaedic Research Laboratory, University of Pennsylvania, Philadelphia, PA
abein@sas.upenn.edu

**Disclosures**: Alexander J. Bein (N), Ashley K. Fung (N), Stephanie N. Weiss (N), Nathaniel A. Dyment (N), Louis J. Soslowsky (N)

**INTRODUCTION:** Tendon healing follows a typical wound healing process involving transient and heterogeneous cell populations. Collagen XII, a fibril-associated collagen, regulates tendon cell and matrix organization [1], and *Col12a1* expression increases post-injury. Tamoxifen-inducible Cre mouse models permit spatial and temporal knockdown, and these models are advantageous for investigating the specific role of collagen XII in *de novo* tissue formation following injury. However, these models may also target other intrinsic or extrinsic cell populations that do not contribute to the healing response, such as vascular cells and cells in the adjacent tissue, and the efficiency of different spatial Cre drivers for collagen XII knockdown are unknown. Therefore, the objective of this study was to evaluate the efficiency of *Col12a1* knockdown in the healing tissue versus native tendon using three tamoxifen-inducible Cre mouse models ( 1) Rosa-CreER$^{T2}$ model to ubiquitously target cells contributing to the healing response; 2) αSMA-CreER$^{T2}$ model to target peritenon-derived progenitor cells that infiltrate into the injury; and 3) Scx-CreER$^{T2}$ to target tendon-derived cells) and two tamoxifen dosage protocols (short- and long-dose). We hypothesized that 1) the Rosa-CreER$^{T2}$ model would result in the greatest knockdown independent of region, 2) the αSMA-CreER$^{T2}$ model would exhibit increased knockdown in the healing tissue compared to the native tissue, and 3) the Scx-CreER$^{T2}$ model would show greater knockdown in the healing tissue with the long-dose tamoxifen protocol.

**METHODS:** Male Rosa-CreER$^{T2}$;*Col12a1*$^{flox/flox}$ (RosaKO), αSMA-CreER$^{T2}$;*Col12a1*$^{flox/flox}$ (αSMAKO), and Scx-CreER$^{T2}$;*Col12a1*$^{flox/flox}$ (ScxKO) mice with their respective Cre- littermate controls were used (n=8/group, IACUC approved). At 90 days old, mice underwent bilateral patellar tendon injury surgery as described [2], and Cre excision of the conditional alleles was induced via four IP injections of tamoxifen (100mg/kg body weight). The short-dose group received tamoxifen at days -1, 0, 1, and 2 days post-injury, and the long-dose group received tamoxifen at -3, 0, 3, and 6 days post-injury, where day 0 is the day of surgery. Mice were sacrificed two weeks later, and left knees were fixed for three hours in 4% paraformaldehyde prior to cryo-embedding. Injured patellar tendons were sectioned axially at a thickness of 40μm, and sections were microdissected using a 25G needle to ensure isolation of the healing tissue and the adjacent, native tendon struts. The tissue was digested, RNA was isolated as described [3], and qPCR was performed for *Col12a1* expression. ΔCt values were normalized to the housekeeper gene, *Abl1*. Statistics: Two-way ANOVAs for genotype and tamoxifen dosage protocol were conducted within each region, and paired t-tests were conducted to compare *Col12a1* expression in the native and healing regions. Significance was set at $p<0.05$.

**RESULTS:** Supporting our hypothesis, the RosaKO model demonstrated the highest knockdown compared to control regardless of region and tamoxifen dosage protocol with substantial decreases in *Col12a1* expression (~117-2,200-fold decrease, **Figure 1A**). The short-dose protocol in RosaKO mice also resulted in greater knockdown compared to the long-dose protocol in both the native (~22-fold decrease) and healing (~5.5-fold decrease) regions. Contrary to our hypothesis, *Col12a1* expression surprisingly increased in the healing region of αSMAKO mice with the short dose protocol (~2.5-fold, **Figure 1B**), and no differences between ScxKO and control mice were observed in any region or tamoxifen dosage protocol (**Figure 1C**). However, expression was increased in the long dose group in the healing region of ScxKO compared to the short dose group. Finally, *Col12a1* expression was elevated across several groups in the healing region compared to its respective native region.

**DISCUSSION:** During patellar tendon healing, infiltrating peritenon-derived αSMA+ cells are the primary contributors to the healing response prior to differentiating into Scx+ cells by two weeks post-injury [4]. Our previous data showed that *Col12a1* expression is increased one-week post-injury and returns to uninjured levels by six-weeks post-injury. Therefore, we expected that targeting *Col12a1* knockdown to αSMA+ cells during early healing would result in knockdown within the healing, *de novo* tissue. However, no knockdown was demonstrated in the αSMA model, even when tamoxifen was administered through 6 days post-injury, and this suggests that this Cre driver may not be sufficient in this model. Similarly, while no knockdown in the healing region of the ScxKO model may be attributed to the timing of Scx expression during tendon healing, there was no significant knockdown in the native region either, and this model also may not be effective in *Col12a1* knockdown. Additionally, both short and long-dose protocols were tested to consider the metabolism rate of tamoxifen in maximizing knockdown to the healing tissue, and in the RosaKO model, greater *Col12a1* knockdown with the short dose protocol indicates that administering tamoxifen on consecutive days before and after injury is more efficient. Finally, as expected, we observed that *Col12a1* expression was generally greater in the healing tissue than the native region, suggesting that collagen XII plays a critical role in tendon healing. Future studies will investigate this role by inducing knockdown of *Col12a1* at the time of tendon injury in a Rosa-CreER$^{T2}$ model.

**SIGNIFICANCE:** Compared to αSMA-CreER$^{T2}$ and Scx-CreER$^{T2}$, the Rosa-CreER$^{T2}$ model achieves substantial *Col12a1* knockdown when induced at time of tendon injury. Our results highlight the importance of carefully considering an appropriate tamoxifen-inducible Cre model when targeting specific genes.

**REFERENCES:** [1] Izu et al, Matrix Biol 2021, [2] Lin et al, J Biomech 2006, [3] Leiphart et al, ORS 2022, [4] Dyment et al, PLoS One 2014.

**ACKNOWLEDGEMENTS:** This study was funded by NIH/NIAMS R01AR078790 and the Penn Center for Musculoskeletal Disorders (P30AR069619).

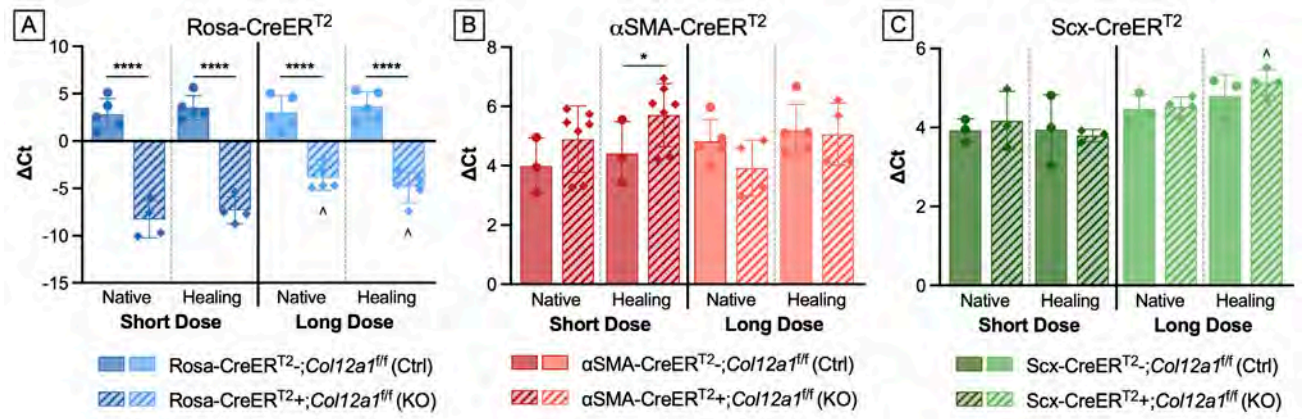


**Figure 1:** (A) The Rosa model achieved dramatically reduced expression of *Col12a1* expression in both the native and healing regions in mice administered the short and long dose tamoxifen protocols. The short dose groups also demonstrated greater knockdown compared to their respective long dose group. (B) In the αSMA model, *Col12a1* expression was surprisingly increased in the short dose, healing region of KO mice, while no other differences were observed. (C) In the Scx model, *Col12a1* expression was higher in the long dose, healing region of KO mice compared to its respective short dose group. (*p<0.05, ****p<0.0001, ^p<0.05 compared to short dose protocol)

# Aberrant Bone Morphogenetic Protein-2 Signaling in C57BL/6 Mice Is Reflective of Human Patients Diagnosed with Osteoporosis

Daniel Halloran, Ph.D.
CHOP, Orthopaedic Surgery

Bone Morphogenetic Protein-2 (BMP-2) is a key regulator of osteogenesis and osteoblast maturation. However, the signaling pathways of BMP-2 are disrupted in patients diagnosed with osteoporosis (OP), a bone disorder caused by a decrease in bone mineral density (BMD). While these patients are unresponsive to BMP-2, there is an upregulation of BMP Receptor Type 1a (BMPRIa), but the BMP-signaling pathway is not activated. To bypass the necessity for exogenous BMP-2, a novel synthetic peptide, CK2.3, is endocytosed into cells and activates BMP-signaling, specifically non-canonical SMAD pathways. CK2.3 enhances osteoblast activity from OP patients while simultaneously decreasing osteoclast activity. While these data have been shown in OP patients, the role of BMP-2 and CK2.3 in a mouse model has not been elucidated. Therefore, we utilize the C57BL/6 (B6) mouse strain and predict that bone forming cells obtained from these aged-mice will exhibit aberrant BMP-signaling that is reflective of OP patients. We show that BMP-2 does not increase bone growth or enhance osteoblast activity in 15- and 20-month mice, however, the expression of BMPRIa is upregulated, similar to OP patients. In these mice, CK2.3 effectively upregulates osteogenesis and osteoblast activity, while it limits the activity of osteoclasts in all age groups. As such, these data indicate that an aging B6 mouse model is reflective of OP patients and can be utilized to investigate aberrant BMP-signaling.

**Patient-specific *Adamtsl2* D167N Knock-in Mice Recapitulate Key Skeletal Features of the Short Stature Syndrome Geleophysic Dysplasia**

**Author Names:** Nandaraj Taye[1], Deborah Seifert[2], Zerina Balic[1], Timothy Mead[2], Dirk Hubmacher[1]

[1]Orthopedic Research Laboratories, Department of Orthopedics, Icahn School of Medicine at Mount Sinai, New York, NY

[2]Department of Pediatrics, Case Western Reserve University School of Medicine & University Hospitals Rainbow Babies and Children's, Cleveland, OH

Geleophysic dysplasia (GD) is caused by recessive mutations in *ADAMTSL2* (GD1, ~50% of cases) or dominant mutations in *FBN1* (GD2, ~50% of cases) or *LTBP3* (GD3, <1% of cases). Signs of GD become apparent in the first year of life and include severe short stature (-4 to -8 SD), short fingers and toes (brachydactyly), joint contractures, bone shape abnormalities, thick skin, characteristic facial features, and a pseudomuscular build. Complications from progressive heart valve disease and narrowing of the large airways cause mortality in 33% of affected children before the age of 5. Despite high childhood mortality and lifelong morbidity, no disease-modifying treatments for GD1 are available. To model disease progression of GD1 and enable efficacy testing of mechanism-based therapeutic approaches, we generated a mouse model for severe GD1 by introducing the *ADAMTSL2 c.499G>A* (p.D167N) mutation in the mouse *Adamtsl2* locus ("D167N"). Homozygous D167N mice had reduced postnatal survival and developed short stature. The limb bones were significantly shorter and showed characteristic shape changes, including tubular metatarsals and egg-shaped (ovoid) vertebrae. In addition, a "moth-eaten" appearance of metatarsals and phalanges suggested delayed mineralization. In the lung we observed bronchial obstruction by vesicular structures, which we also reported for *Adamtsl2* knock-out mice. Heart histology showed dysplastic aortic, pulmonic, and mitral valves. Collectively, abnormalities in the skeletal, cardiac, and pulmonary system of D167N mice recapitulate the syndromic features of human GD1. On a molecular level, secretion of ADAMTSL2-D167N was reduced by 80%, which could be rescued by treatment with the chemical chaperone 4-PBA. In conclusion, we generated a mouse model that recapitulates key signs of severe GD1. In addition, we obtained molecular evidence for using chemical chaperones as a potential therapeutic approach to treat GD1, which we will now test in pre-clinical trials, using the D167N GD1 mouse model.

**Quantitative Assessment of Bone-Selective MRI Techniques for Craniofacial Imaging**

Nada Kamona[1,2], Brandon C. Jones[1,2], Hyunyeol Lee[1,3], Connor S. Wagner[4], Sandhya Konar[1], Makayla Clark[1], Elaine Li[1], Hee Kwon Song[1], Chamith S. Rajapakse[1,5], Scott P. Bartlett[4], Felix W. Wehrli[1]

*[1]Department of Radiology, Perelman School of Medicine, University of Pennsylvania. [2]Department of Bioengineering, University of Pennsylvania. [3]School of Electronics Engineering, Kyungpook National University, Daegu, South Korea. [4]Division of Plastic, Reconstructive, and Oral Surgery, Children's Hospital of Philadelphia. [5]Department of Orthopaedic Surgery, University of Pennsylvania*

**Purpose:** CT is the clinical standard imaging modality for evaluating and surgical planning of craniofacial skeletal pathologies. However, ionizing radiation exposure remains a problem, especially for children and infants who may require multiple scans at a very young age. There have been few approaches utilizing magnetic resonance imaging (MRI) for high-resolution skull imaging as a radiation-free alternative to CT. Our lab developed an ultrashort echo-time (UTE) solid-state technique that generates bone-selective images by means of echo subtraction. The dual-RF, dual-echo, three-dimensional ultrashort echo (DURANDE) sequence exploits the sensitivity of bone proton magnetization to RF pulse duration to further suppress soft-tissues. DURANDE has previously demonstrated enhanced bone-signal and suppression of soft-tissues and air, and has been evaluated against CT both *ex vivo* and *in vivo*. In this work, our goal is to quantitatively assess the strengths and limitations of our proposed sequence (DURANDE) against other MRI sequences.

**Methods:** Healthy adults (n=10, 4 females, ages 26.1±2.3 yr) were imaged at 3T with three MRI sequences: dual-radiofrequency and dual-echo (DURANDE) ultrashort echo time, zero echo time (ZTE), and gradient echo (GRE, also known as "black-bone" MRI). Bright-bone images from DURANDE were generated by echo subtraction exploiting the bone signal intensity dependence on RF pulse duration and echo time, while ZTE bright-bone images were obtained via logarithmic inversion after bias field correction. A semi-automatic segmentation method was used to generate three skull segmentations per participant, and the overlap of the binary masks was quantified using dice similarity coefficient (DSC). Based on 3D renderings, three craniometric distances were measured: glabella to opisthocranion, left frontozygomatic to right frontozygomatic sutures, and vertex to basion. Lin's concordance correlation coefficient (CCC) was used to test the agreement among measurements from the three MRI sequences.

**Results:** Comparisons of bone image sections from DURANDE, ZTE and low-flip-angle short-TE GRE are depicted in **Figure 1**. The average ± standard deviation of DSC among scan pairs was 81.2%±12.7%, 78.3%±12.8%, and 76.3%±14.2% for DURANDE versus ZTE, DURANDE versus GRE, and ZTE versus GRE, respectively. However, this agreement is dependent on slice location; DSC is higher for superior slices in the cranial vault, and lower in inferior slices containing the sinuses. Based on Lin's CCC (**Table 1**), there was high agreement among all scan pairs across all craniometric distances ($r_{ccc}$>0.99). Since ZTE images require two bone segmentation thresholds, there is increased ambiguity in the overlap of the histograms pertaining to bone/air and bone/soft-tissues boundaries, resulting in erroneous classification of bone voxels in the sinuses. Unlike ZTE, DURANDE has an overall higher contrast-to-noise ratio around the sinuses, the zygomatic bone, and upper maxilla, which made bone segmentation and rendering more accurate.

**Discussion & Conclusion:** We evaluated three MRI sequences for craniofacial imaging by assessing the similarities among their skull segmentations and craniometrics measurements in healthy adults. All three MRI techniques yielded good agreement in the skull images and comparable craniometric measurements. The main benefit of ZTE is the very low level of acoustic noise it generates as the gradients are not ramped down between views, which is beneficial in terms of patients' comfort. However, the limitation of ZTE-type sequences is the need for bias-field correction and further post-processing algorithms to suppress soft-tissues and separate bone from air, the latter is further limited by the overlap of the histogram of bone and air. DURANDE's strength is its straightforward dual-echo subtraction implementation; it is self-normalized and does not require elaborate image post-processing to discern air from bone, yielding superior bone-contrast images.

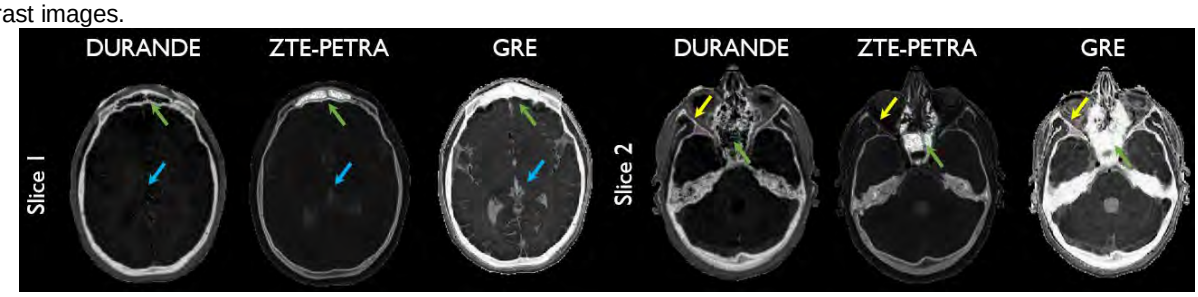


**Figure 1:** Axial images of one participant (24 yo female) acquired with three sequences; DURANDE, ZTE, and GRE. The bright-bone image in DURANDE is generated by echo subtraction, while that for ZTE is obtained via logarithmic inversion after bias field correction. GRE images are inverted to make the bone bright. Note that air appears black in DURANDE and white in ZTE, while both air and bone have the same voxel intensity in GRE. DURANDE clearly resolve thin bone structures (yellow arrows) and can differentiate bone from air at the sinuses (green arrows). When compared to GRE, both ZTE and DURANDE have superior soft-tissue suppression (blue arrows).

**Table 1:** Mean difference in craniometric measurements, and Lin's concordance correlation coefficient (CCC) between scan pairs across all participants (n=10). All craniometric values were determined from the 3D renderings using the ruler tool in *3D Slicer*.

| Scan pair | Mean difference in craniometrics (mm, mean ± STD) | | | CCC (r, [95% confidence interval]) | | |
|---|---|---|---|---|---|---|
| | Glabella to opisthocranion | Left to right frontozygomatic suture | Vertex to basion | Glabella to opisthocranion | Left to right frontozygomatic suture | Vertex to basion |
| DURANDE vs ZTE | 0.25 ± 1.16 | 0.38 ± 1.25 | 1.73 ± 1.21 | 0.99 [0.96, 1.00] | 0.95 [0.81, 0.99] | 0.96 [0.88, 0.99] |
| DURANDE vs GRE | 0.21 ± 1.13 | 0.01 ± 1.26 | 0.90 ± 1.06 | 0.99 [0.97, 0.99] | 0.95 [0.83, 0.99] | 0.98 [0.94, 1.00] |
| ZTE vs GRE | 0.04 ± 1.14 | 0.37 ± 0.83 | 0.83 ± 1.55 | 0.99 [0.95, 1.00] | 0.97 [0.89, 0.99] | 0.97 [0.91, 0.99] |

# An essential telomere protein for muscle stem cell function and regeneration during homeostasis, disease, and aging

Ji-Hyung Lee[1] and Foteini Mourkioti[1,2,3]

[1]Department of Orthopaedic Surgery, Perelman School of Medicine, University of Pennsylvania, Philadelphia, PA 19104, USA.
[2]Department of Cell and Developmental Biology, Perelman School of Medicine, University of Pennsylvania, Philadelphia, PA 19104, USA.
[3]Penn Institute for Regenerative Medicine, Musculoskeletal Program, Perelman School of Medicine, University of Pennsylvania, Philadelphia, PA 19104, USA.

Skeletal muscle exhibits extraordinary regeneration after muscle injury and this ability exclusively depends on the activity of residential stem cells called muscle stem cells (MuSCs). Disruption of MuSC action leads to impaired muscle regeneration and it is observed in several muscle disease such as muscular dystrophies and muscle aging. Telomeric repeat binding factor 2 (TRF2) is a DNA binding element of shelterin complex, which protects telomere from undesired DNA damage responses and recombination. TRF2 has been reported to have both telomeric and extra-telomeric functions with cell type and tissue specific manner. However, nothing has been studied about the TRF2 as a regulator of MuSCs behavior. We found that TRF2 expression was dynamically changed in MuSCs during muscle regeneration. Intriguingly, TRF2 was downregulated in both dystrophic and aged MuSCs without affecting the expression of other shelterin component, TRF1. MuSC-specific removal of TRF2 severely impaired muscle regeneration and DMD progression deteriorated by TRF2 deletion in MuSCs of mdx mice. *In vivo* imaging of Pax7-positive cells illustrated that MuSC population was declined by TRF2 deletion in MuSCs. However, acute cell death was not observed in TRF2 knockout MuSCs implying that stem cell depletion is independent from cellular apoptosis. Proliferation test showed that loss of TRF2 inhibits MuSCs propagation after muscle injury. These results demonstrate that TRF2 is an an indispensable factor for adequate MuSC function and muscle regeneration. Findings from this study propose TRF2 as an intrinsic gatekeeper of appropriate MuSC function and provide new strategies to overcome skeletal muscle disease.

# Enhancing Zone-Specific Rotator Cuff Enthesis Regeneration via Non-Cellular Extracellular Vesicle-Mediated MSC Differentiation

Zizhao Li[1], Yoon Ho Roh[1], Catherine Wang[1], Yujia Zhang[1], Jina Ko[1], and Su-Jin Heo[1]
[1]University of Pennsylvania, Philadelphia, PA

**DISCLOSURES:** Li (N), Roh (N), Wang (N), Zhang (N), Ko (N), and Heo (5-4WEB Medical)

**INTRODUCTION:** The rotator cuff is vital for shoulder movement and joint stability. However, tears at the rotator cuff enthesis site are very common **[1]**. Surgical interventions are often used, but re-tearing can happen due to scar tissue formation and insufficient vascularization at the repaired enthesis **[3-4]**. Furthermore, the intricate structure of the rotator cuff enthesis, segmented into distinct tendon, fibrocartilage, and bone zones, necessitates zone-specific approaches for effectively addressing its heterogeneity. Cell-based approaches have emerged to promote the healing of tendon and fibrocartilage phases within the enthesis. Notably, recent scientific focus has converged on extracellular vesicles (EVs), lipid-bound vesicles that carry variety of biological cargo, including RNAs, DNA, and proteins measuring ~30-200 nm in diameter **[5]**. Research has highlighted the substantial potential of EVs derived from various cell sources to enhance targeted delivery and improve therapeutic outcomes within the musculoskeletal domain **[6-7]**. For instance, extensive studies have corroborated that EVs sourced from tenocytes and mesenchymal stromal cells (MSCs) possess a remarkable capacity to induce tenogenic and chondrogenic differentiation **[8-10]**. Thus, this study aims to comprehensively characterize EVs extracted from distinct cell types: tenocytes (isolated from bovine Achilles tendons, T-EV) and mesenchymal stem cells (isolated from bovine bone marrow, MSC-EV). Further, we explore the impact of these EVs on recipient MSC proliferation and differentiation, thereby evaluating their therapeutic potential for zone-specific rotator cuff enthesis regeneration.

**METHODS:** To isolate EVs, juvenile bovine (< 3 months) tenocytes and MSCs (P1) were cultured in basal media until they reached approximately 90% confluency. T-EV and MSC-EV were then obtained by ultracentrifugation using our well-established protocol **[11-12]**. EV size distributions and total protein concentration were determined using nanoparticle tracking analysis (NTA). EV samples were stained with tetraspanin-specific fluorescent antibodies (CD63-568, and CD81-647) and subjected to super-resolution STORM imaging using an ONI Nanoimager microscope. The acquired STORM data underwent analysis through the Collaborative Discovery (CODI, ONI) online analytic platform to decipher the tetraspanin protein composition within the EVs. T-EV and MSC-EV were labeled with a lipophilic carbocyanine DiOC18 dye (DiO) to enable tracking of EV uptake in recipient bovine MSCs. Under EV-free pre-cultured conditions, two types of EVs were introduced to recipient MSCs at different concentrations (0-10k EVs/cell) to investigate how EVs isolated from two distinct cell types influence MSC proliferation and differentiation. On Day 3, fresh EVs were introduced alongside media replacement. Recipient MSC viability and proliferation were assessed by utilizing the Cell Counting Kit-8. On Day 7, TRIzol reagents were employed to isolate mRNA from the EV-recipient MSCs. Gene expression levels of tenogenic, and chondrogenic markers such as Type- I or II collagens (Col-1, Col-2), SOX-9, Tenascin C (TN-C), Aggrecan (ACAN)) were analyzed by RT-PCR, with GAPDH as the reference gene. Statistics was performed with ANOVA with Tukey's post hoc test.

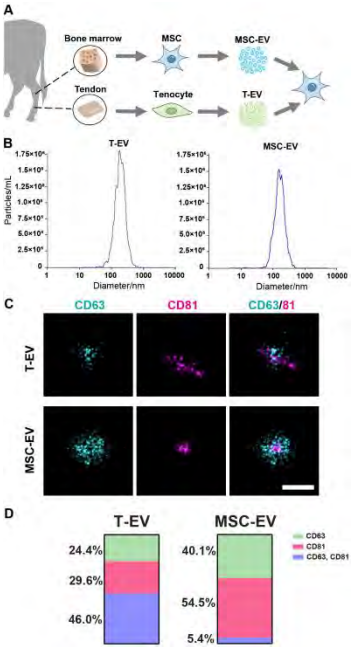


**Fig. 1:** (A) Schematic illustration of T-EV and MSC-EV isolation process and in vitro testing. (B) Quantitative NTA results. (C) Representative STORM images of individual T-EV and MSC-EV (Green: CD63, Red: CD81; scale bar = 200 nm). (D) Tetraspanin co-localization analysis of T-EV and MSC-EV.

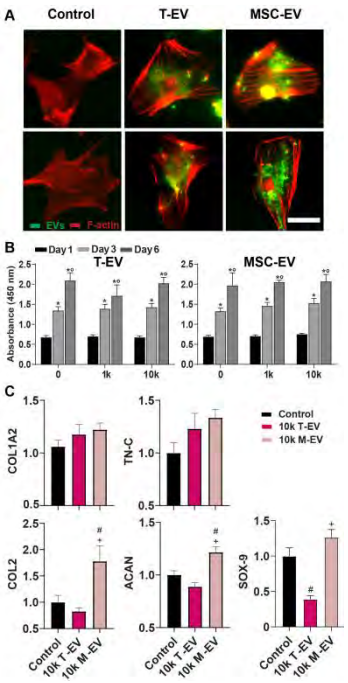


**Fig. 2:** (A) Representative fluorescence images of MSCs treated with EVs (bar = 50 µm). (B) MSC proliferation determined by CCK8 assay. [*: $p < 0.05$ vs. Day 1, ○: $p < 0.05$ vs. Day 3, n = 6/group, mean ± SD]. (C) Gene expression relative to GAPDH on Day 7 [#: $p < 0.05$ vs. Control, +: $p < 0.05$ vs. 10K T-EV, n = 6/group, mean ± SD].

**RESULTS:** Two distinct types of EV were successfully extracted and the NTA unveiled that T-EV and MSC-EV predominantly exhibited size distributions with mean sizes of 196.8 nm and 195.2 nm, respectively (**Fig. 1B**). Visual identification of T-EV and MSC-EV surface markers was accomplished by detecting the CD63/CD81 tetraspanins using STORM imaging at the individual levels (**Fig. 1C**). The significant enrichment of CD63 and CD81 tetraspanins and its ratio in EV membranes serve as a common indication of EVs and are employed as a biomarker for the detection of single-level EVs. Analysis in **Fig. 1D** demonstrated the existence of three different EV subpopulations in T-EV and MSC-EV: CD63 single-positive EVs, CD81 single-positive EVs, and CD63/CD81 double-positive EV subpopulations accounted for 46%, with relatively fewer single-positive subpopulations (CD63 only: 24.4%, CD81 only: 29.6%). Conversely, in MSC-EV, the dominant subpopulation consisted of CD81 single-positive EVs, comprising 54.5% of the total. CD63-positive EVs and double-positive EVs constituted 40.1% and 5.4% of the overall MSC-EV indicating two distinct EV populations. Representative fluorescence images exhibited the uptake of T-EV and MSC-EV by recipient bovine MSC, while no fluorescence was observed in the non-EV treated control group (**Fig. 2A**). The MSC proliferation rates remained consistent regardless of EV type and concentration (**Fig. 2B**), indicating the absence of EV-induced cytotoxicity. Interestingly, EV-treated MSCs demonstrated pronounce expression of tenogenic and fibrous markers (COL1A2 and TN-C) (**Fig. 2C**). MSC-EV treatment led to an enhancement in expression levels of chondrogenic gene (COL-2, ACAN, SOX-9) expression levels, while intriguingly showing a decrease with T-EV treatment (**Fig. 2C**).

**DISCUSSION:** This study has effectively examined the potential of bovine T-EV and MSC-EV to augment in vitro tenogenesis and chondrogenesis, presenting promising implications for the repair of the rotator cuff enthesis. Our approach encompassed a comprehensive characterization, including EV size determination, visualization of EV surface markers, and classification of distinct EV subpopulations. Notably, our findings indicated rapid EV uptake within 30 minutes, and the introduction of EVs to recipient MSCs did not lead to reduced cell proliferation rates when compared to the control group, underscoring the non-toxic nature and compatibility of EVs. Most intriguingly, the group treated with MSC-EVs exhibited heightened chondrogenic gene expression, while the T-EV treated group demonstrated diminished tenogenic/fibrogenic gene expression. These outcomes strongly propose the regulatory influence of distinct EV sources on gene expression. Moving forward, our study's trajectory will encompass the application of mass spectrometry and RNA sequencing to profile protein and RNA levels within both EV types. Concurrently, ongoing extended in vitro and in vivo investigations will ascertain the viability of EV therapy for the repair and regeneration of the rotator cuff enthesis. These cumulative efforts are poised to advance our understanding of EV-mediated interventions in musculoskeletal healing and underscore their therapeutic potential in clinical applications. **SIGNIFICANCE:** This study introduces a novel non-cellular EV-based approach that effectively promotes chondrogenic, tenogenic, and fibrous differentiation of MSCs. The implications of our findings extend to the promising potential for zone-specific regeneration and repair of the rotator cuff enthesis, particularly in combination with biomaterial systems.

**REFERENCES:** [1] Apostolakos+, *M.L.T.J.* 2014; [2] Sahoo+, *JSES Int.* 2015; [3] Sambandam+, *World J Orthop.* 2015; [4] Oh+, *Clin Orthop Surg.* 2018; [5] Nakase+, *Sci Rep.* 2016; [6] Zou+, *J. Nanobiotechnology* 2023; [7] Kodama+, *Bone Rep.* 2022; [8] Xu+, *CT.* 2019; [9] Yu+, *Acta Biomater.* 2020; [10] Connor+, *J. Bone Miner.* 2019; [11] Ko+, *Adv. Biosyst.* 2020; [12] Reynolds+, *J of Extracellular Bio.* 2023. **ACKNOWLEDGEMENTS:** This work was supported by the NIH (P50 AR080581, R56 HL163168) and NSF (CMMI-1548571).

***Facile method to functionalize injectable hyaluronic acid hydrogels with BMP-2 mimetic peptides***

Stacy A. Love[1,2], Matthias Recktenwald[1], Sebastián L. Vega[1,2*]
[1]Department of Biomedical Engineering, Rowan University, Glassboro, NJ, [2]Department of Orthopaedic Surgery, Cooper Medical School of Rowan University, Camden, NJ

***Introduction*:** We recently modified hyaluronic acid (HA), a macromolecule in orthopedic ECMs, with norbornene (HAnor) and tetrazine (HAtet) which, upon coming together, self-polymerize into a hydrogel in the absence of a catalyst. This innovative system allows for targeted injections at precise sites, and by methacrylating HAnor (HAnorMe), macromers can be pre-functionalized with thiolated peptides via an aqueous Michael-addition reaction. Using this scheme, injectable hydrogels pre-functionalized with adhesive thiolated peptides (cRGD) were formed. Bone morphogenetic protein-2 (BMP-2) is a highly osteoinductive molecule, and we formed injectable hydrogels modified with thiolated BMP-2 mimetic peptides (cDWIVA). We demonstrated enhanced alkaline phosphatase (ALP) expression of encapsulated mesenchymal stem cells (MSCs) *in vitro*, and nascent bone formation *in vivo*. One major disadvantage of this platform is the need to pre-functionalize the HAnor macromer with peptides prior to gelation, which is time-consuming and limits the flexibility in concentration variation. To overcome this limitation, we hypothesized that by forming peptides with a nor group, they, along with HAnor could react and covalently bind with HAtet, resulting in a self-forming hydrogel with a much more rapid and flexible peptide functionalization scheme.

***Methods*:** Sodium hyaluronate was converted to its tetrabutylammonium salt and modified with norbornene or tetrazine. Synthesis of nor-modified RGD peptides (sequence: nor-GYGRGDASPG, norRGD) was achieved using a solid-state peptide synthesizer, with molecular weight confirmed via MALDI-TOF analysis. The BMP-2 mimetic DWIVA peptide (sequence: GCGGGDWIVAG) was procured from GenScript. Hydrogel functionalization with norPeptides during catalyst-free gelation was confirmed by mixing 5 wt% HAnor and HAtet macromers with and without 2 mM norRGD onto a cylindrical mold. MSCs (P5, 10,000 cells/cm$^2$) were then seeded atop the hydrogels and adhesion on the norRGD hydrogels was confirmed by staining MSC nuclei with Hoechst (1:1000) and cell body with phalloidin (1:400). DWIVA bioactivity was determined by seeding MSCs (P5, 3,000 cells/cm$^2$) on glass coverslips in either growth medium (GM), osteogenic medium (OM), or GM supplemented with 2 mM DWIVA. Samples were stained for alkaline phosphatase (ALP) after 7 days, and ALP fluorescence was quantified using ImageJ.

***Results*:** Peptide-functionalized hydrogels are formed by mixing HAnor, HAtet, and norPeptide, resulting in a Diels Alder reaction between norbornene and tetrazine moieties (**Fig. 1a**). The successful synthesis of norRGD peptides was confirmed via MALDI-TOF analysis (**Fig. 1b**). MSCs on self-forming hydrogels, with or without norRGD, displayed improved adhesion in norRGD-modified hydrogels (**Fig. 1c**). On glass, DWIVA induced increased expression of osteogenic biomarker ALP when compared to GM group (p-value < 0.05) (**Fig. 1d,e**).

***Conclusion*:** It is possible to synthesize peptides with norbornene moieties for the purpose of easily functionalizing our injectable HA hydrogels. This technique allows for increased flexibility in biochemical functionalization and will allow for the ability to rapidly evaluate the effects of BMP-2 mimetic peptides on MSC osteogenesis across a wide range of peptide concentrations. Currently, we are synthesizing a norDWIVA peptide and exploring other peptides like norKIPKA, which correspond to another osteogenic domain of the BMP-2 molecule.

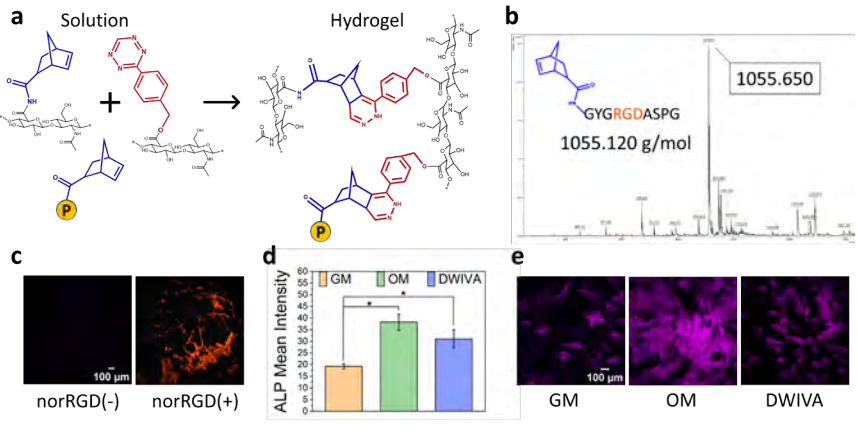


**Figure 1.** Schematic showing self-forming HA hydrogel formation with peptide functionalization: blue norbornene, red tetrazine, and peptide denoted as "P" (**a**); MALDI-TOF mass spectrum confirms norRGD presence (**b**); MSCs seeded on top of injectable hydrogels functionalized with and without norRGD (**c**); ALP mean intensity value for cells seeded on glass in growth medium (GM), osteogenic medium (OM), and GM supplemented with 2mM DWIVA (**d**); confocal images of data from plot d (**e**). * p < 0.05

# TAILORING THE RELEASE PROFILE OF A SMALL MOLECULE AGONIST TO STIMULATE HEDGEHOG SIGNALING DURING TENDON-TO-BONE INTEGRATION

J. Marcelin (1), R. Madi (1), T. Kamalitdinov (1), X. Jiang (1), S. Assi (1), D-H. Kim (1), S. Keith Lang (1), R. L. Mauck (1), A. Kuntz (1), N. Dyment (1)

(1) Department of Orthopaedic Surgery, University of Pennsylvania, Philadelphia, PA, USA

Disclosure: None

**INTRODUCTION:** Tendon injuries frequently occur at the tendon-to-bone insertion site (i.e., enthesis) and tendon-to-bone repair often leads to disorganized scar tissue formation [1]. The hedgehog (Hh) signaling pathway is a critical regulator of enthesis fibrocartilage formation and maturation during growth and development [2-4]. Thus, this pathway is a promising target for improving tendon-to-bone repair by promoting the formation of a functionally graded zonal enthesis. We previously demonstrated that stimulation of the Hh pathway via genetic activation or systemic Hh agonist injections promoted tendon-to-bone attachment formation following anterior cruciate ligament reconstruction (ACLR) [5]. Due to the important role of Hh in many tissues within the body [6], there is a need to develop localized therapies to avoid off-target effects while still effectively leveraging this pathway to improve repair outcomes. Therefore, we developed an electrospun scaffold release system containing various concentrations of SAG, a small molecule Hh signaling agonist, for use in the promotion of tendon-to-bone integration.

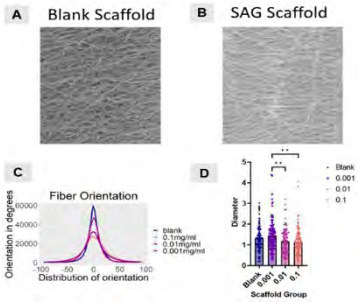


**Figure 1: SEM of blank (A) vs. SAG (B) scaffold. Fiber orientation (C) and diameter (D) measurements. **p<0.01.**

**METHODS:** Scaffold Fabrication: A 35 wt% PCL solution in DMF/THF was prepared with varying concentrations of the Hh agonist (SAG) (0, 0.001, 0.01, 0.1 mg/ml). The solution (2mL) was electrospun onto a rotating mandrel using an 18G needle at 15kV (8 m/s, 2.5 ml/hr). SEM Analysis: Fibril alignment and diameter were measured using the OrientationJ plugin in FIJI, based on FEI Quanta 600 ESEM images. Mechanics Assessment: Scaffold strips (1x20mm) were longitudinally cut, weighed, and their cross-sectional area measured using a custom non-contact laser device. Strips were uniaxially loaded at 1%/s until failure (Instron 5542). SAG Release Study: Blank and SAG-infused scaffolds were cultured, and conditioned media (CM) collected over 28 days. CM samples from various days were applied to bMSC cultures for 4 days. Gli1 gene expression was assessed by qPCR to measure Hh activity, comparing to direct SAG additions. Tunnel Integration Study: TTT surgeries were conducted on 12 mice to assess the impact of SAG release on tunnel integration. Graft tail tendons with scaffolds were passed through tibial tunnels and evaluated on day 14 post-surgery. Mineralized Cryosectioning, qPCR, and Imaging: Limbs were processed, sectioned undecalcified, and analyzed for AP staining. Statistical Analysis: Fiber diameter, scaffold mechanical properties, and in vivo qPCR and AP activity were compared using one-way ANOVA ($p<0.05$). Gli1 expression from in vitro release was assessed through two-way ANOVA with Sidak's post-hoc tests ($p<0.05$).

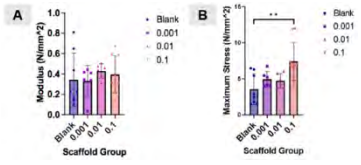


**Figure 2: Modulus (A) and maximum stress (B) values from uniaxial stress relaxation and failure tests of PCL scaffolds. **p<0.01.**

**RESULTS:** SAG incorporation affected fiber alignment but not diameter of electrospun PCL scaffolds: Using the OrientationJ plugin to measure fiber alignment from SEM images, we found that SAG incorporation reduced the overall fiber alignment ($SD_{blank} = 15.8^o$, $SD_{0.01} = 19.1^o$, $SD_{0.001} = 25.3^o$, $SD_{0.1} = 26.6^o$) in the scaffold (Fig. 1C). However, fiber diameters of the SAG scaffolds were not significantly different from the blank scaffold (Fig. 1D). SAG incorporation increased maximum stress but not modulus: We found that SAG incorporation did not alter modulus (Fig. 2A) but did increase maximum stress (Fig. 2B) in the highest concentration (0.1mg/ml) group compared to blank scaffolds. Delivery of conditioned media to bMSCs increased Gli1 expression in a dose- and time-dependent manner: As expected, we found a significant increase in Gli1 expression with 3nM (2-fold) and 300nM (70-fold) added directly to the media ($p<0.05$, Fig. 3A) vs control media. Additionally, Gli1 expression increased in the SAG scaffolds in a dose- and time-dependent manner ($p<0.05$) (Fig. 3B). Gli1 expression did not change with time in the blank scaffolds and the expression levels were comparable to the control media (C in Fig. 3A). Gli1 expression was significantly higher for all SAG concentrations (0.001, 0.01, and 0.1 mg/ml) compared to blank scaffolds in CM collected on day 2, with expression levels being comparable to 300nM media for the 0.01 and 0.1 mg/ml scaffolds. Interestingly, while Gli1 expression remained elevated in the 0.1 mg/ml SAG scaffold for CM collected out to day 26 ($p<0.05$), both the 0.01 and 0.001 mg/ml groups saw reduced Gli1 expression with time of CM collection, which resulted in 0.01 mg/ml at day 26 and 0.001mg/ml at days 8, 16 and 26 not being statistically different than blank scaffolds (Fig. 3B). Localized delivery of SAG to the bone tunnels increased Gli1 activity and alkaline phosphatase activity: We isolated tissue from the medullary canal (Fig. 4A), including the drilled tunnel, and performed qPCR, showing an increasing trend in Gli1 expression in the 0.01 and 0.1 mg/ml scaffolds at post-operative day 14 (Fig. 4B). Additionally, AP activity in the medullary canal and tunnel was significantly higher in the 0.1 mg/ml group compared to the blank scaffold ($p<0.05$, Fig. 4C).

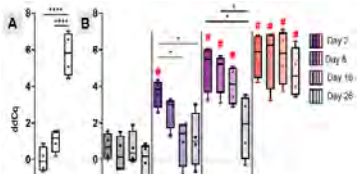


**Figure 3: Gli1 ddCq for controls (A) and blank vs the different concentrations of SAG at the four timepoints (B). ****p<0.0001, *p<0.05; # p<0.05 vs. blank.**

**DISCUSSION:** In this study, we incorporated the small molecule Hh signaling agonist, SAG, into electrospun PCL scaffolds and found that these scaffolds could release SAG *in vitro* and *in vivo* while maintaining bioactivity. The SAG incorporation had a dose-dependent effect on fiber orientation (Fig. 1B) producing an increase in maximum stress but not modulus of the scaffold (Fig. 2). The *in vitro* release profile was dose dependent with CM from the 0.1 mg/ml concentration stimulating sustained, elevated expression of Gli1 in treated bMSCs (Fig. 3), whereas the other doses saw reductions in Gli1 expression to baseline levels by the end of the one-month release experiment. When the scaffolds were inserted within the bone tunnels of a TTT *in vivo* model, the 0.01 and 0.1 mg/ml groups resulted in an increasing trend in Gli1 expression (Fig. 4B). The SAG scaffolds also showed an increasing trend in AP activity, with the 0.1 mg/ml group having significantly greater AP activity than blank scaffolds (Fig. 4C), indicative of increased fibrocartilage and bone mineralization within the bone tunnel regions. This result is consistent with our previous work using systemic injections of a Hh agonist [5]. Future studies will apply the SAG-delivering scaffolds in our more clinically-relevant, yet lower throughput, ACLR model to improve the tendon-to-bone integration processes.

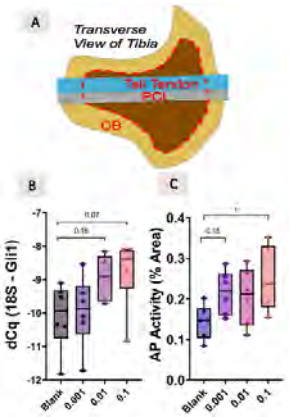


**Figure 4: Schematic representation of the TTT (A) including the area (red dotted line) used to calculate Gli1 gene expression (B) and AP activity (C).**

**ACKNOWLEDGEMENTS:** Work supported by NIH R21 R21AR078429, P30AR069619, R01AR076381, F31AR079840 (TK), and (T32-AR007132).

**REFERENCES:** [1] Kamalitdinov, T et al., *JOR*, 2020 [2] Lu, H et al., *Annu. Rev. Biomed. Eng.*, 2013 [3] Liu, C-F et al, *PLoS One*, 2013 [4] Dyment, N et al., *Dev Biol*, 2015 [5] Kamalitdinov, T et al., bioRxiv, 2022 [6] Ingham, P et al., *Nat Rev Genet.*, 2011.

**Unveiling Osteoporosis: High-Resolution Compositional Analysis of Human Bone Biopsies Using O-PTIR**

Sofia Mehmood[1], Yana Bronfman[2], Edward DiCarlo[2], Nancy Pleshko[1], and William Querido[1*]

1. Department of Bioengineering, College of Engineering, Temple University, Philadelphia PA
2. Department of Pathology and Laboratory Medicine, Hospital for Special Surgery, New York NY
* William.Querido@temple.edu

Osteoporosis is a degenerative bone disease that affects millions of people worldwide. Currently, there is a gap in understanding how tissue-level compositional properties of bone underly the poor bone quality associated with osteoporosis. Historically, infrared (IR) spectroscopy has been used to assess tissue composition, but traditional modalities cannot achieve a high enough spatial resolution to capture features of the building blocks of bone quality and integrity (mineralized collagen fibrils and bundles on the order of 500 nm). Recently, a new modality called optical photothermal infrared (O-PTIR) spectroscopy was developed to allow for IR data collection at 500 nm resolution (Figure 1), which may contribute to elucidating the submicron origins of impaired bone health. The goal of this research is to determine the feasibility of O-PTIR spectroscopy and imaging to assess the sub-micron-scale composition of human bone biopsies with osteoporosis in order to gain insight in disease development and progression. Ten human iliac crest biopsies embedded in thick blocks of polymethyl methacrylate (PMMA) were acquired from the Hospital for Special Surgery (New York, NY). Standard assessment of bone tissue structure was carried out by histology, micro computed tomography (microCT), and scanning electron microscopy (SEM). O-PTIR data from cortical and trabecular tissues were collected using the mIRage Sub-Micron IR Spectrometer (Photothermal Spectroscopy Corp), both as point spectra and single wavenumber images at specific peaks of interest, including the Amide I (protein), $PO_4$ (mineral), and PMMA peaks. The images were analyzed using ratio mapping and RGB overlays. Initial methodology establishment involved 3D modeling and printing a custom sample holder so that the thick-block samples could fit into the microscope stage. O-PTIR spectra showed typical bands associated with bone tissue composition, with minimal interference from PMMA. Sub-micron imaging of osteons and trabecula showed the visualization of lamella as well as individual osteocyte lacunae and Haversian canals. Quantitative analysis of the thousands of point spectra collected at cortical and trabecular bones reveals overall trends in tissue-level composition across all samples, including in mineral content, carbonate content, and mineral crystallinity. The findings indicated that O-PTIR spectroscopy and imaging is an effective method at analyzing the sub-micron tissue composition of human bone biopsies embedded in standard thick PMMA blocks, which may elucidate how the tissue-level composition of bone is associated with osteoporosis. Future directions will involve implementing a machine learning approach to provide deeper insight into the relationship between sub-micron tissue composition and structural properties of bone obtained by microCT and SEM.

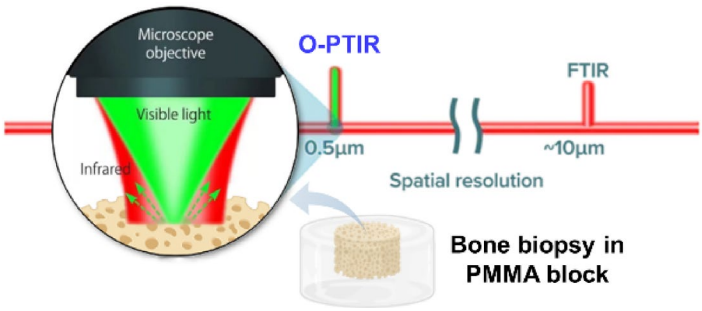


Figure 1: Diagram of how O-PTIR spectroscopy may be used to assess human bone tissue at higher spatial resolution than conventional Fourier transform infrared (FTIR) spectroscopy

# Cold Plasma treatment reduces *S. aureus* biofilm virulence factor and quorum sensing *in vitro*.

**Autumn Melvage [1], Carly Smith[1], Amanda Connelly[1], Noreen Hickok[1], Theresa A. Freeman[1]**
[1] Department of Orthopedic Surgery, Thomas Jefferson University, Philadelphia, PA
Theresa.Freeman@jefferson.edu

**Introduction:** Orthopedic infections constitute a distressing array of conditions that cause significant pain, alter the course of one's life and pose life-threatening risks. *Staphylococcal aureus* (ATCC 25923; *S. aureus*) not only reside in biofilms which protect them from direct killing by antibiotics and immune cells, but also use virulence factors to hijack, subvert, and disrupt immune cell function. Cold atmospheric plasma (ionized gas consisting of charged particles, UV radiation, electric currents, and ROS) treatment has emerged as an innovative treatment strategy to kill microorganisms, reduce bacteria virulence factor expression, and disrupt quorum sensing. Virulence factors can trigger cell death, alter the tissue environment, and disrupt immune cell-signing. For examples Superoxide dismutase (SodA) neutralizes reactive oxygen species (ROS) produced by immune cell NADPH oxidases. Panton-Valentine Leukocidin (PVL; luk-PV) creates pores in the cell membrane or the mitochondria of leukocytes, such as neutrophils, to trigger ROS release and apoptosis. Hemolysins like alpha-hemolysin (Hla) secrete a pore-forming toxin that causes cell lysis and death. In contrast, quorum sensing is a process bacteria use to communicate. AgrB and SarA regulate quorum sensing and virulence factors. AgrB is part of the Agr system complex that produces auto inducing peptide that allow bacteria react to the density and push forward transcription of virulence factors. SarA aids in triggering transcription of both the Agr system and virulence factors. Taken together, these components render the immune cell less effective. This study investigates the effect of cold plasma treatment on *s. aureus* killing, biofilm disruption, ROS response, virulence factor and quorum sensing gene expression in *in vitro*.

**Methods: *In vitro* biofilm production and cold plasma treatment:** *S. aureus* biofilms were grown on PCL discs placed in a 12-well plate in TSB for 48 hrs. Discs were rinsed in cold PBS to remove planktonic bacteria, before a 30 sec plasma treatment (sweeping motion). Discs were incubated in fresh TSB and at 37ºC for 4 hrs. **Bacterial isolation**: Discs were placed in a new 12-well plate and sonicated for 15 min. in 1 mL of PBS. **log CFU/m**: Serial dilutions were performed, and plated onto Petri films, incubated overnight, and the colonies counted. **qPCR:** RNA was isolated usingTRIzol™ Reagent, quantified using a NanoDrop, made into cDNA (Takara™ RNA to cDNA EcoDry™ Premix), and qPCR was performed for the following virulence factors: SodA, Luk-PV, hla, AgrB, and SarA compared to subculture. **Crystal Violet Stain:** Plasma treated, untreated and no biofilm discs are fixed with menthol, stained with crystal violet, and distained with acetic acid. The absorbance was record at 590nm. **Statistical analysis:** Experiments were independently performed (=> 2x), in quadruplicate. GraphPad Prism 8 (GraphPad Software, San Diego) statistical software was used to identify outliers, determine significance, and graph results.

**Results: Bacterial Killing:** Biofilm on PCL discs treated with J-Plasma had a 0.33-fold reduction in CFU (p=.0008) compared to the untreated discs. **Crystal Violet Staining:** Biofilm on PCL discs treated with J-Plasma had a 1.6-fold reduction in absorbance (p=.0062) absorbance compared to untreated discs. The effects of J-plasma treatment on gene expression (by qPCR) of bacteria in biofilms grown on PCL discs is shown in Table 1. (signif. ** = p≤ .0001;* = p≤.1)

**Table 1. Average Fold Change (qPCR) 4 hrs post-Treatment**

| Virulence factor/quorum sensing | SodA | luk-PV | hla | AgrB | SarA |
|---|---|---|---|---|---|
| Biofilm w/ no Treatment | 22.47 | 16.50 | 2.02 | 8.92 | 4.35 |
| J-Plasma Treated Biofilm | 0.38** | -7.02** | -3.27** | 3.53** | 0.66* |

**Discussion: T**he results indicate cold plasma treatment has the ability to actively reduce biofilm both thru direct killing and disruption. Additionally, the treatment with cold plasma significantly reduces both virulence factor and quorum sensing genes expression. Taken together, treatment with cold plasma should aid in immune cell killing of *s. aureus* infections. Importantly, this type of treatment can be used in conjunction with other treatments. Additional studies *in vivo* will better assess the immune reaction to these treatments.

**Significance/Clinical Relevance:** Cold plasma offers a non-antibiotic treatment option to address the serious issues of surgical site infection and anti-biotic resistance. Understanding biofilm gene expression in response to treatment is a helpful tool to determine how disruption of staph immune evasion will promote effective clearing by immune system.

**ACKNOWLEDGEMENTS:** This work was supported by NIH grant R01AR076941 (Freeman) from NIAMS. Special thanks to Emilee Brockner and Rachel Evans from the Hickok lab for help with bacterial protocols.

**Perichondrium-resident progenitor cells cause osteochondroma formation.**

Christina Mundy[1], Sadhana Ramesh[1], Sarah Catheline[2] , and Maurizio Pacifici[1]
[1] *Translational Research Program in Pediatric Orthopaedics, Division of Orthopaedic Surgery, Children's Hospital of Philadelphia, Philadelphia, PA*
[2] *University of Rochester Medical Center, Rochester, NY*

Hereditary Multiple Osteochondroma (HMO) is a rare, pediatric skeletal disorder characterized by benign cartilaginous tumors called osteochondromas (OCs) that form along the border between the growth plate and perichondrium. Most HMO cases are caused by loss-of-function mutations in the heparan sulfate (HS)-synthesizing enzymes EXT1 or EXT2, resulting in a systemic decrease in HS levels. HS deficiency increases the availability of growth factors and signaling proteins, thus driving aberrant chondrogenesis and osteochondroma formation. However, it remains unknown as to what cell population(s) (i.e., chondrocytes, perichondrial progenitors or both) are responsible for osteochondroma formation. Our current HMO mouse model uses *AggrecanCreER* to conditionally ablate floxed *Ext1* in both perichondrium and growth plate chondrocytes, making it difficult to pinpoint a cellular origin. Ex vivo studies from our lab previously showed that interference with HS alters perichondrial phenotype and border function and leads to ectopic chondrogenesis, indicating that perichondrium could be a major culprit in osteochondroma formation. To determine whether the same holds true in vivo, we ablated floxed *Ext1* by mating with *Pdgfrα*-Cre-ER mice. Using tdTomato as a reporter, image analysis showed that *Pdgfrα* reporter activity specifically characterized progenitor cells in perichondrium in long bones and ribs but not adjacent growth plate chondrocytes. MicroCT and histological images of long bones and ribs from *Ext1$^{f/f}$; Pdgfrα-CreER; tdTomato* mice revealed that appreciable osteochondromas did develop along those skeletal elements over time. Immunohistochemistry showed that perichondrial cells were Tomato positive and chondrocytes within the OCs themselves were SOX9 positive. In additional in vitro studies, populations of perichondrial/periosteal cells were treated with the HS antagonist Surfen. Compared to controls, the treated cultures exhibited a sharp upregulation of such chondrogenic markers as *Sox9*, *Acan* and *Col2a1* and increases in cartilage proteoglycan production. Together, the data reveal that perichondrial progenitor cells are responsible for osteochondroma formation. Their normal mesenchymal phenotype and perichondrium/growth plate border function are clearly deranged upon loss of *Ext* expression and drop in HS levels.

# YAP regulates periosteal progenitor cell proliferation through both cell intrinsic and extrinsic co-transcriptional programs

Madhura P. Nijsure[1], Annemarie Lang[1], Elizabeth Seidl[1], Christopher J. Panebianco[1], Miriam Baitner[1]Gabrielle Tanner[1], Dakota L. Jones[1], Yasaman Moharrer[1], Annapurna Pranatharthi-Haran[1], Greg Szeto[2], Nathaniel Dyment[1], Joel D. Boerckel[1]
University of Pennsylvania[1], Seagen[2]

Bone fracture repair activates the transcriptional regulator, YAP, in periosteal cells and initiates periosteal cell proliferation. Deletion of YAP, and its paralog TAZ, from Osterix-expressing cells impairs periosteal cell proliferation and periosteal expansion[1]. The transcriptional mechanisms by which YAP drives periosteal expansion are unclear. YAP does not directly bind to DNA but forms a complex with other transcription factors to regulate transcriptional activity. It is therefore important to identify both YAP transcriptional programs and the associated transcription factor partners.

To this end, we used a gain-of-function model to induce expression of constitutively active YAP ($YAP^{S127A}$) upon treatment with doxycycline. We isolated periosteal cells from 4-day old fracture calluses and treated them with 1μM doxycycline in vitro. We performed orthogonal Bulk mRNA sequencing (RNA-seq) and Assayed for Transposase Accessible Chromatin with sequencing (ATAC-seq) to quantify YAP-induced messenger RNAs and YAP-regulated chromatin accessibility, respectively. This analysis identified YAP target genes and putative transcription factor binding partners in periosteal cells.

Gene set variation analysis revealed 236 gene sets most relevant to progenitor pool expansion during fracture repair (Fig 1A). $YAP^{S127A}$ activation significantly enriched gene sets involving cell cycle progression and Smad2/3 signaling and suppressed gene sets marking caspase pathways involved in apoptosis. Specifically, $YAP^{S127A}$ upregulated both cell intrinsic factors, such as Cdk6, and cell extrinsic or secreted factors, such as Bmp4 and Cyr61. Analysis of DNA motifs present in differentially accessible chromatin revealed enrichment of chromatin loci containing the consensus binding motifs of the TEAD and Smad2/3 transcription factors (Fig 1B). $YAP^{S127A}$ activation elevated canonical YAP-TEAD complex target genes and enriched Smad2/3-target gene sets, supporting roles for both TEAD and Smad2/3 as putative transcriptional co-effectors of YAP in periosteal osteoblast precursors. We further validated YAP-TEAD binding in periosteal cells by immunoprecipitating YAP and probing for TEAD (Fig 1C).

Finally, to define the impact of YAP/TAZ signaling on cell proliferation in vivo, we deleted YAP/TAZ from Osterix expressing cells in mice. There was a significant decrease in proliferation and cell numbers of both Osterix-targeted cells and non-targeted cells, confirming that YAP/TAZ signaling functionally regulates periosteal progenitor proliferation through both cell intrinsic and extrinsic mechanisms (Fig 1D).

Together, these data reveal that YAP and TAZ regulate proliferation-associated gene expression partially through TEAD and promote functional periosteal expansion for fracture repair.

References:

1. Kegelman+, JBMR 2020

# Trans-endplate diffusion across the spectrum of human disc degeneration

Brianna S. Orozco[1,2], Sarah E. Gullbrand[1,2]
[1]University of Pennsylvania, Philadelphia, PA; [2]Corporal Michael J. Crescenz VA Medical Center, Philadelphia, PA
**Disclosures:** BSO (N) - Brianna.Orozco@Pennmedicine.upenn.edu, SEG (6)

**INTRODUCTION:** The intervertebral discs are the largest avascular structures in the body and depend primarily on diffusion via the vertebral endplates to receive nutrients and expel waste products.[1] Due to the avascularity of the intervertebral discs, it has been suggested that reduced disc nutrition is a significant contributor to the degenerative process.[1] Studies have shown that the reduction of disc nutrients can occur due to the calcification of the endplate that impairs diffusion to the disc.[2] However, alterations in trans-endplate transport across the spectrum of spinal degeneration and the relative contributions of pathology in the boney and cartilage endplate remain poorly understood. In this study, human cadaveric endplate samples were used to assess and correlate trans-endplate diffusion with the structure, composition, and mechanical function of the boney and cartilage endplate to determine factors affecting trans-endplate transport across the spectrum of disc degeneration.

**METHODS:** Four lumbar spines (1 male, 3 female, 50-70 yo) were obtained from human cadavers (Science Care). T2-weighted MRIs were obtained for disc Pfirrmann grading, and T2 mapping was used quantify nucleus pulposus (NP) T2 relaxation times.[3] Spinal motions segments (n=20) were dissected. From each disc, tissue samples of nucleus populous and annulus fibrosus were obtained from each motion segment and underwent biochemical assays including DMMB to quantify GAG concentration, PicoGreen to quantify DNA, and Hydroxyproline for collagen quantification. From these segments, two cylindrical cores (n=18) with a diameter of 10 mm and an average thickness of 2.50 mm were obtained that included endplate-cartilage interface with trabecular bone. One core was used for passive diffusion experiments (**Figure 1A**) using a custom diffusion chamber. The upstream chamber was loaded with 1.1 mg/mL of sodium fluorescein (MW = 367.27), and triplicates of the downstream chamber were collected every hour for 6 hours. Fluorescence was read via a microplate reader, and the concentration of the downstream chamber calculated based on a fluorescein standard curve. Total diffusion was quantified by calculating the area under the curve (AUC). Endplate cores were then fixed and µCT scanned with a resolution of 7.40 µm to evaluate boney endplate morphometry and cartilage thickness following repeated µCT after staining the cores overnight with Lugol's solution.

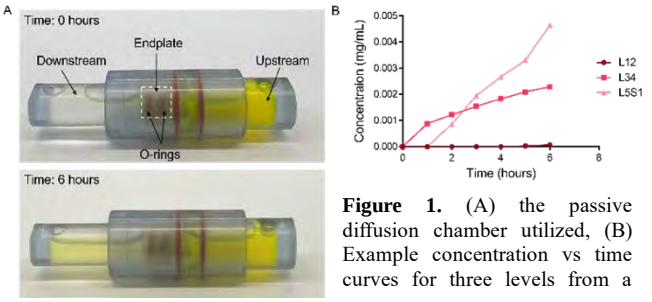


**Figure 1.** (A) the passive diffusion chamber utilized, (B) Example concentration vs time curves for three levels from a

**RESULTS:** Diffusion experiments demonstrated significant variability in trans-endplate diffusion across donors and spinal levels within the same donor (**Figure 1B**). Correlations between NP T2 and diffusion revealed a bimodal relationship between diffusion and disc health. When discs were stratified further by Pfirrmann Grade, there was a significant positive linear correlation between NP T2 and diffusion for Pfirrmann Grade 2 discs, however, there was a trend towards increasing diffusion with decreasing NP T2 relaxation time in Pfirrmann Grade 3 discs (**Figure 2A**). Comparison of NP GAG content between samples with low (AUC < 5) and high (AUC > 5) diffusion demonstrated that NP GAG content trended lower in samples with high diffusion (**Figure 2B**). 3D µCT reconstructions demonstrated substantial variability in boney endplate porosity across levels even from the same donor, which could affect passive diffusion (**Figure 2C**). However, no significant correlation was found between endplate bone volume fraction (BV/TV) and passive diffusion (**Figure 2D**). Cartilage endplate thickness measured from Lugol's enhanced µCT (**Figure 2E**) was found to significantly inversely correlate with passive diffusion, demonstrating that as cartilage endplate thickness increases, passive diffusion decreases (**Figure 2F**).

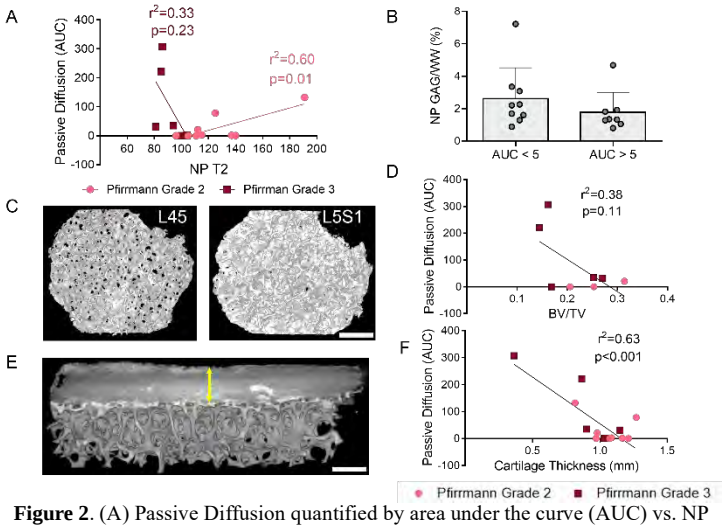


**Figure 2**. (A) Passive Diffusion quantified by area under the curve (AUC) vs. NP T2, (B) Nucleus Pulpous GAG Content compared to AUC, (C) Images of µCT that show porosity of samples among the same donor, (D) Passive Diffusion (AUC) not correlated with BV/TV, (C) Image of a endplate cross-section showing stained cartilage endplate (indicated by the arrow) with Lugol's Solution, (F) Passive Diffusion (AUC) correlated with cartilage thickness. Scale = 0.5 mm.

**DISCUSSION:** Our results suggest that trans-endplate diffusion is not altered in a linear fashion across the spectrum of disc degeneration, as both healthy (high NP T2) and degenerative (low NP T2) discs exhibited high trans-endplate diffusion – a trend also observed in prior human MRI studies of diffusion into the disc.[4] A limitation of the current study is that our sample set contained primarily moderately degenerative discs, and therefore we are currently expanding our sample set to include more healthy and severely degenerative discs to more rigorously quantify the spectrum of disease. Our data also suggests that cartilage endplate thickness is the main structural factor affecting solute transport under passive diffusion. Prior studies have demonstrated the effect of cartilage endplate composition on diffusion, which is currently being investigated in our ongoing work, in addition to cartilage endplate mechanical properties.[5] Interestingly, only weak correlations between diffusion and boney endplate density were observed, in contrast to our prior work in a rabbit disc degeneration model.[6] It is possible that the boney endplate may have a greater impact on disc nutrition during convective transport. It has shown that dynamic loading induced convective flow can augment transport into the disc, and future work will focus on understanding the endplate structure-function properties conducive to enhanced transport under convective flow.[7]

**SIGNIFICANCE**: The results from this study further our understanding of the pathomechanisms of disc degeneration, which can ultimately contribute to improved diagnostics and treatments for this debilitating condition.

**REFERENCES:** [1] Maroudas+ *J. Anat*., 1975 [2] Benneker+ *Spine*, 1976 [3] Ashinsky+ *J. Anat*., 2020 [4] Rajasekaran+ *Spine*, 2004 [5] Dolor+ *J. Plos One, 2019* [6] Ashinksky+ *ASBMR*, 2020 [7] Sampson+ *J. of Biomechanics*, 2019

**ACKNOWLEDGEMENTS:** This study was supported by the Department of Veterans' Affairs.

**Establishing Optogenetic RhoA Tools in Tenocytes to Study the Cellular Response to Tendinopathy**

Elizabeth Seidl[1,2], Erin E. Berlew[1,2], Paula Camacho Sierra[1], Joel D. Boerckel[1,2]
[1]Department of Orthopaedic Surgery, University of Pennsylvania, Philadelphia, Pennsylvania
[2]Department of Bioengineering, University of Pennsylvania, Philadelphia, Pennsylvania

A healthy Achilles tendon and corresponding tenocytes exist in tensional homeostasis, a tensioned state allowing them to be loaded. Microdamage present in tendinopathy alters the tensional state of the tissue, altering the collagen matrix. After de-tensioning, the matrix becomes disorganized and degraded with an increase in matrix metalloproteinases (MMPs)[1].

When investigating the mechanisms of the cellular response to de-tensioning optogenetic tools allow for better spatial and temporal control over tools such as blebbistatin. Utilizing a previously engineered, single-component optogenetic BcLOV4 tool, RhoA is recruited to the membrane in the presence of blue light stimulation, activating RhoA signaling subsequently controlling actin polymerization within a cell[2].

The ability to utilize this tool in tenocytes allows for the precise control over cell tensioning due to actin polymerization. When utilizing the optoRhoA tool, we are able to evaluate the plasmid's integration into the cell utilizing an mCherry fluorescent reporter attached to the tool. Utilizing a lentivirus packaging system and a design of experiment approach we systemically varied conditions of lentivirus infection to allow for uptake of the optoRhoA tool in cultured tenocytes. The virus is made by transfection of the engineering optoRhoA plasmids into HEK cells. Two days later, the virus is harvested from the media. The cells were infected utilizing a Polybrene transfection reagent. Starting with the addition of 400 μ L of virus into a 35 mm plate and a concentration of 5 μ g/mL of Polybrene, various variables were manipulated to allow for the uptake of the optoRhoA tool into isolated mouse tenocytes. 50% more virus, 50% less virus and a higher concentration of Polybrene, 10 μ g/mL were all utilized for infection without expression of mCherry within the cells. However, removal of antibiotics from the growth media during infection, 10 μ g/mL concentration of Polybrene saw successful uptake of the optoRhoA tool by observation of mCherry fluorescence. Under these conditions 400 μ L of virus was used to infect isolated human tenocytes in a 35 mm plate. Additionally, 800 μ L of virus under these conditions was used for successful infection of isolate mouse tenocytes. Successful uptake of the optoRhoA tools in both mouse and human tenocytes presents a novel system to precisely study cellular response to tensile stresses relevant to tendinopathy.

[1] Jones, Dakota L et al. "Mechanoepigenetic regulation of extracellular matrix homeostasis via Yap and Taz." Proceedings of the National Academy of Sciences of the United States of America vol. 120,22 (2023): e2211947120. doi:10.1073/pnas.2211947120
[2] Berlew, Erin E et al. "Single-Component Optogenetic Tools for Inducible RhoA GTPase Signaling." Advanced biology vol. 5,9 (2021): e2100810. doi:10.1002/adbi.202100810

Grant NIH/NIAMS P50AR080581 from the National Institute of Arthritis and Musculoskeletal and Skin Diseases of the NIH.
Support has also been provided by the Perelman School of Medicine at the University of Pennsylvania.

# A 'Clickable' Hydrogel for Annulus Fibrosus Repair After Intervertebral Disc Herniation

Emily E. Sharp[1-3], Karen L. Xu[1,2], Zhiliang Cheng[1], Jason A. Burdick[4], Sarah E. Gullbrand[2,3], and Robert L. Mauck[1-3]
[1]Dept. of Bioengineering, [2]Dept. of Orthopaedic Surgery, University of Pennsylvania, Philadelphia, PA, [3]Translational Musculoskeletal Research Center, Corporal Michael J. Crescenz VA Medical Center, Philadelphia, PA, [4]BioFrontiers Institute and Dept. of Chemical and Biological Engineering, University of Colorado, Boulder, CO

**Disclosures:** Sarah E. Gullbrand (6), Robert L. Mauck (8, 6, 4)

**INTRODUCTION:** Aging, trauma, and overuse can lead to intervertebral disc (IVD) herniations, where the nucleus pulposus (NP) extrudes beyond the boundaries of the annulus fibrosus (AF). This disrupts the functional role of the IVD and can result in significant pain. Microdiscectomy, where the herniated NP tissue is surgically excised, is the gold standard of care, but does not restore AF mechanical integrity, and reherniations may occur through the unrepaired defect. Multifunctional biomaterials may overcome this limitation and achieve functional AF repair. We developed a norbornene-modified hyaluronic acid (NorHA) hydrogel that satisfies baseline AF repair criteria (biocompatible, injectable, mechanically compatible)[1] and is capable of spatiotemporal controlled delivery via click chemistry. Click chemistry is a class of reactions where two small molecules rapidly and strongly bind to one another and has recently been successfully leveraged for therapeutic delivery *in vivo*.[2] In this study, we evaluated the durability of click-functionalization, characterized hydrogel material properties, and demonstrated an *ex vivo* AF repair.

**METHODS:** Hydrogel Fabrication: NorHA synthesis and hydrogel fabrication were accomplished using established protocols.[3] Percent crosslinking was 50% (unless otherwise specified) and hydrogel weight percent varied between 3-5%. Click-functionalization was achieved via the addition of thiol-PEG-azide (TPA) to the hydrogel precursor solution. The level of TPA modification varied from ~3.3% (TPA1) to ~13.2% (TPA4). Upon UV exposure, hydrogel photocrosslinking and azide-modification occur simultaneously. Click Validation: Here, the click counterpart to azide is dibenzocyclooctyne (DBCO). 3 wt% NorHA and NorHA-TPA hydrogels, of varying degrees of azide-modification, were fabricated, allowed to swell overnight in PBS, and incubated in a 30 μM DBCO-modified Alexa Fluorophore (AF-488-DBCO) solution for 1 hour. Hydrogels were imaged via an Axiozoom microscope for up to 4 weeks and incubated in PBS on an orbital shaker at 4 C between imaging. Mechanical and Rheological Properties: 3 and 5 wt% NorHA and NorHA-TPA4 hydrogels were tested using a stress relaxation protocol (10% strain at 0.05%/s followed by stress relaxation for 10 min.) to determine the equilibrium modulus. To assess gelation kinetics, 5 wt% NorHA and NorHA-TPA4 precursor solutions were exposed to UV light for 180 seconds and storage modulus was assessed via rheology at 1% strain at 1 Hz. Curves were fitted with a one phase association exponential fit to determine Tau values (i.e., time to gelation). Cytocompatibility: Bovine AF cells (40,000 cells/cm$^2$) were seeded on sterile 3 wt% NorHA and NorHA-TPA4 hydrogels additionally modified with thiol-RGD peptide (1 mM). Cell viability and proliferation were monitored over 7 days via the AlamarBlue assay, and cells were imaged on day 3 to investigate cell adhesion. Gel Retention in AF defects: A cruciate injury to the AF was created in bovine caudal discs, and the defect was either left empty or filled with 5 wt% NorHA-TPA4 with a crosslinking density of 80%. The explant was cycled under physiologic loading (300 N) for 10,000 cycles using an Instron. Statistical Analysis: All statistics were conducted in GraphPad Prism with significance thresholds of *p<0.05 and **p<0.01. Outliers were removed from each dataset and significant differences were detected using the appropriate ANOVA test.

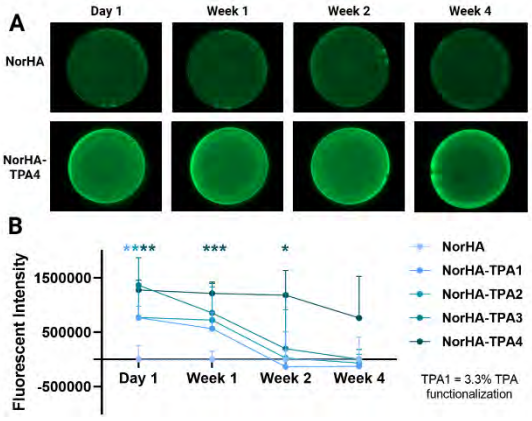


**Figure 1**: A) Hydrogels with varying levels of TPA incubated in AF-488-DBCO and washed for up to 4 weeks. B) Fluorescent intensity when varying TPA modification. n=4

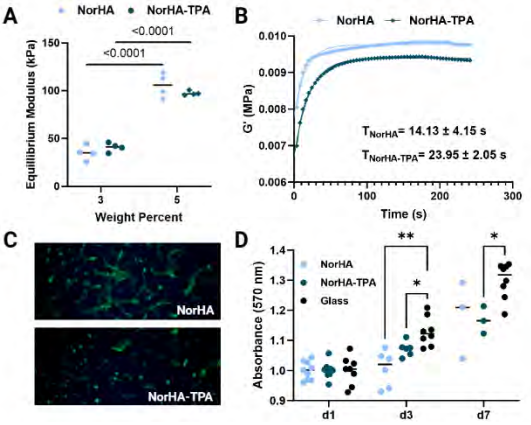


**Figure 2**: A) Equilibrium moduli for NorHA and NorHA-TPA4 hydrogels of varying weight percent. B) Gelation kinetics of hydrogels with respective Tau values. C) Day 3 images of AF cells seeded onto hydrogels. D) AlamarBlue data of cells seeded onto hydrogels for up to a week. n=≥3

**RESULTS:** DBCO-modified fluorophores preferentially bound to NorHA-TPA hydrogels, and the degree of this attachment could be tailored based on degree of azide-modification (Fig. 1). Specifically, increasing azide-modification increased DBCO-fluorophore attachment and prolonged length of attachment. Hydrogel mechanics could be tailored by changing weight percent (Fig. 2A). While the addition of TPA did not impact bulk hydrogel mechanics, it slightly slowed gelation kinetics as indicated by larger Tau values for NorHA-TPA hydrogels; overall, gelation remained rapid (<30 s) (Fig. 2B). Additionally, AF cells readily adhered to the hydrogels by day 3 (Fig. 2C) and cell proliferation increased over time (Fig. 2D). Lastly, NorHA-TPA gel mediated repair of an annular defect and remained within the defect following 10,000 physiological compression cycles (Fig. 3).

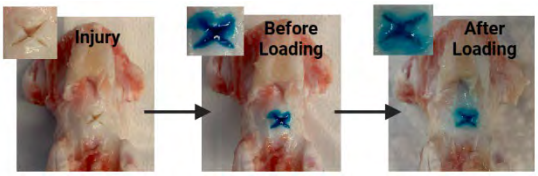


**Figure 3**: AF repair via NorHA-TPA (blue) before and after physiologic loading for 10,000 cycles. n=1

**DISCUSSION:** NorHA hydrogels are promising candidates for tissue repair due to their injectability, biocompatibility, and biodegradability, but do not inherently possess controlled delivery capacity. Here, we demonstrated that NorHA hydrogels can be functionalized to enable controlled delivery via secondary azide-alkyne click reactions. The addition of TPA enhanced attachment of DBCO-modified fluorophores and varying the degree of azide-modification enabled tailoring of the extent and duration of attachment. This suggests that DBCO-modified therapeutics or nanocarriers can be effectively tethered to the hydrogel, localizing the therapeutic with considerable control over its release profile. Importantly, TPA incorporation did not adversely impact hydrogel mechanics, mechanical tunability, or gelation kinetics. Cell adhesion and proliferation were also not affected by TPA addition, although there are observable differences in cell morphology, which may be due to increased hydrophobicity of the NorHA-TPA hydrogels. Excitingly, *ex vivo* testing demonstrated that NorHA-TPA remained within the annular defect over 10,000 cycles of physiologic loading. Future work will explore these hydrogels *in vivo* via subcutaneous implantation and disc injury models, in addition to evaluating DBCO-modified therapeutic and nanocarrier attachment to the hydrogel and therapeutic release profiles.

**SIGNIFICANCE:** Our 'clickable' hydrogel has the potential to repair the AF following herniation, transforming clinical practices and creating superior surgical alternatives and outcomes for patients. Broadly, this novel multifunctional biomaterial can be employed to repair multiple different tissue types and injuries, revolutionizing how we approach dense connective tissue repair.

**REFERENCES:** 1. Long, RG, *et. al.*, J Biomech. Eng. (2016) 2. Peplow, M. Nature Biotech. (2023) 3. Gramlich, WM, *et. al.*, Biomaterials (2013)

**ACKNOWLEDGEMENTS:** This work was supported by the Department of Veterans Affairs and the NIH. The authors would also like to gratefully acknowledge Dr. Kyle Vining and Dr. Ryan Locke for their contributions.

A Novel MR-Based Fluid-to-Fat Ratio to Improve the Accuracy of Knee Effusion Diagnosis in Children

Elizabeth Silvestro MSE, Iman Naqvi, Jie C. Nguyen, MD, MS, Raymond Sze MAMS MD, Flaura Winston MD PhD, and Michael Hast, PhD

While guidelines exist for quantifying knee effusion in adults, no such guideline exists in children. Assessment of pediatric knee effusions remains subjective and rater dependent. Confounding factors include weight, sex differences, and variability in suprapatellar fluid volume. To date, no standardized quantitative methods are widely used in MR-based diagnosis and estimating pediatric knee effusions. This study evaluates the accuracy of a novel fluid-fat ratio in its ability to improve the diagnosis of pediatric knee effusion, taking into account confounders.

Methods & Materials: A retrospective study of eighty 8-10-year-old patients with knee magnetic resonance imaging (MR) examinations was analyzed. The outcome of interest was a clinical diagnosis of effusion. The purposeful sample included 10 per group of eight subpopulations defined by the following patient characteristics: weight class (healthy/overweight), diagnosis(physiologic/effusion), and gender (male/female). Exclusion criteria included chronic conditions or prior instrumentation, images without reports, and poor image quality. Images analyzed included sagittal intermediate–weighted, sagittal, and axial T2-weighted fat-suppressed pulse sequences. Images were segmented (Materialise Mimics) to create the patella, femur, subcutaneous fat, and suprapatellar fluid volumes. 2D measurements of the suprapatellar fluid were measured at the thickest point on all slices, and subcutaneous fat was measured at a mid-sagittal slice. 2D fluid-fat thickness ratio and 3D fluid-fat volumes were calculated. Three-way ANOVAs and pairwise comparisons were performed to determine accuracy overall and within subpopulations.

Results: There was a positive association between diagnosis of effusion and 2D ratio ($p < 0.0001$) and weight class ($p= 0.0352$), with no significant interaction between factors. The effusion diagnosis was associated with the 3D ratio ($p= 0.0011$). The association of the 2D ratio was present in healthy-weight males (2D: 2.6 to 1.2, 3D: .09 to .03), overweight males (2D: 2.4 to 0.9, 3D: 0.15 to 0.02), and healthy weight females (2D: 0.032, 3D: 0.21 to 0.007), but not for overweight females; shown in figure 1 below. The 2D and 3D ratios were correlated (R2:0.79).

Conclusions: The new 2D or 3D MR-based fluid-fat ratios show early promise as new quantifiable metrics for effusion diagnosis, except in overweight girls. Future research should examine whether misdiagnosis or other factors might explain the lack of association between the ratios and effusion in overweight girls.

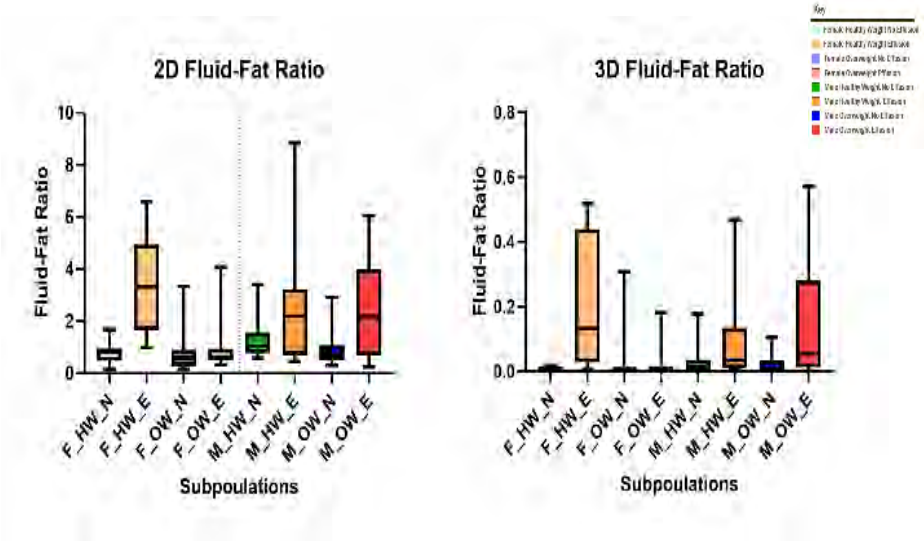


Figure 1. Box-and-whisker of the 2D and 3D fluid-fat ratio for -10-year-old patients in each of the subpopulations defined by the characteristics: weight class (healthy/overweight), diagnosis(physiologic/effusion), and gender (male/female).

# Cold plasma treatment of established periprosthetic infection mobilizes the innate immune response.

**Carly J. Smith[1], Amanda Watkins[2], Autumn Melvage[1], Amanda Connelly[1], Thomas P. Schaer[2], Theresa A. Freeman[1]**

[1]Department of Orthopedic Surgery, Thomas Jefferson University, Philadelphia, PA
[2]University of Pennsylvania, School of Veterinary Medicine, Kennett Square, PA
Theresa.Freeman@jefferson.edu

**INTRODUCTION:** Orthopedic periprosthetic infections are dangerous and often associated with the formation of biofilms on implanted materials. Biofilms present one of the most significant challenges to successful treatment as they are naturally more resistant to antibiotics and immune cell infiltration [1]. Thus, there is an increasing need to explore non-antibiotic therapies to treat these infections. Cold plasma, an energized gas which produces a cocktail of reactive products including reactive oxygen and nitrogen species (ROS/RNS), is an emerging non-antibiotic candidate which offers a unique approach to infection control [2]. ROS/RNS can both inhibit bacterial pathogenesis through direct killing and can promote innate immune cell degranulation [3]. The goal of this study is to investigate the benefits of using cold plasma for *Staphylococcus aureus* (*S. aureus*) infection treatment in an orthopedic model of surgical revision.

**METHODS:** *Animals and Surgical Procedure:* At the index surgery (Day -7) male Sprague-Dawley rats were anesthetized and a craniolateral incision between the vastus lateralis and the biceps femoris was created to access the femur. 1.7 mm titanium screws were placed at the proximal and distal ends, and a mid-diaphyseal empty drill hole was created to expose the medullary cavity. A collagen sponge impregnated with 250 µL of *S. aureus* ATCC 25923 at 1 x $10^6$ CFU (infected) or saline (uninfected) was positioned over the screws and the empty hole. Seven days later, a revision surgery (Day 0) was performed through the previous incision. An 8-hole plate was secured using 1.7 mm titanium screws with 2 proximal and 2 distal to the open mid-diaphyseal hole. Infected animals were treated with either 0.3% betadine (n=5) or 30 seconds of J-plasma® (n=5). End-term timepoints were taken at 6-hours, 4-days, and 14-days post-revision. *Plasma Treatment:* Plasma was administered during revision surgery for 30-seconds using the J-plasma® device at power 70 (Apyx Medical). *Microbial Analysis:* The tissue or hardware was vortexed in 5 mL sterile phosphate buffered saline (PBS). Serial dilutions of the fluid from the muscle or hardware were transferred to Petri films, incubated at 37 C for 24 hours, and counted to determine log CFU/mL. *RNA Analysis:* RNA sequencing and gene expression analysis (NovoGene) was performed on periprosthetic soft tissue from 3 rats/group. RT-qPCR was used to confirm the results. *Histology:* Tissue is fixed in 4% paraformaldehyde (PFA) for >24 hours before being embedded in paraffin blocks. 5 µM sections were used for staining.

**RESULTS:** Plasma treatment does not significantly reduce bacterial CFUs at 4- or 14-days post-revision. Interestingly, the correlation between bacterial CFU and IL-1β in the infected muscle did not correlate, possibly indicating subversion of the innate immune response. However, after plasma treatment CFU and IL-1β became highly correlated. When a Pearson's correlation matrix of gene expressions (determined by qPCR) of several key cytokines (IL-1β, IL-17, IL-6, and NOS2) was compiled, the same pattern was observed, from no correlation with infection alone, to significant correlations after plasma treatment. Taken together, this indicates a renewed and coordinated innate immune response after plasma treatment. Additional evidence of a renewed innate immune response was observed when lymph node size was compared. A significant reduction in lymph node size as early as 6 hrs post-plasma treatment was observed. In addition, RNA sequencing data comparing plasma treatment to betadine treatment confirmed these results. GSEA confirmed significant enrichment in genes involved in "Neutrophil Activation Involved in an Immune Response" and "Neutrophil Chemotaxis."

**DISCUSSION:** Cold plasma is a possible non-antibiotic candidate for treating bacterial infections [2, 3]. While bacterial load was not decreased after plasma treatment *in vivo*, our results do suggest renewed activation of a more "classical" immune response associated with improved bacterial sensing and destruction. Infiltration of neutrophils and reduction in lymph node size indicates restoration enhanced innate immune response is localized to the treated muscle tissue. This type of therapy may provide an opportunity for applying a synergistic treatment which would build on the plasma treatment generated response to eradicate the infection more effectively. As such, cold plasma treatment may be a viable addition to the clinical standard of care of antibiotic application, to disrupt the biofilm and combat infection-related quiescence of innate immunity to improved outcomes following revision surgery.

**ACKNOWLEDGEMENTS:** This work was supported by NIH grant R01AR076941 (Freeman) from NIAMS. Special thanks to Samantha Gonzalez and Abigail Lucas for their help with histology and quantification.

**REFERENCES:**

[1] Silva, V. *et al.* Biofilm formation of multidrug-resistant mrsa strains isolated from different types of human infections. *Pathogens* **10**, (2021).
[2] Nguyen L et al., Cold atmospheric plasma is a viable solution for treating orthopedic infection: a review. 2018 Dec.
[3] Smolková B et al., Critical Analysis of Non-Thermal Plasma-Driven Modulation of Immune Cells from Clinical Perspective. 2020 Aug

# Passive loading has a partial role of mechanobiology in postnatal tendon development.

Yuna Usami[1], Takanori Ito[1], Koyo Nogi[1], Riku Saito[1], Takanori Kokubun[1,2]
[1]Graduate School of Health, Medicine, and Welfare, Saitama Prefectural University, Saitama, Japan,
[2]Department of Physical Therapy, School of Health and Social Services, Saitama Prefectural University, Saitama, Japan
Email:usami-yuna@spu.ac.jp

**Disclosures:** All authors have no disclosures

**INTRODUCTION**: The tendon is critical for transmitting muscle-generated loads to joint movement. The tendon developmental process involves multiple biological organizations from the embryonic to the early postnatal period. Some previous studies showed muscle contraction is essential for tendon differentiation and growth [1,2]. These studies focused on the developmental mechanism of the embryo phase through the analysis of transgenic mice. However, postnatal is also the foundation phase for proper mechanical function [3], and regeneration abilities already exist. [4] Our previous work has demonstrated that major genes, such as Scleraxis, changed dynamically during the embryo and postnatal phase in Achilles tendon development. Especially postnatal tendon development showed a relationship between biological events and developing locomotion ability because Scx expression increased with locomotion changes. [5] These results indicated the importance of the postnatal development phase to understand the detailed mechanism of mechanobiology of tendon development. [6] However, little is known about how postural changes affect tendon development as mechanical stimulation, unlike the embryo phase. In muscle contraction-inhibited models in previous studies, the joint motion by external loading with changing the physical movement may induce the mechanobiological response via passive stretching of the muscle-tendon complex. But there are no studies referred to this point and unveiled yet. Our objective of this study is to explore the roles of internal and external mechanical forces to contribute to postnatal tendon maturation. Utilizing the denervation and arthrodesis model, we made a each-controlled model of both internal muscle contraction and external joint movement with loading mechanical force models. (Fig.1) Our central hypothesis is that the mechanical force generated by muscle contraction and external tension from joint movement with loading promotes tendon maturation in the early postnatal.

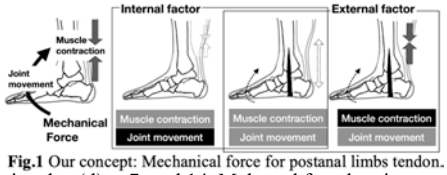


**Fig.1** Our concept: Mechanical force for postanal limbs tendon.

**METHODS**: All animal procedures were approved by the Animal Care and Use Committee at Saitama Prefectural University (2021-14). Experimental Design. We divided wild-type C57BL/6 mice into four different models: sciatic nerve denervation model (DN) induced flaccid paralysis, Ankle Arthrodesis Model (Arth) to limit joint movement, both DN and Arth (DA), and Sham in P7 mice. We developed a novel arthrodesis model; Arth placed a 0.15mm diameter stainless needle retrogradely through the calcaneus and across the tibiotalar joint. Achilles tendons were harvested from the post-operative day (d) at 7, and 14. Male and female mice were distributed evenly between groups. The ankle dorsiflexion test. The self-made dorsiflexion equipment with an X-ray device detected the degree of ankle dorsiflexion angle traction by a heavy sinker. Functional Gait. Gait was analyzed by DeepLabCut (DLC) [7] marker-less pose estimation with deep learning and to detect mechanical force for the limb following interventions. Cage activity. Quantity of exercise detected from cage activity before 1 day collect d14 sample using DLC. Gross Image. Zeiss Semi305 captured the whole tendon before each analysis. Histology. The cryosections were used for AlcianBlue/Hematoxylin and Eosin (HE). Mechanical Test. Functional properties of the tendon were assessed using the biomechanical testing system Univert, and tendon cross-sectional area (CSA) was measured from three evenly spaced width and depth measurements from a high-resolution digital camera of both top and side views of the tendon. Transmission electron microscopy (TEM). Ultra-thin sections were stained with 0.2% Oolong Tea Extract/PBS for 30 min followed by lead citrate for 10 min and photographed, and digital images were acquired using EM1010, JEOL, and DegitalMicrograph, Gatan, Inc. Statistics. Statistical analyses included Student's t-test, one-way ANOVA tests followed by Tukey multiple comparison corrections, and Kruskal-Wallis with Dunn's multiple comparisons test.

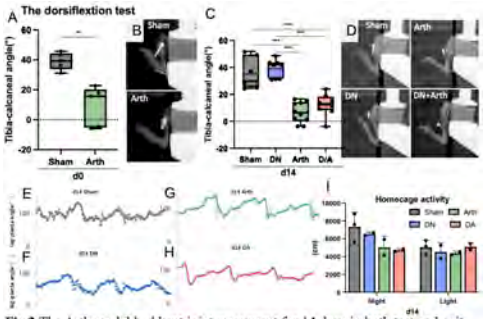


**Fig.2** The Arth model had kept joint movement for 14 days in both test and gait.

**RESULTS SECTION**: First, we developed a novel Arth model, and the capacity to inhibit joint movement of Arth was kept between d0 to d14 (Fig.2A-D, n=8-10, $p < 0.05$). Moreover, DN at d14 showed a large dorsiflexion angle during gait (Fig.2E-H). The DN and DA tendon width at d14 was significantly lower than the Sham (Fig.3A, n=4, $P < 0.05$). We observed a decrease in locomotion in the group with the pin inserted compared to Sham (Fig.2E). DN and DA tendon trend to decreased tensile mechanics (Fig.3C). TEM images showed DN and DA showed a trend toward an increase in collagen fiber gaps compared to Sham.

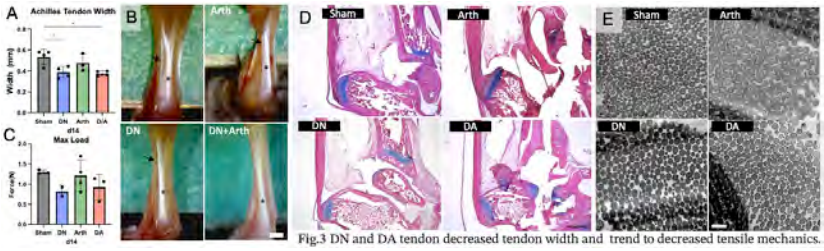


Fig.3 DN and DA tendon decreased tendon width and trend to decreased tensile mechanics.

**DISCUSSION**: Our results indicate that both muscle contraction and external force disrupt increasing tendon size and tensile mechanics (Fig.3A-C). External loading has a part of critical role in stimulating tendon development as well, but this effect is smaller than internal loading depending on muscle contraction. Recent studies focused on the postnatal phase are increasing; however, many of them used transgenic techniques for the tendon itself. The tendon development of these animals is affected by two major effects: the direct effect of the deletion of specific genes and the indirect effects of the phenotype of gene editing. This indirect effect is an alteration of physical movement depending on the changed monophony. However, the discussion of transgenic research only referred to the direct effect. In this study, we showed the data of cage activity as the external mechanical stimulation, and the intervention group showed a decreased cage activity. In tendon development, these mechanical effects in the postnatal phase give us the key aspect of tendon maturation.

**SIGNIFICANCE/CLINICAL RELEVANCE**: An improved understanding of the tendon maturation mechanism during postnatal will be crucial to governing early tenocyte maturation. If tendon mature mechanism induced by mechanical force harnessed therapeutically, such as rehabilitation, it could provide a clue in the clinical treatment of tendon healing or childhood disease.

**REFERENCES**: 1. Arvind et al., *Ann N Y Acad Sci*, 2018; 2. Havis E et al. *Development*. 2016; 3. C Fan et al., *Cell Rep*. 2020; 4. DA Kaji et al., *eLife*, 2020; 5. Usami Y et al., *bioRxiv*, 2023; ;6. Usami Y et al., *Research Square*. 2022; 7. Mathis et al., *Nat Neurosci*. 2018
**ACKNOWLEDGEMENTS**: Work supported by The Nakatomi Foundation and Kawano Masanori Memorial Public Interest Incorporated Foundation for Promotion of Pediatrics.

# Neutrophil influences macrophage behavior but not healing outcome in Volumetric Muscle Loss (VML) Fibrosis

Ricardo Whitaker and Kara Spiller, PhD

Volumetric Muscle Loss (VML) is a debilitating condition defined by the rapid loss of muscle mass, leading to permanent impairment. The current standard of care is highly inefficient and clinical trials using decellularized matrix to fill the defect showed only a 37% improvement in muscle force. Furthermore, the molecular/cellular processes governing VML repair are poorly understood, hindering treatment development. **The goal of this study is to uncover the dysfunctional immune response following VML to instruct better treatments.**

We employed a murine model of VML using subcritical size injuries (Regenerative), and critical size injuries (Fibrotic). Fibrotic macrophages displayed a higher inflammatory and less reparative phenotype, observed via flow cytometry. Interestingly, splenic macrophages displayed a similar phenotype, suggesting systemic repercussions from this local injury. NanoString of FACS-sorted macrophages indicated a broad and indiscriminate gene downregulation of Fibrotic macrophage at Day 1after injury. This suggests that changes in macrophage phenotype occur soon after injury, and prior to onset of fibrosis.

NanoString and Luminex analyses of whole-muscle and blood, respectively, displayed a higher expression of neutrophil chemokines and G-CSF after Fibrotic injuries. Muscle flow cytometry analysis confirmed an increase in neutrophils in Fibrotic injuries compared to Regenerative ones. These results point to neutrophils as possible macrophage modulators.

Similar analyses on neutrophil demonstrated an increase in apoptosis in Fibrotic neutrophil, with little differences in gene expression compared to Regenerative neutrophils. Partial neutrophil depletion improved macrophage phenotype by decreasing inflammatory and increasing reparative markers expression, at the gene and protein level. However, no improvement in muscle structure was observed. These results demonstrate that although partial neutrophil depletion improves macrophage phenotype, that is not enough to leverage tissue healing.

We have performed, to our knowledge, the most thorough macrophage characterization, locally and systemic, in VML. These novel results can instruct the development of efficient therapies for VML.

**Microinterfaces in bicontinuous hydrogels enable rapid 3D cell migration.**

Karen L. Xu[1,2,5,6], Nikolas Di Caprio[1,2,7], Hooman Fallahi[3], Mohammad Dehghany[2,4], Matthew D. Davidson[2,7,8], Brian C. H. Cheung[9], Lorielle Laforest[5,6], Mingming Wu[9], Vivek Shenoy[2,4], Lin Han[3], Robert L. Mauck[1,2,5,6], Jason A. Burdick[1,2,7,8]

[1]Department of Bioengineering, University of Pennsylvania, Philadelphia, PA, USA
[2]Center for Engineering Mechanobiology, University of Pennsylvania, Philadelphia, PA 19104, USA
[3]School of Biomedical Engineering, Science and Health Systems, Drexel University, Philadelphia, PA, 19104 USA
[4]Department of Materials Science and Engineering, University of Pennsylvania, Philadelphia, PA 19104, USA.
[5]McKay Orthopaedic Research Laboratory, Department of Orthopaedic Surgery, Perelman School of Medicine, University of Pennsylvania, Philadelphia, PA, USA
[6]Translational Musculoskeletal Research Center, Corporal Michael J. Crescenz VA Medical Center, Philadelphia, PA, USA
[7]BioFrontiers Institute, University of Colorado Boulder, Boulder, CO, USA
[8]Department of Chemical and Biological Engineering, University of Colorado Boulder, Boulder, CO, USA
[9]Department of Biological and Environmental Engineering, Cornell University, Ithaca, NY, USA.

## INTRODUCTION

Cell migration is critical for tissue development and regeneration but requires extracellular environments that are conducive to motion. Cells may actively generate migratory routes in vivo by degrading or remodeling their environments or may instead utilize existing ECM microstructures or microtracks as innate pathways for migration. While hydrogels in general are valuable tools for probing the extracellular regulators of 3D migration, few have recapitulated these natural migration paths. Here, we developed a biopolymer-based (i.e., gelatin and hyaluronic acid) bicontinuous hydrogel formed through controlled solution immiscibility whose continuous subdomains and high micro-interfacial surface area enabled rapid 3D migration of meniscal fibrochondrocytes, particularly when compared to homogeneous hydrogels. Our findings introduce a new design that leverages important local interfaces to enable rapid cell migration with implications for repair of meniscus tissue.

## METHODS

Material Fabrication: Bicontinuous hydrogels were fabricated through the mixing of guest-host (GH) physical networks (adamantane-modified hyaluronic acid (AD-HA) and cyclodextrin-modified HA (CD-HA)) with covalent gelatin networks (transglutaminase crosslinked) (Fig 1A). All studies performed were conducted with 5 wt% gelatin, 1 U/mL transglutaminase and 0, 1 or 3 wt% GH, where 1 and 3 wt% GH hydrogels were bicontinuous, and 0% was a homogenous control group. In vitro Cell Interactions: Meniscal fibrochondrocyte (MFC) spheroids were formed through 48-hour culture and then embedded within bicontinuous hydrogels. Cell outgrowth was assessed by staining actin cytoskeletons and averaging radii of outgrowth from the spheroid edge.

## RESULTS

We developed a bicontinuous (Fig 1A) network due to the immiscibility of the combined guest-host (GH) physical crosslinking [1] of HA and covalent (i.e., transglutaminase) crosslinking of gelatin (Fig 1A). These hydrogels introduced microinterfaces between gelatin-rich and gelatin-poor domains, serving as microtracks that supported cell migration (Fig. 1B). As such, these microtracks provided paths in the bicontinuous hydrogels (1, 3%) that supported rapid cell migration when compared migration in the homogenous control group (0%, Fig 1C). This work addresses how the biophysical structure of bicontinuous hydrogels influences cell migration, introducing a potential design criterion to improve tissue engineered approaches to repair meniscus defects.

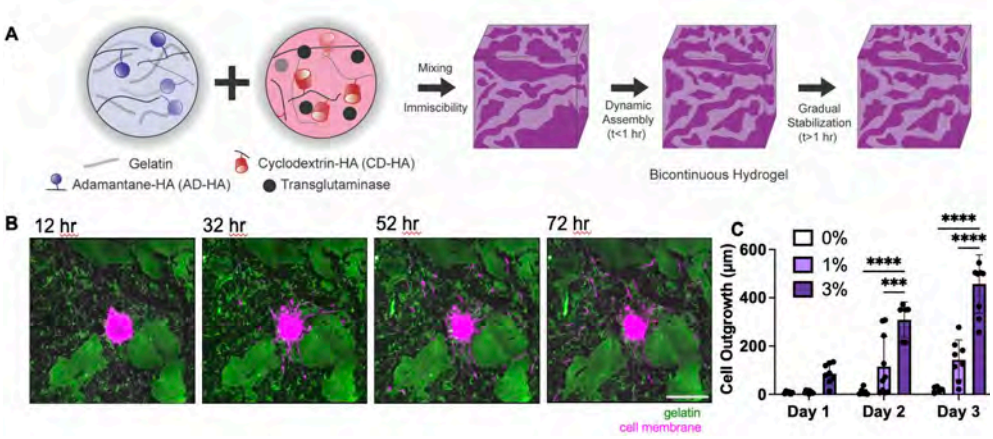


**Figure 1: A) Schematic of bicontinuous hydrogel fabrication. B) Representative images of cell outgrowth in bicontinuous hydrogel (3% group). Scale bar = 200 $\mu$m. C) Quantification of cell outgrowth across experimental groups over time. n= 6-10 spheroids per group. Two-way ANOVA with Tukey post-hoc. ***p ≤ 0.001, ****p ≤ 0.0001**

## ACKNOWLEDGEMENTS

This work was supported by the Center for Engineering Mechanobiology (CMMI: 1548571) and the National Institutes of Health (F30 AG074508, R01 AR056624).

## REFERENCES

[1] Rodell et al. *Biomacromolecules*. 14, 11, 4125–4134, 2013

# Serum Biomarkers Discovered by SomaScan in Patients with Severe Low Back Pain

**Tate Q, MD, MS[1], Markova DZ, PhD[2], Kepler CK, MD, MBA[2], Zhang Y, MD, PhD[1,3]**

[1]Departments of Physical Medicine & Rehabilitation, University of Pennsylvania; Philadelphia, PA;
[2]Department of Orthopedics, Thomas Jefferson University; Philadelphia, PA;
[3]Section of Rehabilitation Medicine, Corporal Michael J. Crescenz Veterans Affairs Medical Center, Philadelphia, PA.

**Introduction.** Low back pain is a common clinical problem. Although imaging studies are widely used to evaluate back pain, the link between low back pain and intervertebral disc (IVD) degeneration on images is unclear in many cases. Biomarkers for discogenic pain have been examined with candidate marker approaches in the past. In this study, we used a proteomic approach to examine 1512 serum proteins. Biomarkers identified include molecules known to correlate with back pain, as well as novel molecules.

**Methods.** Whole blood samples were obtained from 29 patients with severe low back pain before surgery and 11 healthy controls. Patient-reported outcomes were collected preoperatively and the degree of IVD degeneration was classified using Pfirrmann grade on preoperative imaging. Serum was separated from the whole blood, and 55 µl of serum was used to quantify protein levels by SomaScan (SomaLogic, Denver, CO).

**Results.** Biomarker signatures discovered clearly distinguish patients with low back pain from normal controls. Further, a comparison of back pain patients < 40 years of age and similarly aged healthy controls showed that inflammation-related pathways were upregulated in the patients, with leukocyte proliferation pathway the most enriched, and STAT3 (signal transducer and activator of transcription 3) showing the largest number of protein-protein interactions. Among the downregulated biomarkers comparing these two cohorts, SMAD protein phosphorylation pathway was the most enriched, and IL6 (interleukin 6) the most connected. Markers in older back pain patients ≥ 40 years of age differed from younger patients in immune-related pathways, while CD36 (cluster of differentiation 36) has the most interactions with other proteins. Overrepresented pathways and proteins with the largest network connections may be effective treatment targets.

**Significance.** This is a preliminary study of the serum of 40 subjects including participants with severe low back pain prior to undergoing low back surgery, and normal controls. Of the 1500 proteins studied, 370 proteins were identified as significantly different between the two groups. Future work includes studying these differences in a larger case-controlled population, expanding the number of proteins considered, and completing a confirmative, quantitative assay for key markers. Following up with patients for their function and pain level would further confirm the diagnostic and prognostic values of the biomarkers identified.

**Acknowledgements.** We gratefully thank the University of Pennsylvania (Penn) for funding the SomaScan. We gratefull thank the patients and volunteers at Thomas Jefferson University for donating blood samples.

# Biochemical and Mechanical Modulations of Age-Dependent ECM-Based Hydrogel Systems for Meniscus Zone-Specific Repair

Se-Hwan Lee[1], Zizhao Li[1], Yujia Zhang[1], Dong Hwa Kim[1], Jason A. Burdick[2], Robert L. Mauck[1], and Su-Jin Heo[1]
[1]University of Pennsylvania, Philadelphia, PA, [2]University of Colorado, Boulder, CO.

**Disclosures:** Lee (N), Li (N), Zhang (N), Kim (N), Burdick (N), Mauck (4-Mechano-therapeutics, 5-4WEB Medical, 8-JOR Spine), and Heo (5-4WEB Medical)

**INTRODUCTION**: Repairing injuries within the meniscal avascular zone poses a significant challenge due to its limited intrinsic healing capacity **[1]**. The meniscus represents a complex tissue wherein biological and mechanical properties intricately vary across distinct zones **[2]**. It is well understood that the extracellular matrix (ECM) components of the meniscus undergo changes during tissue development, thereby influencing cellular phenotype and function **[3]**. Our recent work introduced bovine meniscus decellularized meniscus ECM (MeDEM)-based hydrogel systems, and demonstrated that DEM components could enhance meniscus cell proliferation and differentiation **[4]**. However, the intricate interplay between biochemical and mechanical alterations in the DEM during tissue development and their modulation of cellular responses remains elusive. Hence, this study delves into the impact of age-dependent DEM across a range of physiologic stiffnesses on cellular behavior, coupled with comprehensive proteomic analysis of the materials. Moreover, addressing meniscus tears might require injectable materials characterized by diverse properties tailored to specific meniscus tissue zones. Here, we further advance our investigation by developing a stiffness-tunable MeDEM based injectable hydrogel system by coupling DEM methacrylated hyaluronic acid (MeHA) and assessed how these hydrogels regulate cell phenotypes, thereby offering insight into their therapeutic potential.

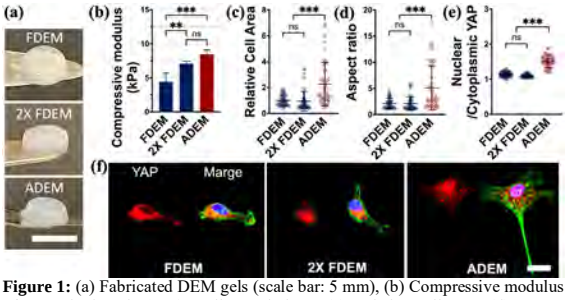


**Figure 1:** (a) Fabricated DEM gels (scale bar: 5 mm), (b) Compressive modulus of DEM hydrogels (n=5). Cell morphology: (c) Relative cell area, (d) Aspect ratio, (e) YAP nuclear localization (ns: not significant, **: p<0.01, ***: p<0.001), (f) Immunofluorescence images (Red: YAP, Green: F-actin, and Blue: DAPI; scale bar: 20 $\mu m$).

**METHODS:** Fetal (3rd trimester) and adult (<30 months) bovine menisci were decellularized using our established protocol **[5]**. FDEM (Fetal MeDEM), 2X FDEM (twice the concentration of FDEM), ADEM (Adult MeDEM), or FADEM (FDEM and ADEM mixed in a 1:1 ratio) pre-gels were prepared by digesting in an acetic acid solution **[4-6]**. 'Soft' (35% modified) and 'stiff' (100% modified) MeHA were synthesized and additionally, a combination of 'Soft and Stiff' MeHA in a 1:1 ratio was created. To achieve stiffness-tunable hydrogels, 1.5% FADEM was blended with 1.0% Soft, Stiff, or Soft/Stiff MeHA, with the inclusion of Irgacure 2959 for UV light-induced crosslinking. Subsequently, DEM-based MeHA hydrogels were crosslinked in a cylindrical mold under UV light at 37 ℃ **(Fig. 1a)**. The mechanical properties of the hydrogels were evaluated to measure their compressive moduli **[6]**. For proteomic characterization, gene ontology (GO) analysis was conducted on mass spectrometry data from four different donors per group to explore the correlation of specific proteins involved in both the mechanical and biological characteristics of the age-dependent DEM systems. Juvenile bovine mesenchymal stem cells (MSCs; P2) were seeded onto the hydrogels and cultured in basal growth media. At day 3, cells were stained with Phalloidin, primary antibodies against YAP, and DAPI, and images were captured. Cell area, aspect ratio, and YAP nuclear localization were quantified using ImageJ. Expression of Collagen type-I (COL1A2), SOX-9, and TGF were determined via RT-PCR on Day 7 with GAPDH as a housekeeping gene.

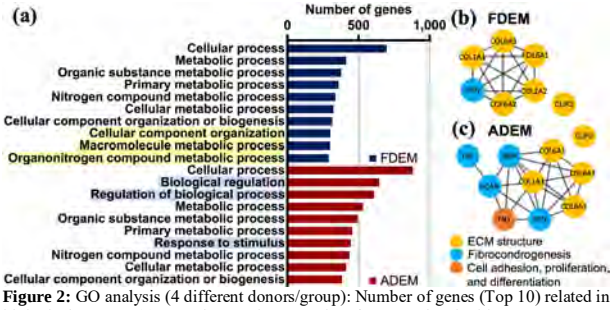


**Figure 2:** GO analysis (4 different donors/group): Number of genes (Top 10) related in biological process (a), Protein-protein networks of genes related with ECM structure, Fibrocondrogensis, cell adhesion, proliferation, and differentiation in FDEM (b) and ADEM (c).

**RESULTS:** ADEM hydrogels had a higher stiffness compared to FDEM hydrogels, and increasing FDEM concentration yielded a comparable compressive modulus to ADEM hydrogel **(Fig. 1b)**. Enhanced cell area, aspect ratio, and YAP nuclear localization were evident on ADEM hydrogels, while an elevated concentration of FDEM (resulting in increased stiffness, 2X FDEM) yielded no significant changes, suggesting the dominance of biochemical effects in the age-dependent DEM system. Proteomic analysis revealed an abundance of proteins related to biological regulation, response to stimuli, and biological processes in the ADEM system as compared to FDEM **(Fig. 2a)**. Remarkably, among the top 30 proteins constituting the majority of DEM systems, fibrochondrogenesis-related genes were prominent in ADEM **(Fig. 2c)**, including key regulators of cell adhesion, proliferation, and differentiation, including Fibronectin (FN1), forming a highly interconnected network **(Fig. 2c)**. Next, to enhance material injectability and better match specific tissue zones, stiffness-tunable DEM-based MeHA hydrogels were developed, exhibiting a wide range of stiffnesses **(Fig. 3a)**. MSCs cultured on FADEM-based stiffness-modulated MeHA demonstrated elongation and alignment on the stiff system **(Fig. 3b)**, with elevated YAP nuclear localization **(Fig. 3c)**. Notably, Stiff MeHA-based FADEM groups exhibited heightened COL1A2 expression **(Fig. 3d)**. Interestingly, chondrogenic markers SOX9 and TGF were higher across all MeHA-supplemented groups. Remarkably, the introduction of MeHA to DEM not only boosted chondrogenic gene expression but notably, stiff MeHA stimulated fibrochondrogenic gene expression in MSCs **(Fig. 3d)**.

**DISCUSSION:** This study explored the potential of age-dependent MeDEM hydrogel systems for meniscus repair, focusing on their biomechanical and biological effects. Notably, ADEM hydrogels exhibited increased stiffness, and adjusting FDEM concentration yielded similar stiffness levels. Interestingly, the 2X FDEM hydrogels showed minimal effects on cell behavior, suggesting biochemical factors might outweigh mechanical influences from this fetal source material. Proteomic analysis highlighted distinct GO profiles in FDEM and ADEM systems, with fibrochondrogenesis-related genes abundant in ADEM, indicating age-dependent DEM processing results in meniscus-derived ECM of differing composition. The innovative development of stiffness-tunable DEM-based MeHA hydrogel systems allowed precise control over stiffness, revealing the role of stiffness in regulating cellular behaviors. Stiff MeHA upregulated fibrous and chondrogenic gene expressions, while soft and soft/stiff MeHA enhanced chondrogenic gene expression in MSCs. Overall, our findings emphasize the importance of considering both biochemical and mechanical cues for effective meniscus repair strategies, with implications for tailored zone-specific meniscus repair. Current research endeavors are directed towards utilizing RNA-seq to investigate the impact of age-dependent ECM on transcriptome profiling in meniscus cells, to unveil underlying molecular mechanisms. Additionally, ongoing in vivo animal tests are being conducted to assess the therapeutic potential of these findings.

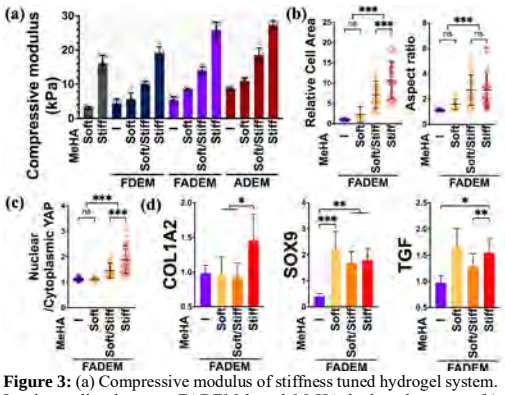


**Figure 3:** (a) Compressive modulus of stiffness tuned hydrogel system. In vitro cell culture on FADEM based MeHA hydrogel system: (b) Relative cell area, Aspect ratio, and (c) YAP nuclear localization, (d) Gene expression (*: p<0.05, **: p<0.01, ***: p<0.001, ns: not significant).

**SIGNIFICANCE:** The newly developed tunable DEM-based MeHA hydrogel system holds promise for effectively addressing zone-specific repair and regeneration in meniscus injuries.

**REFERENCES:** [1] Yan+, *Front Cell Dev Biol* 2021; [2] Murphy+, *J Mech Behav Biomed Mater* 2019; [3] Acun+, *Biomaterials* 2021; [4] Lee+, ORS 2023; [5] Lee+, ORS 2022; [6] Gao+, *Adv Funct Mat* 2017; [7] Mauck+, *J Biomech Eng* 2000. **ACKNOWLEDGEMENTS:** This work was supported by the National Institutes of Health (K01 AR077087, R56 HL163168).

# YOUR FEEDBACK IS IMPORTANT!

## Please take a minute to complete the survey to help with future Symposiums

**https://upenn.co1.qualtrics.com/jfe/form/SV_0MLsd8ERk8eKoRM**

QR Code to Survey